RMIT UNIVERSITY

Investigations of TiO_2 NP as Radiation Dose Enhancement Agent: In Vitro and Phantom Based Studies

A Thesis submitted to the School of Graduate Research in fulfilment of the requirements for the degree of

Doctor of Philosophy (PhD)

By:

Esho Qasho Youkhana

BSc (General Physics)

MSc (Plasma Physics)

In the Discipline of Medical Radiations

School of Health and BioMedical Sciences

College of Science, Engineering and Health

RMIT University

Melbourne, VIC, Australia

September 2017

Declaration

I hereby certify that except where due acknowledgement has been made, all of the work described within this thesis is the original work of the author alone; the work has not been submitted previously, in whole or in part, to qualify for any other academic award; the content of the PhD thesis is the result of work which has been carried out since the official commencement date of the approved research program; and, any published (or unpublished) ideas and/or results from the work of others are acknowledged in accordance with the standard referencing guidelines, and ethics procedures and guidelines have been followed.

Esho Qasho Youkhana

September 2017

Acknowledgments

I am grateful to all whom have helped me and contributed in one way or another with their valuable assistance to have the opportunity and possibility to continue the graduate study of doctoral of philosophy degree and for offering all necessary requirements to complete this research.

First and foremost, I would like to express my deepest appreciation for the invaluable guidance and support of my PhD principle supervisor A/Prof Moshi Geso. This thesis would not have been possible without the continuous advice, helpful suggestions, constant support and friendship he provided over the course of my PhD research, for which I will remain forever grateful. His unsurpassed knowledge and enthusiasm for the exploration of new ideas in scientific research is infectious and has inspired me to constantly seek to become a better researcher.

I am also grateful to my second supervisor Dr. Trevor Ackerly and all staff members, especially Frank Gagliardi, from the William Buckland Radiotherapy Centre, Alfred Hospital, and also Dr. Peter Harty from Australian Radiation Protection and Nuclear Safety Agency (ARPANSA) for so graciously providing facilities and assistance in irradiation work; for the countless hours, during the day and also after hours, which they made available for cell and phantom irradiation whenever it was required.

My research has also given me the privilege of interacting with distinguished researchers in other disciplines, Universities and organizations to whom I will also always be indebted for their willingness to share their knowledge and perspectives. In particular, I would like to express my special thanks to Dr. Bryce Feltis, who helped me

with synthesising NPs and taught me the techniques required to culture cells and supervised my experimental work with cells. I would also like to thank Dr. Anton Blencowe from the University of South Australia for his valuable guidance and assistance with NPs surface modification. I would also express my gratitude to Professor Rick Franich from Physics Department at School of Science Cluster for his assistance in scanning PRESAGE dosimeters with optical CT scanner. A special thanks goes to Dr. Matthew Field and the staff at RMIT Microscopy and Microanalysis Facility and also to Sioe Volaric from the Department of Chemical and Biomolecular Engineering at the University of Melbourne for permitting the use of facilities and providing technical assistance with NPs characterisation work. I must also make special mention of Harris Panopoulos and Stan Poniger the cyclotron engineers at the Centre for PET- Austin Health for permitting to use the centre facilities and for their valuable assistance with NP activation via proton beam.

I also would like to acknowledge several researchers and staff in the School of Health and Biomedical Science, RMIT University; A/Prof Paul Wright and Dr. Julie Quach for allowing the use of certain pieces of equipment from the teaching laboratory. Special acknowledge to the contribution and friendship of colleagues from Medical Radiation Research Group, especially Dr. Madeleine Shanahan and Clare Smith. I acknowledge the support I have received for my research through the provision of an Australian Government Research Training Program Scholarship and from the School of Health and Biomedical Sciences, RMIT University. Finally, I want to acknowledge the financial support from the Ministry of Higher Education and Scientific Research under the scholarship program of the Human Capacity Development Program (HCDP) in Kurdistan region/Iraq.

Dedication

Every challenging work needs commitment, determination and self-efforts as well as support and guidance from others especially those who were very close to our heart

In the completion of my doctoral thesis, I dedicate my humble effort to my sweet and lovely wife "Jolyana" and the angels in my life: my daughters "Yonella & Elinora" Without their support and understanding, I would have not achieved my goal.

I love you all

I dedicate this simple work to my mother who always encourage and making me be whom I am. In addition, I dedicate this thesis to my sisters, family, friends and teachers.

Contents

List of Figures

List of Tables

Abbreviations and Acronyms

Abbreviation	Definition
1D, 2D, 3D	One, Two, Three dimensional
APTS	AmenoPropyl Trimethoxysilane
ASTM	American society for testing and materials
ATP	Adenosine triphosphate
AuNPs	Gold nanoparticles
BiNPs	Bismuth-based nanoparticles
C.S.	Compton scatter
CT	Computed tomography
D	Dose
D.E.	Dose enhancement
DBTDL	Dibutiltin dilaurate
DCFDA	Dichlorofluorescein diacetate
DEF	Dose enhancement factor
DMSO	Dimethyl sulfoxide
DNA	Deoxyribonucleic Acid
DU145	Prostate cancer cells
EDTA	Ethylenediaminetetraacetic
FBS	Foetal bovine serum
FCM	Flow cytometry
FTIR	Fourier transform infrared spectroscopy
HaCaT	Human keratinocyte cells
HC	High current
HVL	Half value layer
IARC	International agency for research on cancer
IC	Ionisation chamber
IGRT	Image-guided radiotherapy
IMRT	Intensity modulated radiotherapy
LCV	Crystal violet lactone
LET	Linear energy transfer
LFCM	Laser fluorescence confocal microscopy
LINAC	Linear accelerator
LMG	Leucomalachite green
LQ	Linear quadratic model
MEM	Minimum essential *media*
MSDS	Material Safety Data Sheet
MU	Monitor unit
NADPH	Nicotinamide adenine dinucleotide phosphate
OCT	Optical computed tomography

OD	Optical density
P.E.	Photoelectric effect
PDD	Percentage depth dose
PE	Plating efficiency
PEGTS	PolyEthylene Glycol Trimethoxysilane
PET	Positron-emission tomography
RMMF	RMIT microscopy and microanalysis facility
RNA	Ribonucleic acids
ROS	Reactive oxygen species
SEF	Sensitivity enhancement factor
SF	Survival fraction
SPECT	Photon emission computerised tomography
SPR	Surface Plasmon resonance
SRS	Stereotactic radiosurgery
SXRT	Superficial X-ray therapy
TEM	Transmition electron microscopy
TGA	Thermogravimetric analysis
$TiCl_4$	Titanium chloride
TiO_2 NPs	Titanium dioxide nanoparticles
TiONts	Titanium nanotubes
TLD	Thermoluminescent detectors
VMAT	Volumaetric modulated radiotherapy
VOC	Volatile organic compound
XPS	X-ray photoelectrons spectroscopy
XRD	X-ray diffraction
Z	Atomic number
Z_{eff}	Effective atomic number
λ	Wavelength
μ	Linear attenuation coefficient
μ/ρ	Mass attenuation coefficient
μ_{en}/ρ	Mass energy absorption coefficient
ρ	Physical density
ρ_e	Electron density

Publications

JOURNAL ARTICLES:

Youkhana E. Q., Gagliardi F., Geso M. *"Two-dimensional scanning of PRESAGE® dosimetry using UV/VIS spectrophotometry and its potential application in radiotherapy.*" Biomedical Physics & Engineering Express. 2016; **2**(4): p. 045009.

Youkhana E., Feltis B., Geso M. *Radiation Dose Enhancement by Anatase TiO_2 NPs.* Medical Physics. 2016; **43**(6): p. 3677.

Geso M., Youkhana E., Feltis B. *Anatase Titanium dioxide nanoparticles (TiO_2 NPs) as a radiosensitization agent for radiation therapy: in vitro and phantom based studies*. Australasian Physical & Engineering Sciences in Medicine (APESM). 2016; **39**(4): p.1120-1121.

Youkhana E. Q., Feltis B., Blencowe A., Geso M. *Titanium Dioxide Nanoparticles as Radiosensitisers: An In vitro and Phantom-Based Study*. International Journal of Medical Sciences. 2017; **14**(6): p. 602-614.

Youkhana E. Q., Geso M. *Titanium Dioxide Nanoparticles (TiO_2 NPs) Activation by Proton Beam for Radiologic-Imaging.* Theranostic. 2017; (in preparation).

Youkhana E. Q., Algithami M., Feltis B., Geso M. *A comparative study between Clonogenic and MTS assays as a tool for quantifying radiation dose enhancement induced by nanoparticles*. Nanomedicine: Nanotechnology, Biology and Medicine. 2017; (in preparation).

CONFERENCE PRESENTATIONS:

Youkhana E., Feltis B., Geso M. Radiation Dose Enhancement by Anatase TiO_2 NPs. *American Association of Physicist in Medicine (AAPM) 58th Annual Meeting & Exhibition*, 29 July – 4 August 2016, Washington DC, United States of America.

Youkhana E., Feltis B., Geso M. Anatase Titanium dioxide nanoparticles (TiO_2 NPs) as a radiosensitization agent for radiation therapy: *in vitro* and phantom based studies. *Engineering and Physical Science in Medicine (EPSM)*. 6-10 November 2016, the Australian Technology Park (ATP), Sydney, Australia.

Abstract

Radiotherapy is one of the basic methods for cancer treatments. This extremely valuable and effective technique deliver high therapeutic doses of ionising radiations to the malignant cells to shrink tumours and kill cancer cells in a way that is safer and more reliable. The source of this ionising radiation is typically high energy photon or electron beams, which are potentially carcinogenic and/or deadly to all cells at high dosage. Therefore, the major obstacle of planning and delivery of radiotherapy is the preservation of healthy surrounding tissues by limiting the delivered radiation dose to the tolerance levels of normal tissues while still ensuring the effective targeting of tumour volumes to eradicate it.

Developments in the field of nanotechnology have potentially provided effective radiotherapy techniques through the use of high and medium atomic number (Z) nanostructure materials as radiosensitisation agents. The high Z nanoparticles (NPs) such as gold, bismuth compound, iodine and gadolinium have already been successfully utilised as radiosensitiser agents when applied to tumours for *in vitro*, *in vivo* and even in some preclinical trials. However, the high and medium Z materials are more toxic than low Z elements, therefore investigation of radiosensitasation induced by low Z elements have become more attractive. Several studies have been conducted to test the low Z nanoparticles as dose enhancing agents. Most of these studies were in the field of UV and X-rays of kilovoltage energy ranges. This thesis' research extends thier application to include the most common form of radiotherapy i.e. using megavoltage range of X-rays. The aims of this thesis are focused on investigations of employing low Z materials and particularly anatase titanium dioxide nanoparticles (TiO_2 NPs) as potential radiosensitisation agent and as imaging agent too.

This research was conducted by two main ways, one by using phantoms (PRESAGE® dosimeters) and the other by *in vitro* using two types of cell lines, cultured human

keratinocyte (HaCaT) and prostate cancer (DU145) cells, and both methods were aimed at determining the effects on NPs on the radiation dose enhancement at both low (kilovoltage) and high (megavoltage) radiotherapy X-ray beams. Furthermore, TiO_2 NPs were activated via proton beam to investigate for their suitability as diagnostic agent hence this nano-compound qualifies to be true theranostic agent.

Several characteristics of TiO_2 NPs, which make them ideally suited for application in radiotherapy, are investigated throughout this research. Anatase TiO_2 NPs were synthesised, characterised and functionalised to allow dispersion in culture medium for *in vitro* studies and halocarbons (PRESAGE® chemical compositions) for phantom based studies. The fabricated PRESAGE® dosimeters/phantoms were scanned to obtain the physical and radiological properties and further to determine the radiation dose enhancement induced by TiO_2 NPs. Clonogenic and cell viability assays were employed to determine cells survival curves from which the dose enhancement levels "radiosensitisation" are deduced. The dose enhancement produced experimentally by 0.5, 1 and 4 mM TiO_2 NPs concentrations for phantom and *in vitro* studies irradiated with 1-8 Gy ranges of radiation doses was quantified for kilovoltage and megavoltage energies of external X-ray radiation sources. Furthermore, the TiO_2 NPs were activated via proton beam and the energy spectrums were acquired using Germanium detectors. The radiolabeled anatase TiO_2 NPs were imaged using positron emission tomography (PET) scanner.

One aspect of this research was to demonstrate that the TiO_2 NPs were typically synthesised to achieve highly pure and uniform anatase nanocrystalline structure. This form of NPs creates more free radicals and effectively generates more reactive oxygen species (ROS) since it has larger surface to volume ratio. These features combined have a high impact in damaging DNA molecule of biological system during irradiation.

In phantom studies, the radiation modifying effects of incorporating of PEG functionalised anatase TiO_2 NPs in the formulation of the water equivalent 3D PRESAGE® dosimeter were explored. The dose enhancement factors (DEFs) were quantified and then the results were validated with the biological studies. The results clearly demonstrates that the sensitivity of the dosimeter increases to the radiation doses with the concentration of the TiO_2 NPs incorporated in the composition of the PRESAGE® dosimeter. Furthermore, the measured DEF was significant at 80 kV compared to the negligible dose enhancement detected at 6 MV X-ray energy beams.

The *In vitro* studies, TiO_2 NPs proved to be cytocompatible to cells, even at very high concentrations. The DEFs were deduced from the data analysed in the form of cell survival curves. The result indicates that radiosensitisation induced by TiO_2 NPs was significant at kilovoltage range of energy which the maximal dose enhancement was observed at 80 kV. Furthermore, significant radiosensitisation was observed for *in vitro* study at megavoltage energy beam. Higher radiosensitisation were obtained for low energy x-rays compared to the high energy ones. Generally, with the inclusion of TiO_2 NPs in the target, same fraction of cells were destroyed with lower radiation doses compared to the case of absence of TiO_2 NPs. This means if the TiO_2 NPs are added to the biological target, a reduction of external dose of an order of magnitude can be achieved to deliver the same local control as without the inclusion of TiO_2 NPs for treatments with kilovoltage and megavoltage X-rays beams. This reduction of delivered radiation dose to the target results in reducing the dose to the surrounding normal tissues during treatment that is the primary concern in all radiotherapy treatment procedures. Hence, TiO_2 NPs are considered to be an efficient dose enhancer agent and have a great potential value for future clinical radiotherapy applications.

In addition, the radiobiological effect of amino functionalised anatase TiO_2 NPs on HaCaT and DU145 cell lines were investigated. The linear (α) and the quadratic (β)

radiobiological-parameters were extracted from the cell survival curves in order to describe the DNA damage by radiation. The results clearly demonstrate that α value significantly increases with the inclusion of TiO_2 NPs while β values do not show any predictable trend. This increase in α value indicates that the probability of double strand DNA breakage increases with the presence of NPs in the target. Accordingly, the DEF results for *in vitro* and phantom based studies showed good agreement with the hypothesis of α value increases as a consequence of inclusion TiO_2 NPs in the target.

There are measurable differences in the level of produced DEF between biological and phantom based studies at MV energy. The PRESAGE® dosimeters showed lower enhancements in radiosensitivity than cell in culture studies. This is due to PRESAGE® dosimeters is only able to detect the free electron generated as a result of photoelectric effect, Compton scatter and/or Auger effect and not being suited to detect the generated ROS (Biochemical effects) due to a lack of free water molecules in its structure, whereas cells can be affected by many other biochemical factors, such as the generated ROS which is added to the stress caused by generated electron free radicals, and this result in higher radiosensitivity. Therefore, the ROS generated from amino functionalised anatase TiO_2 NPs upon exposed to radiotherapy X-ray energy beam was investigated. Aqueous solutions without and with the presence of TiO_2 NPs was exposed to 6 MV beam. The result clearly shows that the level of generated ROS was proportionally dependent on the TiO_2 NPs concentration. This explains that biochemical effects need to be considered as a key factor for enhancing the cellular radiosensitivity with the presence of nanoparticles, which would be an important consideration for *in vitro* and *in vivo* radiosensitivity measurements.

Finally, the TiO_2 NPs are proposed as a reliable potential candidate for producing nuclear medical radioisotopes via proton activation. The results demonstrate that intense peak was observed at 511 keV which correspond to the γ-ray resulted from electron-positron

annihilation. This γ-ray peak is the most important radioisotope for potential nuclear medicine imaging applications using PET. Recently, several innovative for new radiopharmaceutical evolution potentially suggest β- and α emitters. Therefore, the produced ^{47}Sc radionuclide is a promising therapeutic agent for preparing radiolabeled antibodies due to its favorable β^- emission energy (162 keV) which decays to stable ^{47}Ti (100% β^- emission), and to its moderate half-life ($T_{1/2}$ = 3.35 d).

To conclude, this research shows that TiO_2 NPs improve the efficiency of dose delivery, which has implications for future radiotherapy treatments. The TiO_2 NPs can also be used as a potential imaging agents hence with these findings renders these NPs as theranostic agents with dual effects (i.e. imaging and dose enhancer agent) simultaneously if it is in the targets.

Thesis Outline

This thesis is mainly divided into three main sections for validation the radiation dose enhancement induced by TiO_2 NPs and this include: Section A: Synthesis and characterisation of TiO_2 NPs, Section B: Phantom studies using PRESAGE® dosimeters, Section C: Cell culture studies. Furthermore, it presents one of the potential applications of PRESAGE® dosimetry in radiotherapy. Finally, it reports the potential use of TiO_2 NPs activated via proton beam as imaging agent in nuclear medicine applications.

Chapter 1: Is an introduction to basic radiation physics, detailed description of the interaction of radiation with matter, radiobiology, introduction to TiO_2 NPs, and to 3D PRESAGE® dosimetry in radiotherapy.

Chapter 2: Contains detailed description of nanotechnology in radiotherapy, and a review of previous and current work on radiation dose enhancement using high and low atomic number (Z) materials such as gold, bismuth compound, and titanium dioxide nanoparticles. This chapter also provide analysis of the radiation attenuation and absorption coefficient and theoretically calculate the effects of radiation dose enhancement with the presence nano-sized materials. Finally, the objectives of the thesis are also explained.

Chapter 3: The methodology of the thesis is described and is divided into three sections. **Section A:** synthesis of anatase TiO_2 NPs for *in vitro* and phantom based studies and then characterise them. **Section B:** PRESAGE® dosimetry studies and this include fabrication and characterisation of PRESAGE® dosimetry, irradiation of PRESAGE® dosimeters with different X-rays modalities, and scanning techniques and procedures of this type of phantoms. **Section C:** describes the general protocols for radiobiological studies using cell culture. The protocols specify the correct preparation of anatase TiO_2 NPs for *in vitro* studies,

cell culture protocol, cell irradiation methodology with conventional clinical X-rays radiotherapy beams, cell survival curves measurements employ colorimetric (MTS) and clonogenic assays techniques. Present protocols for observing TiO_2 NPs localisation inside the cells and measuring their cytotoxicity. Protocol for detecting the reactive oxygen specious (ROS) are described.

Chapter 4, Section A: This chapter present the obtained results and discussions of the experimental works conducted for synthesising and characterisation of anatase TiO_2 NPs and this include; the size distribution, chemical compositions, crystal structure and surface modification characteristics of the synthesised nanoparticles. The results demonstrate that anatase crystal phase of TiO_2 NPs were synthesised with average size of about 30 nm. The NPs were successfully modified with Aminopropyl trimethoxysilane (APTS) and Poly (ethylene glycol) trimethoxysilane (PEGTS) for in vitro and phantom based studies respectively.

Chapter 5, Section B: Reports and discusses the results obtained from phantom based studies using PRESAGE® dosimeters and this includes; physical characteristics, radiological properties, and radiation dose enhancement effects induced by NPs. The physical characteristics results comprise the maximum absorption wavelength dependence and the radiation dose sensitivity of different radical initiators of PRESAGE® dosimeters. The maximum absorption was found to be at 630 nm and the PRESAGE® dosimeter with iodoform radical initiator was observed to have higher sensitivity that PRESAGE® dosimeter with chloroform radical initiator. The radiological properties include dose-response relationship, post response photo-stability and the water equivalency characteristic of the PRESAGE® dosimeters. The results demonstrate that the fabricated water equivalent PRESAGE® dosimeters have linear response relationship to radiation and are stable under

certain conditions. This chapter also involves for the first time investigations of feasibility of employing different concentrations of the synthesised anatase PEG functionalised TiO_2 NPs in the prepared PRESAGE® dosimeter for validation and quantification of the radiation dose enhancement employing low (kV) and high (MV) energy X-ray radiotherapy beams. The calculated dose enhancement factor (DEF) was observed to be maximum at kV and minimal at MV beams.

Chapter 6, Section C: Contains the obtained results and discussions for *in vitro* studies and this includes; localisation of anatase amine functionalised TiO_2 NPs inside the cells, the toxicological characteristic, and the radiosensitisation effects induced by various concentration of these NPs. The nanoparticles were observed as a black dots clustered in the cells cytoplasm with no toxicity. The cell survival curves for the different concentrations of anatase amine functionalised TiO_2 NPs at kilovoltage (kV) and megavoltage (MV) energy X-ray radiotherapy beams were obtained by MTS and clonogenic assays and the radiosensitisation induced by NPs were estimated. The radiosensitisation results from the physical and biochemical effects such as generation of free radicals and ROS respectively. The calculated DEFs were extrapolated from cell survival curves at 80% survival and the maximum DEF value for kilovoltage energy range is identified to be at 80 kV. The radiobiological parameter obtained from the cell survival curves such as alpha and beta values are analysed; the alpha value is found to increase as TiO_2 NPs concentration increases. The generated ROS was proportionally dependent on TiO_2 NPs concentrations.

Chapter 7: Dedicated to the investigation of high-resolution 2D scanning feasibility study for PRESAGE® dosimeters, for the first time, using UV/VIS spectrophotometry (CLARIOstar microplate reader) and to simulate the tissue inhomogeneity behaviour. This chapter starts with an introduction to and review of PRESAGE® dosimeters scanning

techniques and its advantage over other dosimeters, followed by experimental methods, results and discussion. The water equivalent PRESAGE® dosimeter was fabricated with the inclusion of an inhomogeneity and the 2D dose distribution of megavoltage X-ray beams was obtained. The PDD curves and beam profile were validated against ionisation chamber measurements and the agreement is well within experimental uncertainties which demonstrate that performance of CLARIOstar microplate reader as a valid 2D dosimetry instrument. The dose distribution beyond the inhomogeneity were investigated which with this technique were relatively easily and quickly compared to optical CT or film dosimetry. There is also a potential to extend this method to obtain 3D dosimetry scanning by repeat measurements at various PRESAGE® angulations and then reconstruct the data in a volume.

Chapter 8: Devoted to investigate the activation of anatase TiO_2 NPs by proton beams that potentially can be employed for imaging application using PET scanner through the generation of gamma emitters (0.511 MeV). This chapter reports an introduction and review to commonly available radioisotopes employed as radioactive tracers and to nanoparticles recently tested as potential radioactive tracers in nuclear medicine applications, followed by experimental methods, results and discussion. The results demonstrate that this activation generate positrons and radionuclides with certain level of activity such as vanadium (^{48}V) that potentially can be used for imaging and radiotracing agent in nuclear medicine applications. Therefore, TiO_2 NPs can be considered as theranostic agents due to their compatibility for enhancing the radiation dose (chapter 5 & 6) and as potential imaging agent.

Chapter 9: This chapter reports the general conclusions and future directions for this study.

CHAPTER ONE

Introduction and Theory

I. Introduction and theory

This chapter contains an introduction and theory to radiotherapy and basic radiation physics. It explains the methods of X-rays production by conventional clinical modalities. In addition, a brief introduction to the cell biology and the effect of radiation interaction processes at an atomic level of biological system (*in vitro*) are described to facilitate a better understanding of the biological target damage caused by radiation. This chapter also provides an introduction into applications of nanotechnology in radiotherapy, and particularly the properties of titanium dioxide nanoparticles (TiO_2 NPs) as radiosensitiser. Furthermore, it presents an overview of the fundamental theory and applications of PRESAGE® dosimeter that is employed to validate *in vitro* studies of this thesis.

1.1 Introduction to radiation therapy (radiotherapy)

Malignant tumours have being the major cause of mortality during this century [1]. Latest world cancer statistics, December 2013, by international agency for research on cancer (IARC) reported that 8.2 million death resulted from cancer, and around 14.1 million new cases were diagnosed in 2012, compared with 7.6 million and 12.7 million, respectively, in 2008 [2]. In Australia, over 100,000 new cases of cancer are diagnosed each year [3]. Radiotherapy has currently become one of the primary and effective methods for cancer treatment, which involves delivery of high ionizing radiation dose [4]. During the course of their cancer patient's treatment, slightly more than 50% of all cancer patients require radiotherapy [5]. Radiotherapy took advantages of ionising radiation and has been used for over 100 years to treat cancer tumour [6]. In the very beginning of introducing radiation

therapy, X-rays in kilovoltage energy range were designed for cancerous tissues treatment, but such radiation had a limited effect on deeply seated tumours. This is due to the low beam penetration abilities and sometimes delivering high doses (above threshold) to the healthy tissues, which it passed through to the tumour affecting these normal tissues. Later, serious efforts have been shown to overcome this shortcoming and as a result major advances have been made. One of these development was introducing electron linear accelerated (LINAC) within the last decade. The LINAC generates electron beams of megavoltage energy range and high energy X-rays (in the range of megavoltages) for radiation therapy uses. These are currently the most common sources of ionizing radiations used in clinical centres to deliver radiotherapy doses as required. In addition development in computers and information technology, over the last few decades, have made it possible to replace a conventional two dimensional (2D) radiotherapy using simple rectangular fields based on plan X-ray imaging to sophisticated three dimensional (3D) conformal radiotherapy techniques [2]. Consequently, improvements in the dose distribution and skin sparing effects have been achieved by such high energy X-rays and continues to improve the effectiveness of radiotherapy in cancer treatment as an appropriate and almost tailored dose can be delivered to the tumours without producing serious reactions to the surrounding normal tissues or to the skin. As well as producing high energy X-rays, electron LINACs can also be used for generating extremely high energy electron beams (4 to 20 MeV) which are used for superficial cancer treatments and as a result most of the kilovoltage X-rays for such application have been replaced. In addition to the improvements of delivering various beam energy to the patient, technological sophistication in radiotherapy equipment provide better tumour targeting resulting in minimizing radiation dose to the surrounding normal tissues such as stereotactic radiosurgery (SRS) and intensity modulated radiotherapy (IMRT) that produce conformal dose to the tumours with high accuracy [2, 4]. Image-guided radiotherapy

(IGRT), which is currently available in many radiotherapy centres and helps to achieve better tumours localisation by using imaging equipment which enhances the precision delivery of radiation doses to the tumours [7, 8]. Today in modern radiotherapy centres, LINACs are the most common modality employed for cancer treatments. However brachytherapy, which uses gamma-rays from radioactive sources such as iridium-192 or high radioactive source cobalt-60, are serving as an alternative modality in radiotherapy for treating special types of cancer and in the meantime being less dependent on electrical energy [9]. Clinical applications uses other radiotherapy methods such as particle radiation therapy, this include heavy ion and proton beams which find their way to radiotherapy applications and are currently used in cancer treatment [10, 11]; whereas the high installation and maintenance costs, they are less common. Particle radiotherapy provides localised dose concentrations at the specified tumours and has proved its ability of orbital tumours management such as base of skull sarcomas, this high focused energy beam deposited in tissue is commonly known as the Bragg peak. Although, particle therapy can have therapeutic complications where in the cases of accidental exposure to normal tissues can cause serious damages [12, 13].

1.2 Basic radiation physics

In general, radiation is classified as ionizing and/or non-ionising radiation. Cancer treatment mainly utilizes ionising radiation, as it is more relevant in radiotherapy because it can kill cells efficiently by damaging their deoxyribonucleic acid (DNA) molecules. Radiation having sufficient energy to ionize atoms termed as ionizing radiation. Photons (gamma and X-rays) are most commonly used in radiotherapy, moreover other ‘particle type’ such as electrons, alpha, beta, protons, neutrons and heavy ions are used. The interaction of ionising radiation with the biological target causes damage in the structure of biological

system. The term ionization is further classified into two categories, indirectly ionising and directly ionising radiation. The directly ionizing radiation, type used in radiotherapy, is the direct interaction of charged particle (electron, proton and alpha particle) with matter which loses energy along the ionising track in the medium and then damage the target cells. The procedure of ejecting an electron from an atom as the incident particle have enough energy is called ionisation, while the absence of sufficient energy result in only movement of electron from lower energy levels to high energy levels which is called excitation. The secondary ionising radiation that is known as delta (δ)-rays can be produced if, in some condition, the ejected electrons have enough energy to eject further electrons [14]. However, in two multi-steps process the indirectly ionising radiation, which include uncharged particles (photons & neutrons), deposit their energy in the target. Initially, absorbing radiation by the atoms will release charged particles, where photons release either electron or electron positron pairs and may release heavy ions or protons. Undoubtedly, interaction of photon with the target atoms will release secondary electrons that eventually produce a track of ionisation in the material. Incident radiations are responsible for most of the targets damage that result from energy deposited by this secondary electron [15]. That is why they are termed indirectly ionising radiation. In the following sections, a brief overview of electron interaction (directly ionising radiation) with target and X-ray or photon production is explained.

1.2.1 Production of X-rays

X-rays used in medical applications such as diagnostics or therapy are produced by two main different mechanisms, as a consequence two types of X-rays are generated; Bremsstrahlung X-ray and characteristic X-ray. In conventional X-ray tube or typical linear accelerator, electrons are generated and accelerated in vacuum and aimed at a high atomic

number (Z) target such as tungsten. Hence, irradiative "collision" interaction between the field of an atomic nucleus and the high-speed electron will generate a type of X-rays known as bremsstrahlung (braking radiation) [14]. In such an interaction, an electron passing near an atomic nucleus will lose energy by changing its direction due to the attractive force of the target nuclei. This lost energy will be irradiated as bremsstrahlung X-rays. Energy lost by the electron is equal to the energy of generated X-ray. Whereas, the other type of X-rays is generated when the high speed electron interact with the target atoms and eject K-shell orbital electron, due to unstable atom, electron from higher energy levels (L and M) will drop and fill the vacancy of the ejected electron in the lower energy level and therefore photon will be emitted, this emitted photon is called characteristic X-rays. The emission of bremsstrahlung X-rays may have any energy up to the initial electron energy but the characteristic radiations are emitted at discrete energies [14]. The mechanisms of both interactions are illustrated in **Figures (1-1) and (1-2)**.

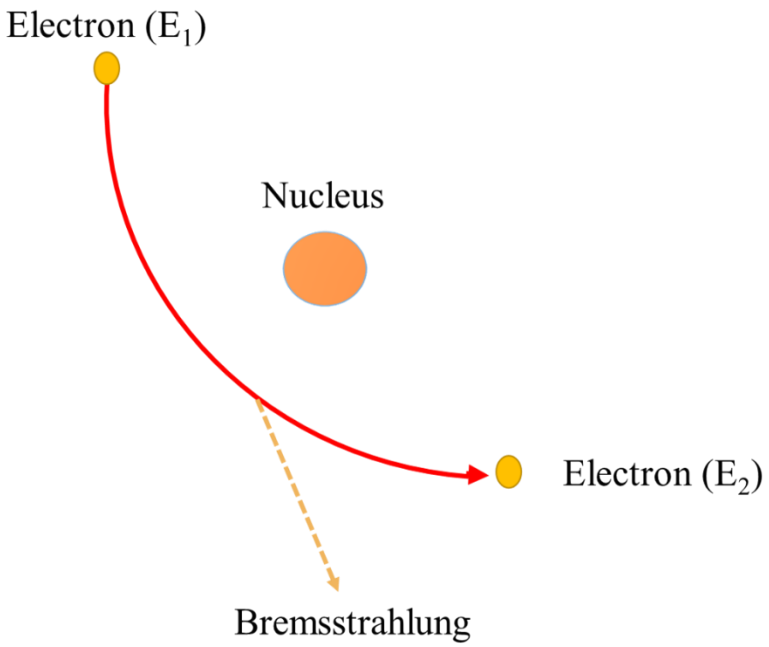

Figure 1-1: Schematic diagram for bremsstrahlung X-rays production.

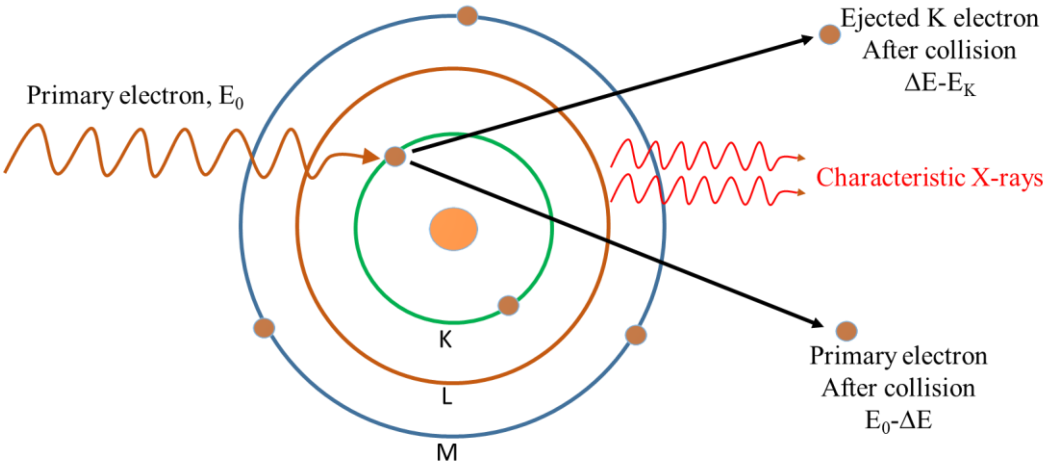

Figure 1-2: Schematic diagram for characteristic X-rays production

1.2.2 Interaction of radiation with matter

Early experiments showed the ability of X-rays in penetrating matter. A photograph shows a human hand bone was produced by two French physicists with in nearly one month of X-rays discovery [16]. This event has attracted researchers to deeply investigate the interaction between X-rays and objects. They demonstrated that the action of interaction initiate when an incident photon transfers along the path of the medium resulting in the release of secondary electrons from the atoms in the medium. The incident photon either causes target atoms to be excited or ionised depending on the photon energy. The probability of photon-atom interaction mechanism is mainly depend on Z number, X-rays energy, electron density and mass density of the target medium [14]. Four processes will occur when photon beam traverses through a medium, which are photoelectric, Compton scattering, pair production effects and photonuclear reaction.

1.2.2.1 Photoelectric effect

The primary photoelectric effect "absorption" starts when the incident photon releases the most inner orbital (K-shell) electron from the atom. Photons having energy partially higher than atomic electron binding energy will eject electron from the k-shell level and the photon will be completely absorbed hence the term absorption. The kinetic energy of released electron is equal to the difference of photon energy and electron binding energy. As a result of electron escape, outer orbital electron will drop and fill the vacancy left in the inner orbit. Consequently characteristic X-rays or fluorescent photon will be emitted with energy exactly equal to the difference in levels energy (ΔE). The local orbital electrons may absorb this generated characteristic X-ray and emit an orbital electron which is called Auger electron. These electrons are characterised as secondary photoelectric effect. The photoelectric effect is illustrated schematically in **Figure (1-3)**.

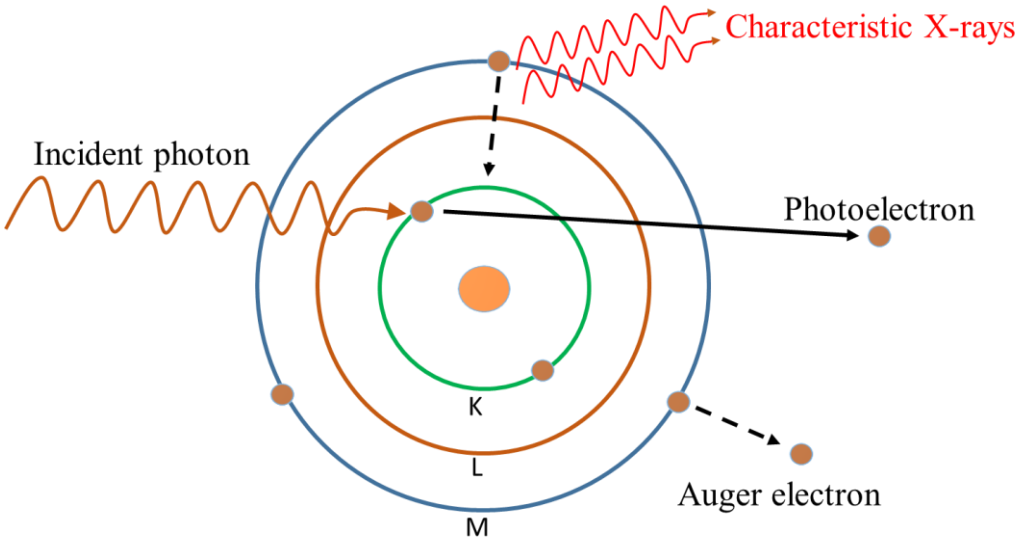

Figure 1-3: Schematic diagram for photoelectric interaction

Photon energy and atomic number of the absorbing materials are the two depending factors that the probability of photoelectric effect occurs. The relationship between the incident photon energy (E) is proportional to the cubic atomic number (Z^3). Medium such as water or biological tissue require appropriate absorption photon energy > 0.1 MeV, whereas for high Z number materials such as lead, photoelectric absorption dominates at photon energies < 0.1 MeV [14, 17].

1.2.2.2 Compton interaction

Compton interaction occurs when a photon interacts with loosely bound electron (free electron) with energy much higher than electron binding energy. Only a portion of original photon energy is received by the outer orbital (M-shell) electron while the rest of the energy is carried out by the deflected photon which moves in a new direction as scattered photon. The very outer electron is then released from the atom. In the interaction when the incident photon energy is much higher than k-shell electron binding energy; therefore, Compton scattering will dominate photoelectric effect. Compton interaction obviously depend on free electron at a very outer-shell orbit and is independent on the material Z number [14]. **Figure (1-4)** is the schematic illustration of Compton scattering.

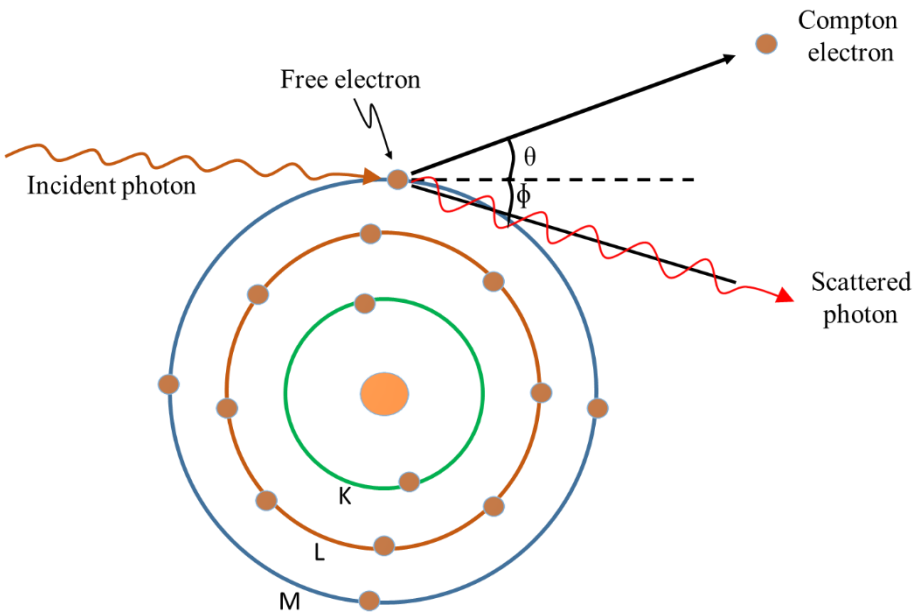

Figure 1-4: Schematic diagram for Compton interaction

1.2.2.3 Pair production

Pair production interaction occurs when the photon energy becomes more than 1.024 MeV. Pair production process involves the interaction between incident photon and the magnetic field of a nucleus. In order to be absorbed, the incident photon energy must be more than twice the electron rest mass energy (0.511 MeV). Consequently, photon disappears and electron-positron pair will be created. The probability of pair production rises with the photon energy and Z number of the absorber. The positron combines with one of the free electrons in its vicinity to give rise to two annihilation photons, each of 0.511 MeV. Since momentum is converted in the process, the two photons are ejected in opposite directions [14], as illustrated in **Figure (1-5)**.

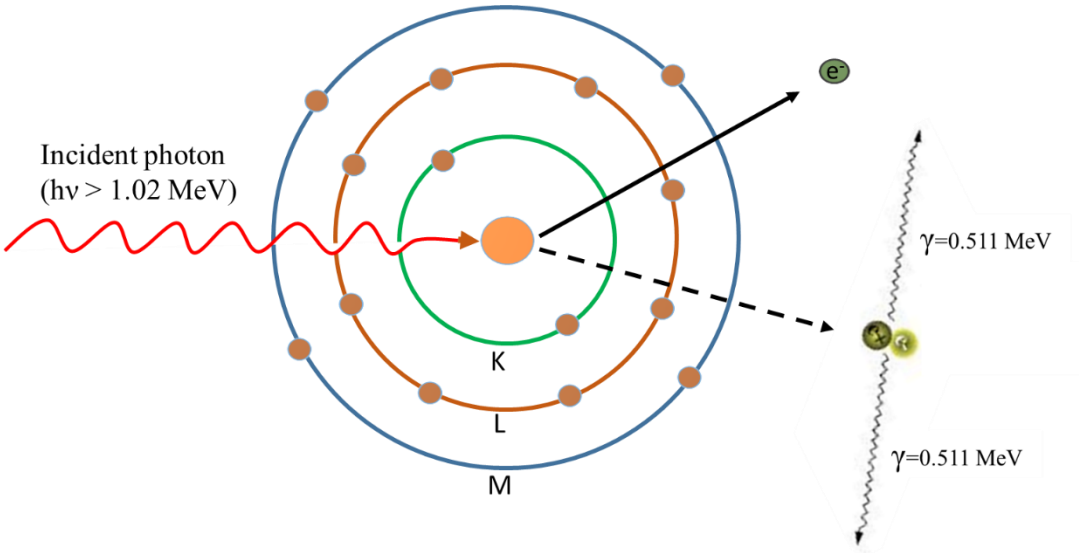

Figure 1-5: Schematic diagram for Pair production interaction showing the production of annihilation radiations.

1.2.2.4 Photo-nuclear reaction

The photonuclear reaction is a physical process in which an extremely high-energy gamma ray (or x-ray) photons (nearly above 10 MeV) is absorbed by an atomic nucleus and causing the nuclei to inter an exited state which promptly decays by emitting protons (p), neutrons (n), or heavier particles from the nuclei and is then transformed into the nucleus of one or more other elements. The resulting daughter nuclei have a lower energy and mass (more stable) than the decayed parent nucleus. There are many possible reactions which some of them are (γ,n), (γ,2n), (γ,np), (γ,α), (γ,n2p), (γ,2np). The incident gamma ray photons energy must exceed the binding energy of the nucleons (proton, neutron) to be ejected from an atomic nucleus. The cross section (denoted by Greek letter σ) is the probability of interaction between a bombarding particle and the target nucleus. The cross section depends on the energy of the incident particle and on the properties of target nuclei. The total cross

section for all possible photonuclear reactions is called the gamma ray absorption cross section for a nucleus [14, 15].

In summary, photoelectrons, scattered X-rays, Compton electron, Auger electron and positrons are emitted from the atoms due to the interaction of X-rays with matter. Thus, the target atom will be ionised resulting in deposition of radiation energy "dose". These low energy electrons are responsible for the damage caused to the biological systems. Hence, in the following section the attenuated fraction of photon energy by the material is described.

1.2.3 Measurement of absorption and attenuation coefficients

The photoelectric and Compton effect determines the absorption coefficient of the material for X-rays. The incident X-rays on any material will either be absorbed (P.E.) or scatter (C.S.) or involve in positron emission while the rest of the beam will traverse the target intact with no changes to its energy. In other words, the beam will be attenuated. The intensity (I) of radiation passing through a material of thickness (x) can be described as an exponential function "Lombar-Beer law" as equation (1-1) [14].

$$I(x) = I_0 \exp^{-\mu x} \quad \ldots\ldots\ldots\ldots\ldots\ldots \quad (1\text{-}1)$$

I(x) is the transmitted intensity through the absorber that do not interact with the material, I_0 is the incident intensity on the absorber, x is the material thickness (distance travelled) and μ is the linear attenuation coefficient (cm^{-1}) results from absorbing or removing

a fraction of photon while traversing through the material during attenuation process therefore x should be in cm. This coefficient is mainly depending on photon energy, target atomic composition and the density of the material. Mass attenuation coefficient (μ/ρ) is determined by removing density factor and only taking atomic composition of the material into account [14]. Furthermore, photon absorption and attenuation processes convert part or all of its energy to kinetic energy of electrons. Therefore, by using mass energy absorption coefficient (μ_{en}/ρ) and mass energy attenuation coefficient (μ/ρ), the absorbed or attenuated fraction of photon energy by the material can be obtained.

From radiotherapy prospective, the absorption and attenuation coefficients from the interaction of radiation with biological target help to determine the sum of energy delivered to the target i.e. the radiation dose [15]. Hence, the biological effects of deposited radiation can be predicted. Therefore, a brief introduction to the cell biology and the influence of incident radiation on the biological system is explained in the following sections.

1.3 Introduction to radiobiology

Tumours are a category of biological tissue and are therefore living organisms. The study of targeting ionising radiation on the biological systems is called radiobiology [16]. Biological systems exposed to the ionizing radiations will absorb some or all of the radiation energy and undergo special interactions [14] as stated previously **(sections 1.2.2)**. This interaction between biological materials and ionising radiations result in DNA damage and therefore cell death if the damage is unrepairable. In radiotherapy, it is very important to investigate how the tumour cell death occurs, which is the main objective, and in turn needs a good understanding of relevant aspects of the cell biology.

1.3.1 Cell biology

Cell is the basic structural, functional and biological unit of all known living organisms. A cell is the smallest unit of live organs that can replicate independently. The study of cell is called “cell biology”. All organisms that are made from cells are arranged into more complex structures such as organs and tissues. Reproduction and responding to their environment are some of the essential functional aspects of the cells. In general, cells differ from each other but they have some common characteristics which therefore are classified as either prokaryotic or eukaryotic. Prokaryote cells were the first form of live on earth [17]. They are smaller, simpler, lack membrane-bound organelles such as the nucleus and independent; for example, the general type of these cells is bacteria. Eukaryote cells are about fifteen times wider than a typical Prokaryote cells and can be as much as thousand times greater in volume. The main distinguished feature of Eukaryote cells as compared to Prokaryotes cells is the presence of membrane-bound (plasma membrane) which isolate the inside components of cell from environment in which specific metabolic activities take place. Most important among these is a cell nucleus that houses the cell DNA molecules. Eukaryote cells usually exist in multicellular organisms such as plants and animals [17]. Ordinarily, creature cells are 5-20 μm in diameter. Organelle is the well-known name for the internal components of these cells, which include the nucleus, mitochondria, ribosome, cytoskeleton, Golgi apparatus, smooth endoplasmic reticulum, rough endoplasmic reticulum, vesicles, centrosome and lysosomes. Outside the cells wall include these structures capsule, fimbriae (pili) and flagella that cannot be found in animal cells and can exist in prokaryote cells, **Figure (1-6)** shows human keratinocyte (HaCaT) cells under high magnification microscope.

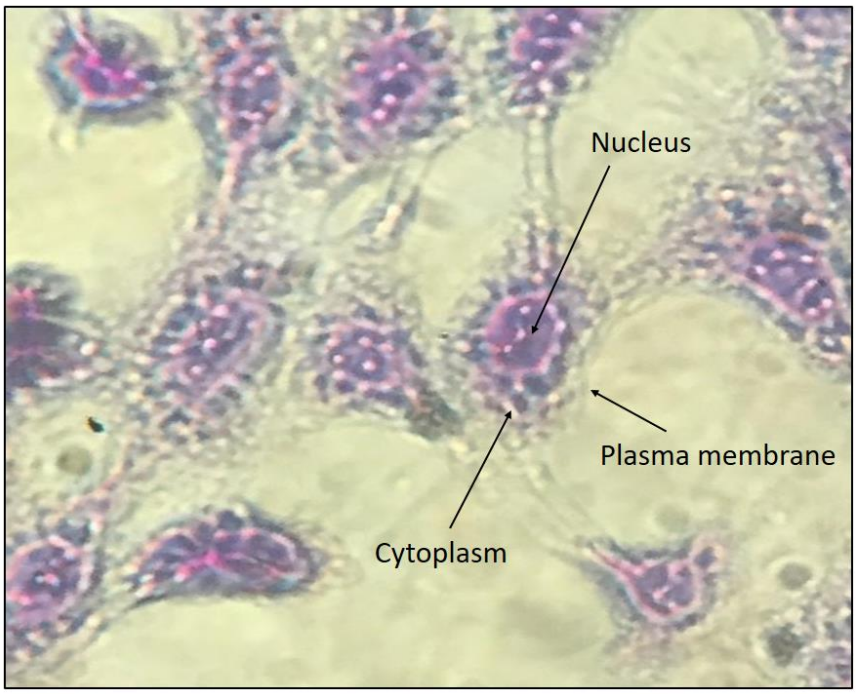

Figure 1-6: HaCaT cells under high magnification microscope.

Cells experience diverse cellular processes for maintaining functions such as metabolism and growth. There are two main processes of metabolise organic molecules and cells harvest nutrients in to energy which are catabolism (breakdown pathway) and anabolism (biosynthetic pathway) [17]. In the first process (catabolic process) complex molecules are broken down by cells with the help of enzymes to generate energy. For example, cellular respiration, which consume oxygen as a reactant along with the organic fuel. In the second process (anabolic metabolism) complex molecules are constructed when cells consume energy. For example, synthesizing protein from amino acids, which other than anabolic pathway, it is also known as biosynthetic pathways. In order to produce energy, the breakdown of the complex sugar such as glucose takes place via a process called glycolysis within a biochemical cycle (Kreb's citric acid cycle). Glucose will be broken down to make adenosine triphosphate (ATP) which is a form of energy, when the glucose is absorbed inside

the cells via diffusion process. This generated energy will be utilized by cells for all its functions such as cell proliferation, protein synthesis and cell movement. Nucleus, which is the largest organelle in a cell, controls all cellular functions. The nucleus contains genetic material in the form of deoxyribonucleic acid (DNA) molecules. DNA is organised into discrete units called chromosomes that carry the genetic information. Every chromosome is comprised of a material called chromatin, a complex of proteins, and DNA [17]. The DNA strand can be damaged by ionising radiation resulting in cell death and mutation. It has been founded that DNA and chromosome structure is the essential and primary target in the biological system damaging by ionising radiation [16].

1.3.2 DNA damage by ionising radiation

In section **(1.2.2)** the interaction of ionising radiation with mater has been briefly detailed which describes the processes of free radicals and secondary electrons production via photoelectric effect and Compton scattering. Generation of free radicals (secondary electrons) can be considered as a consequence of the direct or indirect interaction processes. Direct process usually involves high linear energy transfer (LET), for example, neutrons and alpha particles emission. The direct interaction between ionising radiations and targets' atoms will result in atoms to end up being ionised or excited. The generated free radicals will interact with other atoms and then causes a chain of biological impacts. Dissimilar to the direct process, indirect process can be defined as the interaction between ionising radiation and atoms or molecules rather than targets, such as water molecules, causing water derived free radicals. The free radicals react with nearby molecules or target in a very short time resulting in breakage of chemical bonds or oxidation (addition of oxygen atom) of proteins, DNAs or the effected molecules. The disruption of the chemical bonds will create new bonding and

cross linkage between these macromolecules that will affect cells' vital function. The major effect in cells is DNA breaking since DNA consists of a pair of complementary double strands. The DNA double strand structure can be broken by either single strand breakage or double strand breakage. However, the latter is believed to be much more important (effective) biologically. Most single strand breakage can be repaired normally as the two strands complement each other, so using the template from the intact strand can serve as template for repair of its damaged strand and therefore may result in minor biological consequences only if the repair is incorrect. In cases of double-strand breaks, however, repair is more difficult and leads to erroneous re-joining of broken ends which causes significant effects leading to severe biological damage. These so-called disrepairs result in induction of mutations, carcinogenesis or leads to cell death [16]. The single and double strand breaks are illustrated in **Figure (1-7)**.

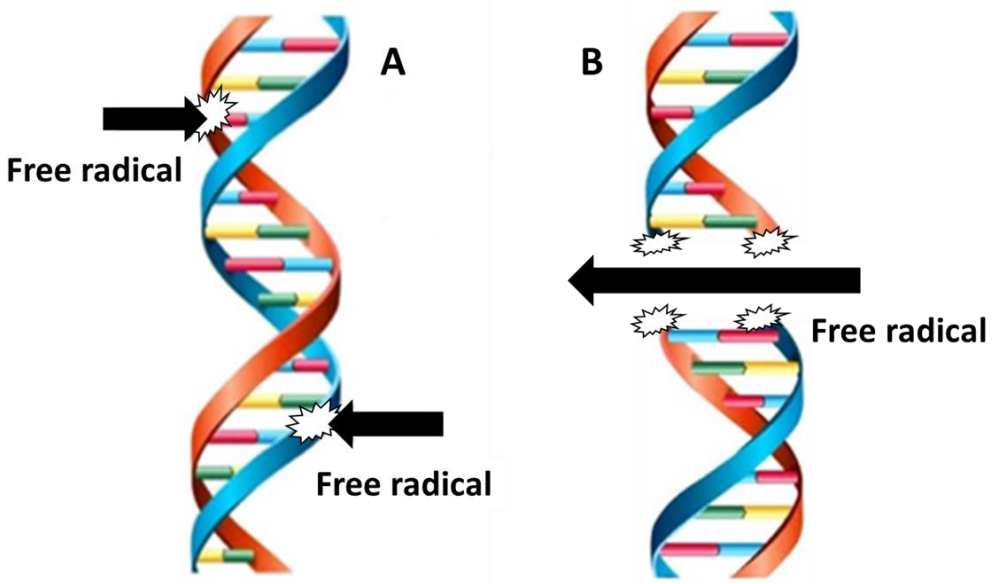

Figure 1-7: Illustrate free radical damaging DNA, A) Single strand break, B) Double strand break.

Ionising radiations may cause chromosomes aberration or chromatid aberration at higher doses. Chromosome is a thread-like structure of ribonucleic acids (RNA) and proteins exist in the nucleus of most living organs, carrying genetic information arranged in linear sequence. Chromatid is a two progeny strands of a duplicated chromosome joined at the centromere during meiosis or mitosis [16]. Chromosome breakage or aberration is shown in **Figure (1-8)**.

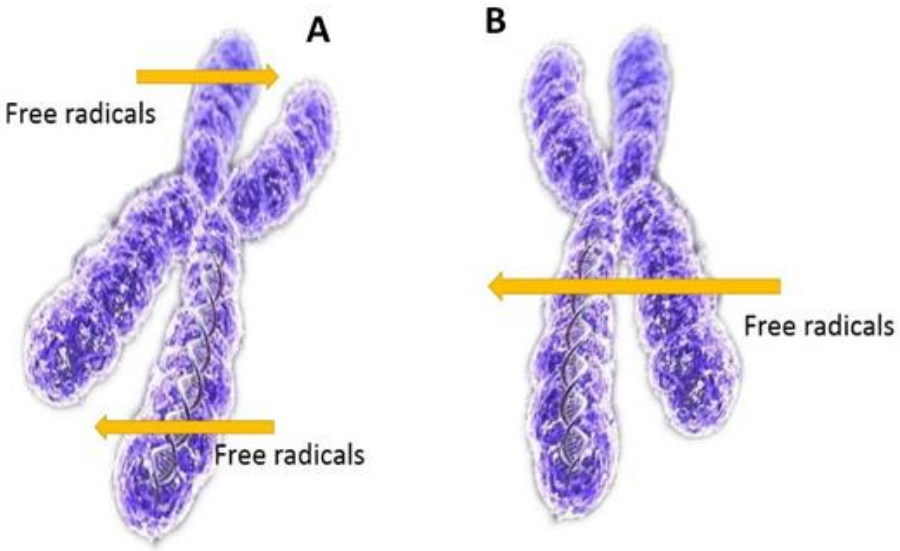

Figure 1-8: Illustration of chromosome breakage cause by free radical A) Two separate free radical breaks two chromosome B) Single free radical breaks two chromosome.

Evaluation the damage caused to the biological target by ionising radiation is through utilising cell survival curves. Cell survival curves are the relationships between the absorbed radiation dose and the fraction of cells retaining their reproductive integrity as measured *in vitro* [16]. The cell-surviving fraction is displayed on a logarithmic scale. The shape of cell survival curve depends on the cell line and the type of irradiation. Cell survival behaviours at densely and sparsely ionising radiations are described in **Figure (1-9)**. At densely ionising radiation (High LET), such as neutrons, cell survival curve is straight line; while, at the

sparsely ionising radiation, X-rays, cell survival curve begin with a linear slope at low doses, followed by a shoulder and afterward turn out to be straight again at high doses. The cell survival curve is described utilising radiobiological models and the most widely recognized models used is the linear quadratic (LQ) model which then is employed to fit the cell survival curve.

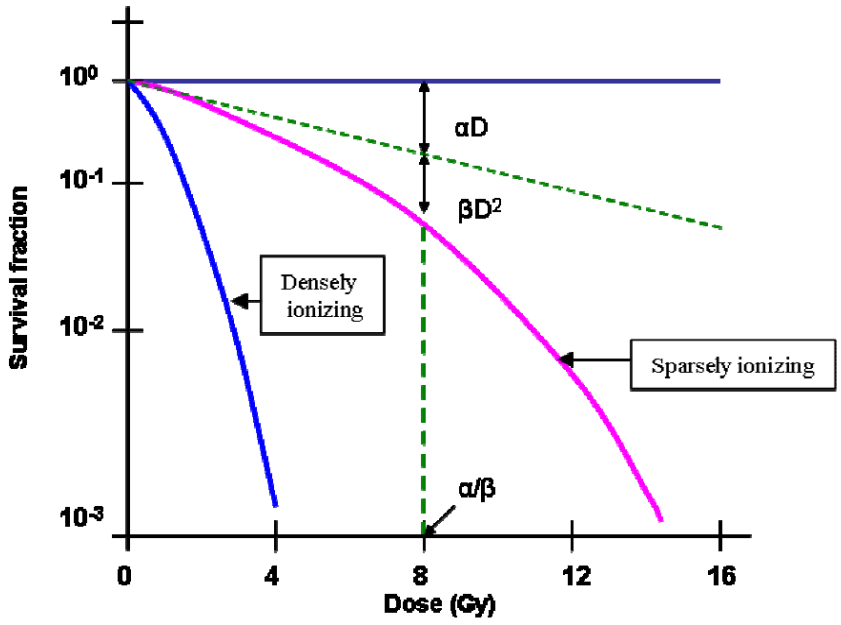

Figure 1-9: Typical shape of cell survival curve for mammalian cells with the fraction of cells surviving as plotted on a logarithmic scale against dose on linear scale. The linear quadratic model is described by the linear component (αD), which is proportional to the dose and quadratic component (βD^2), which is proportional to the square of dose. The α/β ratio is the value where the linear and quadratic components are equal [16].

The LQ model describes cell killing, both for tumour and healthy tissues by providing a satisfactory and practically useful explanation of fractionation and dose-rate effects observed at the macroscopic level [18]. Therefore, the LQ model can be used in particular for estimating the effect of delivered radiation doses on cells (i.e equipoise between healthy tissue complications and the probabilities of tumour cure) [18]. The LQ model suggests two

parameters for representing the sensitivity of cell death by radiations. One of the parameter (α) is proportional to the dose, while the other parameter (β) is proportional to the square of the dose [16]. Equation (1-2) described the model.

$$S = e^{-\alpha D - \beta D2} \qquad \ldots\ldots\ldots (1\text{-}2)$$

S is the cell surviving fraction at dose D (for example the dose at 8 Gy as in **Figure (1-9)**) where α and β are constants. α represent the linear portion of the cell survival curve and β represent the quadratic component of the curve [16]. The linear part of the survival curve (α) demonstrates the probability of an interaction between the two chromosome breaks which is relative to the dose. At low doses, linear part of the survival curve, the two chromosome breakages results from the single electron been generated from the absorption of radiation interaction [16]. While at high doses, quadratic part of survival curve (β), the breakages of both of the two chromosomes results from two different electrons (**Figure 1-10**). The probability of this interaction is proportional to the square of the radiation dose [16]. Two chromosome breaks may cause the asymmetric exchange type aberration that results the cell's loss of reproductive ability. The linear and quadratic contributions to cell killing that are proportional to the dose and square of the dose respectively are equal at a dose that is equal to the ratio of α to β as illustrated in equation (1-3) [16]:

$$\alpha D = \beta D^2 \quad \rightarrow \quad D = \frac{\alpha}{\beta} \qquad \ldots\ldots\ldots (1\text{-}3)$$

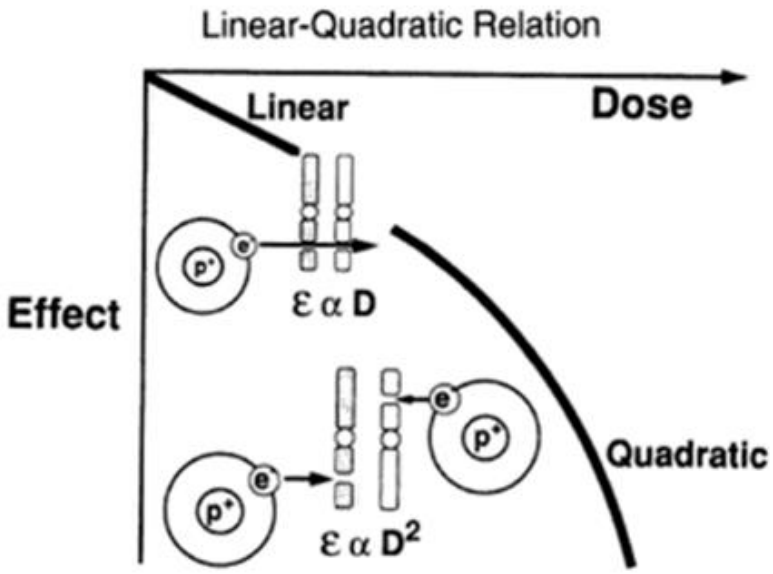

Figure 1-10: Relation between chromosome aberrations and cell survival curve. At low doses, the two chromosomes breaks are the consequence of a single electron set in motion by the absorption of X-ray or γ-ray. The probability of an interaction between the beaks is proportional to dose; this is the linear portion of the survival curve. At higher doses, its showing the two chromosomes breaks as a result of two separate electrons. The probability of this interaction is proportional to the square of the dose. The survival curve bends if the quadratic component dominates [16].

The presence of nanoparticles in the biological target leads the researchers to innovate and use various models for quantifying the radiosensitisation induced by NPs; such specific theoretical and experimental models adopted for *in vitro* studies are shown in **Figure (1-11)**. Only one of the most used models was employed in this thesis.

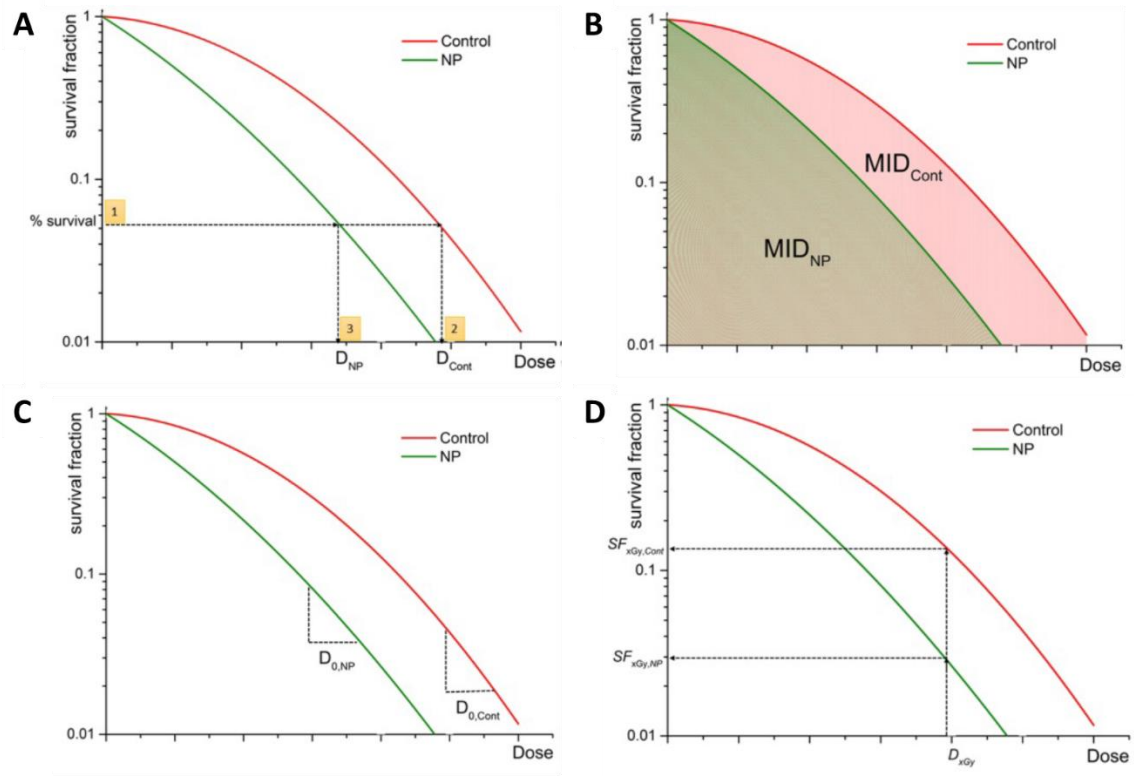

Figure 1-11: Graphical representation of quantifying the radiosensitisation effect induced by NPs from cell survival curves employing different models, A) Dose Enhancement Factor (DEF), B) Sensitizer Enhancement Ratio (SER), C) Radiosensitivity Enhancement Factor (REF), and D) Radiation Enhancement Ratio (RER) [19].

One of these models is termed the Dose Enhancement Factor (DEF) which is employed to quantify the difference between cell survival curves **(Figure 1-11 A)**, and is defined as the ratio of the dose delivered in the control cell culture (i.e. without NPs), divided by the dose delivered in cells treated with NPs at % survival as illustrated in equation (1-4) [19].

$$DEF_{x\%} = \frac{D_{control}}{D_{NPs}} \quad \text{(For x\% survival)} \qquad \ldots\ldots\ldots (1\text{-}4)$$

This model is the most commonly used as it correlates well with clinical outcomes because the selected percentage region of the cell survival curve is nearly at dose of 2 Gy which is considered to be the best characterised region employed for data analysis with this model since 2 Gy represent the typical individual dose of conventional radiotherapy fractionation delivery [19]. Therefore, this model was adopted in this study for quantification the radiosensitivity induced by TiO_2 NPs for *in vitro* studies, which is described in details in chapter six of this thesis.

Alternative models are also employed to describe the cell survival curve. The model termed as Sensitizer Enhancement Ratio (SER) has quantified the radiobiological impact of NPs by calculating the ratio of the Mean Inactivation Dose (MID) of control cells to treated cells with NPs [19], as in equation (1-5) **(Figure 1-11 B)**.

$$SER_{NP} = \frac{MID_{control}}{MID_{NPs}} \quad \text{..... (1-5)}$$

Further model used for quantifying the radiobiological effect of NPs depends on the straight portion of the high dose region of the survival curve (. This model is termed as Radiosensitivity Enhancement Factor (REF) which is the ratio of the slope ($D_{0,NPs}$) of the survival curve with NPs to the slope of control ($D_{0,control}$) [19], as described in equation (1-6) **(Figure 1-11 C)**.

$$REF = \frac{D_{0,control}}{D_{0,NPs}} \qquad \ldots\ldots\ldots (1\text{-}6)$$

This model applies at any point near exponential part of the survival curve when the dose reduces the cell survival to 37% of its value. The REF calculations are better suited at high dose levels and with the multiple target models providing a better description of the experimental data compared to the linear-quadratic model [19].

The other model used to characterise the radiobiological effect of NPs is termed Radiation Enhancement Ratio (RER) **(Figure 1-11 D)**, and is defined as the ratio of survival fraction without and with NPs at a given radiation dose as shown in equation (1-7) [19].

$$RER_{xGy} = \frac{SF_{xGy,control}}{SF_{xGy,NPs}} \qquad \ldots\ldots\ldots (1\text{-}7)$$

This model is limited to cell survival studies as it requires an accurate determination of the absorbed dose in the presence of NPs and assumes no change in the radiation quality; however, it has the advantage of directly describe the variation amount of the biological response caused by the NPs at a specific radiation dose.

The damage caused by the ionising radiations to the biological materials is highly dependent on the number of radiation interactions and the dose deposited. Therefore, the presence of high concentration of nanostructure material in the tumour cells will enhance the probability of physical and biochemical effects due to further free radicals or reactive oxygen

species (ROS) production by the interactions previously reported **(Section 1.2.2)** and these effects are schematically described in **Figure (1-12)**. These generated ROS and/or secondary electrons will then result in more chromosome breakages causing a significant damage to the DNA molecules in the cells and hence leading to cell death.

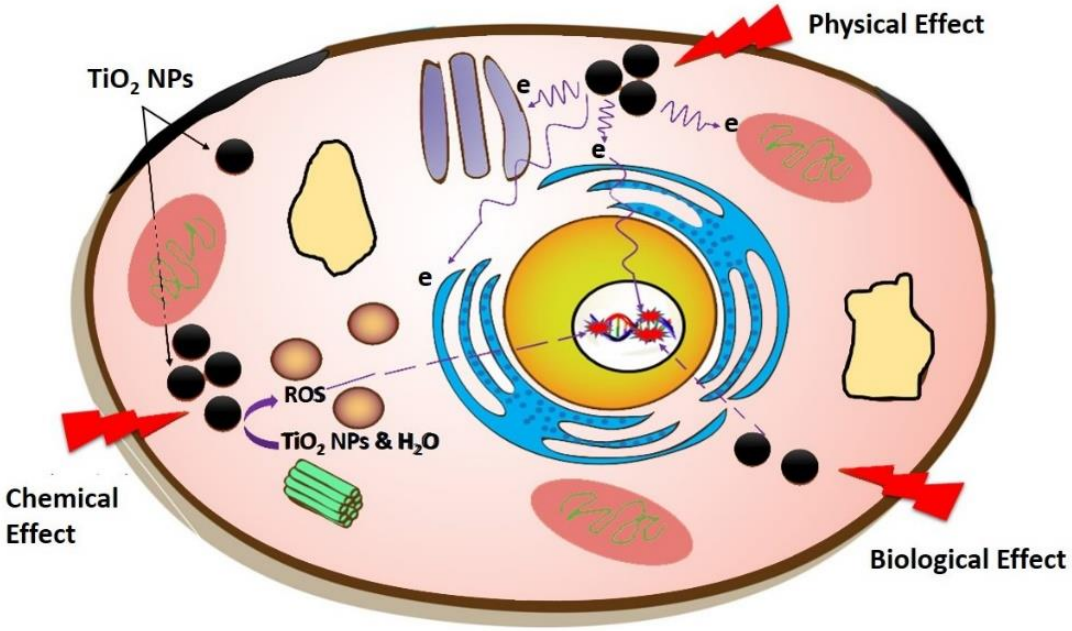

Figure 1-12: Schematic diagram showing interaction of X-ray with TiO_2 NPs result in the production of secondary electrons and ROS through physical and biochemical effects.

Low atomic number nanoparticles are targeted in to the biological target for this study. A brief introduction of such nanoparticles "TiO_2 NPs" is given in the next section.

1.4 Introduction to titanium dioxide nanoparticles (TiO_2 NPs)

Nanostructures and nanoparticles have now become common words in research and in daily life [20]. Invention of nanoscale materials had a huge impact in various applications including medicine. These nanoparticles have attracted considerable attention of scientists because of its wide potential applications especially biomedical applications which therefore resulted in an exponential growth of literature and publications in nanomedicine fields [21]. The possibility of effective diagnoses of diseases and their treatments has been shown to have bright future with the use of nanoparticles, typically with cancer. Researchers indicates that using nanoscale materials have particular features over conventional drugs in the management of malignant diseases such as targeted drug towards tumours based on nanotechnology drug delivery techniques [22]. Today these nanostructures can be synthesised and modified with various chemical reagents that allow them to be conjugated with antibodies or drugs of interest and this have opened a wide range of potential applications in biotechnology, targeted drug delivery and more importantly diagnostic imaging and treatments. The following sections will describe the nanoscale characteristic and provide an explanation of synthesis and properties of nanostructure samples used in this study that are titanium dioxide nanoparticles (TiO_2 NPs).

1.4.1 Nanometer size materials properties

In terms of diameter, coarse particles are between 2500 and 10000nm, while fine particle are sized between 100 and 2500 nanometre (nm) and ultrafine particles covers a range between 1 and 100 nm. Nanomaterial's can be defined as microscopic structures that

consist of number of molecules or atoms in the range of 1-1000 nm diameters [23, 24]. Accordingly, ASTM (American Society for Testing and Materials) developed the standard definition for nanoparticles as ultrafine particle with lengths in two or three dimensions smaller than 0.1 micrometer (100nm) and greater than 0.001 micrometer (1nm) in diameter range [25]. Materials brought from bulk to nanometer size materials will exhibit significant changes in their atomic basic properties such as electrical conductivity, melting point, structure, magnetic and optical characteristics [26, 27]. Moreover, cells can retain nanoparticle to longer duration more than bulk particle because of their small size [28], which is one of the advantages of using nano-sized particles for this study. Another advantage of materials being in nanoscale is the quantum confinement effects (size dependent phenomena) where the electrons become more confined in the particle as the particles size decreases (below the Bohr radius of the semiconductor materials) and result in the edge of the valance and conduction bands split into quantized, discrete, electronic levels [29]. In addition, unlike bulk materials, the quantized energy level characteristic in nanoparticles means the spacing of the band gap and electronic levels increases with particle size decrease which is due to the electron-hole pairs are now much closer and the Coulomb interaction between these pairs can no longer be neglected giving an overall higher kinetic energy [26]. Furthermore, the surface-to-volume ratio is much higher in nanoparticles than bulk materials. For radiotherapy aspiration, as hundreds of atoms can be packed in each nanoparticle, delivering one nanoparticle to the target results in transporting hundreds of atoms and therefor the probability hike of radiation interaction [30]. Also Surface Plasmon Resonance (SPR), which is the resonant oscillation of conduction electrons at the mediator between a positive and negative permittivity material stimulated by incident light, is one of the dubbed nanoparticle characteristic where free electrons are restricted in what is called quantum boxes. It has collective oscillation frequency that is the fundamental principle of color-

based bio-sensing technology for applications in the area of biology, and medical sciences [26]. Finally, nanoparticles have much greater surface area per unit mass compared to the bulk particles, this means more atoms at the surface compared to those inside; therefore, the chemical reactions occurs at the surface for nanoparticles are much more and reactive than larger particles for a given mass [27]. The surface atoms been active chemically are due to having fewer adjacent coordinate atoms and more dangling bonds [27, 31]. Nanoparticle properties can be controlled through the surface characteristic factors. Indeed, further electronic states in the band gap will be induced at any modification to the nanoparticles' surface and hence changes the chemical and physical characteristic of the nanoparticles [31].

In the next section, an introduction including physical and chemical characterisation of titanium dioxide nanoparticles (TiO_2 NPs) which have been selected for this research is described.

1.4.2 Titanium dioxide nanoparticles (TiO_2 NPs)

Titanium (Ti), is assumed to be the ninth most abundant element in the earth's crust. The average concentration of Ti in the earth's crust is 4400 mg/kg [32]. The absence of Ti as in metallic state in nature can be attributed to its great affinity for oxygen and other elements. The most well known oxidation state of Ti is +4, also +3 and +2 states exist. The most widely metallic compounds utilized in industry are titanium (Ti), titanium dioxide (TiO_2) and titanium chloride ($TiCl_4$). TiO_2 is known as titanium (IV) oxide, titanic acid anhydride, titania, titanic anhydrid, which is the naturally occurring oxide of Ti [32]. It is common that TiO_2 NPs occurs in nature in three obvious crystallographic phases: anatase, rutile and brookite [33]. In this thesis, anatase titanium dioxide nanoparticles (TiO_2 NPs) have been applied due to reasons stated in chapter two. These TiO_2 NPs have numerous and diverse uses

ranging from common products, like sunscreens, to sophisticated devices, environmental and biomedical applications. The significance and variety of these employments have prodded a large amount of researcher interest among fabrication, characterization and fundamental understanding of TiO_2 NPs nanoparticles since past decades [34]. The structural characteristics of different types of crystalline TiO_2 NPs are shown in **Figure (1-13).**

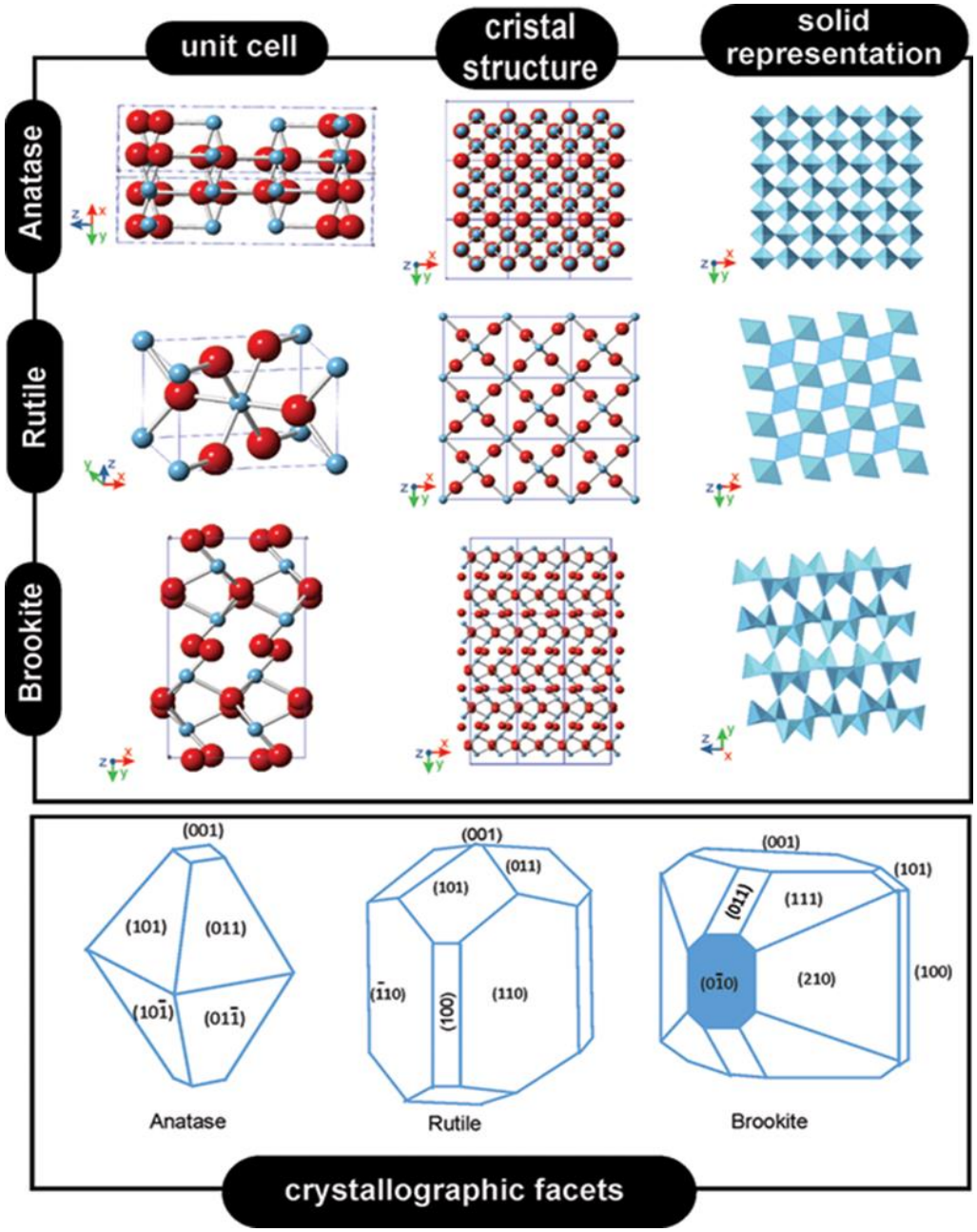

Figure 1-13: Unit cell, crystal structure, solid representation and crystallographic facets of anatase, rutile and brookite titanium dioxide nanoparticles (TiO_2 NPs) [34].

1.4.2.1 TiO_2 NPs synthesis

The Studies of titanium dioxide synthesis that uses diverse techniques has been briefly stated and reviewed since beginning of twentieth century [33]. In this thesis, hydrolysis of titanium chloride ($TiCl_4$) in sulfuric acid solution was used for synthesising anatase TiO_2 nanocrystal.

1.4.2.2 Chemical and Physical Properties of TiO_2 NPs

TiO_2 NPs is a white powder characterised as scentless and non-flammable. It has a molecular weight of 79.87 g/mol, melting point of 1843 °C, boiling point of 2972 °C. The refractive index is 2.488, 2.583 and 2.609 for anatase, brookite and rutile respectively. Anatase relative density is 3.78 g/cm3 and rutile density is 4.23 g/cm3 at 25 °C. TiO_2 NPs is poorly soluble in water. Anatase is chemically more reactive than rutile [32, 35 and 36]. For example, NPs (80/20; anatase/rutile, 3–5 nm; 100 μg/ml) generated 6 fold more reactive oxygen species (ROS) than rutile after UV irradiation [32]. Indeed, exposing anatase to UV light will generate ROS, and therfore has been suggested that anatase TiO_2 NPs has greater toxic potential than rutile TiO_2 NPs [36, 37]. Size, shape, characteristic, surface and inner structure are the main parameters affecting the physiochemical properties of particles. Rutile TiO_2 NPs are considered chemically inert. As previously stated for particle in general; therefore, TiO_2 NPs surface area become gradually larger as the particles become progressively smaller [38]. Surface modification, as coating, influences the activity of TiO_2 NPs. For example, surface modification of TiO_2 NPs by a grafting-to-polymer technique

result in cytotoxicity diminishes [39]. Further study confirmed the effect of TiO_2 NPs surface coating on biological response [40].

In the following sections, a brief introduction in to phantom based studies including PRESAGE® dosimeter and its potential application in radiotherapy is presented which is used to quantify the results of *in vitro* studies in this thesis.

1.5 Introduction to 3D phantom (PRESAGE®) dosimetry in radiotherapy

The technological advances in delivery techniques of radiotherapy, such as 3D conformal radiotherapy, SRS and IMRT techniques, have been playing a major rule in conforming the radiation dose deliver to the target volume is with a maximum fatal dose. This development enhance the therapeutic ratio and provide better tumour targeting while minimizing radiation dose to the surrounding normal organs, hence diminishing radiation-related complications [41, 42]. However, optimisation protocols for these complex treatment delivery techniques involve very steep dose gradients and are subsequently, to a great degree delicate to errors in treatment delivery. To reduce such errors, 3D dosimeters were produced as a relative system for improving dose monitoring and delivery [42]. The 3D dosimeters can be generally classified into two types' gel-based dosimeter [43, 44] or non-gel-based dosimeters [45, 46]. In this thesis, the non-gel based dosimeter were applied which is PRESAGE® dosimeter. Exposing the 3D PRESAGE® dosimeters to a radiation doses will change its optical density and therefore, this change can be quantitatively recorded and represents the dosimeter delivered dose [42]. Furthermore, the uses of PRESAGE® dosimeter has been expanded to the validation of dose spatial distributions and enhance dose in nanoparticle-enhanced radiotherapy via the sensitivity modulated advanced radiation therapy

(SMART) dosimeter [45]. The PRESAGE® dosimeter, which is briefly explained in the following section, is a phantom that helps in measuring the absorbed dose distribution in a full 3D geometry. It is nearly tissue equivalent and can be moulded to any required shape or compose.

1.5.1 The PRESAGE® dosimeter

PRESAGE® is a solid radiochromatic dosimeter made of polyurethane matrix. The solid characteristic of PRESAGE® makes it suitable to be designed as 3D dosimetry that has a potential application in advanced radiation treatment techniques. It is optically clear formulated using three ingredients which are a transparent polyurethane plastic prepolymers mixture, leuco dye (leucomalachite green (LMG)) as a reporter component, halocarbons (chloroform, bromoform or iodoform) as a radical initiator and optionally, for minimising dosimeter damage from UV radiation, ultraviolet (UV) stabilisers can be added [47, 48]. Upon irradiation, radical initiator will generate free radicals because the radical initiators possess unstable/weak covalent bonds with low bond dissociation energies, therefore, such compounds are easily cleaved under specific conditions (heat or radiation) leading to the production of free radical species. These free radicals will oxidise the leuco dye leading to a change in optical density (i.e., colour) (**Figure 1-14**) hence it is called radiochromic dosimeter [47].

Prior and post irradiation, PRESAGE® dosimeter must be stored in a cold (-18 °C) and dark environment to avoid any accidental absorbance change due to exposure to visible or ultraviolet light.

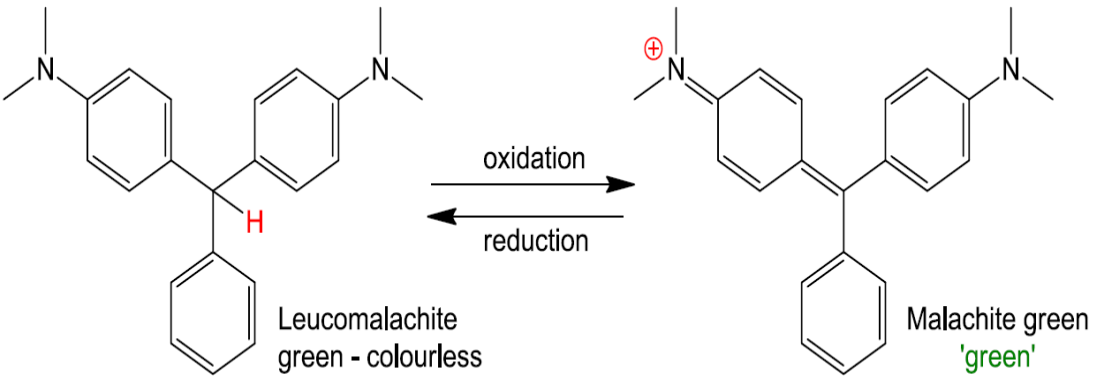

Figure 1-14: Transformation between leucomalachite green dye and its oxidised product [47].

The deformable characteristic of PRESAGE® dosimeter by replacing the polyurethane plastic by a transparent polyurethane rubber made it suitable for deformable designs dosimeter applications [49]. However, the usage of polyurethanes precursors as a matrix for the PRESAGE® dosimeter preparation is manly depending on the logic that these component can be mixed and polymerized at room temperature rather than polyesters or epoxides which require high curing temperature (Above 100 oC) which this temperature is high enough to oxidise the leuco dye prior to irradiation rendering the dosimeter unusable [50, 51].

Polyurethanes are a class of materials known as reaction polymers such as epoxies and polyesters [52, 53]. The polyurethane precursors consist of two components, referred to as Parts A and B; Part A is an aliphatic diisocyanate and Part B is a polymer with hydroxyl functional groups (polyol) [54]. The isocyanate group is highly reactive towards nucleophilic functional groups (e.g., hydroxyl groups). This reaction is generally utilized for polyurethanes preparations that have a wide range of applications [54].

The polymerisation reaction consist of reacting one isocyanate group of the diisocyanate with the hydroxyl group of the polyol to form a urethane linkage (– NH-(C=O)-O) [54, 55]. This reaction produces heat (exothermic) and the rate of curing depends on the presence of a suitable catalyst, concentration of reactive groups and the temperature [56]. The polyurethane catalysts used in this reaction is to enhance the polymerization extent and rate, thus improving the structural integrity of the resin. The most commercial polyurethane catalysts (metal compounds) utilized in the polymerisation reaction is tin-based compounds, such as dibutiltin dilaurate (DBTDL), which is considered the standard catalyst for the promotion of the reaction of an isocyanate with the active hydroxyl groups of a polyol [53, 57-59]. The typical polymerisation reaction is illustrated in **Figure (1-15).**

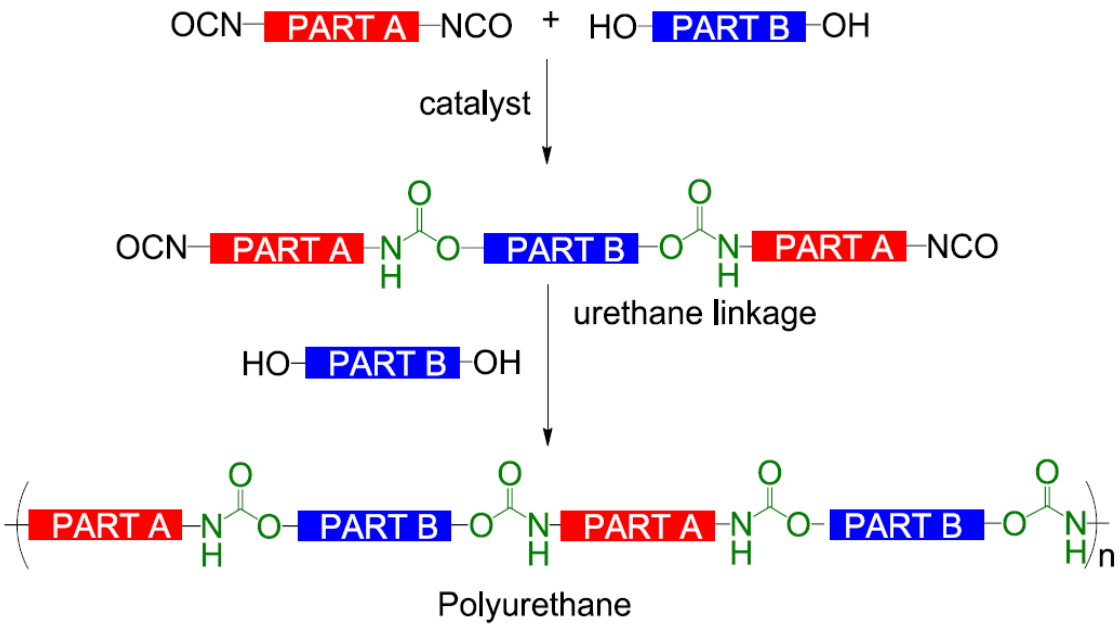

Figure 1-15: Typical chemical reaction between diisocynates and polyols to form polyurethanes [54].

Radical initiators used in the composition of the PRESAGE® dosimeter are classified to: (i) organic peroxides, such as benzoyl peroxide; (ii) azo compounds; and (iii) halocarbons, such as chlorine (Cl), bromine (Br) or iodine (I) [60]. The organic peroxide and azo compounds are inherently sensitive to high temperatures and are unstable, while halocarbons have been shown to be suitable even with high-energy radiation [51]. Halogenated carbons (Halocarbons) are organic compounds containing covalently bonded carbon and halogens. Upon PRESAGE® dosimeter irradiation, the free radicals are generated from the homolysis of the bond between the carbon and the halogen. The number of free radicals produced is directly proportional to the C−X bond dissociation energy where X is either Cl, Br or I [61].

Leuco dyes are a class of chemicals that has featured forms, such as colourless [62]. There are different leuco dyes that are suitable for use as a reporter compound in the PRESAGE® dosimeter formulation, including LMG, orange aminofluoran, green diaminofluoran leuco and crystal violet lactone (LCV) [51]. Although LCV is the most sensitive to radiation dose and most stable post-exposure to radiation, LMG, which is used in this study, is the most desirable leuco dye as a reporter compound in the formulation of the PRESAGE® dosimeter. That is due to the typical visible maximum absorption wavelength (λmax) of its oxidised form (malachite green) is approximately 633 nm compared to 609 nm for LCV [50]. The 633 nm λmax corresponds to LED source or the helium-neon laser output (633 nm) of the commercially available optical scanning systems such as VistaTM (Modus Medical Devices Inc.) and OCTOPUSTM (MGS Research) [63]. Therefore, utilising LMG as a reporter compound allows the PRESAGE® dosimeter to be 3D scanned using these systems with optimum sensitivity.

1.5.2 Applications and limitations of the PRESAGE® dosimeter

Dosimetry systems have been played a major role in the dose distribution verification. In typical clinical use of modern radiation therapy, the need for determination of three dimensional (3D) dose distributions with high resolution and accuracy has been arisen. The development of dosimeter systems over the past decade to achieve this challenge was the invention of a 3D radiochromatic dosimeter (PRESAGE® dosimeter) [64]. The unique 3D dosimeter (PRESAGE®) has a great potential value for use in clinical radiotherapy applications. The other specific applications of PRESAGE® dosimeter include the measurement of electron dose distributions around in-homogeneous tissue within the target volume [65]. In synchrontron microbeams, the peak-to-valley dose ratio was calculated [66]. In addition, the PRESAGE® dosimeter has been tested with beta-emitting radionuclides (e.g., Yttrium-90) and with proton bean for proton therapy application [67- 69].

The potential advantages and features of PRESAGE® dosimeter over the other dosimeters are; it has a transparent properties which is very important from an optical imaging prospective since light has to pass through fewer interfaces on its transit through the dosimeter, therefore minimising optical artifacts and simplifying any optical modeling required [40]. In addition, PRESAGE® dosimeter has efficient dose respond properties that could be employed for measuring surface doses such as electron beam and deeper doses distribution such as photon beams [65]. In contrast to gel dosimeter, the solid characteristic of PRESAGE® dosimeter negating the need for an external mold and can be fashioned in to any required shape which is also easily handleable. Other advantage of such dosimeter is the lake of sensitivity to the atmosphere exposure doses such as oxygen. Furthermore, it has the ability for high accuracy optical CT scanning due to radiochromatic optical contrast as opposed to light scattering contrast [70, 63, 64, 71-76].

In the other hand, there have been some limitations for PRESAGE® dosimeter. Majority of investigations have focused on potential clinical radiation therapy applications of the PRESAGE® dosimeter while a very few studies have demonstrates the influence of modifying PRESAGE® components including polyurethane, leuco dye and radical initiators on the inclusive properties of the PRESAGE® dosimeter such as stability, radiological properties and sensitivity to radiation doses. It has earlier shown that PRESAGE® dosimeter is of high effective atomic number (Z_{eff}) about 8.65 which was due to the high concentration of halocarbons radical initiator in the PRESAGE® composition since these halocarbons are of high Z number [77], therefore PRESAGE® dosimeter was considered to be non-water equivalent dosimeter for kilovoltage energy range (10-100 kV) where photoelectric effect is predominant interaction [78]. Furthermore, the effect of incorporating of high Z metal compounds on the characteristics of the PRESAGE® dosimeter formulation (e.g., sensitivity to radiation dose) has not been well studied. However, most dosimetric applications are performed with relatively low radiation doses (< 5 Gy), therefore such sensitivity characteristic is an important factor to be considered which dosimeter need to have an efficient and linear response to low radiation doses, whilst maintaining tissue equivalent radiological characteristics.

In contrast to gel-based dosimeters, the PRESAGE® dosimeter has been almost invented since a decade [64]. Therefore, there have been no obvious investigations about the mechanism by which the dosimeter changes its optical properties (i.e colour) post irradiation. The only mechanism and potential chemical pathways adopted is that the radical initiator oxides the LMG dye post irradiation and then change the dosimeter colour. Indeed, such information is valuable for further optimisation of the PRESAGE® dosimeter formulation for potential clinical applications.

CHAPTER TWO

Literature Review and Aims

2. Literature review and aims

This chapter present a review of the works investigated about radiation dose enhancement produced by high and low atomic number (Z) materials in general and anatase TiO_2 NPs in particular. Furthermore, it explains how theoretically to calculate the radiation dose enhancement factor (DEF). Finally, the specific objectives of this study are stated.

2.1 Nanotechnology in radiotherapy

There have been various major advancements in the field of radiotherapy during last few decades rendering this treatment safer and more reliable [79]. Most of these developments have been based on advanced technology used to further confine the beam on the targets and for reducing radiation doses to the surrounding healthy tissues [80]. These improvements were brought by invention modern techniques performed by LINACs such as intensity-modulated radiotherapy (IMRT), stereotactic radiosurgery (SRS) and image guided radiotherapy (IGRT) which provide high precision conformal dose and accurate delivery of enhanced radiation dose to the tumours; furthermore, it helps to better localize the tumours using ancillary imaging equipment's. However, these technological improvements in radiotherapy needs to be combined with advanced understanding of tumour's radiobiology properties to have best impact on the treatments [81, 82]. Hence, improving the treatment efficiency of radiotherapy requires serious efforts to complement the technological advancement which radiosensitising agents are one of the strategies that have been utilized for treatment efficiency improvement [82]. The most important improvements approached for radiation therapy comprise developing the radioresistance of health tissue, enhancing radiosensitisation of tumour tissue and reversing the radiation resistance of tumour tissue.

Tumours radiosensitivity has been modified by radiosensitising agents such as using nanoparticles that have played a key role in the enhancement of the radiation therapy by acting both as a therapeutic and as a carrier for other therapeutic. These agents are able to be selectively targeted to cancer cells and hence have a potential to enhance the effects of radiation on the tumours with the objective of delivering efficient radiation doses that can eradicate the cancer cells without exceeding normal tissue tolerance [83]. Currently such agents are used in the form of chemical agents in some special radiotherapy techniques termed "adjuvant" radiotherapy such as Fluorouracil (5-FU). Previously, enhancement of radiosensitivity of tumours by the effectiveness of oxygen as an agent was evaluated. Various examinations have shown that, tissue oxygen content show enhanced radiosensitisation compared to hypoxic cells and this is because of interaction of ionising radiation with oxygen atoms will result in reactive oxygen specious (ROS) generation which are of highly damaging abilities to the DNA molecules hence leading to cell death [84, 85]. Furthermore, chemotherapy drugs such as cisplatin and carboplatin have been investigated as a potential radiosensitiser, these observations have slight dose enhancement that therefore have been deemed as unsuitable strategy for future clinical application [86].

2.2 Dose enhancement by high atomic number materials

Early investigations of radiation dose enhancement were based on loading the target with high atomic number (Z) materials, which were reported in many publications since the middle of last century [87, 88]. Later, many other researchers have studied the interaction of X-ray with high Z materials and have observed an enhancing in dose due to the extra photoelectron production [89, 90]. Investigations were attributed the reason of dose

enhancement in the target to the increase in the number of photoelectrons produced due to the presence of high Z materials which deposit their energy in the target, whereas other studies reported that scattered electrons increases the dose in the vicinity of the high Z materials [90, 91]. Researcher have shown that the increase in the number of photoelectron and/or scattered electron generated will affect the biological system, looking more closely at, when monolayer cells are irradiated with low energy X-ray adjacent to high Z materials, the number of killed cells were increased [92, 93].

The idea of utilizing high Z materials for radiosensitisation of tumours is due to the increase in the cross-section of radiation interaction and therefore produces more free radicals that enhance the dose due to extra photoelectron production [94, 95]. Since this hake in the interaction cross section is mainly due to the increase in the probability of interaction via photoelectric effect 'P.E.', therefore such effect are only significant at low energy X-rays where the probability of 'P.E.' is high. Over the last few decades, such strategies were explored and iodinated contrast agents were used as dose enhancing agents [96]. In phantoms and vitro studies, the potential applicability of iodine radiosensitiser as high Z materials for radiation dose enhancement has been observed [97, 98]. This exploration has continued with investigation of various high Z materials such as gold and bismuth compound nanoparticles. These nanoparticles have created adorable result for improving the outcome in cancer treatment in vitro [82, 99 and 100].

2.2.1 Dose enhancement by gold nanoparticles

Gold nanoparticles unique physicochemical properties have placed it as one of the most efficient and well-studied agents for radiation dose enhancement [82]. Regulla et al

(1998) first described the radiation dose enhancement by gold by measuring dose enhancement effect on cells using gold sheet. Cells were grown on a gold sheet and were irradiated with low energy X-ray ranging from 40-120 KeV, the results showed an excellent dose enhancement in more than measurement [101]. Herold et al (2000) used gold microsphere (1.5 to 3.0 μm). The NPs were injected directly in the tumours to measure the radiosensitization [102]. Different types of cancer cells were used in this study and a reduction in plating efficiency was noticed which means increasing in the numbers of death cells [82]. Hainfeld et al (2006), for the first time, successes in identifying gold nanoparticles (AuNPs) as enhancing contrast agents in radiotherapy for in vivo computed tomography (CT) imaging [103]. The distinctive high absorption coefficient of Au (5.16 $cm^2.g^{-1}$) compared to Iodine (1.94 $cm^2\ g^{-1}$) at KeV, and the significantly higher Z number (Au=79, I=53) lead to a three times greater contrast per unit weight for gold that Iodine [103]. AuNPs was first time applied on mice bearing subcutaneous EMT-6 mammary carcinoma for dose enhancement. AuNPs of 1.9 nm in diameter were delivered to the tumours and 250 KeV X-ray was used for irradiation. Result showed tumours eradication and mice survive for longer time [104]. Various researches, studied the feasibilities of AuNPs for radiotherapeutical application, have been published as a consequence of Hainfeld group first study success. The AuNPs were found to be non-toxic to the rat and were cleared rapidly from the body through Kidney [104]. The safety and toxicity of AuNPs still concern the researchers that need more investigation which they argue that delivering high doses of AuNPs may be linked to toxicity [105]. The solid property enables it to easily be functionalized with biocompatible coating. Many investigations have pointed out that the modulation of polymer coating and biocompatible surface decreases the toxicity of AuNPs [106, 107 and 108].

The capability of AuNPs for dose enhancement has been noticed in vitro experiments [109-113]. Interm of size, AuNPs of 50 nm diameter could achieve the maximum dose

enhancement in comparission to larger and smaller diameter NPs as it has been reported by Chithrani (2010) [113].

Theoretical simulation and measurement of the interactions between AuNPs with various types of surface treatment techniques and beam energies have been investigated by Monte Carlo simulation software [114-119]. Low energy X-ray and gamma rays are found to be more efficient for radiation dose enhancement than high energy X-ray by using this computational simulation. Whereas, the obvious differences in the dose enhancement factors (DEFs) measured by many various investigation can be attributed to the type of code used and some imposed limitations such as the disability to measure the microscopic dose enhancement around the AuNPs that prevent absolute and accurate calculation of the DEFs [120]. Cho (2005), used BEAMnrc/DOSXYZnrc code to estimate DEF for several phantom test using gamma rays, kilovoltage and megavoltage photon beam with various concentration levels of AuNPs in the target [121]. Dose enhancement by gamma rays and low energy X-ray were found to be greater than high energy ones by up to 31%. Another study, Cho et al (2009), observed significant increase in the fluency photoelectron with AuNPs during gamma ray or low energy X-ray irradiation [122]. AuNPs dose enhancement by kilovoltage photon energy have attributed to the increase in photoelectron absorption due to the high Z materials. Clinically where megavoltage energies are predominant, such dose enhancement would not occur because Compton scatter is Z independent [15]. On the other hand, many researches have noticed an increase in cell death using AuNPs with clinically megavoltage energy beam [111, 120, 123 and 124]. In brief, clinical applications of AuNPs for radiation dose enhancement need a complete understanding of the effect of AuNPs size, concentration and polymer coating on this enhancement. This basic information is important for the logical development of AuNPs for clinical applications [82, 125]. Currently, several studies are

investigating new nanoparticle to alter the expensive AuNPs that would be efficient as well. Bismuth-based nanoparticles (BiNPs) are promising in that respect.

2.2.2 Dose enhancement by bismuth compound nanoparticles

Bismuth-based have been utilized for treating a number of medical conditions. The efficiency, costless and treating medical conditions efficacy has made it widely available in many countries worldwide. Clinically bismuth is used as antiulcer drugs [126]. Atmospheric oxygen can oxidise pure bismuth easily. It is found in the ores bismite (bismuth oxide) and bismuthinite (bismuth sulfide) [127]. *In vivo* computed tomography (CT), Bi_2S_3 have been shown an enhancement same as AuNPs [128-130]. PRESAGE® dosimeter doped with Bi_2O_3 has caused a photoelectron and Auger electron emission of low energy that is considered to be responsible for the radiation dose enhancement [109, 131]. Bi_2S_3 NPs have shown to be a suitable contrast agent for radiologic imaging and recently proved to be radiosensitiser agent *in vitro* at kilovoltage range of X-ray energies. Therefore, BiS_2 is considered as valuable theranostic agent at low energy in radiotherapy applications [132].

2.3 Dose enhancement by low atomic number materials

In radiotherapy treatments, a very few number of investigations have been done for measurement of radiation dose enhancement resulting from low atomic number (Z) materials such as phosphorous (Z=15), calcium (Z=20), Titanium (Z=22) and others materials. For typical biological systems, the low Z number species present means that Compton scattering, which is inelastic scattering of the photon by a charged particle, is the predominant

interaction with ionising radiation across the entire energy range of the most interest to medical physics as illustrated in **Figure (2-1)** [133]. Since Compton scattering is dominant, the interaction of ionising radiations with these low Z-number materials will result in only a relatively small number of free radicals generation and hence low chance for significant damages to the DNA molecules in the cells and leads to cell death, which means negligible dos enhancement [133, 134].

In recent years, investigation about improving the image quality and enhancing the radiation effect (radiosensitisation) at the target by using low Z number NPs has been of an increasingly interest by many researchers, especially about nano-sized materials which generate reactive oxygen specious (ROS). This attract can be attributed to the beneficial of ROS generation in biomedical science [135]. However, most of the searches are in simulation field using Monte Carlo simulations or using UV radiation and only a very few investigations have been done for measuring radiation dose enhancement at low range (kilovoltage) of X-ray energies using low atomic number (Z) materials.

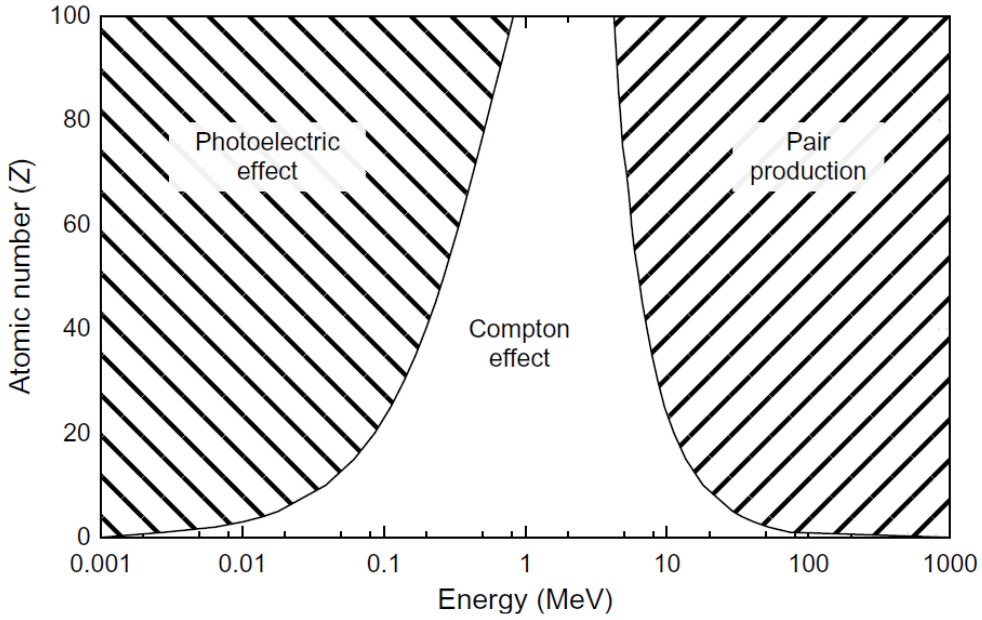

Figure 2-1: A plot showing the dominant process in determining the mass attenuation coefficient as a function of atomic number and X-ray energy. For low atomic number systems such as TiO_2 NPs and at low-energy (kV) portion of this plot, the photoelectric effect is dominant, whereas Compton scattering dominates for the whole energy range of medical interest (i.e MV energy), whereas pair production dominates the high-energy portion [133].

2.3.1 Dose enhancement by anatase titanium dioxide nanoparticles (TiO_2 NPs)

Recently, researchers have shown interest in using TiO_2 NPs for dose enhancement due to its ability in generating ROS [136, 137]. Most of the work done is in the range of using simulation, UV radiation and low energy (kV) X-ray beams. Jiang et al (2008) studied the ability of TiO_2 NPs in generating ROS which was measured by using a fluorescent dye, 2',7'-dichlorofluorescein diacetate (DCFH-DA). Sodium hydroxide was used to cleave the acetate group from the reduced dye (DCFH). In the presence of hydrogen peroxide (H_2O_2) or oxidizing species generated by nanoparticles, DCFH was oxidatively modified into a highly fluorescent derivative, dichlorofluorescein (DCF), which was detected using a

spectrofluorometer (absorbance/emission maxima, 485 nm/535 nm). Also they established TiO_2 NPS size dependent ROS activity using nine different sizes. Their observation demonstrates increase in the level of ROS with particle size and that highest ROS activity was observed for TiO_2 NPs of 30nm and to be constant above 30 nm [134]. Chan et al (2011) investigated the interaction of two crystalline phases of TiO_2 NPs with HaCaT cells. According to surface properties, they have shown that TiO_2 NPs in anatase phase, in addition to having larger surface area and creation of free radicals; allow spontaneous ROS generation, which has a high impact in damaging DNA molecules, while rutile TiO_2 NPs did not after dispersion [136, 137]. However, both anatase and rutile TiO_2 NPs generate ROS when interact with cellular components but anatase phase showed to interact more effectively with cells as it's found to be collected in the nuclei whereas rutile phase TiO_2 NPs are found as small cluster or as single particle in the cytoplasm [136]. Jun-Jie et al (2012) determined the phototoxicity in human skin keratinocytes using TiO_2NPs with different crystal phase and molecular sizes under UVA irradiation. They showed that the smaller particle size the higher cell damage and rutile phase showed less phototoxicity than anatase TiO_2 NPs [136]. Helen et al (2012) succeeded in optimizing treatment *in vivo* of deeper tumour using X-rays instead of UV light that is limited by the penetration depth. Titania nanoparticles were doped with gadolinium to optimize the localized energy absorption from a conventional medical X-ray unit. They showed that TiO_2 NPs irradiated by kilovoltage X-rays can result in ROS generation leading to DNA damage and then cell death. They also demonstrated that rare earth doped Titania nanoparticles injected in intratumoural can enhance the efficiency of radiotherapy *in vivo* where the tumour volume was reduced by around half in its original value by exposing it to 3 Gy of 200kV X-ray irradiator [139]. Mirjolet et al (2013) showed the ability of titanium nanotubes (TiONts) to penetrate human glioblastoma [one of the highly resistive tumours] cells *in vitro* and stay in the cytosol for over 10 days with no

cytotoxicity [140]. Babaie et al (2014) reviewed the characteristic of TiO_2 NPs as radio sensitizers. TiO_2 NPs and amino silanized oxidized silicon NPs provide oxidative stress by embedding in mitochondrial membranes, since TiO_2 NPs has a lot of water, oxygen and hydroxides in its structure, it will generate ROS that act as a radio sensitizer. Also TiO_2 NPs interact with radiation, free radicals such as OH•, H• and HO• (which are well known radio sensitizers) are generated [137]. Increasing the level of oxygen atoms in TiO_2 NPs such as Ti-peroxide have also been tested to be effective radiosensitiser as have been investigated by Nakayama, M., et al (2016) [141]. However, this has only been tested with low energy X-rays which have very limited uses in radiotherapy. Most of the investigation where in the range of applying UV-radiation, gamma radiation and/or low energy X-ray beams. Accordingly, anatase TiO_2 NPs in the range of about 30 nm have been selected for this thesis which is extending the potential applicability of TiO_2 NPs in radiotherapy to include wider ranges of energies by including the most commonly used beam in radiotherapy (i.e megavoltage beam) which has not been investigated to date and is one of the objectives of this study as indicated in **section (2.6)**.

2.4 Analysis of radiation attenuation and absorption in the presence of low Z materials

The interaction of X-ray with atoms in any target result in the incident photons lose all or some of their energy where in photoelectric interaction, all of the X-rays energy is converted into kinetic energy for the ejected electron while in Compton scattering, part of the incident X-ray eject Compton electron and the rest will scatter as scattered photon. In soft tissue the most dominant X-ray interaction at kilovoltage energy range is Compton scatter,

while in the presence of TiO_2 NPs in the target, the most dominant interaction is the photoelectric effects [72]. This clearly can be observed from the attenuation and absorption data obtained from Hubbell physical data [72], which the value for mass attenuation coefficient (μ/ρ) and mass energy absorption coefficient (μ_{en}/ρ) for Ti is noted to be higher than the value for water as shown in **Figure (2-2)**. For example, at 40 keV photon energy, the μ/ρ for Ti and water are 2.21 cm^2/g and 0.268 cm^2/g respectively. At the same energy, the value of μ_{en}/ρ for Ti and water are 1.9 cm^2/g and 0.0695 cm^2/g respectively. These values indicate that more energy will be deposited and hence an increase in the generated photoelectrons will result from the presence of TiO_2 NPs compared to the tissue alone.

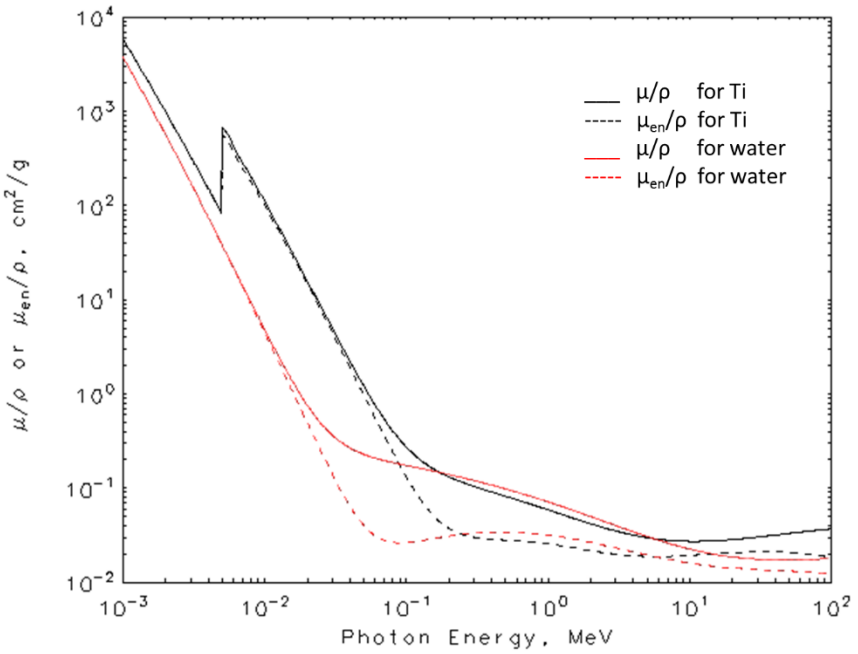

Figure 2-2: Mass attenuation coefficient (μ/ρ) and mass energy attenuation coefficient for Ti and water as function of energy.

2.5 Theoretical calculation of radiation dose enhancement by nanoparticles

Radiation dose enhancement can be indicated by dose enhancement factor (DEF) which is defined as *the ratio of absorbed dose in the target doped with nanoparticles over the absorbed dose in the target without nanoparticles* as illustrated in equation (2-1).

$$\text{DEF} = \frac{\text{Dose deposited in target with TiO2 NPs}}{\text{Dose deposited in target without TiO2 NPs}} \qquad \text{……. (2-1)}$$

Roeske et al (2007) developed a method for calculating DEF for various high Z materials by analyzing the mass energy absorption coefficient (μ_{en}/ρ) [142]. They derived a mathematical formula for determining DEF values for poly energetic beams using the following equation (2-2):

$$\text{DEF} = 1 + \frac{k_{NP} \int_{E=0}^{E\,max} \psi(E)\left(\frac{\mu_{en}}{\rho}\right)_{NP,E} dE}{\int_{E=0}^{E\,max} \psi'(E)\left(\frac{\mu_{en}}{\rho}\right)_{water,E} dE} \qquad \text{…… (2-2)}$$

μ_{en}/ρ= the mass energy absorption coefficient

E= energy ranging from background 0 to maximum

Ψ= energy fluency

Ψ′= differential photon energy fluency

NP= nanoparticles

K_{NP}= mass composition of the nanoparticles

The above equation does not take into consideration the backscatter radiation created at the interface of high and low Z materials; it underestimates the dose enhancement by a factor of about 2 [142].

In addition, DEF values could also be evaluated by analysing the μ_{en}/ρ values for mono-energetic beam, which have been reported for gadolinium and iodine elements [143, 144]. The ratio of the μ_{en}/ρ values of nanoparticles to water is the DEF value as shown in equation (2-3).

$$DEF = \frac{\left[\frac{\mu_{en}}{\rho}\right]_E^{water+NP}}{\left[\frac{\mu_{en}}{\rho}\right]_E^{water}} = \frac{w_{NP}\left[\frac{\mu_{en}}{\rho}\right]_E^{NP} + (1-w_{NP})\left[\frac{\mu_{en}}{\rho}\right]_E^{water}}{\left[\frac{\mu_{en}}{\rho}\right]_E^{water}} \quad \text{…….. (2-3)}$$

NP = nanoparticles

μ_{en}/ρ = mass energy absorption coefficient

w_{NP} = fraction by weight of NP in the mixture

E = energy of the monochromatic beam

Indeed, materials with high Z value enhance the radiation dose more effectively than materials with lower Z value as shown in **Figure (2-3)** [142].

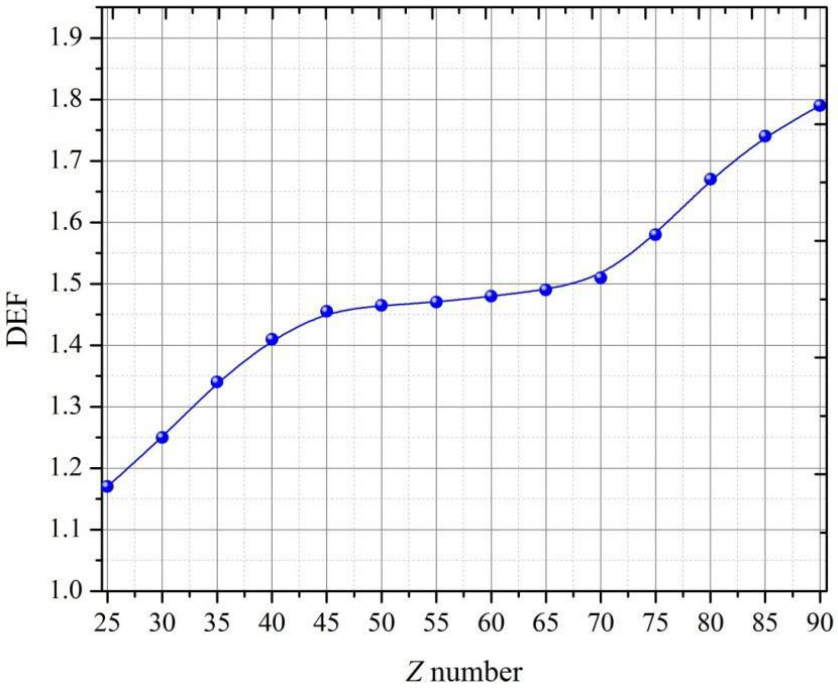

Figure 2-3: DEF values against various Z numbers for 140 kV energy [142]

The DEF distribution curve shown in **Figure (2-3)** is only showing the effects of physical parameter, such as generated secondary electrons, for enhancing the radiation dose. Whereas recently it has been hypothesised that for *in vitro* and *in vivo* studies there are a very important factor, biochemical effects such as ROS, that have a high impact in enhancing the radiation dose and it is not considered in this DEF distribution curve.

2.6 Thesis objectives

Recently, researchers interest have attracted to investigate the nanoparticles enhanced radiation dose at the target for radiotherapy that holds potentially very promising value in the treatment of cancer with minimal effects on normal tissues. This new technique aims to increase the differential radiation dose delivered to the target compared to the dose received by the surrounding healthy tissues. The main objective of this thesis is to investigate and pioneer the dual applications of anatase TiO_2 NPs on cancer therapy as radiation sensitiser and imaging (potential theranostic agent). Therefore, it's important to deeply study the characteristic of such nanoparticles and assessment in terms of *in vitro* and phantom based studies must be conducted to justify the anatase TiO_2 NPs promising benefits for cancer treatments that outweigh any risks before consider them for clinical trials. This thesis mainly assesses the potential theranostic application of anatase TiO_2 NPs in medical radiations. The studies are conducted using both PRESAGE dosimeter and cell in culture to quantify the produced dose enhancement factor (DEF) by anatase TiO_2 NPs for low (kilovoltage) and high (megavoltage) radiotherapy X-rays energies. The most specific aims of this study are listed below:

1. To Synthesis anatase crystal phase of TiO_2 NPs and modify them using coupling agents such as PolyEthylene Glycol Trimethoxysilane (PEGTS) which makes the NPs hydrophobic and then dispersible in halocarbons (PRESAGE® chemical composition) for phantoms based studies and also with AmenoPropyl Trimethoxysilane (APTS) in order to make the NPs hydrophilic and then capable to be dispersed in cells-culture medium for *in vitro* studies. The physical and chemical characteristic of the synthesized TiO_2 NPs were

studied by employing characterization techniques such as Transmition electron microscopy (TEM), X-ray photoelectrons spectroscopy (XPS), X-ray diffraction (XRD), Thermogravimetric analysis or thermal gravimetric analysis (TGA) and Fourier transform infrared spectroscopy (FTIR).

2. Fabricate water equivalent PRESAGE® dosimeters to be employed for phantom based studies and study their characteristic such as physical and radiological properties. Furthermore, explore the radiation dose enhancement induced by anatase PEGS functionalised TiO_2 NPs at kilovoltage and megavoltage radiotherapy X-ray beams using PRESAGE® dosimeters.

3. For the first time, to measure the 2D dose distribution prior and after the inhomogeneous section in PRESAGE® dosimeter using CLARIOstar microplate reader (UV/VIS spectrophotometer) and then simulate the tissue inhomogeneity behavior.

4. To study the inclusion of TiO_2 NPs inside the cells and observe their distribution with in the cells. Two different techniques were employed to confirm the internalisation of TiO_2 NPs into the cells these includes flow cytometry to assess cell population with different concentration of TiO_2 NPs relative to control and light microscopy through cell staining techniques.

5. To assess the cytotoxicity of amine functionalised anatase TiO_2 NPs to cells in regards to different concentration of TiO_2 NPs and incubation time. Cell viability is the end point of the toxicity.

6. Feasibility of employing TiO_2 NPs as radiosensitisation agents for *in vitro* studies using two different cells lines, and then the dependence of the radiosensitisation on the radiation energies including low (kilovoltage) and high (megavoltage) radiotherapy X-rays energies and on the TiO_2 NPs concentrations to be established by two methods: Colorimetric (MTS) and Clonogenic assays. Also, to validate the biological studies by comparing it with phantom based studies.

7. To predict the optimal kilovoltage energy range for maximum dose enhancement factor (DEF) which is determined in both *in vitro* and phantom based studies.

8. To evaluate the radiobiological effect of amino functionalised anatase TiO_2 NPs on different cell lines. Linear quadratic (LQ) model were used to analyse the experimental data which the plotted cell survival curves were fitted with linear quadratic model function and the linear (α) and the quadratic (β) parameters were extracted employing this model which these parameter then describe the DNA damage by radiation.

9. To detect the reactive oxygen species (ROS) and specially hydroxyl radicals ($^{\bullet}OH$) generated from irradiated anatase TiO_2 NPs for low and high X-ray energies.

10. The study will be extended using proton beam, hence possibility of making TiO_2 NPs as theranostic agents (enhancement treatment and imaging).

CHAPTER THREE

Methodology: Materials, Methods and Procedures

3. Methodology: Materials, Methods and Procedures

This chapter presents the materials, instrumentation and experimental methodologies used in this thesis. It is divided in to three parts and each of these parts is subdivided into several sections. The first part explains the process of synthesising the TiO_2 NPs in anatase crystalline form and TiO_2 NPs surface modification and characterisation. The second part provide details of the chemical components used in PRESAGE® dosimeters fabrication, handling, fabrication process, the methods of preparing and dispersing the TiO_2 NPs in polymeric matrices, explaining the procedure of the PRESAGE® dosimeter irradiation with kilovoltage and megavoltage X-ray beams and last section of this part presents the techniques used for optical density measurements such as UV/VIS spectrophotometric, confocal microscope, optical CT scanner and CLARIOstar microplate reader. Finally, this chapter displays cell culture protocols, the TiO_2 NPs association with cells, cytotoxicity measurements, irradiation procedure using different X-ray modalities, at the end of the third part, the method of obtaining cell survival curve and ROS detection is presented.

3.1 SECTION A: Synthesis of nanoparticles for PRESAGE® dosimeter and *in vitro* studies

3.1.1 Synthesis anatase crystalline phase of TiO_2 NPs

Anatase crystalline phase TiO_2 NPs were synthesised according to a previously published procedure [145].The main material is titanium chloride ($TiCl_4$) in the synthesising procedure. The process details are schematically shown in **Figure (3-1)**.

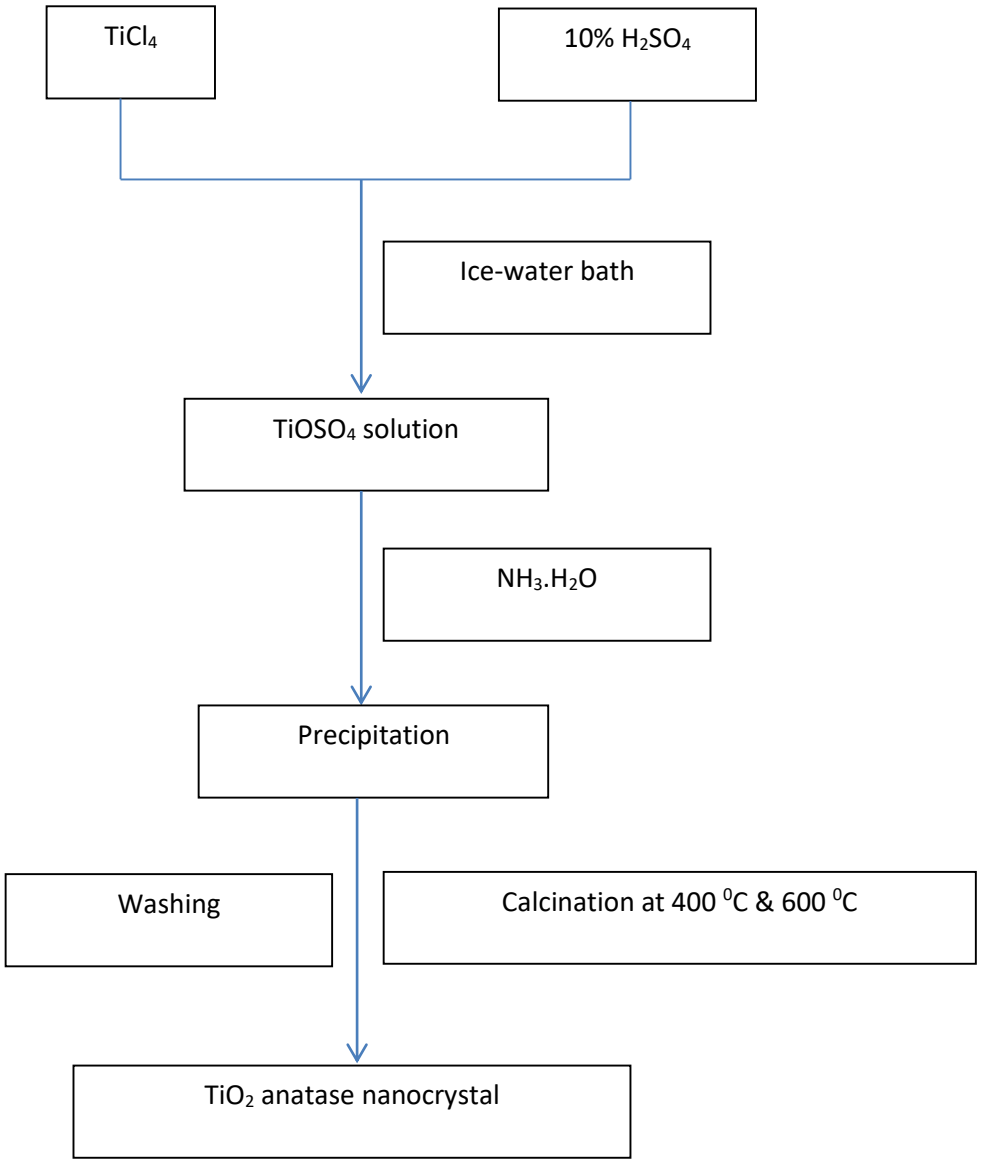

Figure 3-1: Schematic diagram of preparation nanocrystal anatase TiO_2 NPs.

Briefly, sulfuric acid (15 mL, 10% H_2SO_4) was added to Milli Q explain (150 mL) and cooled to 0 °C in an ice-water bath. $TiCl_4$ (10 mL) was slowly (2 mL at a time) added to the solution with vigorous stirring. HCl, white fume, was emitted during the stirring process as a consequence of the $TiCl_4$-water hydrolysis, and after 30 minutes, the mixture was heated to 85 ^oC for 1 h where the grey solution becomes clear colour solution. The pH was adjusted

to 7 via the drop wise addition of concentrated ammonia (30% $NH_3.H_2O$). The mixture colour was vitually seen changed to white as the concentrated $NH_3.H_2O$ was added. The solution was cooled to room temperature and allowed to stand for 12 h. The resulting TiO_2 NPs were washed with Milli Q (2 × 15 mL) and isolated via centrifugation (5000 rcf, 5 min), followed by drying in vacuum (80 °C, 15 Hg) in an oven. The dried TiO_2 NPs were calcinated at 400 ^oC and 600 °C for 2 h. The 400 ^0C produce off-white powders of mixture anatase and rutile TiO_2 NPs after characterisation while the 600 ^0C produce a bright white powder of pure anatase TiO_2 NPs. The pure anatase was selected for this study.

The chemical reaction processes passes through the following reactions.

$$TiCl_4 + H_2O + H_2SO_4 \longrightarrow TiO - SO_4 + 4HCl \quad \text{…….. (1)}$$

The addition of concentrated $NH_3.H_2O$ made the solution to become a white sediment, which can be described as reaction (2).

$$TiO - SO_4 + 2NH_3{:}H_2O \longrightarrow H_2TiO_3\downarrow + (NH_4)_2SO_4 \quad \text{……... (2)}$$

Post filteration, washing and heating, the composition of H_2TiO_3 are TiO_2 and water as in reaction (3).

$$H_2TiO_3 \longrightarrow TiO_2 + H_2O \quad \text{…… (3)}$$

3.1.2 Surface modification of TiO_2 NPs

All the experiments of TiO_2 NPs surface modification were conducted at the chemistry department, Mawson institute, University of South Australia. Two types of TiO_2 NPs were prepared with different surface modifications. Aminopropyl trimethoxysilane (APTS) modified NPs (i.e., amine functionalised TiO_2 NPs) were prepared in order to make the NPs hydrophilic [146-148], and then capable for aqueous dispersion and cell studies. Poly (ethylene glycol) trimethoxysilane (PEGTS) modified NPs (i.e., PEG functionalised TiO_2 NPs) were prepared which makes the NPs hydrophobic [149, 150], and then dispersible in halocarbons for incorporation into PRESAGE® formulations.

3.1.2.1 AminoPropyl Trimethoxysilane (APTS) functionalised TiO_2 NPs

The reaction process is explained in the chemical reaction scheme, **Figure (3-2)**. Bare TiO_2 NPs (200 mg) were suspended in toluene (10 mL) with sonication in a flask complete with stirrer bar, then APTS (200 µL) and butylamine (50 µL) were added. The flask was directly sealed and the mixture was heated at 50 °C for 2 h with constant stirring. After cooling to room temperature, the NPs were isolated via centrifugation (2000 rcf, 30 s) and then resuspended in isopropanol (40 mL) containing concentrated hydrochloric acid (HCl) (0.2 mL). The NPs were isolated via centrifugation (2500 rcf, 180 s) and then resuspended in isopropanol (10 mL). This last washing step was repeated once more to remove the HCl effect, and the amine functionalised TiO_2 NPs were isolated after drying in air for 12 h [146-148].

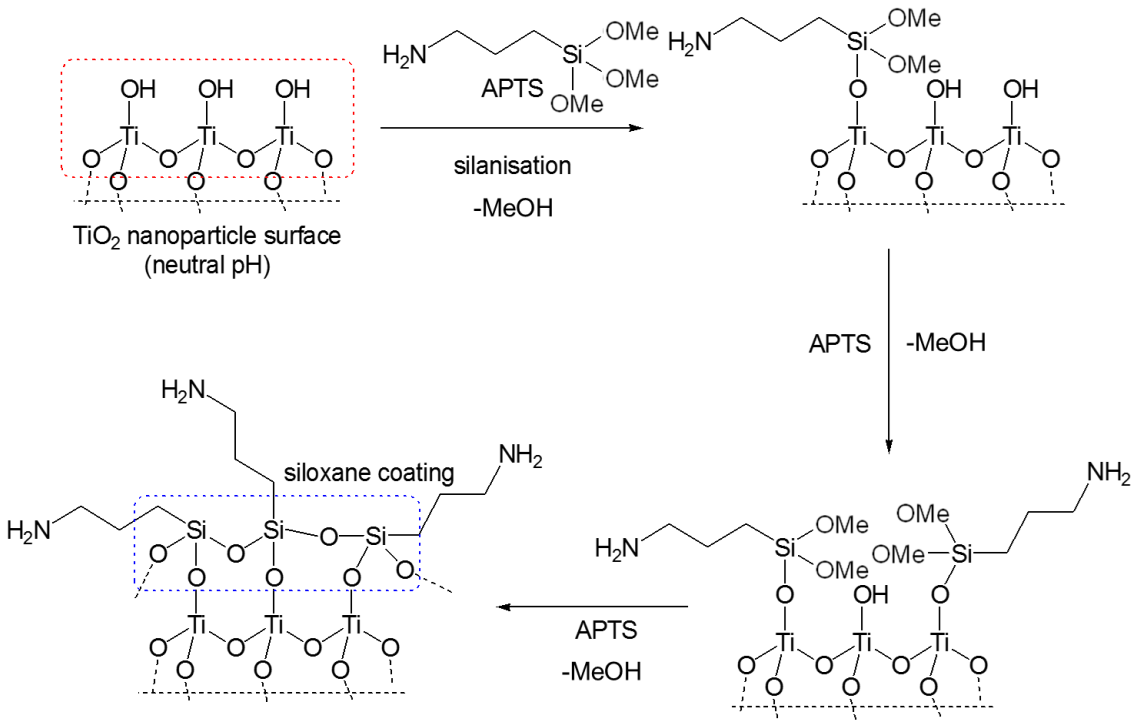

Figure 3-2: The chemical reaction scheme of TiO_2 NPs surface modification with Aminopropyl trimethoxysilane (APTS).

3.1.2.2 PolyEthylene Glycol Trimethoxysilane (PEGTS) functionalised TiO2 NPs

Bare TiO_2 NPs (200 mg) were suspended in toluene (10 mL) with sonication in a flask complete with stirrer bar, then PEGTS (200 µL) and butylamine (50 µL) were added. The flask was directly sealed and the mixture was heated at 50 °C for 6 h with constant stirring. After cooling to room temperature, the NPs were isolated via centrifugation (2000 rcf, 30 s) and then resuspended in isopropanol (40 mL). The PEG functionalised TiO_2 NPs were then isolated via centrifugation (2500 rcf, 180 s) and air-dried for 12 h [149, 150]. The chemical reaction scheme for TiO_2 NPs surface modification with PEGTS is explained in **Figure (3-3).**

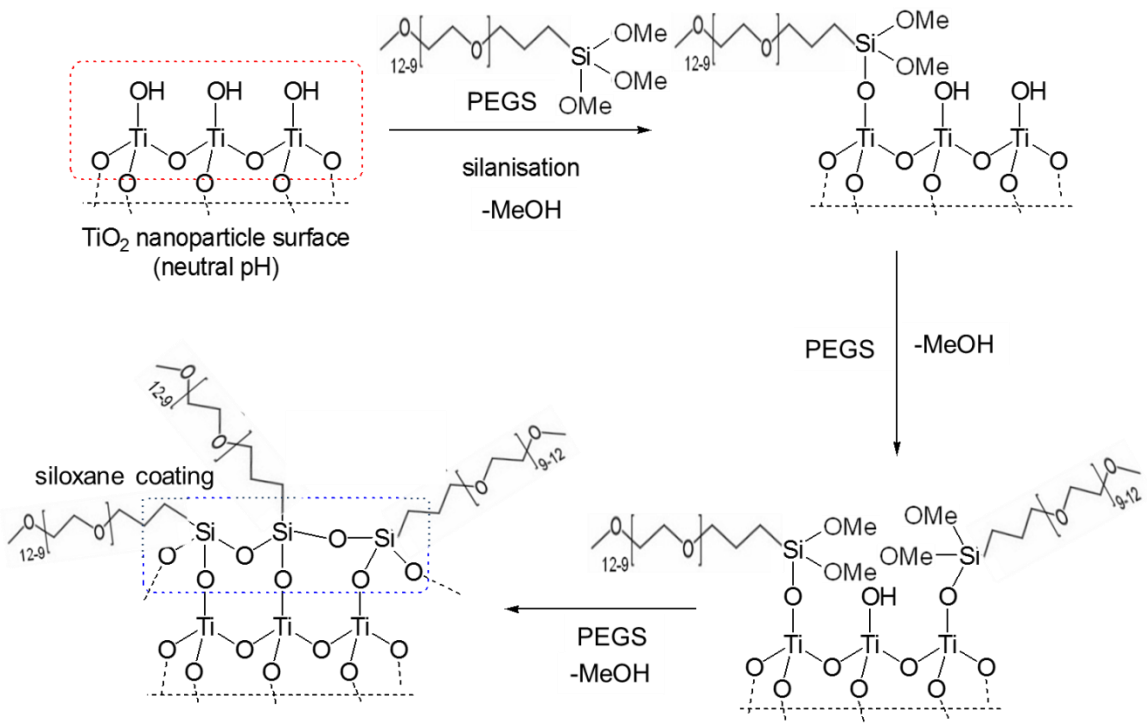

Figure 3-3: The chemical reaction schemes of TiO_2 NPs surface modification with PolyEthylene Glycol Trimethoxysilane (PEGTS).

The characteristics of the synthesised NPs are then determined before making them ready for radiological applications;

3.1.3 Characterization of TiO_2 NPs

Various systems were used to determine the physical and chemical characteristics of the synthesised TiO_2 NPs which includes determination of the NPs size distributions, chemical composition and surface modification characteristic. The methods of characterisation are stated in the following sections.

3.1.3.1 Transmition electron microscopy (TEM)

Transmission electron microscopy (TEM) was performed on a Jeol 1010 TEM (100 KeV) (Joel Inc., Peabody, MA, USA) equipped with Gatan Orius SC600 CCD-2014 camera at RMIT Microscopy and Microanalysis Facility (RMMF), Melbourne, Australia, and was used to determine NP size distributions. TiO_2 NP samples were prepared by dispersion in ethanol (0.1 mg/mL) with sonication for 180 s, and then a drop of the suspension was deposited onto GYCu200 mesh copper holey carbon (25ct) TEM grids and/or GSCu200C-50 strong carbon TEM grids. More than 100 individual NPs were measured to determine the average diameter. The TEM operates on the same principle as the light microscope; the only difference is it uses electrons instead of light. These electrons are then focused by electromagnetic lenses in to a thin and coherent beam. This beam strikes the surface of the specimen and part of it transmit depending on the thickness and electron transparency characteristic of the sample. The transmitted beam is focused through objective lens and collected by CCD camera to generate a projection image that helps to obtain the specimen surface tomography and composition information [151]. **Figure (3-4)** is a schematic diagram and digital image of TEM.

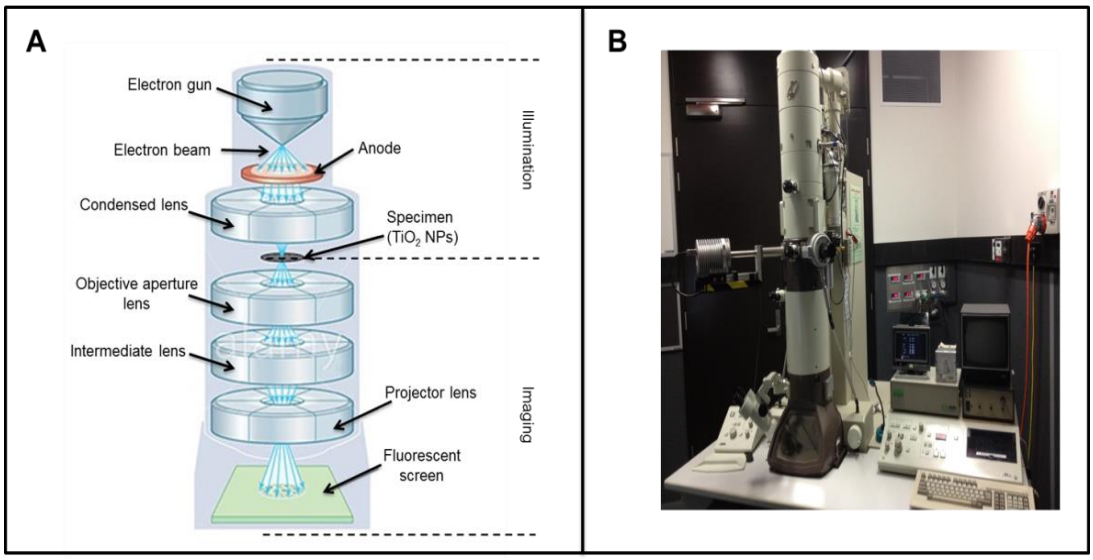

Figure 3-4: A) Schematic diagram of a TEM. Generally, TEM is divided into two mail parts: illumination and imaging system, image not in scale. B) Digital image of TEM.

3.1.3.2 X-ray photoelectron spectroscopy (XPS)

X-ray photoelectron Spectrometry (XPS) at RMIT Microscopy and Microanalysis Facility (RMMF) Melbourne, Australia was performed on a Thermo K-alpha X-ray (Thermo Fisher Scientific Inc., Waltham, MA, USA), and was used to analyse the chemical composition of the TiO_2 NPs. Carbon tape was stacked on 5 mm diameter silicon disks to prevent the conductivity effect of silicon, and then the TiO_2 NPs were spread on top of carbon tape side of the prepared disks. The prepared samples were cleaned with air duster and then loaded in the XPS machine conducted in a vacuum condition around 4×10^{-8} mbar. The principle working idea of XPS is when X-ray bombards TiO_2 NPs samples with sufficient energy, some electrons in a specific bounds states become excited enough to escape the atoms of TiO_2 NPs and are collected by an electron analyser that counts number of ejected electron and measure their kinetic energy. These electrons will produce characteristic set of

XPS peaks that are related to specific material; therefore, the peaks in the energy spectrum of intensity versus characteristic binding energy produced by electron analyser correspond to a specific element [152]. **Figure (3-5)** displays the principle workings of XPS.

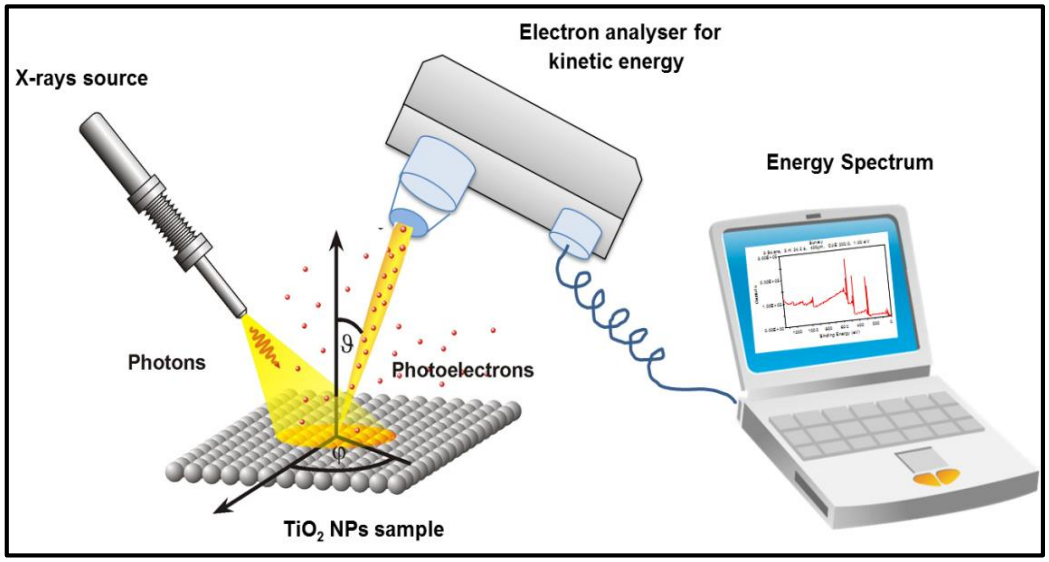

Figure 3-5: The principle working of X-ray photoelectron Spectrometry (XPS). Image not in scale.

3.1.3.3 X-ray diffraction (XRD) spectroscopy

X-ray diffraction (XRD) spectroscopy was performed on a BRUKER Axs D8 ADVANCE (BRUKER AXS Inc., Madison, WI, USA) at the Separation Science and Mass Spectrometry Facility, RMIT University, Melbourne, Australia, and was used to determine the crystalline phase of the TiO_2 NPs. The working principle of XRD is when a beam of X-ray strike a lattice of atoms in the sample at a specific angle, the beam will reflect at the same angle of incident. A detector is used to collect the diffracted beams from different planes of the lattice. The distance between the planes (d-spacing) of the atoms is measured using

Bragg's law. The X-ray scan will generate a characteristic sets of d-spacing that provide a unique pattern which then are compared to the standard reference patterns of materials to allow the identification of the crystal phase and structure of the samples [153]. **Figure (3-6)** is a schematic diagram of XRD.

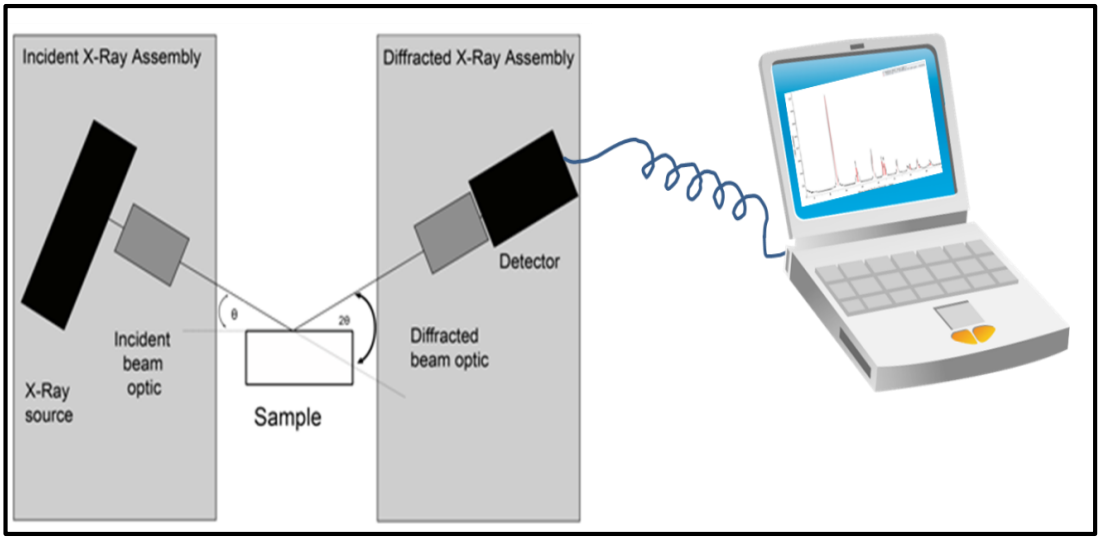

Figure 3-6: Schematic diagram of X-ray diffraction spectroscopy. Image not in scale.

3.1.3.4 Thermogravimetric analysis (TGA)

Thermogravimetric analysis (TGA) was performed on a Perkin Elmer Hyphenated Pyris 1 instrument (Perkin Elmer Inc., Boston, Massachusetts, USA) at the Separation Science and Mass Spectrometry Facility, RMIT University, Melbourne, Australia, and was used to study the TiO_2 NP surface coating characteristics. The TiO_2 NPs were loaded in the instrument and heated over a temperature ranges from room temperature up to 850 °C at a heating rate of 10 °C/min in a nitrogen flow, and then the weight (wt%) loss was recorder. The basic principle of TGA is that the heat of the sample in a furnace gradually raises and the

weight is measured using analytical microgram balance located outside the furnace. As the temperature is rising with time, the sample will lose weight due to reduction, decomposition or evaporation. The TGA tracks and records the change in weight as either a function of temperature or time. The recorded data are then analysed by analysing the characteristic of decomposition patterns to obtain the material surface coating characteristics [154]. **Figure (3-7)** is the schematic diagram and digital image of TGA.

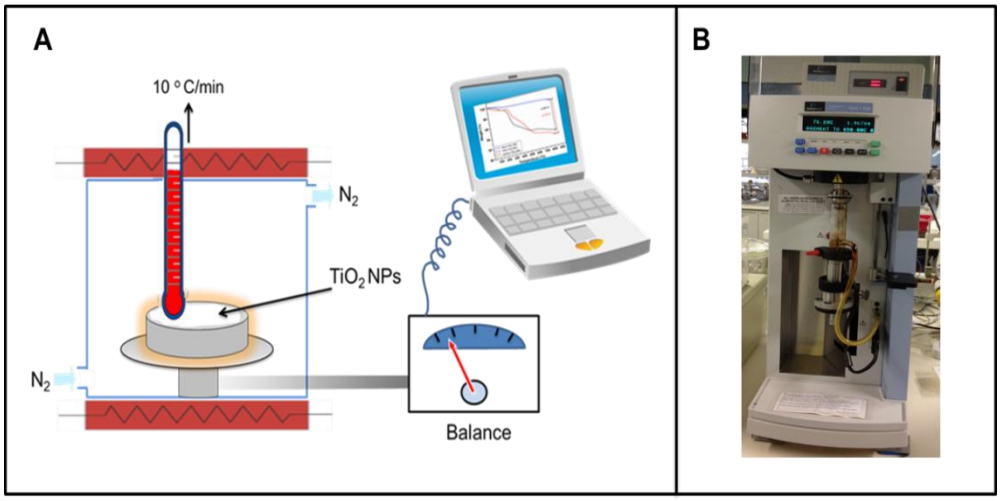

Figure 3-7: A) Schematic diagram of TGA, image not in scale. B) Digital image of TGA.

3.1.3.5 Fourier transform infrared spectroscopy (FTIR)

Fourier transform infrared (FTIR) spectroscopy was performed on a BRUKER TENSOR 27 (BRUKER AXS Inc., Madison, WI, USA), at the School of Chemistry, The University of Melbourne, Melbourne, Australia. The TiO_2 NPs were grinded and impregnated in potassium bromide (KBr) as discs and was used to study the chemical composition of the NP coatings. The KBr have no influence on NPs characteristics due to been chemically/physically stable and does not contain band in the mid IR-spectrum. The FTIR

depend on the fact that most molecules absorb infrared light of the electromagnetic spectrum due to the bonds presents in the molecules structure. The principle of FTIR operation is that the infrared light hits the beam splitter, which in turns sends the light in two different directions of right angles as shown schematically in **Figure (3-8)**. One of the beams goes to the fixed mirror then back to beam splitter while the other goes to sliding mirror. Contrary to the beam reflected by fixed mirror, the beam that back from the moving mirror will have variable total path length due to the motion of mirror. The two beams recombine when they get into the beam splitter creating a destructive and constructive interference due to the difference in path length. The sample absorbs the different wavelengths of the recombined beam spectrum when it passes through the sample. The detector then record the output spectrum as the variation in energy versus time and send it to a computer which analyse the spectrum using mathematical function known as Fourier transform that convers intensity-time spectrum to intensity-frequency spectrum. This last spectrum is used to identify certain functional groups in the sample [155].

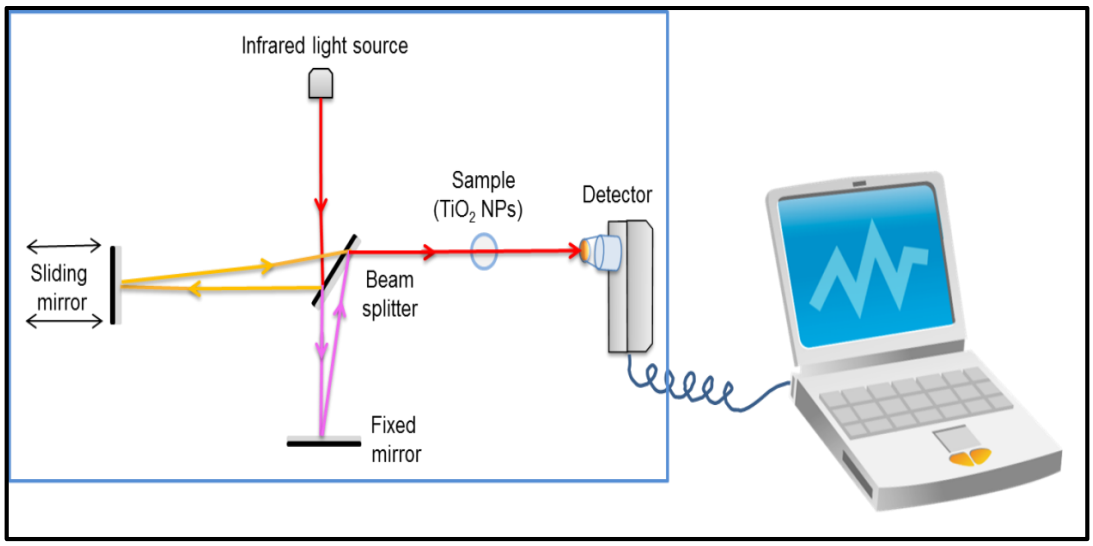

Figure 3-8: Schematic diagram of Fourier transform infrared spectroscopy. Image not in scale.

The dose enhancement induced by anatase PEGS functionalised TiO_2 NPs was investigated through phantom based study employing PRESAGE® dosimeter. Therefore, in the following section a detailed description of PRESAGE® dosimeter preparation and characterisation study using different techniques are stated.

3.2 SECTION B: PRESAGE® dosimeter study:

The following section starts stating the required chemicals for phantom preparation then followed by presenting the methodology of PRESAGE® dosimeter fabrication, irradiation, characterisation, handling and disposal.

3.2.1 Chemicals used for PRESAGE® dosimeter fabrication

3.2.1.1 Polyurethane resins

Polyurethane plastic prepolymers used were Crystal Clear 200 and Crystal Clear 206 (Smooth-On, Easton, PA, USA), which are supplied in two parts (Part A and Part B). Both Crystal Clear 200 and 206 have similar physical properties according to the manufacturer. They only differ in the curing time and the pot life (i.e the period of time before these polymers become unworkable).

The exact chemical compositions of the commercially available prepolymer mixtures are often protected as trade secrets. However, many researchers reported that the typical elemental compositions of polyurethanes are C: 63.3%; H: 9.4%; N: 5.0%; O: 21.3% [63, 64]. The specific gravity of polyurethane used in this study is 1.036 g/cm^3 as determined by the manufacturer.

3.2.1.2 Radical initiators

Halocarbons are the radical initiators used in this study. These chemicals have one or more carbon atoms covalently linked with one or more halogen atoms (e.g., bromine, chlorine or iodine). Two types of halocarbon radical initiators were used in this study which are chloroform and iodoform (Sigma Aldrich- St Louis, MO, USA). These radical initiators are used in the PRESAGE® dosimeter formulation since it has the ability to oxidise the Leucomalachite green (LMG) and then change the optical density (colour) of the PRESAGE® dosimeter.

3.2.1.3 Leuco dyes

The most desirable leuco dye as a reporter compound used in the formulation of the PRESAGE® dosimeter is Leucomalachite green (LMG) which is colourless (Sigma Aldrich-St Louis, MO, USA). This is attributed to the fact that the maximum absorption wavelength (λ_{max}) is at approximately 633 nm for its oxidized form (malachite green), which get along with the helium-neon laser output or LED source (633 nm) of commercially available optical CT scanning systems such as OCTOPUS™ (MGS Research) and Vista™ (Modus Medical Devices Inc.) [63]. At optimum sensitivity, these scanning systems can reconstruct a 3D dosimetry images for PRESAGE® dosimeter with the beneficial of colourless characteristic of the LMG as a reporter compound. Upon PRESAGE® dosimeter exposed to radiation, the optical density of the dosimeter will change as a result of LMG oxidisation, and hence it's employed in the dosimeter formulations.

3.2.1.4 Catalysts

In this thesis, Dibutyltin dilaurate (DBTDL) (Sigma Aldrich-St Louis, MO) was predominately used as catalyst compound. The main reasons for utilising DBTDL in the PRESAGE® dosimeter formulation is for improving the structural integrity of the polymers and accelerating the polymerisation process.

3.2.2 Potential health risks

Direct contact with polyurethane precursors can cause irritation to the skin, eyes and respiratory tract. They may cause allergic reactions to the lungs and skin. Furthermore, the direct contact with leuco dye (LMG) (Type used in this thesis) can cause damage to the eye, tissue and skin. Inhalation of LMG dust may also produce gastrointestinal tracts and severe irritation of respiratory. Moreover, both halocarbons used in this study are toxic and carcinogenic. Most halocarbons are considered volatile organic compounds (VOCs); therefore, inhalation of high concentrations of their vapour may cause incoordination, disorientation, dizziness, vomiting or nausea and ultimately leading to unconsciousness. In general, chronic exposure to some halocarbons is believed to cause liver and kidney damage. Most importantly, halocarbons are air and water pollutants and their release into the environment has substantial risks [156, 157]. Finally, TiO_2 NPs synthesized for this work can carry considerable health risks depending on their characteristics such as composition, morphology and size [158, 159]. The potential human toxicity from combining NPs with the PRESAGE® dosimeters has yet to be investigated.

3.2.3 Chemicals Handling and disposal

The chemicals used in this thesis are considered to be harmful and have serious hazardous to both humans and the environment due to their toxicity and potentially carcinogenic [156]. Therefore, storage and handling of such chemicals was strictly carried out according to the recommendations outlined in the Material Safety Data Sheet (MSDS) supplied by the manufactures. Lab coats, gloves, masks and safety glasses were worn throughout the fabrication procedure. In addition, to limit exposure to hazardous vapours, dusts or fumes, all fabrication methods were conducted in laboratory fumehood with dynamic means of ventilation. All the waste resulted from manufacturing PRESAGE® dosimeters such as the waste solution resulting from cleaning the chemicals containers and dosimeters that have been used or rejected due to damage during the fabrication process were disposed according to the guidelines of the relevant laboratory/University. Such samples were labelled indicating the potential toxic ingredients (e.g. halogenated waste) and then sent to a specialised waste disposal company (Envirochem) that treat waste according to its physical and chemical characteristics.

3.2.4 Storage of the PRESAGE® dosimeters

All the prepared PRESAGE® dosimeter samples were stored in a cold (*ca.* -18 °C) and dark environment prior and post irradiation to avoid any absorbance change (colour fading) and or accidental exposure to visible or external ultraviolet light.

3.2.5 PRESAGE® dosimeter fabrication procedure

PRESAGE® dosimeters were fabricated according to previously described procedures [61, 63]. The PRESAGE® dosimeters were formulated using the following ingredients: polyurethane prepolymer (Crystal Clear 200 and/or 206, 48.9 wt% part A and 44 wt% part B; Smooth-On, Easton, PA, USA), 2 wt% leuco dye (leucomalachite green-LMG) as a reporter component, 0.1 wt% dibutyltin dilaurate (DBTDL) and 5 wt% chloroform (Sigma Aldrich-St Louis, MO) was used as a halocarbon radical initiator. Two parts (A and B) of polyurethane plastic polymers are mixed together to produce an optically clear polyurethane matrix of the PRESAGE® dosimeter which is capable to be scanned optically. The fabrication procedure consists of five steps, as follows: (i) One equivalent polyol (Part B) was thoroughly mixed with two equivalents of the diisocyanate (Part A) to form a prepolymer. (ii) The reporter compound (LMG) and chosen free radical initiator were thoroughly mixed with a specific equivalent of Part B with continued stirring. (iii) The solutions prepared in steps (i) and (ii) were combined together and thoroughly mixed [63]. The catalyst (DBTDL) was added to the prepared solution in step (iii) with continuous starring until all the mixed chemicals been uniformly distributed. The final prepared solution was then poured in to poly (methyl methacrylate) moulds depending on the required shape which were then placed in a chamber (pressure pot) under pressure (ca. 60 psi) for 48 hours for curing. This was done in order to eliminate the formation of air bubbles inside the dosimeters as a result of outgassing [61, 63 and 160].

The PRESAGE® dosimeters have different colour depending on the radical initiators used like chloroform, iodoform or bromoform. Such optical appearance is attributed to the colour of the chemicals used in the composition of PRESAGE® dosimeter that has no effect

on the dosimeter optical properties changing colour with radiation [61, 160]. For example, chloroform and bromoform are colourless; however, if the trace impurities present in such compound such as bromine then they will provide colour. The dosimeters prepared with iodoform will have yellow colours due to the naturally yellow colour of iodoform. The same with LMG, sometimes, because of MG impurities it is slightly green. For the first time, PEG functionalised TiO_2 NPs were homogenously dispersed in radical initiator compounds (chloroform or iodoform) with sonication to afford desired TiO_2 NP concentrations required for the dose enhancement factor measurement with PRESAGE® dosimeters.

3.2.6 TiO_2 NPs Dispersion in polymeric matrix

Dispersing nano-sized materials in liquids is intrinsically challenging due to the presence of unfavourable strong attractive inter-particle forces [161]. This high attractive force between nanoparticle atoms can form aggregates (formation of clusters). This basically minimise the particle surface area and surface activity which is a key aspect of nanoparticles. Furthermore, incompetent dispersion of nanoparticles in liquids may causes poly-disperse agglomerates with different morphologies and sizes on the micron scale, resulting in various interactions and electrical properties that impede potential exploitation of nano-scale phenomenon [162]. As a result, significant care was taken to ensure that the nanoparticles used were well dispersed within the PRESAGE® fluids.

In this study, and for the first time, TiO_2 NPs were embedded in to 3D radiochromatic dosimeters (PRESAGE® dosimeters). In general, the dynamic viscosity of polyurethane resin precursors is approximately 600 cps at 23 °C, which is much higher than that of water (0.928 cps at 23 °C). Therefore, ensuring complete dispersion of TiO_2 NPs in the PRESAGE

dosimeters was challenging and required to develop a reliable and efficient procedure. The most commonly used methods for homogenously disperse nanoparticles in liquids are by using vortex mixture and ultrasonication. In vortex mixture, a rotary motor is used to create a vortex inside liquids while ultrasonication utilised sound waves to break up agglomerated nanoparticles [163]. Ultrasonication system is shown to be more efficient than vortex mixing due to the power of ultrasounds and its ability to disperse nanoparticles in relatively large volumes compared to vortex mixing which is limited to standard test tube volume [162]. Sonication of TiO_2 NPs was performed by using a Branson 2510 ultrasonicator (Branson Ultrasonics Corporation, Danbury, CT, USA), operating at a power of 100 W and frequency of 40 kHz. Desired amount of TiO_2 NPs was added to a predetermined amount of polyurethane resin precursor (part B) in a beaker (made from polypropylene). The preference of chosen part B over part A for dispersing TiO_2 NPs is because Part B has a lower dynamic viscosity than Part A (2.5 and 8 cps at 23 °C, respectively) and does not react with moisture from the atmosphere. Sonication for 30 min at room temperature was sufficient for the TiO_2 NPs concentrations (0.5, 1 and 4 mM) used in this study to homogenously disperse in part B as shown in **Figure (3-9)**.

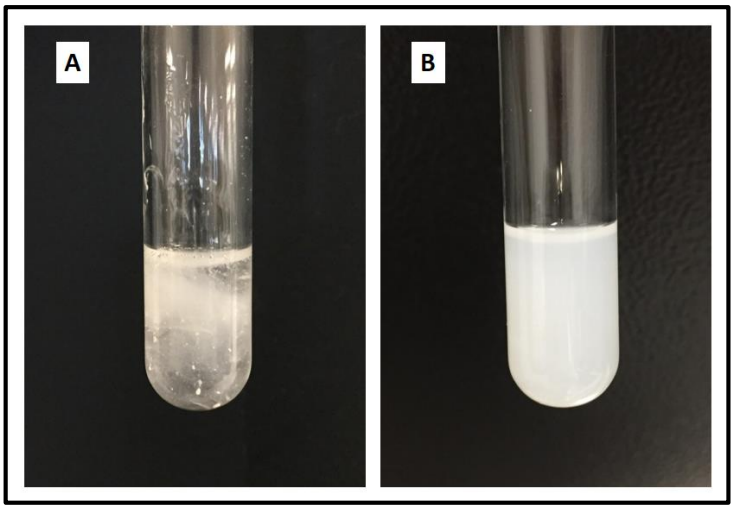

Figure 3-9: Photograph of TiO_2 NPs (A) before and (B) after dispersion in part B polyurethane precursor via ultrasonication for 30 min.

3.2.7 PRESAGE® dosimeter irradiation

All the prepared PRESAGE® dosimeter were irradiated using external sources with energies ranging from kilovoltage to megavoltage beam. The kilovoltage X-rays energy was obtained from a superficial therapy machine, the megavoltage X-rays from a LINAC. All these treatment machines were located at the Alfred Health Radiation Oncology, Alfred Health and/or Australian Radiation Protection and Nuclear Safety Agency ARPANSA, Melbourne, Australia.

3.2.7.1 PRESAGE® dosimeter irradiation with kilovoltage X-rays

PRESAGE® dosimeters were irradiated using superficial X-ray therapy (SXRT) machine (Therapax 3 Series, Pantak Inc., Branford, CT, USA). A range of low energy X-ray beams were used for dosimeters irradiation which were (80, 100 and 150) kV at various radiation doses ranging from 0-25 Gy. At 80 kV energy, irradiations was delivered at a single fraction with a dose rate of 1.090 Gy/min using a 15 cm diameter collimator with filter 5 and 2.2 mm Al HVL (applicator factor: 1.035). At 100 kV, irradiations was delivered at a single fraction irradiation with a dose rate of 1.149 Gy/min using a 15 cm diameter collimator with filter 5 and 4.9 mm Al HVL (applicator factor: 1.039). At 150 kV, irradiations was delivered at a single fraction irradiation with a dose rate of 1.112 Gy/min using a 15 cm diameter collimator with filter 5 and 1 mm copper HVL (applicator factor: 1.051). The source-surface distance (SSD) (i.e. distance from the X-ray source to the PRESAGE® dosimeter) was fixed to 25cm. The setup of irradiation with kilovoltage X-ray beam is shown in **Figures (3-10)**.

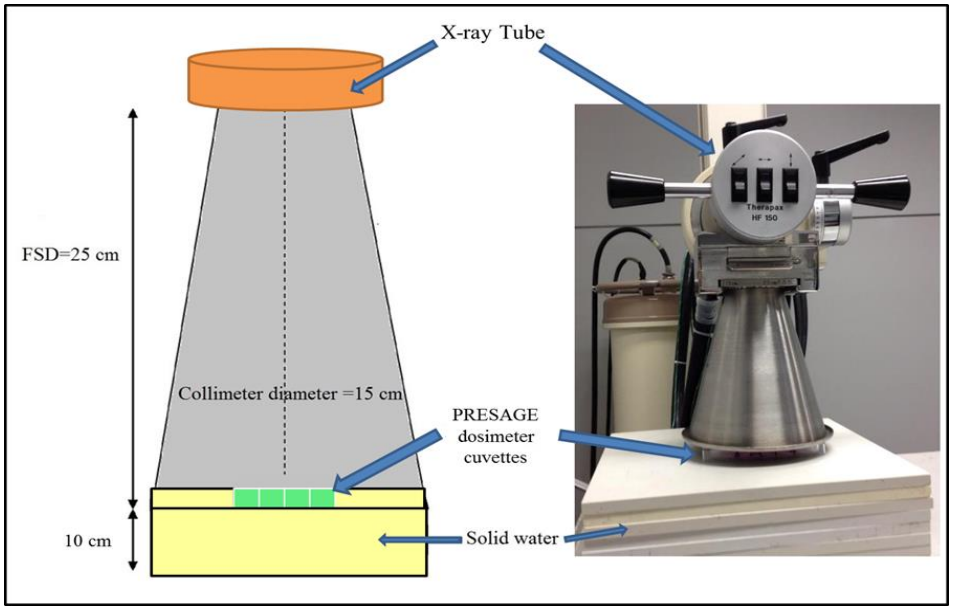

Figure 3-10: The schematic setup picture of PRESAGE® dosimeter irradiation with kilovoltage X-ray beam. Illustrations not to scale. Digital image showing SXRT instrument.

3.2.7.2 PRESAGE® dosimeter irradiation with megavoltage X-rays

Megavoltage irradiation experiments were performed at 6 MV X-ray beam using medical linear accelerator (LINAC) (Clinic 21EX, Varian Associates Inc., Palo Alto, CA, U.S.A.). The PRESAGE® dosimeters were positioned centrally on the cross-plane axis of the X-ray beam to ensure all samples received a uniform radiation dose and placed on top of a solid water phantom (water equivalent plastic) to provide a full scatter environment with field size of 10 cm^2. The collimator and gantry angle were set at 0 ° and at 100 cm SSD. Solid water phantom layer of 5 cm was placed on top of the samples so that the maximal and uniform dose was delivered to the dosimeters. A single fraction irradiation was delivered to the PRESAGE® dosimeters with constant dose rate of 600 MU/min and radiation doses ranging from 0-25 Gy. The process set up is shown in **Figures (3-11)**.

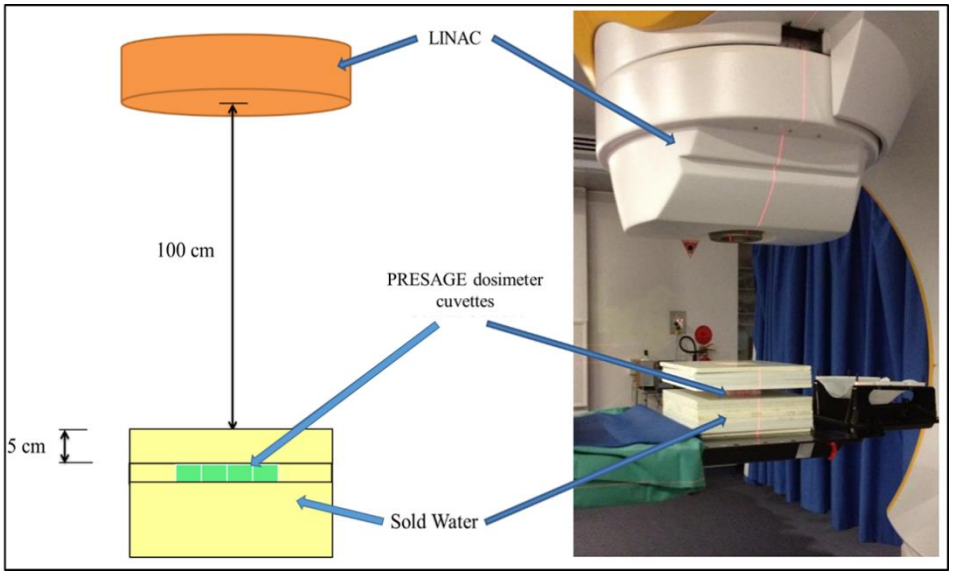

Figure 3-11: The schematic setup picture of PRESAGE® dosimeter irradiation with Megavoltage X-ray beam. Illustrations not to scale. Digital image showing LINAC instrument.

3.2.8 PRESAGE® dosimeters scanning procedure

Three different techniques were employed for scanning the PRESAGE® dosimeters including UV/VIS spectrophotometer, optical CT scanner and CLARIOstar microplate reader as described in the following sections:

3.2.8.1 UV/VIS spectrophotometer

UV-VIS spectrophotometry was performed on a dual-beam Perkin Elmer Lambda 25 UV-VIS spectrophotometer (Perkin Elmer, Waltham, MA, USA), and was used to measure changes in optical density (ΔOD) of the dosimeter cuvettes at an absorption maxima of λ = 633 nm [63, 164].

3.2.8.1.1 The principle of spectrophotometry

The beam of light consists of a stream of photons. Chemical compounds absorb, reflect or transmit light over a certain range of wavelengths depending on their chemical structure. Spectrophotometry is widely used for quantitative analysis which is a measurement of an amount of absorbed or transmitted lights by chemical substance at a particular wavelength. Spectrophotometer is used for this purpose, which is an instrument that measures the fraction of the incident light transmitted through an object. UV-visible spectrophotometer can be classified into two types depending on the range of its wavelengths; Ultraviolet (UV) light, which uses lights over the range (185 - 400 nm), and visible light, which uses light over the range (400 - 700 nm) of electromagnetic radiation spectrum. Hence it's called UV/Vis spectrophotometer.

3.2.8.1.2 Components of spectrophotometer

The basic structure of a UV-VIS spectrophotometer components are illustrated in **Figure (3-12)**. It consists of a light source, a collimator (entrance slit), a monochromator (prism), a wavelength selector (slit), a cuvette for desired PRESAGE® dosimeters, a photoelectric detector, and a digital display or a meter.

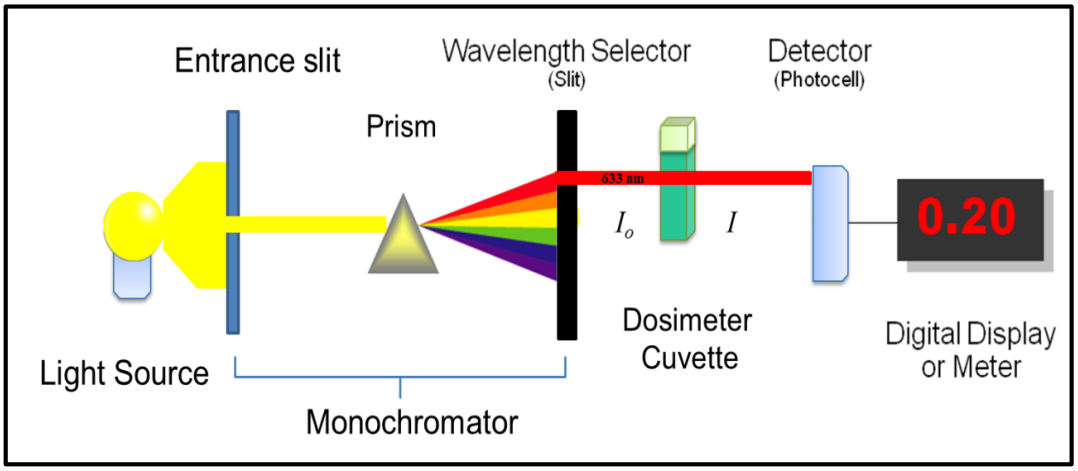

Figure 3-12: Basic components of a spectrophotometer. Image not in scale.

Detailed mechanism of spectrophotometer is described as; in general, the instrument consists of two devices; a spectrometer and a photometer. A spectrometer is a device that produces a desired range of light wavelengths. First an entrance slit that allows a straight beam of light to pass through to a prism that splits it into a spectrum. Then the slit transmits only the desired wavelengths, which for case of PRESAGE® dosimeters, the wavelength absorption maxima (λ_{max}) is 633 nm. A photometer indicates the photoelectric detector that measures the intensity of transmitted light. After the desired range of wavelength of light passes through the dosimeter's cuvette, the photo-detector measures and converts the radiant energy absorbed and then sends a measurable signal to a digital display.

3.2.8.1.3 Optical absorption measurements

The PRESAGE® dosimeters changes colour upon exposure to ionising radiation; therefore, the change in optical density (ΔOD) (absorbance change) at a particular wavelength is recorded. The optical absorption was acquired using a dual-beam Perkin Elmer Lambda 25 UV-VIS spectrophotometer (Perkin Elmer, Waltham, MA, USA). Initially, the

radiochromic response maxima (λmax) of the PRESAGE® dosimeters was determined by measuring the absorption spectrum over the visible wavelength region (400–750 nm) with 1 nm intervals [160, 164], which is then set as optimal wavelength for OD acquisitions in any given radiochromic dosimeter. The OD peak was found at the red region of the spectrum with a λ_{max} at 633 nm; therefore, the spectrophotometer absorption wavelength was assigned to 633 nm for all measurements in this work. The OD values of each PRESAGE® dosimeter cuvettes were recorded pre- and post-irradiation. The change in the OD "ΔOD" was determined by subtracting the measured OD of the irradiated cuvette from the un-irradiated one [63, 160]. Both absorbance and OD terms were used interchangeably in the literature, however, the term OD is most commonly used in 3D dosimetric investigations. Therefore, in this thesis the latter term was used instead of the former.

3.2.8.1.4 Post-response photostability

The colour (recorded ΔOD) fading characteristic of the irradiated PRESAGE® dosimeters is assessed by measuring the absorption at different time intervals ranging from 1-240 hours post-irradiation. The dosimeter cuvettes were stored in a cold (-18 °C) and dark environment in between measurements to avoid any accidental absorbance change due to exposure to visible light or ultraviolet.

3.2.8.2 Optical CT scanning

The design of an optical CT scanner is based on a combination of wide field LED light illumination (cone beam) source and a CCD camera [165] as illustrated in **Figure (3-13)**. The optical CT scanner reconstructs a 3D map of the optical densities of an object

suspended in the scanner's field of view using a series of captured 2D optical projections. The system is designed to work with radiochromic 3D dosimeters such as PRESAGE® dosimeter that have an absorption peak at 633 nm. The dosimeter is submerged in an ethyl benzoate solution (Sigma-Aldrich Pty. Ltd., St Louis, Mo, USA) filled aquarium to provide index refraction matching between the colour of un-irradiated dosimeters and the solution. This helps the blank dosimeter images to show zero contrast and therefore any variations in image optical density are result from irradiation [166]. This scanner is capable to scan dosimeters up to 15 cm diameter and 12 cm long at a volumetric data acquisition with a total scan time of less than 10 mins, which is particularly advantageous from a clinical perspective [167, 168]. However, light scatter artefacts resulting from the wide area of detection is one of the drawbacks of this scanner [169]. Nevertheless, recent methods have been suggested to minimise such imaging artefacts [168, 170].

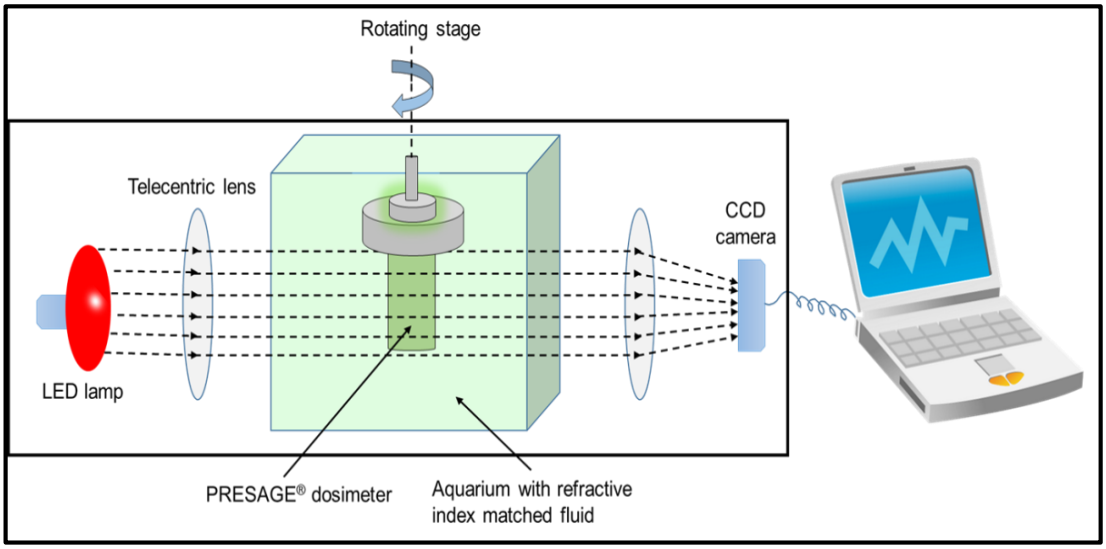

Figure 3-13: Schematic of a typical cone beam optical CT scanner. Image not to scale

3.2.8.2.1 Operation of optical CT scanning

VistaTM cone beam optical CT scanner (Modus Medical Devices Inc., London, ON, Canada) with a 633 nm LED light panel filtered by an optical band pass filter placed in front of the camera. This camera was used for acquiring 3D images for radiochromic (PRESAGE®) dosimeters **(Figure 3-14)**. The scanner was left to warm up for at least 2 h prior to performing any scanning to ensure light source stability. A two-dimensional (2D) projection of ΔOD in the horizontal direction is acquired at each scan; therefore, as the dosimeter rotate over 360º, a set of 512 light intensity transmission projections (1024 × 768 pixels each) were acquired. This resulted in the production of 256 × 256 × 256 elements with a reconstructed voxel resolution of 0.86 × 0.86 × 0.86 mm. A frame rate and a shutter speed were set on 7.5 fps and 133.2 ms respectively. A series of 2D optical image projections are captured through the region of interest while the dosimeter is being rotated and then these multiple slices are used to reconstruct the 3D image using Feldkamp-filter back projection [167].

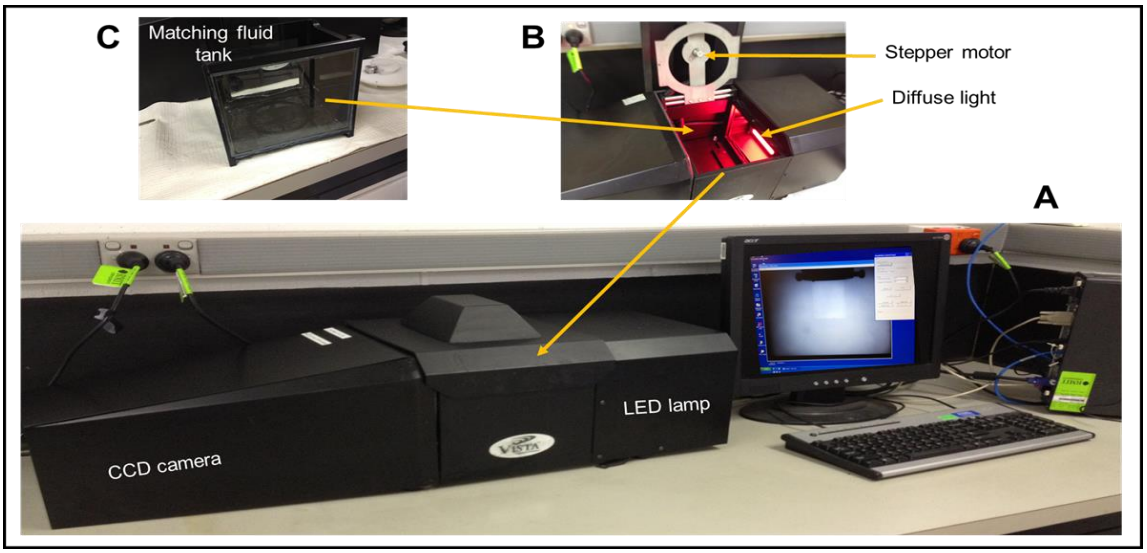

Figure 3-14: (A) Image of the VistaTM commercial optical CT scanner used in this thesis, (B) Interior section showing the LED lamp and rotating stage (C) The matching fluid tank.

3.2.8.2.2 Characterisation of the physical and radiobiological properties of PRESAGE® dosimeter by optical CT scanner

Vista cone beam optical CT scanner was employed, first to analyse the radiation transport characteristics of the PRESAGE® dosimeters in order to determine their water equivalency characteristic. Then the absorption maxima and the dose response relationship were studied by this technique.

3.2.8.3 CLARIOstar microplate reader

For the first time the PRESAGE® dosimeters are scanned with a 2D scanner using CLARIOstar microplate reader. This technique was used to measure the depth dose curve and the beam profile of PRESAGE® dosimeters with high resolution in 2D; moreover, it was employed to investigate the dose distribution beyond the inhomogeneity with in the dosimeter [171]. Detailed description of scanning the PRESAGE® dosimeters with CLARIOstar microplate reader is stated in chapter 7 **(section 7.3.3.1)** of this thesis.

3.2.9 Experimental uncertainties and statistical analysis

It's well-known that in any experimental work, there are limitations and statistical errors either during conducting the experiment or during measurements. In this work we tried to minimise the errors by repeating the experiments and performing the measurements each time under similar conditions as much as possible and with high precision, however, still there were some uncontrolled errors during PRESAGE® dosimeter preparation, irradiation and scanning procedures. In preparation, although the same chemicals and methods are used,

there was a variation in the weight percentage (wt %) of each chemical of approximately ± 0.5% which results in different batches of dosimeters used for various experiments. In irradiation, since different modalities are used, therefore dose delivered varies for both X-ray linear accelerators and superficial X-ray therapy with uncertainty of about ± 5% [171] as measured by ionisation chamber. In scanning, for minimising errors factor and ensure that the ΔOD of the PRESAGE® dosimeter is only resulting from the irradiation, ΔOD values were acquired by subtracting the OD value of each irradiated sample from the un-irradiated sample (control/blank). The influence of significance of the statistical errors were reduced by increasing the number of measurements. All results presented for PRESAGE® dosimeter studies are the means of three independent experiments. Statistical analysis was performed using OriginPro 2016 SR1 v9.3.1.273 software. Two-way analysis of variance (ANOVA) was applied to determine significance, followed by a Tukey test for post-hoc comparisons when significance was indicated. Results were considered to be statistically significant at p values of < 0.05 [172].

In the other hand, the radiosensitasation induced by anatase amino functionalised TiO_2 NPs was investigated through *in vitro* study. Therefore, in the following sections a detailed description of the methods and techniques utilised for determining the radiosensitasation are stated as following.

3.3 SECTION C: *In vitro* studies:

This section presents *in vitro* study using two types of cell lines which includes the experimental methodology of cell culture protocols, the TiO_2 NPs association with cells, cell

irradiation, toxicity and viability measurements and finally reactive oxygen specious (ROS) measurements.

3.3.1 Cell culture protocol

In this study, human keratinocyte (HaCaT) and prostate (DU145) cell lines were used. These cells were cultured in RPMI medium 1640 (1X) and MEM (Gibco by Life Technologies Pty. Ltd., Mulgrave, VIC, Australia) supplemented with 5 % and 10 % heat inactivated foetal bovine serum (FBS, In Vitro Technology Pty. Ltd., Noble Park, VIC, Australia), respectively, and 1 % penicillin streptomycin (Gibco by Life Technologies Pty. Ltd., Mulgrave, VIC, Australia). Cells were grown in 75 cm^2 flasks (Sigma-Aldrich Pty. Ltd., St Louis, Mo, USA), and subcultured at approximately 80 % confluency using trypsin ethylenediaminetetraacetic (EDTA) (Sigma-Aldrich Pty. Ltd., St Louis, Mo, USA). The cells were incubated in a humidified atmosphere at 37 ^oC, 5% CO_2. Cells in passages 4-12 were used in this research. **Figure (3-15)** shows a sample of cell culture flask.

Figure 3-15: A sample of cell culture in 75 cm^2 flask.

3.3.2 TiO_2 NPs preparation for *in vitro* studies

The synthesised anatase crystalline TiO_2 NPs and functionalised with APTS were used for *in vitro* studies in this thesis. The spherical TiO_2 NPs were obtained in a powder format. The mass of the TiO_2 NPs powder was calculated, the dried NP power was dispersed in either RPMI medium 1640 (1X) or MEM (gibco by Life Technologies Pty. Ltd., Mulgrave, VIC, Australia) for human keratinocyte (HaCaT) and prostate (DU145) cells lines, respectively, to provide the desired concentrations in Mol/L. The resulting solutions were sterilised twice, firstly by filtering through a 0.22 μm polysulfonic membranes (Sartorius, Goettingen, Germany), and secondly by sonication for 30 min to make sure the TiO_2 NPs were dispersed uniformly and all bacteria were removed or killed and then it will be ready for use in cell studies. The HaCaT and DU145 cells were seeded at densities depending on the type of plate and/or assay used. In general, cells were seeded in 6, 24 and 96 well culture plates with total of 3×10^5, 1.5×10^4 and 3×10^3 cells per well respectively and then incubated at 37 °C and 5 % CO_2. After 24 h incubation, the cells were exposed to amine functionalised TiO_2 NP concentrations of 0.5, 1 and 4 mM for 24 hours. (The capital letter "M" is referred to molar or molarity, which is defined as the number of dissolved moles of solute per litre of solution (**M=mol/L**) and is the common method of expressing the concentration of a solute in a solution), **Figure (3-16)** shows a typical 24 well plates with and without TiO_2 NPs.

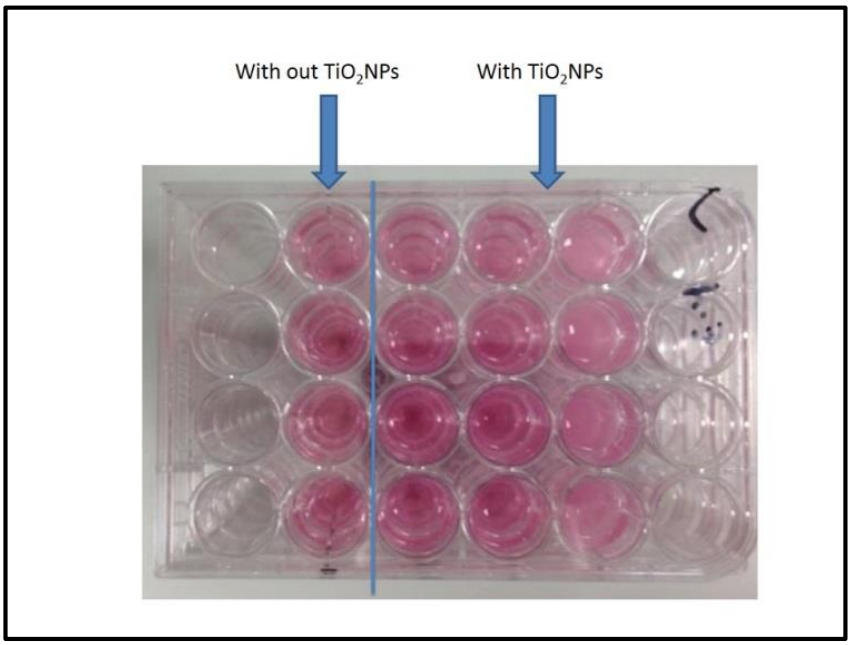

Figure 3-16: The cell culture samples in 96-well plate with and without TiO_2 NPs.

3.3.3 TiO_2 NPs inclusion in cells

The observation of any uptake of TiO_2 NPs by cells was assessed using the following two techniques. In first technique, cell population was assessed by taking advantage of the increased visible-light scattering caused by TiO_2 NPs relative to untreated control; however, this technique is unable to determine the localisation of NPs if they are within the cells or bounded to the cell surface, this method is followed using flow cytometry. In second method, light microscopy was used to image the stained cells and observe for any foreign objects within the cells.

3.3.3.1 Flow cytometry observation

The culture medium was removed and the cells were rinsed with PBS and harvested using 0.05 % trypsin-EDTA (1X) (Gibco by Life Technologies Pty. Ltd., Mulgrave, VIC, Australia). The solution was centrifuged at 300 gs for 5 min and the cells were resuspended in PBS (2 mL). The uptake of TiO_2 NPs by HaCaT cells was determined by flow cytometry (FACS Canto II, BD Biosciences). 10,000 gated events were counted and forward and side-scatter were recorded. Changes in side-scatter were assessed relative to an untreated control cell population.

3.3.3.2 Light microscopy observation

Cells were seeded in slide flasks (Nunc, Roskilde, Denmark) and incubated at 37 °C and 5 % CO_2 overnight. Subsequently, the plated cells were exposed to anatase amine functionalised TiO_2 NPs at concentrations of 1 and 4 mM. After 24 h incubation, cells were washed three times with Milli-Q water, and then fixed in (1:7) oleic acid/ethanol solution for 5 min and stained with a 0.5 % crystal violet in ethanol solution for 15 min. Light microscopy (Leitz DM-IC inverted microscope, Leica Microsystems, Wetzlar, Germany) at 40X magnification with spot pursuit camera was used to capture images of the stained cells and the Spot Advanced software version 4.6 (Diagnostic Instruments Inc., Sterling Heights, MI, USA) were utilised for microscopic analysis.

3.3.4 Cytotoxicity of TiO_2 NPs

The effect of anatase form of TiO_2 NPs on the proliferation and cell viability was experimentally studied. The HaCaT and DU145 cells were seeded into 24-well plates at a density of 3×10^4 cells per well. Cells were then incubated for 24 h at 37 °C and 5 % CO_2, and then treated with amine functionalised TiO_2 NP solutions in culture media at concentrations ranging from 0-30 mM. A tetrazolium dye-based cell viability assay (CellTiter 96® AQueous One Solution Cell Proliferation, Promega Corp., Madison, WI, U.S.A.) was utilized to assess the cytotoxicity of TiO_2 NPs [173]. Cytotoxicity was measured at 24, 48 and 72 h after TiO_2 NP addition. In this preliminary assay, cells were not exposed to any radiation. Measurements of cell viability were used to determine TiO_2 NP cytocompatibility.

3.3.5 Cell irradiation

The cells irradiation methodology followed the design/set-up, energies and procedures previously detailed in the PRESAGE® dosimeter irradiation section of this chapter **(Section 3.2.7)**. The only differences were the target (i.e the target was replaced to cells in culture instead of PRESAGE dosimeter) and the exposed radiation doses which it were ranged from 0-8 Gy. The irradiation processes set-up for kilovoltage and megavoltage are shown in **Figures (3-17) and (3-18)**.

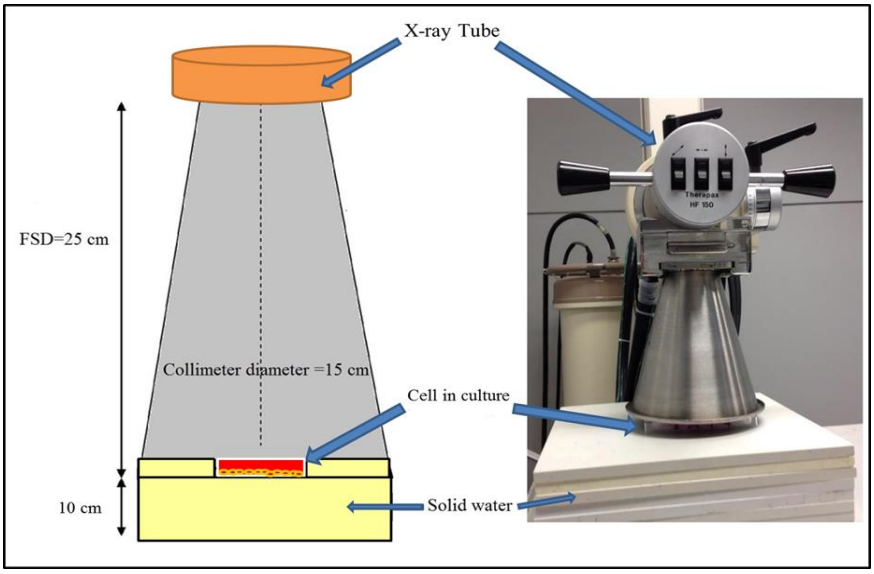

Figure 3-17: The schematic setup of cell irradiation with kilovoltage X-ray beam. Illustrations not to scale. Digital picture showing SXRT machine.

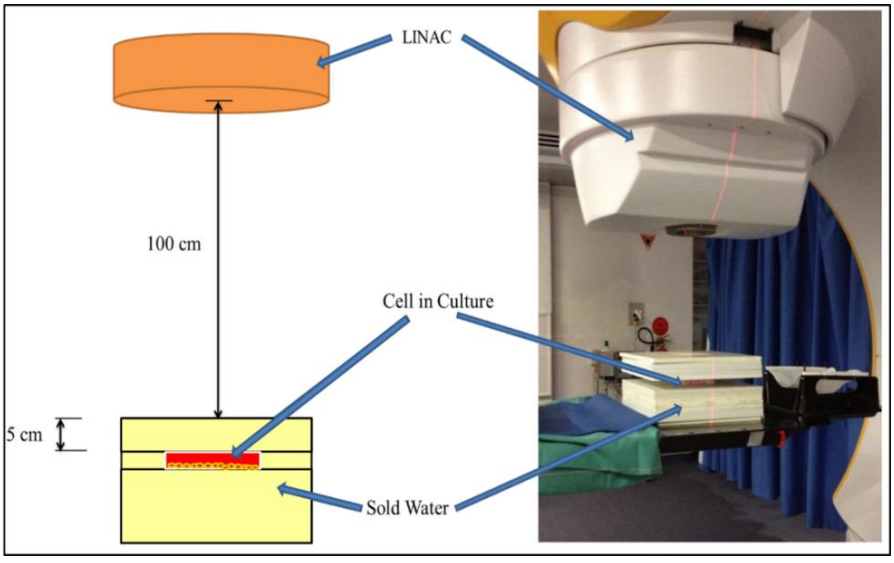

Figure 3-18: The schematic setup of cell irradiation with megavoltage X-ray beam. Illustrations not to scale. Digital picture showing LINAC machine. Build up were placed on top on the plate to ensure maximum dose to the cells. Also, the cell medium was filled to reduce the air gap effects.

3.3.6 Cell survival assays

Two methods were implemented for cell survival measurements:

3.3.6.1 MTS survival assay

MTS assay were employed to obtain cell survival curves using a CellTiter 96® AQueous One Solution Cell Proliferation Assay, (Promega Corp., Madison, WI, USA). It contains (3-(4,5-dimethylthiazol-2-yl)-5-(3-carboxymethoxyphenyl)-2-(4-sulfophenyl)-2H-tetrazolium) and an electron coupling reagent (phenazine ethosulphate; PES). This compound will bio-reduce in to a coloured formazan product if interact with metabolically active cells. This coloured formazan product is soluble for use in tissue culture medium [174]. Metabolically active cells contain dehydrogenase enzymes that produce a cellular reducing agent, either NADPH or NADH (nicotinamide adenine dinucleotide phosphate) [174]. **Figure (3-19)** shows how cellular reducing agents convert the MTS tetrazolium compound to the formazan products.

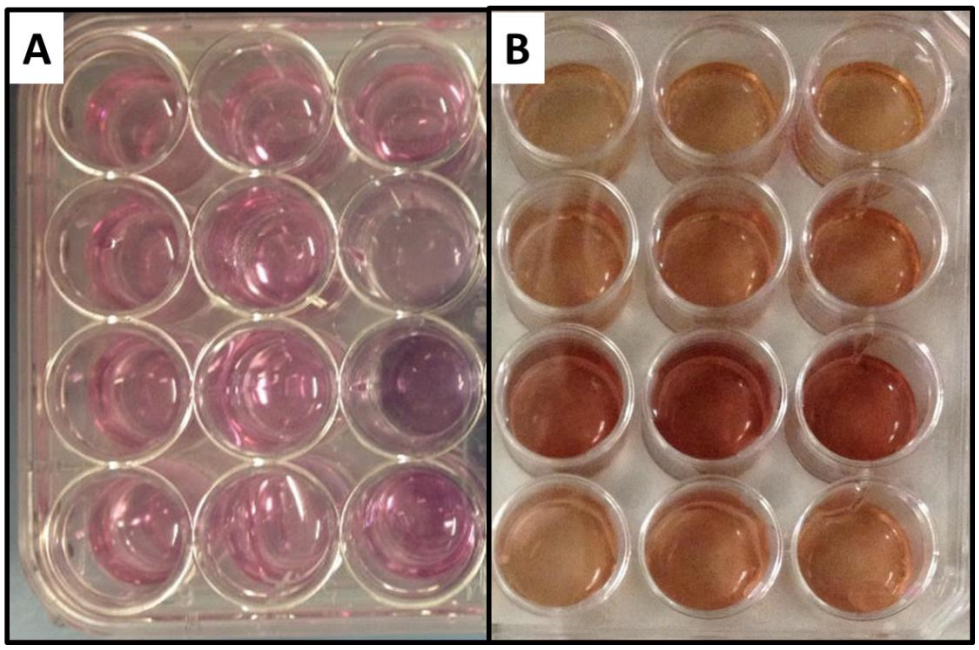

Figure 3-19: The bioreduction process showing changes in MTS tetrazolium chemical structure into formazan products, A) Without MTS reagent, B) With MTS reagent after 45 min incubation in 37 ^{0}C and 5% CO_2.

MTS is a pale yellow compound that will turn into a dark brown formazan product indicating the metabolic activity of the cells. The MTS assay is similar in principle to the MTT [3-(4,5-dimethylthiazol-2-yl)-2,5-diphenyltetrazolium bromide] assay which has previously been used [175]. The advantage of MTS assay over MTT assay is that MTS produces a soluble formazan product, whereas the MTT assay produces a crystalline precipitate that requires an additional step in the procedure of dissolving the crystal before absorbance is measured [174]. **Figure (3-20)** is the schematic diagram of MTS assay.

Cells were seeded in 24 and/or 96-well plates at a density of 1.5×10^4 and 3×10^3 cells per well respectively and incubated at 37 °C, 5 % CO_2 for 18 h. The culture media was removed, and the cells were treated with 0, 0.5, 1 and 4 mM of amine functionalised TiO_2-

NPs (200 µL in fresh media) for 24 h. The culture medium was changed and the cells were then irradiated with kV and MV energies according to the specifications previously stated **(section 3.3.5)**. After irradiation, cells were incubated for 24 h, and the media was changed and then incubated for a further 48 h. Subsequently, the medium was removed and 300 µL of culture medium and 60 µL of CellTiter 96® AQueous One Solution Cell Proliferation Assay reagent were added. The assay is light sensitive and therefore, cell culture plates were wrapped with aluminium foil upon incubation. A CLARIOstar microplate reader (BMG LABTECH Inc, Ortenberg, Germany) was used for measuring the absorbance (optical density) of the solutions at a wavelength of 490 nm. The absorbance was recorded directly after adding the MTS (for background subtraction), and again after 40 min incubation period. Measurements are expressed as a percentage relative to the negative control cells as shown in equation (3-1).

$$Surviving\ fraction = \frac{Absorbance\ of\ irradiated\ cells - background}{absorbance\ of\ control\ cells - background} \times 100\ \% \qquad \ldots (3\text{-}1)$$

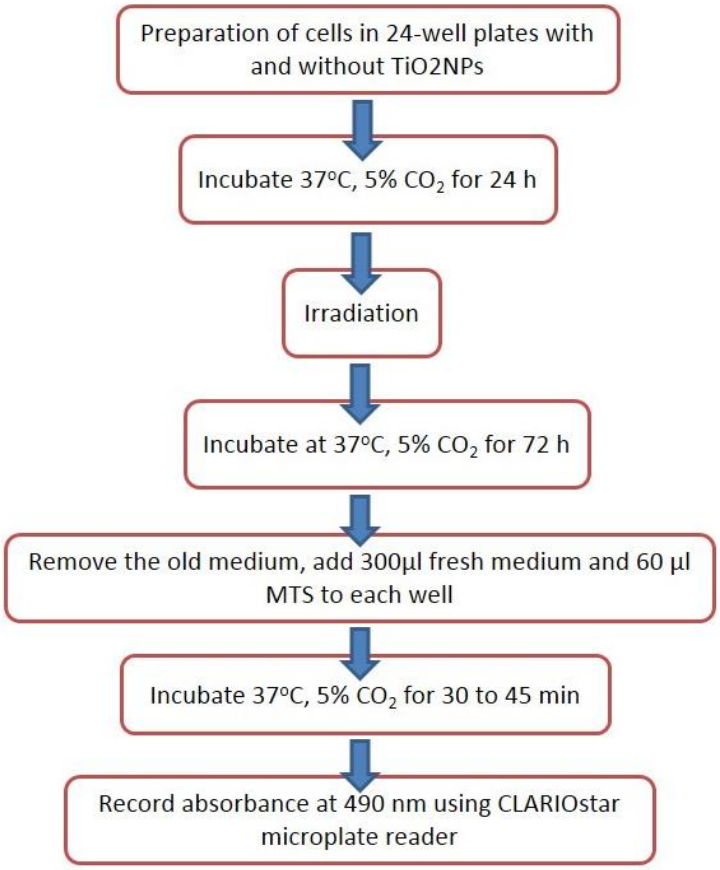

Figure 3-20: MTS assay using CellTiter 96® AQueous One Solution Cell Proliferation Assayn for cell survival measurement.

3.3.6.2 Clonogenic survival assay

Clonogenic cell survival assay was established on 1950s to study the cells-radiation effects [176, 177]. This assay has played an essential role in radiobiology by generating much of the information on the effects of radiation on mammalian cells. The cell is said to be clonogenic if it has the ability to proliferate indefinitely, thereby retaining its reproductive ability to form a large colony that can be visualized, whereas, the cell that go through one or two mitoses in retaining its ability to synthesize DNA and proteins, and is unable to divide and produce continuous progeny is considered dead. The loss of this

ability as a function of radiation doses is described by the dose-survival curve [178]. The steps involved in the clonogenic assay are briefly outlined in **Figure (3-21)**.

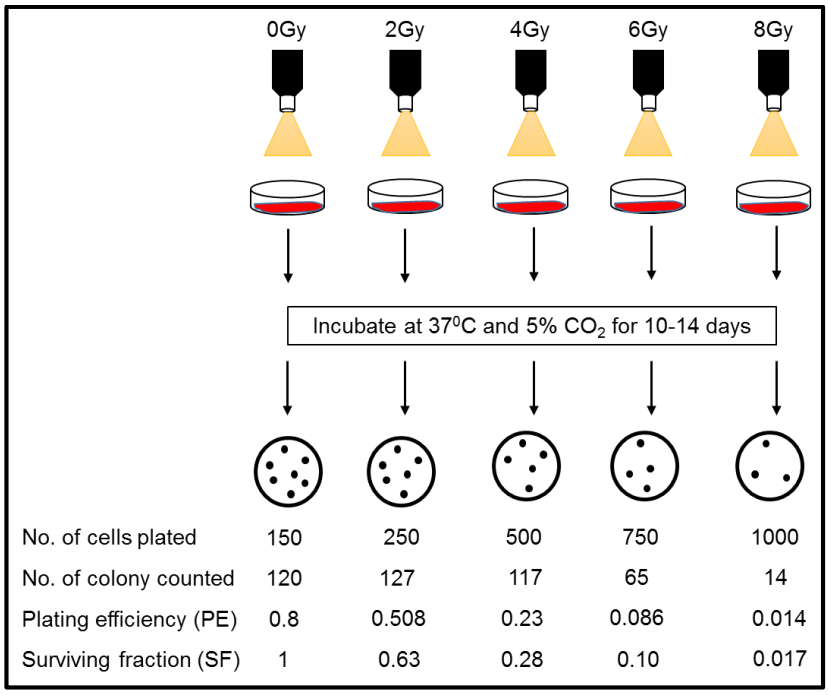

Figure 3-21: Schematic representation of steps involved in setting up a clonogenic cell survival assay.

In this thesis, cells are prepared in a culture medium suspension. The number of cells per milliliter in this suspension is counted using a Coulter counter or a hemocytometer. After counting, cells were seeded in 6-well plates for clonogenic survival assay at densities shown in **Table (3-1)**. Cells were treated with amine functionalised TiO_2 NPs and irradiated in an identical procedure to that described in the MTS assay **(section 3.3.6.1)**, and then incubated at 37 °C, 5 % CO_2 for 14 d. All the cells that make up the colony are the progeny of a single cell. For example, if 150 cells are seeded into 6 well

plates, the number of colonies formed may be anywhere from 0 to 150. It is rarely the case to ideally expect the number to be 150 due to several possible reasons, including errors in counting the number of cells initially plated, suboptimal growth medium, and the loss of cells by trypsinization and general handling.

Table 3-1: HaCaT and DU145 cell seeding densities in 6-well plates for clonogenic survival assays at specified doses.

Dose (Gy)	*Density of seeded cells in 6-well plates (cells/well)*	
	HaCaT	DU145
0	150	250
1	250	500
2	250	750
3	500	1000
4	500	1500
5	750	2000
6	750	2500
8	1000	3000

The cells were then fixed with oleic acid, this is done by removing the culture medium from six well plates and add 0.5 ml of (1:7) oleic acid/ethanol solution onto each well of six plates for 5 min. The cells, after removing the fixing solution, were stained with 0.5 % crystal violet in ethanol solution for 15 min. The plates were then gently washed with water; care must be taken in this step to prevent the colonies from loosening and washing off. The plates were then allowed to air-dry overnight. Next day, the colonies were digitally scanned using a Leica DMD 108 digital micro-imaging instrument (Leica Microsystems CMS GmbH manufacture, Mannheim, Germany), and counted manually in each well of six

plates to obtain the plating efficiency. The term plating efficiency indicates the percentage of cells seeded that finally grow and form a colony. A cluster of blue-staining cells is counted as a colony if it shapes at least 25–50 cells [179] **(Figure 3-22)**. To make sure there are no variations introduced between experiments, it is very important to keep the smaller cut off constant. Average the number of colonies counted for the three experiments of each condition and then divide the counted mean by the number of cells plated, and this will give the plating efficiency (PE) [179, 180] as in equation (3-2).

$$PE = \frac{Number\ of\ colonies\ counted}{Number\ of\ cells\ seeded} \times 100 \quad \ldots (3\text{-}2)$$

The cells surviving fraction (SF) of a given treatment were then calculated after determination of PE. First, normalize all the plating efficiencies of the treated samples to that of the un-irradiated plates (control), considering that to be 100%. Then determine the SF by dividing the PE of the treated cells by the PE of the controls, and then multiplying by 100 as shown in equation (3-3).

$$SF = \frac{PE\ of\ treated\ cells}{PE\ of\ untreated\ cells\ (Control)} \times 100 \quad \ldots (3\text{-}3)$$

Cell survival curve are then obtained by plotting SF against the delivered radiation doses.

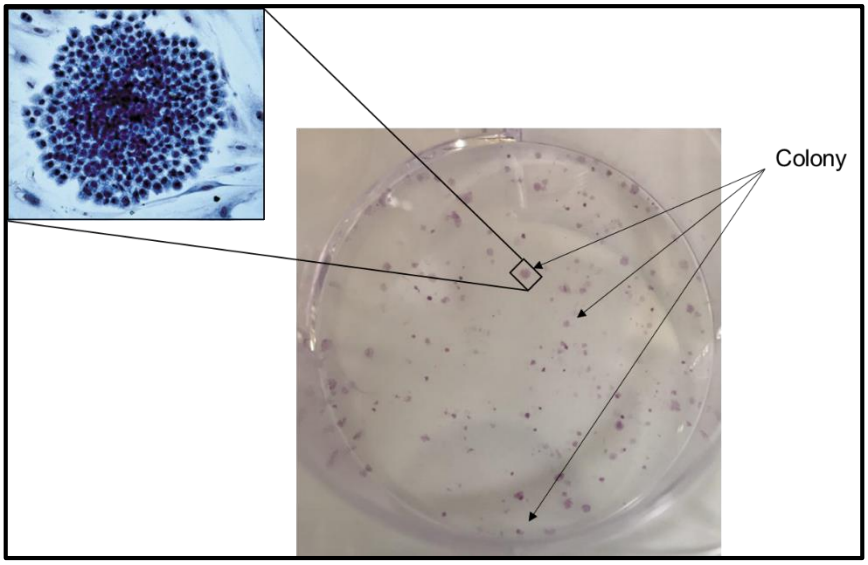

Figure 3-22: Representative picture of colonies.

3.3.7 Dose Enhancement Factor (DEF) measurements

The radiosensitisation induced by anatase amine functionalised TiO_2 NPs for *in vitro* studies were quantified through employing dose enhancement factor (DEF) on the obtained cell survival curves form both MTS and clonogenic assays explained in the previous section. Different X-ray energy beams ranging from kV to MV with various radiation doses were used to study the effect of amine functionalised TiO_2 NPs on the dose enhancement. Furthermore, concentrations of TiO_2 NPs ranging from 0.5 mM to 4 mM were used to investigate the NPs influence on the levels of radiosensitisation. It should be noted that the terms radiosensitisation and dose enhancement are used interchangeably however, it is more appropriate to use radiosensitisation with the cells studies as the particles affects the cells biology too. The DEF represents the ratio of the dose delivered in the control cell culture (i.e.

without TiO_2 NPs) at 80 % survival, divided by the dose delivered in cells treated with TiO_2 NPs that produce 80 % survival as shown in **Figure (3-23)**. Equation (3-4) is employed for determination of the DEF extrapolated at 80% survival from the cell survival curves obtained from MTS and clonogenic assays.

$$DEF_{80\%} = \frac{D_{control}}{D_{TiO2\ NPs}} \qquad \ldots\ldots\ldots (3\text{-}4)$$

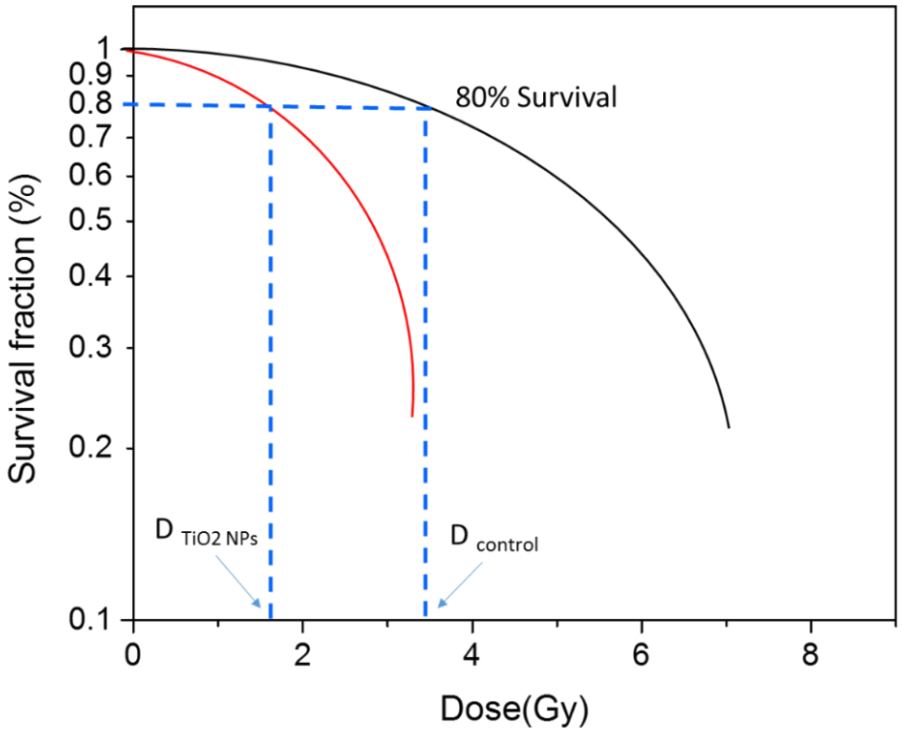

Figure 3-23: DEF extrapolated from cell survival curve at 80% survival.

3.3.8 *In vitro* detection of ROS

This method comprises dissolving 2',7'-Dichlorofluorescin diacetate (DCFDA) (Sigma-Aldrich Pty. Ltd., St Louis, Mo, USA) in dimethyl sulfoxide (DMSO) at a concentration of 100 µM, and stored at -20 °C in the dark. Immediately before use, the DCFDA solution was diluted 1:1000 in PBS (phosphate buffered saline). Black 96 well plates were used in this experiment, with total solution volumes of 200 µL per well (100 µL DCFDA solution). Various concentrations of amine functionalised TiO_2-NPs (0.5, 1 and 4 mM) were prepared in 100 µL PBS. The samples were irradiated with 6 MV X-ray beams from an ELECTA LINAC at doses of 15 or 40 Gy. The nonfluorescent DCFDA is converted to highly fluorescent product post-oxidisation in the presence of ROS. The total fluorescence of the samples was measured using a CLARIOstar microplate reader with excitation and emission wavelengths of 483 and 530 nm, respectively. All fluorescence measurements were performed in the dark and at room temperature.

3.3.9 Statistical analysis

All data represents the mean of three independent experiments. Results are reported as mean ± SEM. Statistical analysis was performed using OriginPro 2016 SR1 v9.3.1.273 software. Two-way analysis of variance (ANOVA) was applied to determine significance, followed by a Tukey test for post-hoc comparisons when significance was indicated. Results were considered to be statistically significant at p values of less than 0.05 (* $p < 0.05$, ** $p < 0.01$, *** $p < 0.001$).

SECTION A

CHAPTER FOUR

Results and Discussions of TiO_2 NPs Characterisation

4. SECTION A: Results and discussions of TiO_2 NPs characterisation

This chapter contains presentations and discussions of the experimental results obtained in synthesising and characterisation of TiO_2 NPs using different characterisation techniques as stated in the following sections.

4.1 Results

Anatase crystal form of TiO_2 NPs were synthesised by chemical reactions **(Figure 4-1)**. The anatase TiO_2 NPs were modified to be soluble in water for *in vitro* study and/or in PRESAGE dosimeter for phantom's study. The size, elemental compositions, chemical structure, purity and surface modification characteristic of the synthesised TiO_2 NPs were studied by utilising techniques such as TEM, XPS, XRD, TGA and FTIR. The TiO_2 NPs characterisation results are expressed in details in the following sections.

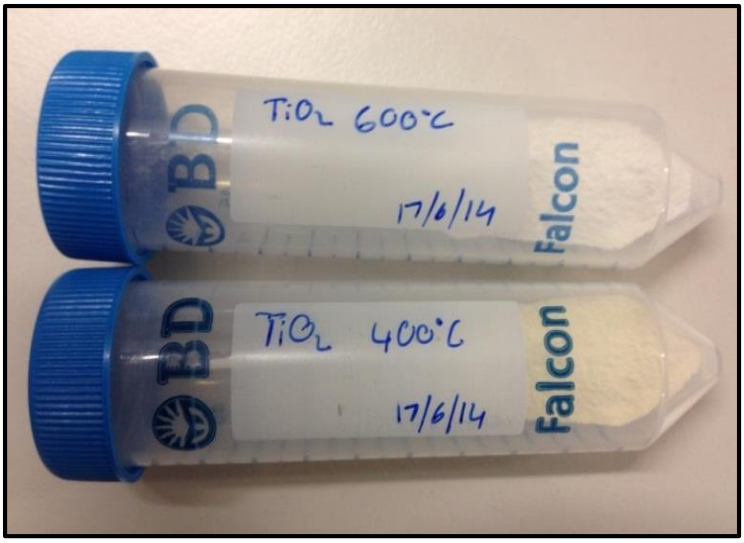

Figure 4-1: Synthesised TiO_2 NPs and calcinated at 400 ºC and 600 ºC.

4.1.1 TiO_2 NPs characterisation

The nanoparticles were characterized by the following techniques.

4.1.1.1 Transmission Electron Microscopy (TEM)

The synthesised TiO_2 NPs were suspended into ethanol and the TEM image captured revealed NPs to be spherical/parallelepiped with a mean diameter of 30 ± 5 nm for more than 100 particles measured by image j software **(Figure 4-2)**.

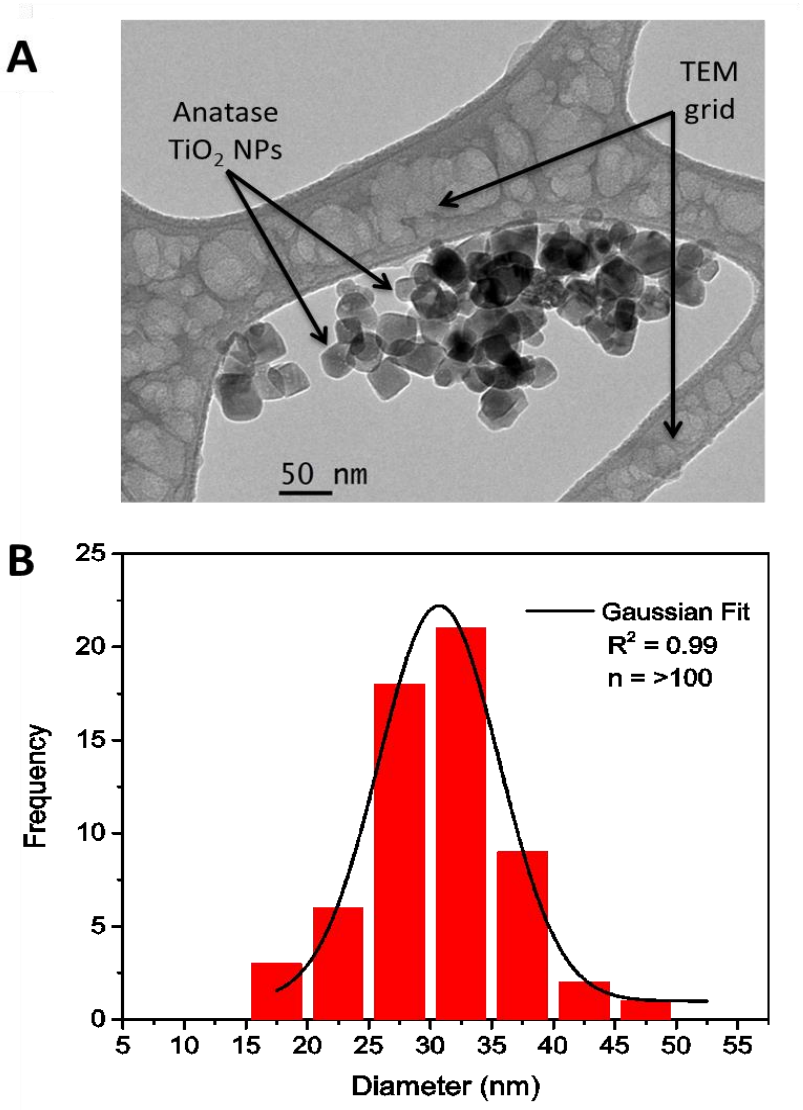

Figure 4-2: A) TEM image of the synthesised TiO_2 NPs (scale bar = 50 nm) B) size distribution of TiO_2 NPs from TEM image.

4.1.1.2 Thermo K-alpha X-ray photoelectron spectroscopy (XPS)

The elemental composition of the TiO_2 NPs was determined via Thermo K-alpha X-ray photoelectron spectroscopy (XPS), which revealed peaks with characteristic binding energies for titanium and oxygen **(Figures (4-3) and (4-4))**. The additional peak for carbon was used to calibrate the relative energies and all peaks are in agreement with previous studies [181] **(Figure 4-3)**.

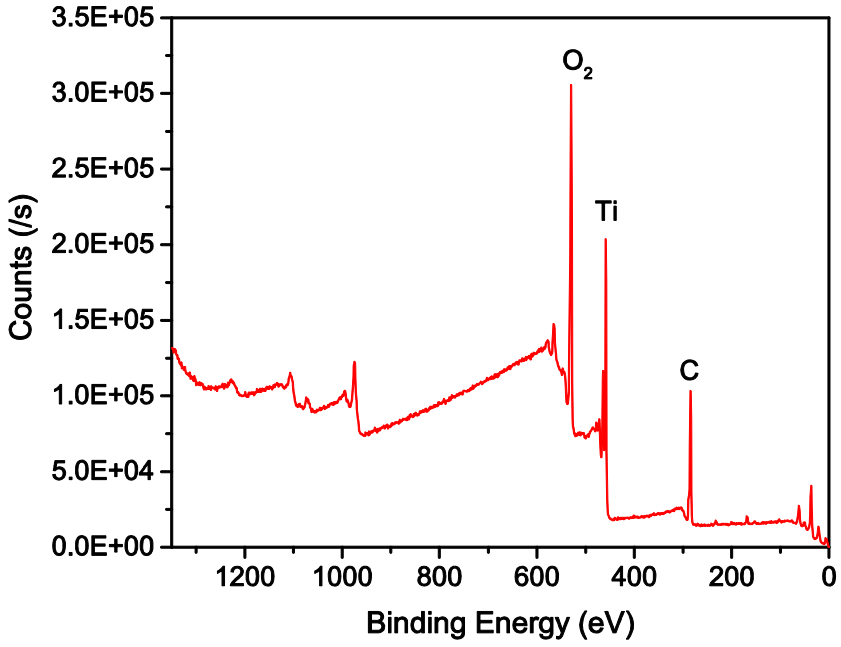

Figure 4-3: X-ray Photoelectron spectroscopic (XPS) spectra of the synthesised TiO_2 NPs.

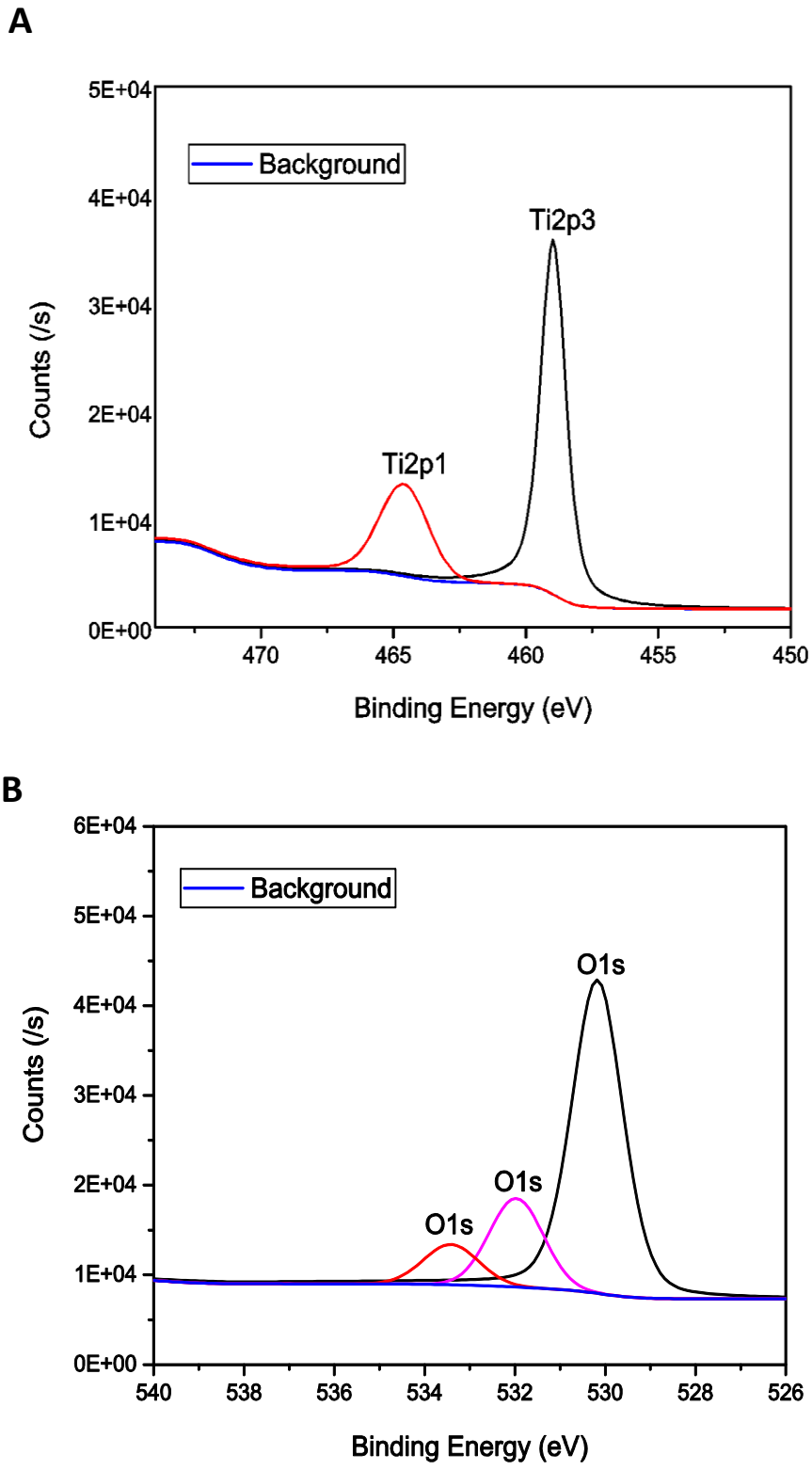

Figure 4-4: A) Titanium, B) Oxygen peaks of XPS spectra of the synthesised TiO_2 NPs.

4.1.1.3 X-ray diffraction (XRD)

X-ray diffraction (XRD) patterns of the synthesised TiO_2 NPs revealed a primary peak at 25.3 angle and numerous smaller peaks that confirmed the TiO_2 anatase structure [182] with an 84.6 % crystal phase **(Figure 4-5)**.

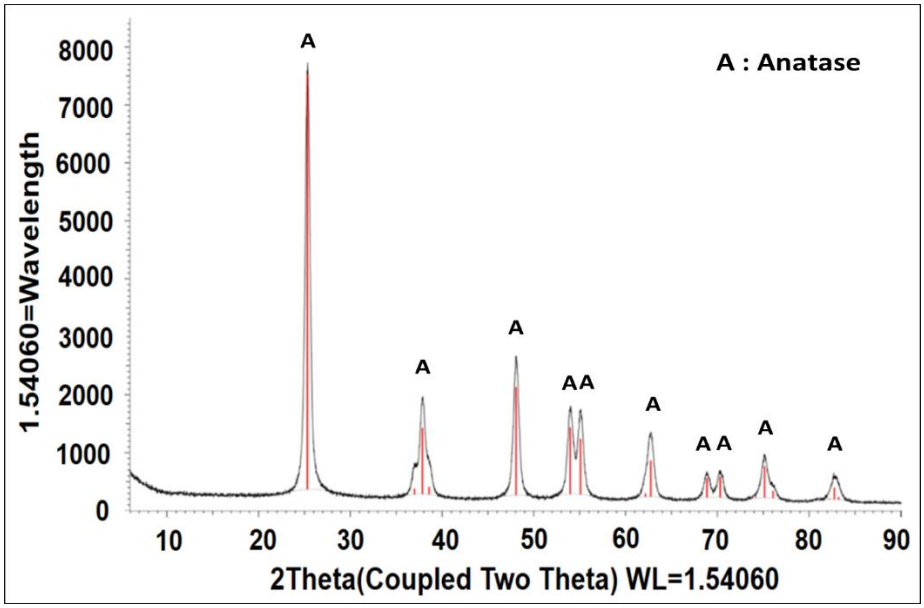

Figure 4-5: X-ray diffraction (XRD) of synthesised TiO_2 NPs.

4.1.1.4 Thermogravimetric analysis (TGA)

Perkin Elmer Hyphenated TGA was used to characterize the surface modification of synthesised TiO_2 NPs. The samples experience only one main step-down loss of weight over temperature ranges of 270-550 °C through TGA test **(Figure 4-6)**. In comparison to bare TiO_2 NPs, TGA analysis of the amine- and PEG-functionalised TiO_2 NPs revealed in total ~

6-7 wt% loss over temperature ranges up to 850 °C, which is attributed to the decomposition of the organic coating.

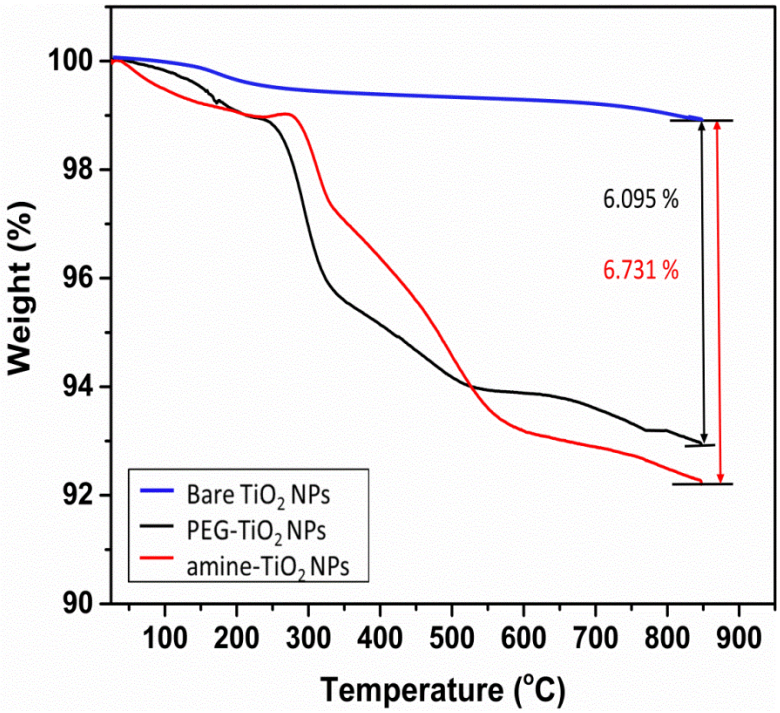

Figure 4-6: TGA curves recorded at a heating rate of 10 °C/min in a nitrogen flow for functionalised TiO_2 NPs.

4.1.1.5 Fourier transforms infrared spectroscopy (FTIR)

Fourier transform infrared spectroscopy (FTIR) studies were carried out in the 400–4000 cm^{-1} frequency range **(Figure 4-7)**. For the infrared absorption spectra, the samples were formed into pellets with KBr and the spectra were recorded on a BRUKER FTIR Spectrometer. IR spectroscopy in the transmission mode gives qualitative information about the way in which the adsorbed molecules are bonded to the surfaces as well as the structural information of solids.

Fourier transform infrared spectroscopy (FTIR) of the bare and functionalised TiO_2-NPs showed a typical TiO_2 pattern ranging between 500 ~ 700 cm^{-1}, which is attributed to Ti–O–Ti vibrations in the TiO_2 lattice [150, 183]. The absorption peak at 1639 cm^{-1} and the broad band at 3344 cm^{-1} in all samples are attributed to the surface hydroxyl groups (OH) present in the TiO_2-NPs **(Figure 4-7 (a, b, c))** [148, 183]. The band at 993 cm^{-1} (Ti–O–Si) confirms the condensation reactions between the methoxy groups of APTS and the TiO_2-NPs surface hydroxyl groups has occurred **(Figure 4-7, (c))** [148, 150]. The peak at 1047 cm^{-1} is due to the (Si–O–Si) asymmetric vibrations indicating occurrence of condensation reaction with the silanol groups **(Figure 4-7, (c))** [147]. The peaks at ~1130 cm^{-1} for the amine and PEG functionalised TiO_2-NPs are consistent with C–N and C-O vibrations, respectively, which demonstrate successful grafting to the surface of the modified nanoparticles [150]. Peaks at 1384 cm^{-1} and 2931 cm^{-1} in all samples were attributed to the asymmetrical C–H vibrations [147, 148 and 183].

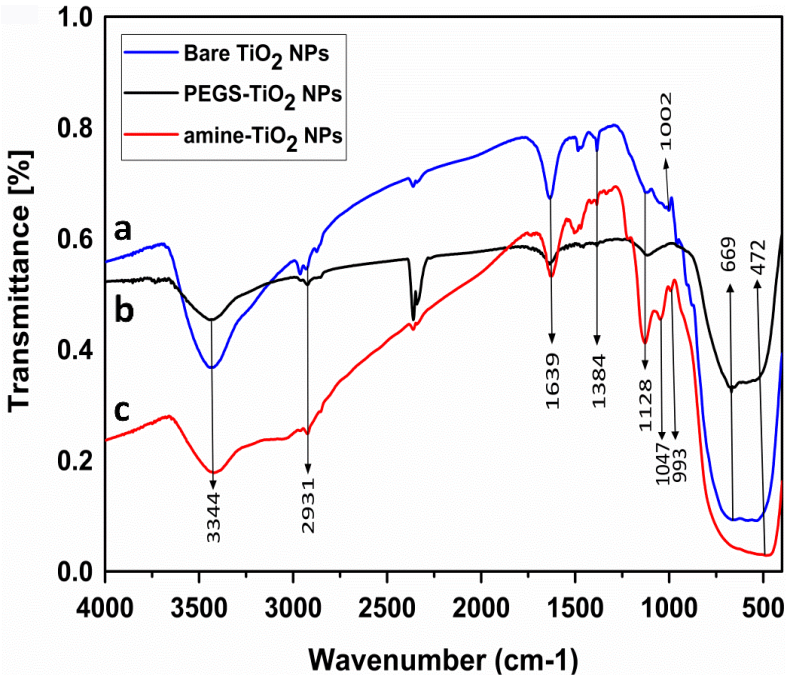

Figure 4-7: FTIR spectra for bare and surface functionalised TiO_2 NPs.

4.2 Discussion

The synthesised TiO_2 NPs for this study were characterised to be uniform nano-crystalline structures with highly pure phase of titania anatase [145]. The XPS peaks at 458.9, 464.6, and 530.1-533.4 eV are characteristic binding energies of $Ti2p_{3/2}$, $Ti2p_{1/2}$ and O1s, respectively, which are indicators of the titanium and oxygen signals in the TiO_2 lattice **(Figure 4-4)**. The TiO_2 composition by weight is 59.93% for Ti and 40.06% for O_2. The anatase crystal form of TiO_2 is preferable as the anatase structure creates more free radicals, has a larger surface area to volume ratio and therefore generates ROS more effectively than other types of TiO_2 NPs [184-188]. All these features in combination have a high impact on DNA damage to target cells during irradiation. However, the peak at 284.97 eV is attributed to the C1s binding energy resulting from the carbon holding TiO_2 NPs. While the peak at 401.12 eV is attributed to N1s binding energy of nitrogen gas used to flow through the system in order to eliminate and/or minimise the effects of oxygen or other environment gases in the measurements. Data from the TiO_2 NPs calcined at 600 ^{o} C indicated that the anatase phase was predominant and no impurity phases were observed as indicated in the XRD analysis **(Figure 4-5)**.

The surface modification reactions are referred to as a silanisation. The TiO_2 NPs have hydroxyl groups on their surface at neutral pH. These hydroxy groups act as nucelophiles and attack the silane of the siloxy bonds (Si-OMe) resulting in the formation of a Ti-O-Si bond and elimination of ethanol (MeOH). The siloxy groups (SiOMe) can also be hydrolysed by water to form silanols (Si-OH) that can react with other SiOMe groups resulting in Si-O-SI bonds and a cross-linked siloxane coating. Subsequently, the bare TiO_2-NPs were functionalised through silanization with either 3-aminopropyl trimethoxysilane (APTS) or poly (ethylene glycol) propyl trimethoxysilane (PEGTS) to afford amino- and

PEG-functionalised NPs that could be easily dispersed in aqueous and organic solutions, respectively **(Figure 4-8)**.

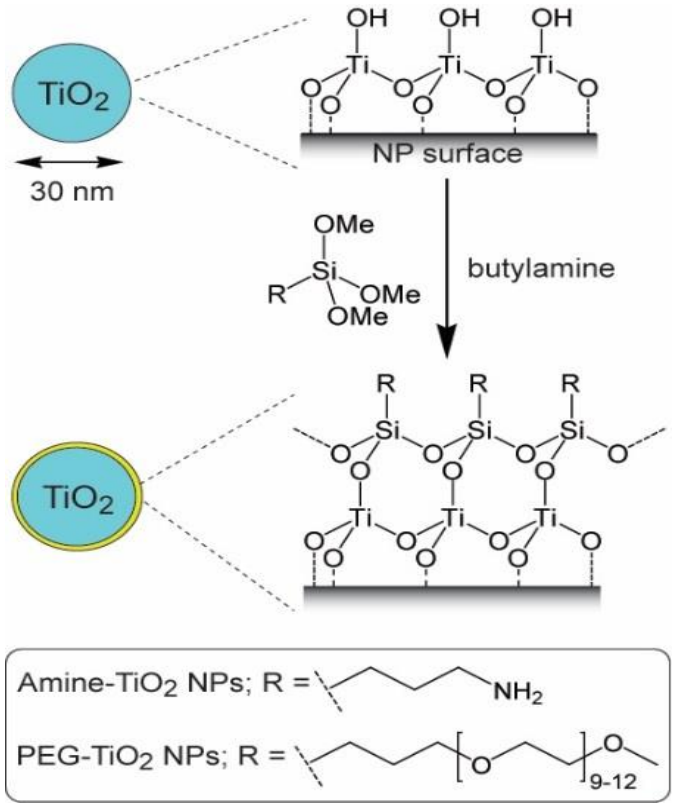

Figure 4-8: Surface modification of TiO_2-NPs via silanisation with APTS and PEGTS.

TGA analysis of the functionalised TiO_2 NPs showed that coatings were ~ 6-7 % of the total NP mass **(Figure 4-6)**. This indicates that most of the observed dose enhancement or radiosensitisation results from X-ray interaction with the TiO_2 NPs as stated in chapters five and six, as the bulk of the particle is mainly composed of Ti and oxygen atoms. The peaks at 1047 and 1128 cm^{-1} observed in the FTIR spectra demonstrates that the APTS and PEGTS surface coatings were successfully grafted on the TiO_2 NPs.

In conclusion, all these characteristics investigation of the NPs indicate that pure anatase TiO_2 NPs were synthesised with the preferred size, average of 30 nm, for ROS generation. Furthermore, the TiO_2 NPs were successfully modified to disperse in PRESAGE chemical composition and in water for phantom and *in vitro* studies respectively which these studies are described in details in the following two chapters.

SECTION B

CHAPTER FIVE

Results and Discussions of Phantom Based Studies Using PRESAGE® Dosimeter

5. SECTION B: Results and discussions of the phantom based studies using PRESAGE® dosimeters

The aim of this chapter is to present and discuss the results obtained from phantom based study using PRESAGE® dosimeters. This part of the study involves mainly investigating and for the first time the feasibility of employing the synthesised anatase PEG functionalised TiO_2 NPs in the prepared PRESAGE® dosimeter for determination of the radiation dose enhancement utilising low and high energy radiotherapy X-ray beams. These radiation dose enhancement results caused by the generated free electrons as a result of TiO_2 NPs exposed to X-ray radiotherapy type radiations.

5.1 Results

The physical properties of the prepared PRESAGE® dosimeters such as maximum absorption wavelength dependence and the radiation dose sensitivity were studied first. In addition, the analyses of the radiological characteristics of the PRESAGE® dosimeter were presented as the dose-response relationship, post response photo-stability and the water equivalency characteristic of the PRESAGE® dosimeters. Also, the uniformity distribution of the synthesised anatase PEG functionalised TiO_2 NPs in the chemical compositions of PRESAGE® dosimeter were assessed. Furthermore, the experimental validation and quantification of the radiation dose enhancement induced by different concentrations of anatase PEG functionalised TiO_2 NPs employing both kilovoltage (kV) and megavoltage (MV) X-ray beam were determined. Finally, the dose enhancement factor (DEF) was calculated as a ratio between the slope of the curve of the TiO_2 NPs doped dosimeters optical density (OD) and the slope of the curve of the non-doped dosimeters OD (control).

5.1.1 PRESAGE® dosimeters

Two different types of PRESAGE® dosimeters in regards to the used halogenated carbon radical initiators (chloroform, iodoform) were fabricated as in method stated previously in chapter 3 **(section 3.2.5)**. The images of the prepared PRESAGE® dosimeters are shown in **Figure (5-1)**. In the following sections a detailed description of the physical and radiological characteristic results of the prepared PRESAGE® dosimeters are presented.

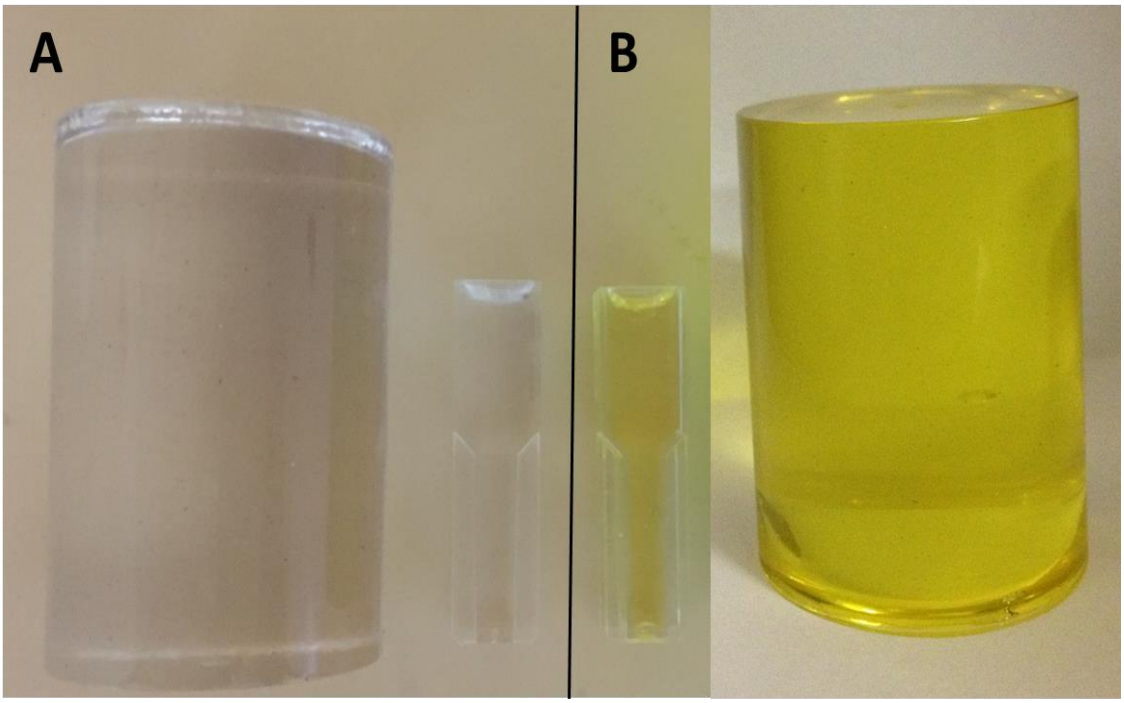

Figure 5-1: Images of the PRESAGE® dosimeters with different halogenated carbon radical initiators (A) Chloroform and (B) Iodoform.

5.1.2 Physical properties of PRESAGE® dosimeters

In literature, the general characteristics of PRESAGE® dosimeter are well investigated and established [189]. In this thesis, some of the important physical properties for the both formulation types of PRESAGE® dosimeters are studied such as the mean physical density (ρ), electron density (ρ_e), effective atomic number (Z_{eff}), and maximum absorption wavelength (λ_{max}). The calculated physical properties for both types of PRESAGE® dosimeter are tabulated in **Table 5-1**. The Z_{eff} was obtained employing Mayneord equation (equation 5-1) [104, 190]. It is observed that the obtained physical density and Z_{eff} number differ for each type of the radical initiator used, where for PRESAGE® with iodoform were higher than PRESAGE® with chloroform.

$$Z_{eff} = \sqrt[2.94]{\sum_{i=1}^{n} a_i Z_i^{2.94}} \qquad \text{..... (5-1)}$$

Table 5-1: Mean physical density (ρ), electron density (ρ_e) and relevant effective atomic number (Z_{eff}) of PRESAGE® dosimeters fabricated with different radical initiators in this study compared to water.

Materials	ρ (Kg.m^{-3})	ρ_e (x10^{29} em^{-3})	Z_{eff}
Water	1000	3.3428	7.42
PRESAGE® (Chloroform)	1045-1047	3.4348	6.62
PRESAGE® (Iodoform)	1089-1097	3.5873	14.37

The identification of the absorption maxima (λ_{max}) was the other important parameter to be considered for scanning PRESAGE® dosimeter. The absorbance spectrum is the change in OD as a function of wavelength (λ) and is used to select the optimal λ for OD acquisitions in PRESAGE® dosimeter. The obtained absorption spectra of PRESAGE® dosimeter with both chloroform and iodoform radical initiators after exposed to 6 MV radiotherapy X-ray beam are shown in **Figure (5-2)**. The absorption λ_{max} is found at a peak of 633nm that is the visible red region of the energy spectrum.

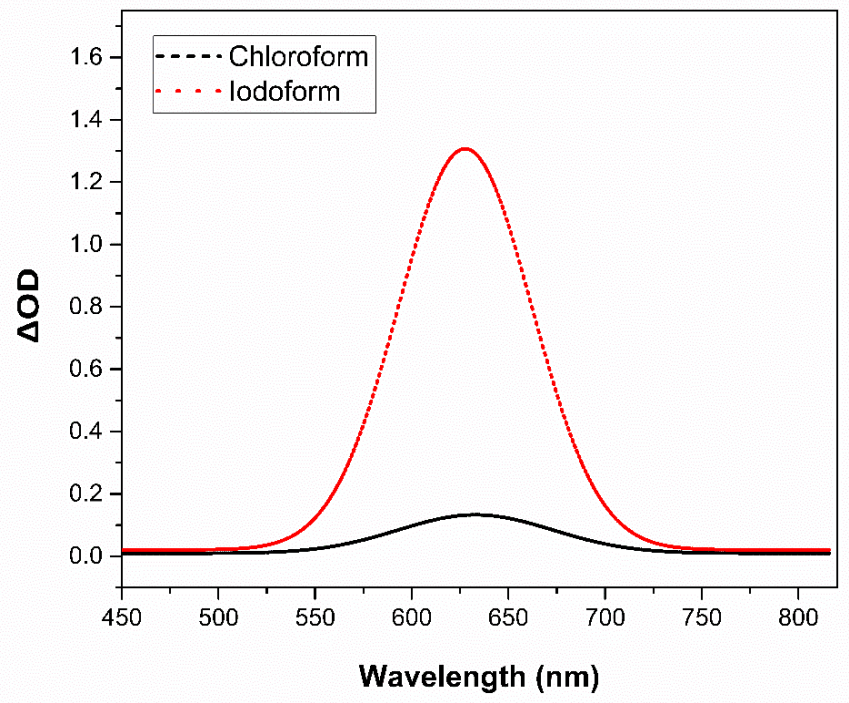

Figure 5-2: Absorption spectra of PRESAGE® dosimeters with both chloroform and iodoform radical initiator after exposure to 25 Gy of 6 MV radiotherapy X-ray beam, showing the absorption maxima to be at 633 nm. The reference cuvette (control) is used as a baseline to establish the zero value.

5.1.3 Radiological characteristic of PRESAGE® dosimeterss

The results of radiological properties of PRESAGE® dosimeters such as dose-response relationship with optical density, radiation sensitivity, post-response photostability and water equivalency characteristic will be presented in the following sections.

5.1.3.1 Leucomalachite green (LMG) oxidation in PRESAGE® dosimeters

The LMG in PRESAGE® dosimeter oxidise by forming a carbon centred radicals as a results of X-ray radiation induced homolysis of alkyl halocarbons, its hypothesised that the carbon centred radicals extract the methane proton from LMG resulting in a resonance stabilised radical cationic form of the dye as shown in **Figure (5-3**). These radicals' possibly dimerisation with halide radicals that displace the halide anion or some other processes such as electron transfer leading to convert the cationic radicals to the cationic malachite green (MG) [190].

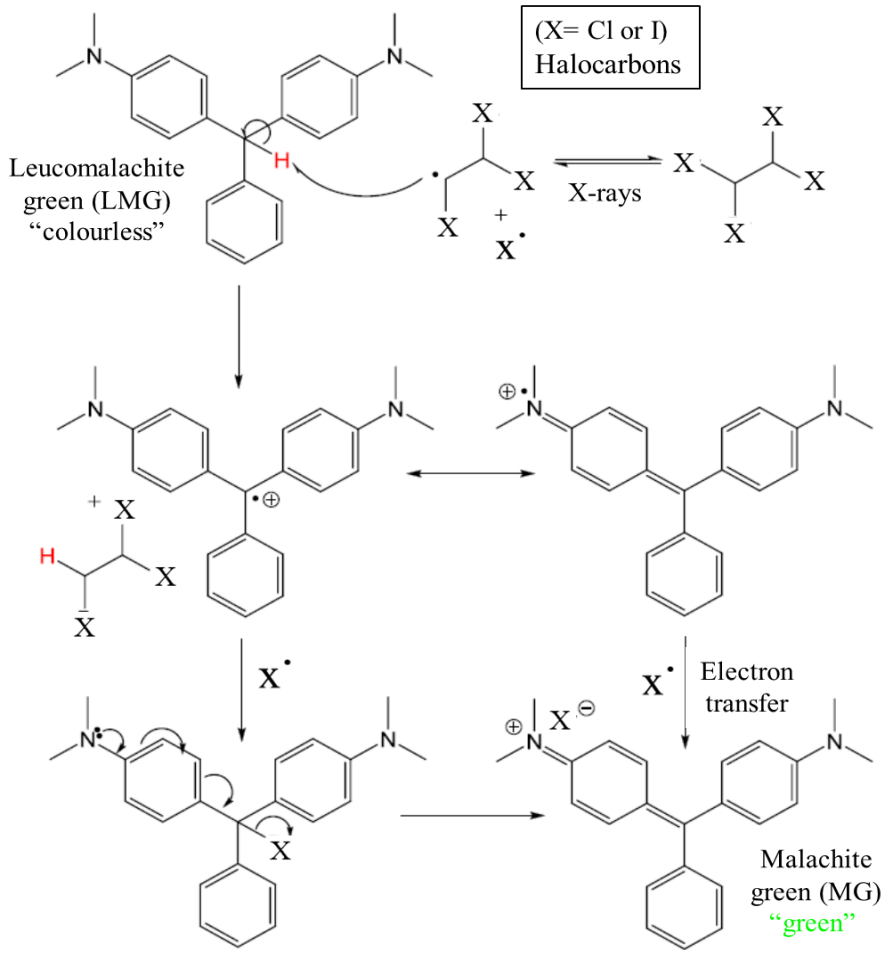

Figure 5-3: Proposed chemical scheme of leucomalachite green (LMG) oxidation via radicals to malachite green (MG).

5.1.3.2 Dose-response relationship of PRESAGE® dosimeters

The linearity characteristic of PRESAGE® dosimeter towards X-ray radiation doses was investigated in this study. The absorption spectra of PRESAGE® dosimeter with chloroform and/or iodoform halocarbons formulation are displayed in **Figures (5-4)** and **(5-5)** respectively. The absorption spectra acquired for both types of PRESAGE® dosimeters are the measured absorbance changes at λ = 633 nm versus radiotherapy X-ray radiation

absorbed doses. However, the intercepts of the dose–response relationship plots are nearly zero and good correlation coefficient linearity ($R^2 > 0.99$) for the dose response is observed in both halocarbons dosimeter formulations over the applied radiation doses range.

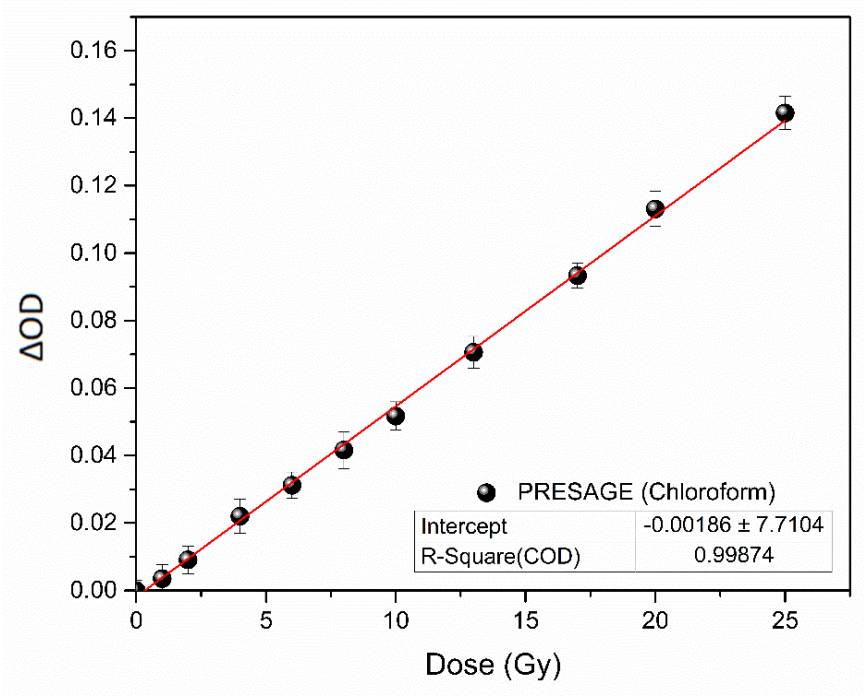

Figure 5-4: Recorded absorbance changes as a function of absorbed radiation dose for chloroform PRESAGE® dosimeter formulations at 6MV energy. Error: ± standard deviation in the measurement (*n*=3). Correlation coefficient parameters of fitted line are shown in the bottom right inset.

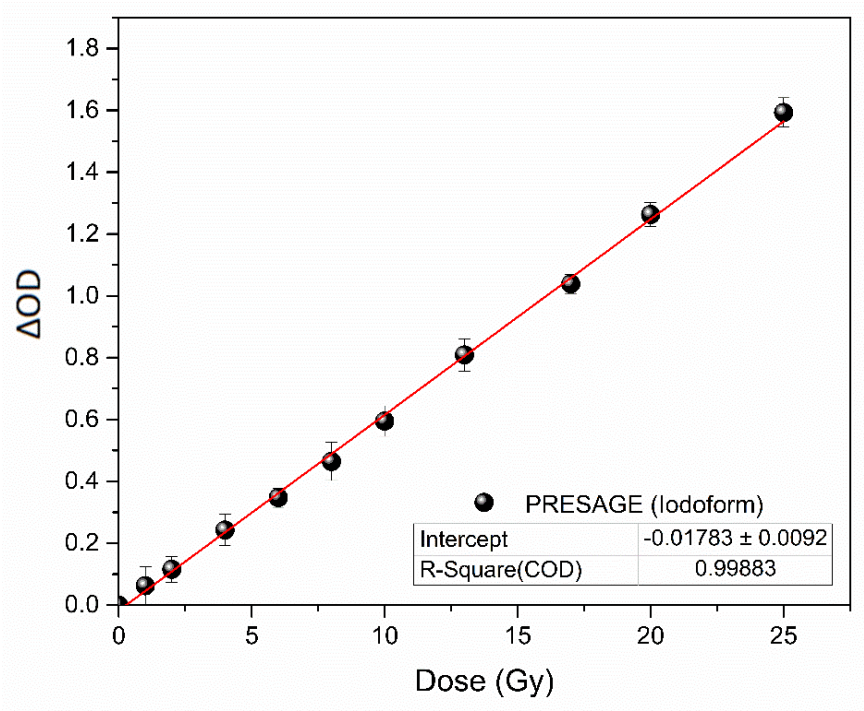

Figure 5-5: Recorded absorbance changes as a function of absorbed radiation dose for iodoform PRESAGE® dosimeter formulations at 6MV energy. Error: ± standard deviation in the measurement (*n*=3). Correlation coefficient parameters of fitted line are shown in the bottom right inset.

5.1.3.3 Sensitivity of PRESAGE® dosimeters

The sensitivity, which is other radiobiological property, of chloroform and/or iodoform–based PRESAGE® formulation towards radiation doses was studied. The sensitivity is expressed as the change in optical density (optical linear attenuation coefficient) per radiation doses ($Gy^{-1}.cm^{-1}$). The sensitivity enhancement factor (SEF) was defined as the ratio between the slope of iodoform–based PRESAGE® formulation and the slop of chloroform–based PRESAGE® formulation [191]. The change in optical density versus the absorbed radiation dose varied significantly between the two types of halocarbons used, and this is clearly visible to naked eye as shown in **Figure (5-6)**. It is observed that the slope of the dose response curve for iodoform-based PRESAGE® formulation (slope = 0.06328 Gy^{-}

^{1}.cm^{-1}) showed significantly higher sensitivity than chloroform-based PRESAGE® formulation (slope = 0.00565 Gy^{-1}.cm^{-1}) resulting in the SEF to be 11.2 at the same applied radiation dose and halocarbons molar concentration.

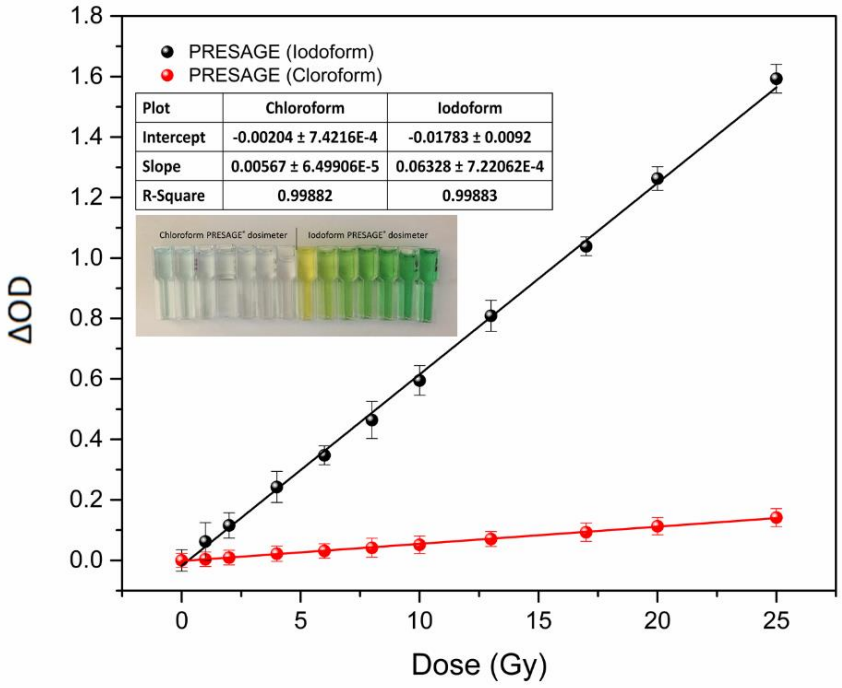

Figure 5-6: Recorded absorbance changes as a function of absorbed radiation dose for chloroform and iodoform PRESAGE® dosimeter formulations at 6MV energy. Error: ± standard deviation in the measurement (*n*=3). Correlation coefficient parameters of fitted line are shown in the top left. Insets: digital images showing chloroform and iodoform PRESAGE® dosimeter exposed to different doses with 6 MV X-ray beams.

5.1.3.4 Post-response photostability

The post-response photostability of PRESAGE® dosimeters with different radical initiators was investigated. The results shown in **Figure (5-7)** clearly demonstrate that both types of halocarbons used in PRESAGE® dosimeter's formulation had reasonable effect on the post-response photostability over a period of 10 days from the day samples been exposed

to X-ray radiation. On the other hand, the influence of PEG functionalised TiO_2 NPs on the photofading of the PRESAGE® dosimeters was studied **(Figure 5-7)**. The recorded ΔOD was also stable over the same period of time. It was observed that chloroform and iodoform PRESAGE® compositions without (control) and with inclusion of 1 mM TiO_2 NPs showed photofading of the rates of~ 5.9 - 6.8 and 4.3 - 5.1% respectively, post 240 hour exposure to 4 Gy dose of X-rays and when stored in a cold (-18 °C) and dark environment. Finally, it was found that the amount of delivered dose have no influence on the photofading of both PRESAGE® formulation investigated.

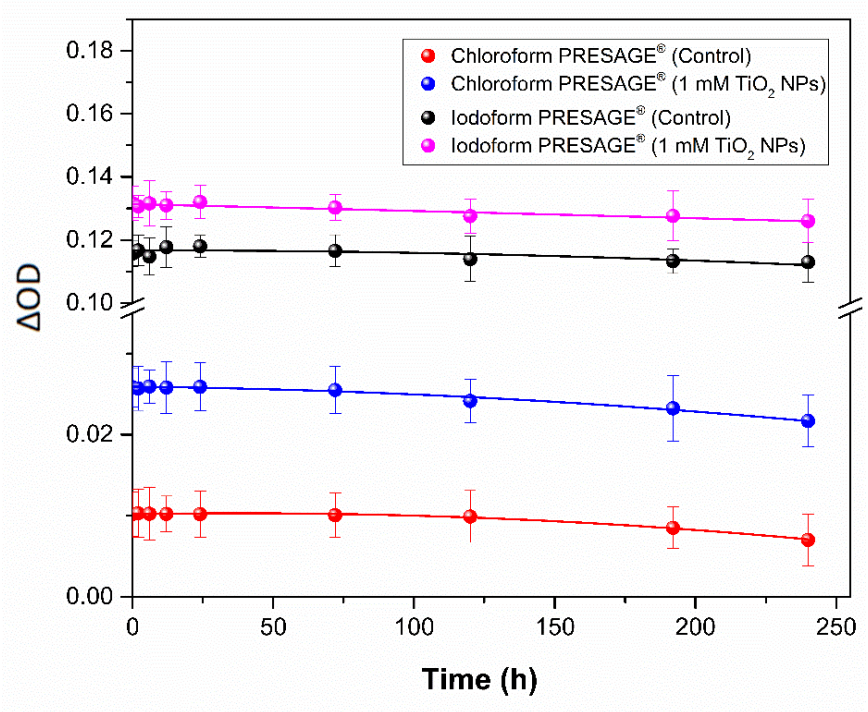

Figure 5-7: Variation in optical density against time for different halocarbons based PRESAGE® formulations after exposed to 4 Gy dose at 80 kV X-ray energy beam. Each PRESAGE® composition is referred to the type of radical initiator used with and without inclusion of TiO_2 NPs. Error bars: ± standard deviation in the measurement (*n*=3). The best fitting approach was achieved at Polynomial fitting of second order.

5.1.3.5 Percentage Depth Dose (PDD) measurement

One of the essential characteristics of PRESAGE® dosimeter to meet application specific dosimetry requirements is the water equivalency in order to be applied in future clinical radiotherapy techniques; hence, this property was examined in this study. **Figure (5-8)** represent the experimental percentage depth dose curve (PDD) acquired for PRESAGE® dosimeters using optical CT scanner and for water using ionisation chamber at 6 MV X-ray beam energies and under full scatter conditions as described in chapter 3 (**section 3.2.7)**. Dose variation with depth was measured up to approximately 6 cm in the PRESAGE® dosimeter. The findings demonstrate that the shape of the PDD curves in the PRESAGE® dosimeters is matching to those obtained by ionisation chamber measurements with a variation of about 2%.

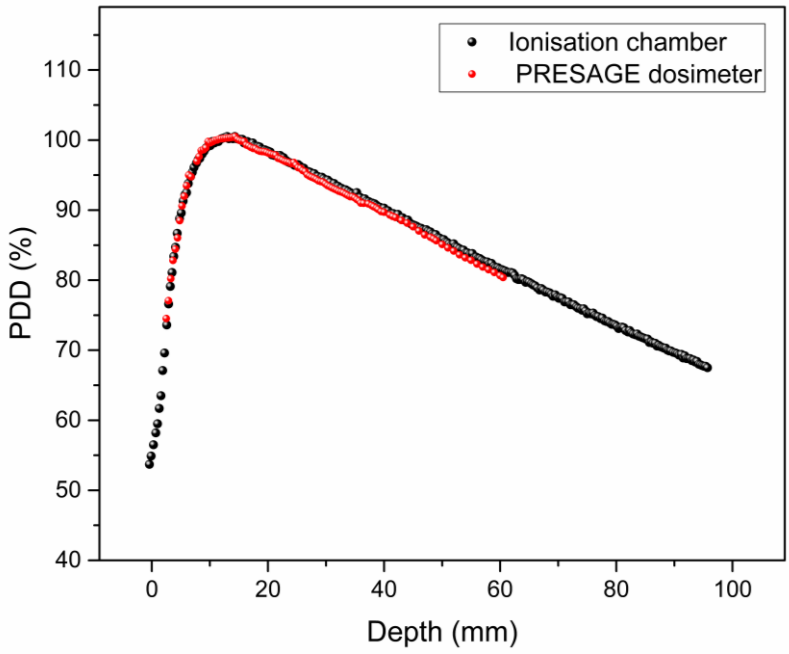

Figure 5-8: Measured relative percentage depth dose (PDD) curves for PRESAGE® dosimeter and ionisation chamber at 6 MV energy beam.

5.1.4 Dose enhancement induced by TiO_2 NPs

In this study, X-ray radiotherapy energy beams ranging from kilovoltage (kV) to external megavoltage (MV) were employed to determine the dose enhancement induces by PEG functionalised TiO_2 NPs in PRESAGE® dosimeter.

5.1.4.1 Low energy "kV" X-ray irradiation

The first experimental validation and quantification of the radiation enhancement caused by PEG functionalised TiO_2 NPs at kV energy X-rays of the type used in superficial X-ray therapy (SXRT) beams was determined by phantoms. PRESAGE® dosimeter, for the first time, was doped with PEG functionalised TiO_2 NPs during the preparation procedures as previously stated in chapter 3 **(section 3.2.6)**. The PRESAGE® dosimeter can be easily loaded with NPs and our group have previously used this approach [45, 192-193]. PEG functionalised TiO_2 NPs concentrations of 0, 0.5 and 1 mM were used to investigate NP dose enhancement. It was not possible to go beyond 1 mM of NPs concentration, for example 4 mM (the case employed for *in vitro* study (Chapter 6)), as this high concentrasion was shelding the incident light of spectrophotometer passing through the PRESAGE® dosimeter samples and resulting in artefacts. The samples were irradiated using SXRT machine with beam energies of 80, 100 and 150 kV and for radiation doses of 0-25 Gy. **Figure (5-9)** is a photograph of PRESAGE® dosimeter samples without and with 1 mM TiO_2 NPs before and after exposed to various doses of 80 kV X-ray beams.

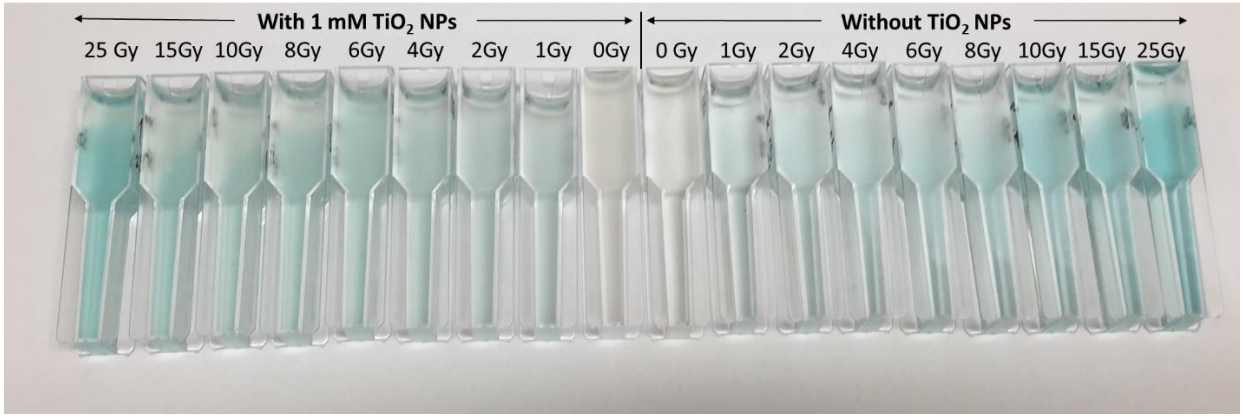

Figure 5-9: Photographs of the reference PRESAGE® dosimeter cuvettes without (control) and the same formulation with 1 mM PEG functionalised TiO_2 NPs (a) before and (b) after exposure to 80 kV X-ray energy beam.

Dose enhancement in PRESAGE® dosimeters doped with PEG functionalised TiO_2 NPs is obtained by measuring the change in optical density (ΔOD) using a UV-VIS spectrophotometer as previously stated in chapter 3 **(section 3.2.8.1**) compared to the case of without NPs. The dose enhancement factor (DEF) was determined as a ratio between the slope of the curve of the TiO_2 NPs doped dosimeters OD and the slope of the curve of the undoped dosimeters OD (control) as in equation (5-2) [191, 194].

$$DEF = \frac{Slope_{\ curve\ of\ dosimeter\ with\ PEGs\ TiO2\ NPs}}{Slope_{\ curve\ of\ dosimeter\ without\ PEGs\ TiO2\ NPs}} \quad \ldots\ldots\ldots (5\text{-}2)$$

The ΔOD of the dosimeters versus the applied radiation dose at 80, 100 and 150 kV energy beams are shown in **Figures (5-10) (5-11) and (5-12)** respectively. An excellent linear correlation coefficient ($R^2 > 0.99$) for the dose response was observed for both the control and NP doped dosimeters over the applied radiation doses range. However, a

noticeable enhance in the sensitivity of PRESAGE® dosimeters doped with PEG functionalised TiO_2 NPs compared to control (without TiO_2 NPs) was observed for samples irradiated with 80 kV compared to 100 and 150 kV X-ray energy beam. The sensitivity enhancement (dose enhancement) was inversely dependent on energy and the calculated DEF for different concentration of TiO_2 NPs and at each kV energy are documented in **Table (5-1)** shown in the following section.

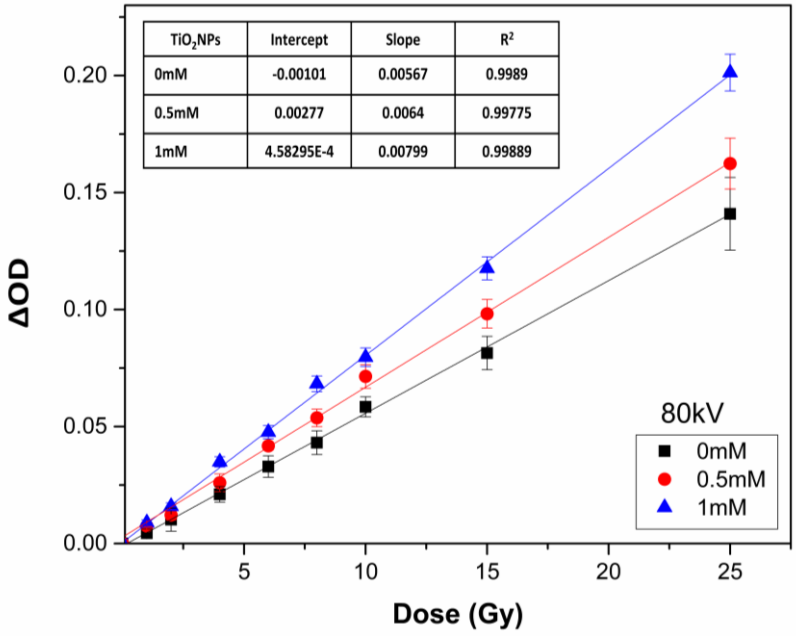

Figure 5-10: Recorded optical density changes (ΔOD) as a function of absorbed radiation dose for the chloroform PRESAGE® formulation without and with different concentrations of PEG functionalised TiO_2 NPs at 80 kV X-ray energy. Correlation coefficient parameters of each fitted line are shown in the inset of the graph. Error bars: ± standard deviation (*n* = 3). The optical density (OD) was measured using UV/Vis spectrophotometer.

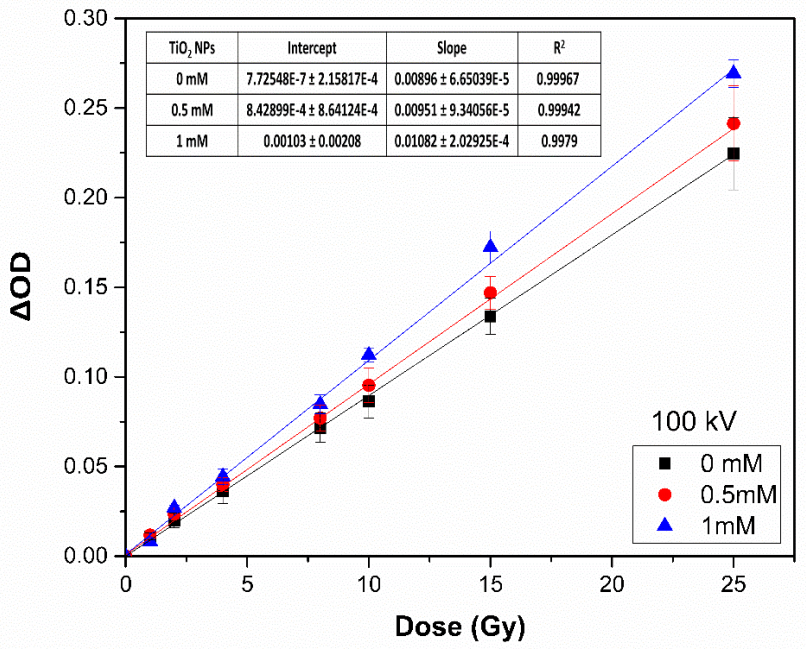

Figure 5-11: Recorded ΔOD as a function of absorbed radiation dose for the chloroform PRESAGE® formulation without and with different concentrations of PEG functionalised TiO_2 NPs showing the response to 100 kV X-ray energy. Correlation coefficient parameters of each fitted line are shown in the inset of the graph. Error bars: ± standard deviation (*n* = 3). The OD was measured using UV/Vis spectrophotometer.

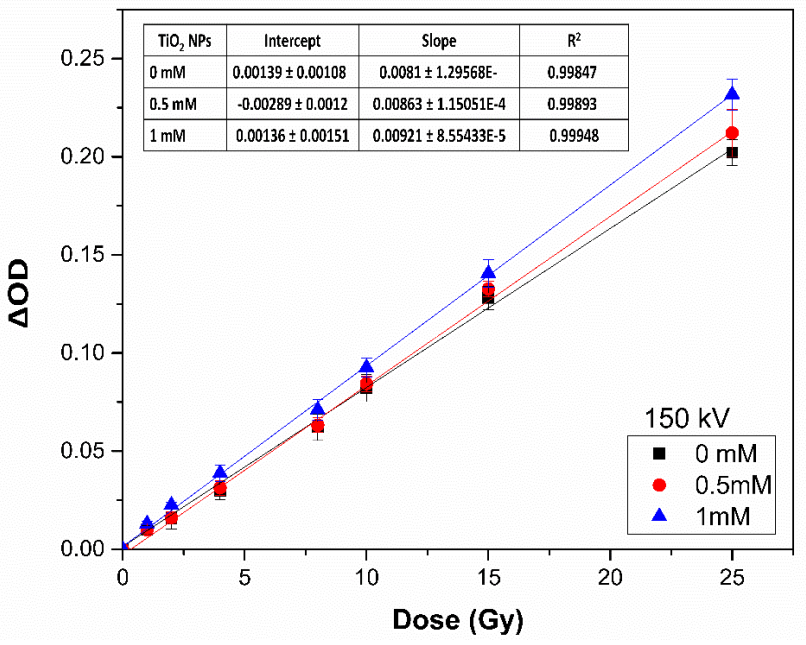

Figure 5-12: Recorded ΔOD as a function of absorbed radiation dose for the chloroform PRESAGE® formulation without and with different concentrations of PEG functionalised TiO_2 NPs showing the response to 150 kV X-ray energy. Correlation coefficient parameters of each fitted line are shown in the inset of the graph. Error bars: ± standard deviation (*n* = 3). The OD was measured using UV/Vis spectrophotometer.

5.1.4.2 High energy "MV" x-ray irradiation

The methods described in the previous section **(5.1.4.1)**, were repeated to measure the dose enhancement of PEG functionalised TiO_2 NPs in PRESAGE® dosimeter irradiated with 6 MV beams (high energy beams). A slight dose enhancement **(Table 5-1)** was detected for 0.5 and 1 mM NPs concentrations with the PRESAGE® dosimeter as shown in **Figure (5-13)**.

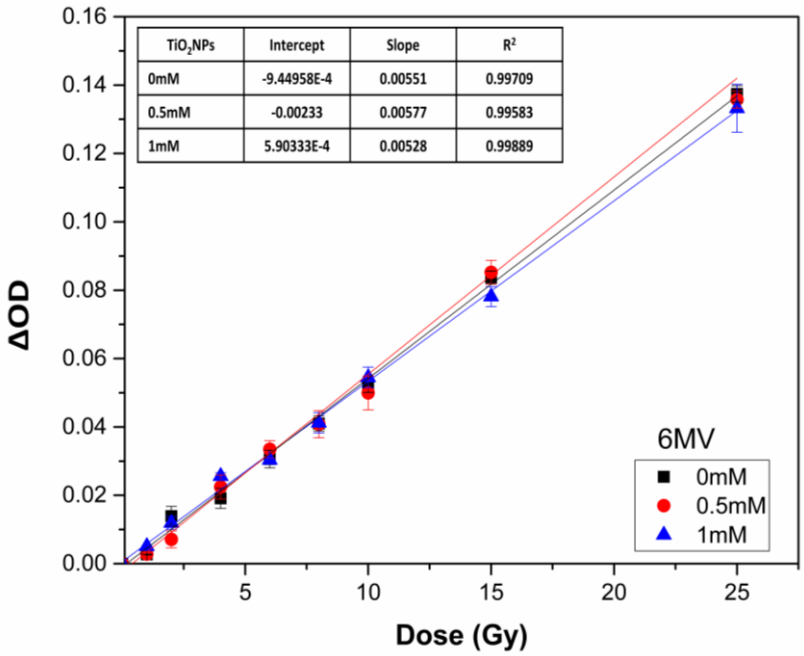

Figure 5-13: Recorded ΔOD as a function of absorbed radiation dose for the chloroform PRESAGE® formulation without and with different concentrations of PEG functionalised TiO_2 NPs showing the response to 6 MV X-ray energy. Correlation coefficient parameters of each fitted line are shown in the inset of the graph. Error bars: ± standard deviation (*n* = 3). The OD was measured using UV/Vis spectrophotometer.

Dose enhancement factors at low (kV) and high (MV) X-ray energy beams and for each concentration of PEG functionalised TiO_2 NPs are tabulated as shown in **Table (5-2)**. The numbers represent a percentage increase, for example "1.40" means enhance of 40 %.

Table 5-2: Calculated DEFs for different concentrations of PEG functionalised TiO_2 NPs in PRESAGE® dosimeter irradiated with low (kV) and high (MV) X-ray energy beams.

PEG functionalised TiO_2 NPs concentrations	**DEF**			
	80 kV	***100 kV***	***150 kV***	***6 MV***
0.5 mM	1.12	1.061	1.065	1.04
1 mM	1.40	1.20	1.13	1.03

In brief, a large dose enhancement is obtained when PRESAGE® dosimeters are exposed to low energy X-rays while very small dose enhancements are observed when exposed to high energy X-rays (in megavoltage ranges).

5.2 Discussion

In this chapter, the discussion is divided in to two main sections. The first section will explain the reasons behind the main findings of physical and radiological properties of PRESAGE® dosimeters and the second section will contain explanation for the reasons behind dose enhancement induced by PEG functionalised TiO_2 NPs.

5.2.1 Physical and radiological properties of PRESAGE® dosimeter

The results of phantom studies confirms that the incorporation of the halogenated carbons (iodoform and chloroform), only one is used at a time, as a radical initiators in the composition of PRESAGE® dosimeter resulted in variations in the physical and radiological properties of the dosimeters. It is observed that the obtained physical properties such as physical density and Z_{eff} of PRESAGE® dosimeters with iodoform radical initiator were higher than those obtained when chloroform radical initiator is used **(Table 5-1)**. This increase in physical density and Z_{eff} is due to the high atomic number (Z) and density of iodine (Z=53, ρ=4.008 g.cm^{-3}) compared to the chlorine (Z=17, ρ=1.489 g.cm^{-3}). A comparison between these two radicals PRESAGE® formulation and water in regards to the Z_{eff} and physical density (**Table 5-1**) demonstrate that characteristic of chloroform PRESAGE® formula is more water equivalence than iodoform PRESAGE® formula, therefore, PRESAGE® fabricated with chloroform is selected to be applied for dose enhancement measurements in this thesis. These results are in good agreement with previously published results [189, 190]. However, the absorption λ_{max} of PRESAGE® dosimeters with both radical initiators after exposure to 6 MV beam are found at a peak of 633nm **(Figure 5-2)** which is the visible red region of the energy spectrum. This absorption λ_{max} is comparable to the oxidised form of leucomalachite green (LMG) and is in good agreement with previous study [63]. Furthermore, the absorption λ_{max} of PRESAGE® dosimeter (633 nm) corresponds to the LED source of commercially available VistaTM OCT scanner (Modus Medical Devices Inc.) [63]. Therefore, such PRESAGE® dosimeter can be used as a 3D dosimetry using VistaTM OCT scanner system.

The radiological properties of the fabricated PRESAGE® dosimeters have been investigated. As previously stated in chapter 3 **(section 3.2.8.1.3)**, the absorption

measurements were calculated by subtracting the relevant measurement of a reference cuvette from the same batch with zero radiation dose (control) from that of the irradiated cuvettes; therefore, the absorbance changes against radiation dose absorbed are in fact only due to the absorbed radiation dose [61, 194]. Consequently, the plots intercept in both chloroform and iodoform PRESAGE® dosimeters were at -0.0018 and -0.0178 respectively, with linear correlation coefficient (R^2) of > 0.99 **(Figure 5-4 & 5-5)**. The interception of chloroform PRESAGE® dosimeter is lower and closer to zero than iodoform PRESAGE® dosimeter suggesting that PRESAGE® dosimeter with chloroform could be used without the need for a correction factor/s in the attenuation function better than iodoform PRESAGE® dosimeter for both kilovoltage energy were P.E. is predominant interaction which is Z dependant (The Z_{eff} values of chloroform PRESAGE® dosimeter is closest to that of water than iodoform PRESAGE® dosimeter (**Table 5-1**)) and megavoltage energy were Compton scatter is predominant interaction which mainly depend on density (The density of chloroform PRESAGE® dosimeter is more water equivalent than iodoform PRESAGE® dosimeter (**Table 5-1**)). Whereas the linearity ($R^2 > 0.99$) of control PRESAGE® dosimeter plot indicate that the response of PRESAGE® dosimeter is reliable and is faithfully following the well-known ionisation chamber linearity characteristic obtained by the same way, also the linearity of PRESAGE® dosimeter plot doped with TiO_2 NPs indicated that the TiO_2 NPs were homogeneously dispersed throughout the dosimeter. In addition, it was noted that the slope of the PRESAGE® dosimeter's response containing iodoform as a radical initiator was significantly higher than chloroform (SEF = 11.2) as shown in **Figure (5-6)**. This indicates that iodoform enhance the sensitivity of the dosimeter to radiation dose more than chloroform. The apparent difference in sensitivity to radiation dose for chloroform and iodoform is attributed to the bond dissociation energy C-X (X = I or Cl). The iodoform C–I and chloroform C–Cl bond dissociation energies are (57.6 $kcal.mol^{-1}$ and 83.7 $kcal.mol^{-1}$) and

the densities are 4.008 $g.cm^{-3}$ and 1.489 $g.cm^{-3}$ respectively. The generated free radicals from the radiolysis of the halocarbon bonds upon PRESAGE® dosimeter exposed to X-ray radiation is directly proportional to the C–X bond dissociation energy [195, 196]. Accordingly, less energy is required to cause homolysis of iodoform and produce free radicals than chloroform which these generated free radicals in turn oxidises more LMG leading to a greater increase in optical density change, hence iodoform have higher sensitivity than chloroform which this could be an advantage for employing iodoform PRESAGE® formulation for applications with very low radiation doses. These findings are in good agreements with previous observations [61, 194]. Moreover, there was no noticeable effect on the post-response photostability of the PRESAGE® dosimeter for both halogenated carbons used in this study and the recorded ΔOD were almost stable over the period of 240 min. These findings are in good agreement with previous studies [160]. In general, the reasonable photofading rates observed with both PRESAGE® compositions without (control) and with inclusion of TiO_2 NPs **(Figure 5-7)** is attributed to the small concentration of halocarbons employed (chloroform < 5 wt% and iodoform <2 wt%) [194]. However, inclusion of metal compounds (TiO_2 NPs) have shown to slightly improve the post-response photostability, where similar results were obtained by others when they include carboxylate compounds in the PRESAGE® compositions [197, 198]. Finally, the PDD results demonstrate that PRESAGE® formulations have identical radiological properties to water (water-equivalent characteristics) as shown in **Figure (5-8)**, due to the PDD data for PRESAGE® dosimeter obtained using optical CT scanner matches those obtained for water from conventional and clinically well used air ionisation chamber. This finding is in agreement with literature investigation [199]. As a result, the fabricated PRESAGE® dosimeters are suited for clinical applications in both kilovoltage and megavoltage clinical X-ray beams.

5.2.2 Dose enhancement induced by TiO_2 NPs

The results of phantom study **(Figures (5-10) to (5-13))** confirms that dose enhancement induced by PEG functionalised TiO_2 NPs at kilovoltage X-ray energy beams (80, 100 and 150) kV, especially at 80 kV as it produce higher dose enhancement which this study focus on, is significant compared to the negligible dose enhancement detected at 6 MV X-ray energy beams **(Table 5-2)**. This is due to the fact that at 80 kV the photoelectric effect (PE) is the dominant process of interaction. While at 6 MV, the interaction of X-ray photons is mainly through Compton scattering. At 80 kV, the probability of interaction via PE is strongly dependent on cubic power of atomic number (Z^3); therefore, the interaction of X-ray photons with Ti atoms in the TiO_2 NPs doped dosimeters will be much higher than the interaction with the control PRESAGE® dosimeter (without TiO_2 NPs) since the effective atomic number of TiO_2 is 18.49 and that of PRESAGE® dosimeter is about 6.62; therefore, taking the probability of interaction via PE to be dependent on Z^3 which results in the ratio of the probability of PE interaction with TiO_2 NPs doped dosimeters compared to the control dosimeters will be about 21.8 and then causes an increase in the interaction probability leading to the generation of copious secondary electrons [181, 192]. These generated secondary electrons could directly or indirectly interact with LMG dye in the PRESAGE® formulation. The direct interaction would be between the generated electrons from TiO_2 NPs and the LMG dye converting it to its oxidised form (MG), whereas the indirect interaction is between the generated electrons from TiO_2 NPs and the radical initiators resulting in the production of further secondary radicals and increasing the extent of LMG dye oxidation. Hence, these generated electrons are responsible for the radiation dose enhancement at the target with 80 kV. Also increasing the TiO_2 NPs concentration in the PRESAGE®

formulation leads to an increase of the dosimeter sensitivity to radiation, which this clearly demonstrates an increase in the number of produced secondary electrons as the concentration of TiO_2 NPs increased. However, at 6 MV, the addition of PEG functionalised TiO_2 NPs in the PRESAGE® formulation slightly increased the physical density of the dosimeter and reduces the density of the free electrons as a result of low free electron density of TiO_2 NPs (2.86×10^{29} e m^{-3}) compared to PRESAGE® dosimeter (3.434×10^{29} e m^{-3}); therefore, the NPs effect on the PRESAGE® dosimeter cancels out. Thus, there is no significant physical dose enhancement detected by PRESAGE® dosimeter at 6 MV energy beams. The slight 4 % dose enhancement determined is likely to originate from the PE contribution, as the energy spectrum of the MV beam shows some residual low energy which will be involved in PEs, which have been previously observed with Au NPs [183, 192]. These reasons combined are reflected in the results of this study, which indicates clearly that the dose enhancements in PRESAGE® dosimeter caused by the inclusion of the TiO_2 NPs were much higher at low energies (especially at 80 kV) compared to those measured at high energies (6 MV).

SECTION C

CHAPTER SIX

Results and Discussions for *In Vitro* Studies

6. SECTION C: Results and discussion for *in vitro* studies

The results obtained for *in vitro* study are reported in the first part of this section then the discussion of those results is presented. The focus of this chapter is on radiosensitisation caused by anatase amine functionalised titanium dioxide nanoparticles (TiO_2 NPs) on two types of cells, prostate cancer (DU145) and human keratinocyte (HaCaT) cell lines which results from the generation of free radicals and increased reactive oxygen specious (ROS). It should be noted that the term *dose enhancement* is replaced in these section with *radio-sensitisation* as the effects of the particles are manifested biologically as well.

6.1 Results

The localisation of anatase amine functionalised TiO_2 NPs inside two different types of cells (HaCaT and DU145) were assessed using various techniques. Then the toxicological characteristic of these NPs were investigated. With both types of cells, various concentrations of amine functionalised TiO_2 NPs using kilovoltage (kV) and megavoltage (MV) X-ray radiotherapy beams were employed to estimate the cells' radiation dose sensitisers by such NPs. Cell survival curves are used as an end point to analyse the radiosensitisation effects by amine functionalised TiO_2 NPs. The dose enhancement factor (DEF) was calculated from the cell survival curves. The analysis of radiobiological parameters was conducted on the obtained survival curves. Finally, the reactive oxygen species (ROS) generated from TiO_2 NPs was detected.

6.1.1 TiO_2 NPs association with cells

The observation of TiO_2 NPs uptake and localisation inside the cells for both types of cells (HaCaT & DU145) was assessed using two different techniques. Firstly, the cell population was assessed using FCM which compares the scattered light resulted from TiO_2 NPs-treated cells with the untreated control, however, this method cannot distinguish if the NPs are within the cells or bounded to the surface. Therefore, in second method, high magnificent light microscopy was employed to observe the foreign objects within the cells.

6.1.1.1 Flow cytometry (FCM) observation

FCM was used to observe the cellular association and/or uptake of NPs by taking advantage of the increased visible-light scattering caused by TiO_2 NPs, relative to the mostly translucent cellular environment. The scattered light are classified to forward scattered light (FSC) and side scatter light (SSC). The FSC represents the size of the cells that is proportional to the size and surface area of the cell and is a measurement of mostly diffracted light, which is detected just off the axis of the incident laser beam in the forward direction by a detector. Whereas, the SSC represents the granularity of the cells which is proportional to cell granularity or internal complexity (i.e. cells with internal complexity will produce more side scattered light) and is a measurement of mostly refracted and reflected light that occurs at any interface within the cell where there is a change in refractive index. In FCM dot plot, each event is represented as a single point on a scatter plot. Intensities of two different channels are represented along the x-axes. Event with similar intensities are clustered together in the same region on the scatter plot. The black region is referred to the population

of light scattered from all events while the red region represent the light scattered from cells population. HaCaT cells were exposed to amine functionalised TiO_2 NP concentrations of 0.5, 1 and 4 mM for 24 h. Untreated cells were used as controls **(Figure 6-1)**. The FSC and SSC were analysed as shown in **(Table 6-1)**. The percentage values represent a ratio of mean FSC or SSC light of cells treated with TiO_2 NPs to the control cells. In treated samples, the percentage intensity of forward scatter (x-axis) shows negligible change (suggesting no change in object size), whereas the percentage of side-scatter intensity (y-axis) increased by 945 % (0.5 mM), 1307 % (1 mM) and 2045 % (4mM) as compared to the granularity of control cells (100%) as shown in **Figures (6-2), (6-3) and (6-4)** respectively. This suggests a strong association between the cells and the NPs in the treated samples, though it does not distinguish between NPs within the cells and those bound to the cell surface.

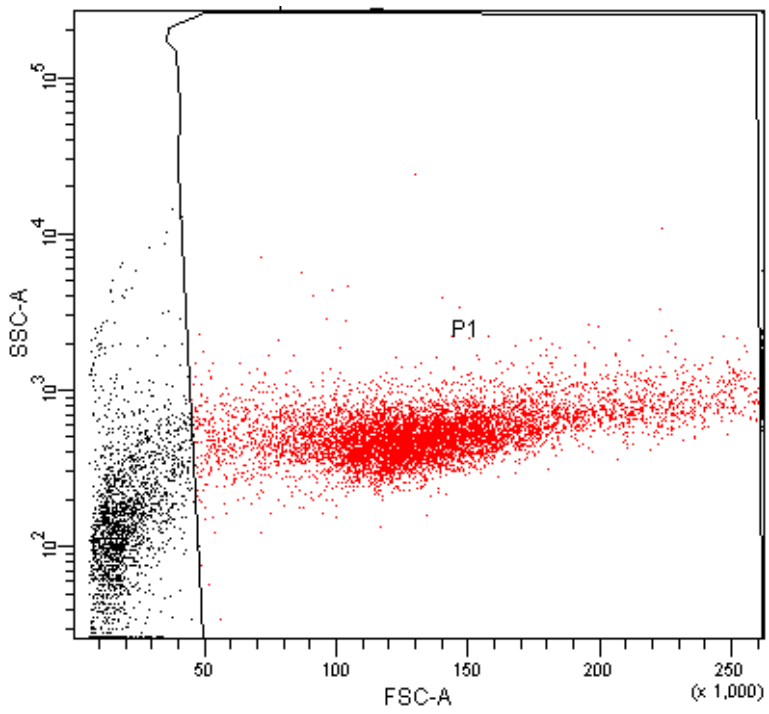

Figure 6-1: Flow cytometry scatter plots of HaCaT cells without any treatment (control).

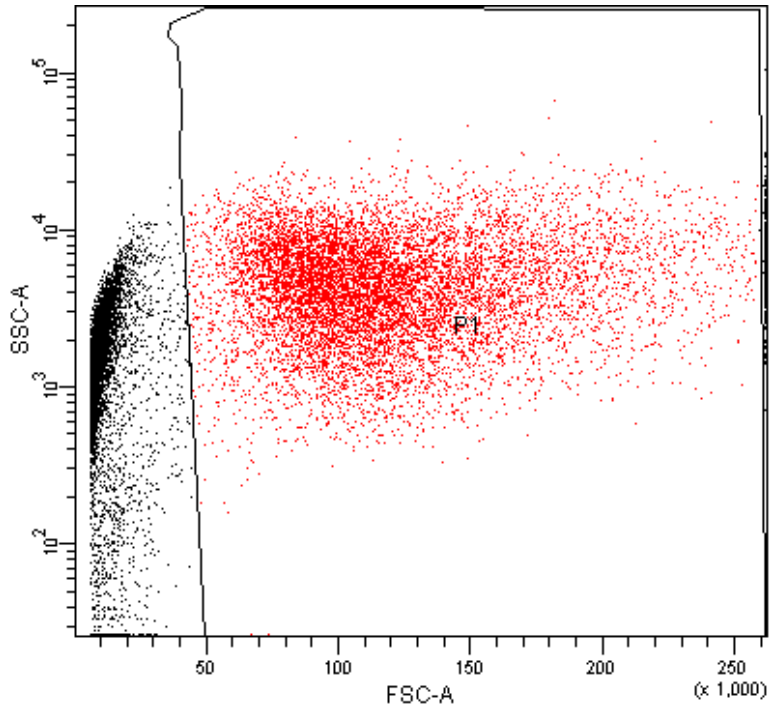

Figure 6-2: Flow cytometry scatter plots of HaCaT cells treated with 0.5 mM TiO_2 NP solutions.

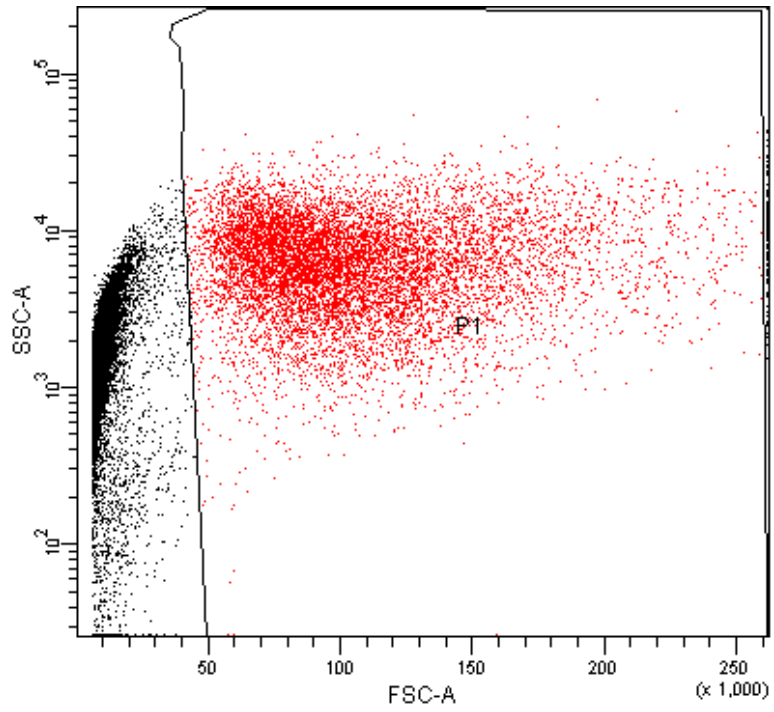

Figure 6-3: Flow cytometry scatter plots of HaCaT cells treated with 1 mM TiO_2 NP solutions.

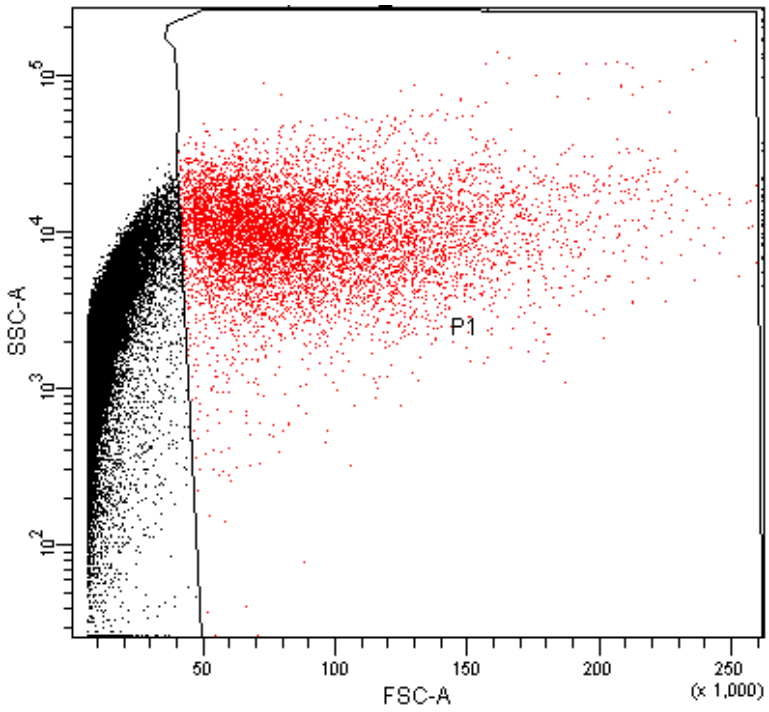

Figure 6-4: Flow cytometry scatter plots of HaCaT cells treated with 4 mM TiO_2 NP solutions

Table 6-1: Recorded forward and side-scatter by flow cytometry for observing various concentrations of TiO_2 NPs association with HaCaT cells.

TiO_2 NPs Concentration (mM)	*% Forward scatter (FSC-A)*	*% Side scatter (SSC-A)*
Control	100.00	100.00
0.5	88.08	945.27
1	79.06	1306.64
4	67.62	2044.93

6.1.1.2 Light microscopy observation

In this thesis, the distribution of TiO_2 NPs inside the cells was investigated by light microscopy. The plated cell and after treated with 4 mM of ~30 nm anatase amine functionalised TiO_2 NPs for 24 h were three times washed with Milli-Q water to remove the NPs attached to the cell's surface. The cells were then fixed in (1:7) oleic acid/ethanol solution for 5 min and stained with a 0.5 % crystal violet in ethanol solution for 15 min that made the nucleus to be stained with blue dye. Light microscopy with 40X magnification observed the TiO_2 NPs as a black dots cluster in the cytoplasm of the cells and these black dots (aggregation of TiO_2 NPs) is clearly shown in **Figure (6-5)**. It was also observed that there were no NPs inside the nucleus.

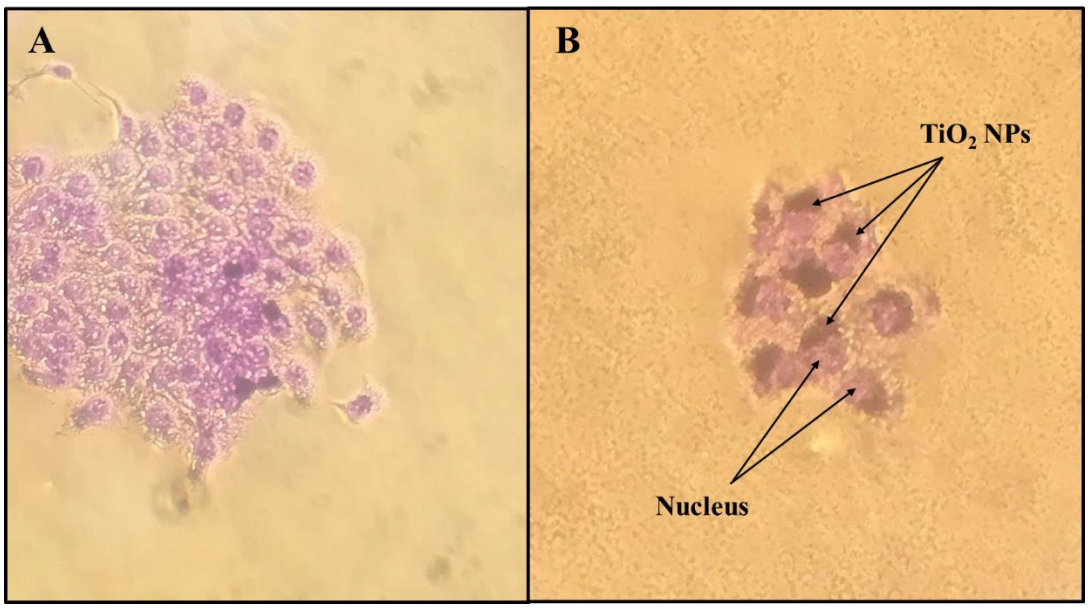

Figure 6-5: HaCaT cells stained with a 0.5 % crystal violet in ethanol, A) without nanoparticles, B) With TiO_2 NPs which aggregate as black dots in the cytoplasm. The TiO_2 NPs are surrounding the nuclei.

6.1.2 Cytotoxicity of TiO_2 NPs

In this study, the toxicity induced by amine functionalised TiO_2 NPs in the cells was examined by measuring the cell viability. Initial studies were performed to explore the time and concentration-dependent cytotoxic effects of TiO_2 NPs. Concentrations up to 30 mM was used to investigate the highest concentration of TiO_2 NPs that can reliably suspended in the culture medium with the cells incubated for up to 72 h without causing visible damage to a monolayer of cells. The TiO_2 NPs with an average size of ~30 nm were specifically prepared for usage with the cells for this type of study. HaCaT and DU145 cell lines were exposed to amine functionalised TiO_2 NPs at concentrations ranging from 0.5 to 30 mM for 24, 48 and 72 h to investigate the kinetic tolerance of these cell lines to TiO_2 NPs. Cell viability was measured via MTS assays [200]. Cell viability was expressed as a percentage of treated cultures (with TiO_2 NPs treatment) to untreated controls (without TiO_2 NPs treatment). The results indicated that TiO_2 NPs were nontoxic for both types of cells up to 4 mM post 72 h of treatment as the cell viability for these concentrations (up to 4 mM) of TiO_2 NPs did not show any statistically significant difference ($p > 0.05$). The effects of amine functionalised TiO_2 NPs on DU145 cell's viability are clearly displayed in **Figures (6-6)**. HaCaT cells show similar result. When cells were exposed to higher concentrations (up to 8 mM), viability remained constant (100 %) after 48 h and again these results did not show any statistically significant difference **(Figure 6-7)**, whereas with further concentrations (up to 30 mM), it was observed that the viability was reduced by up to 22 % post 48 h which statistically show significant difference **(Figure 6-8)**.

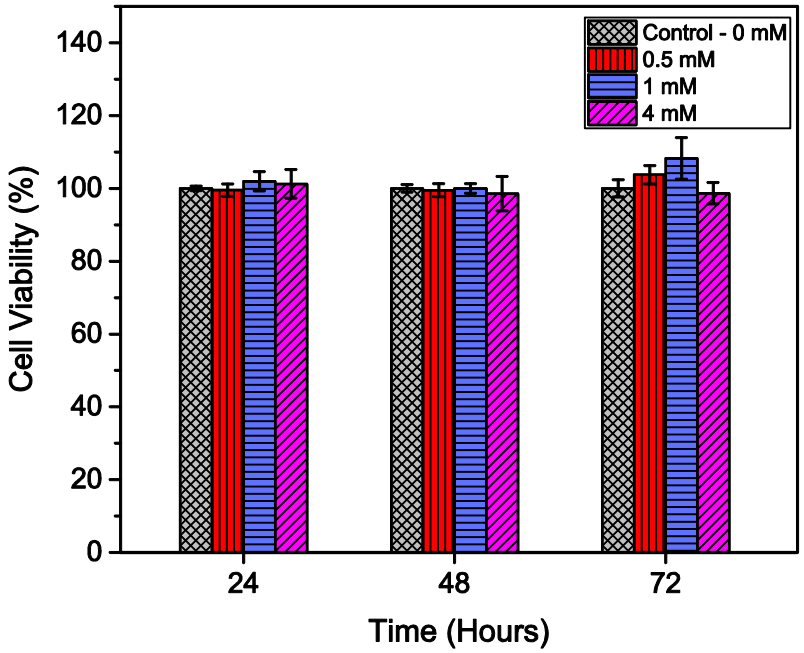

Figure 6-6: Cell viability for DU145 cells exposed to different concentrations of TiO_2 NPs as a function of time. The errors are standard deviation from three independent experiments (mean ± SD, n=3). The data mean comparisons for different concentration at the same time are not significantly different (P > 0.05, ANOVA test). HaCaT cells show similar results.

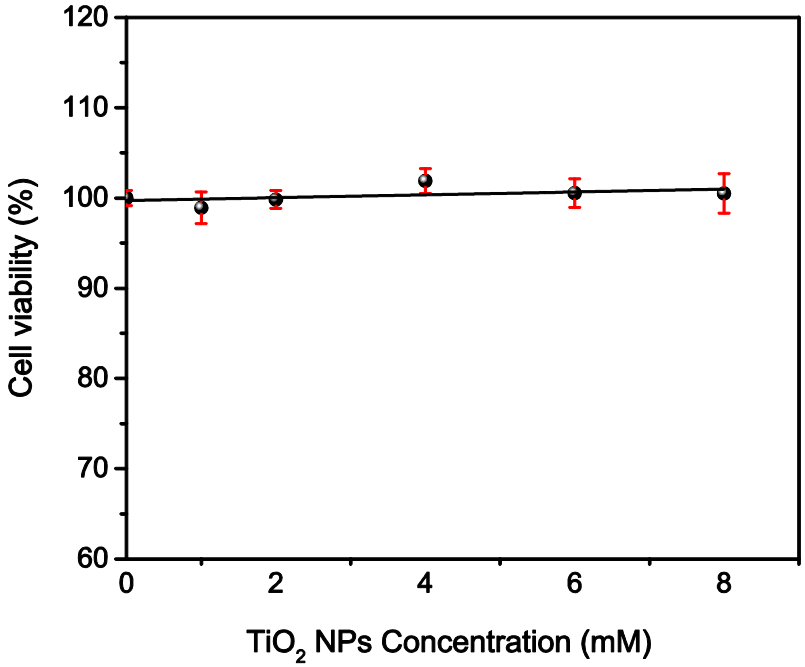

Figure 6-7: Cell viability for HaCaT cells exposed to TiO_2 NPs of concentrations up to 8 mM at 48 h. The errors are standard deviation from three independent experiments (mean ± SD, n=3). The data mean that cell viability remain constant (100%) and is not significantly different with TiO_2 NPs concentrations (P > 0.05, ANOVA test).

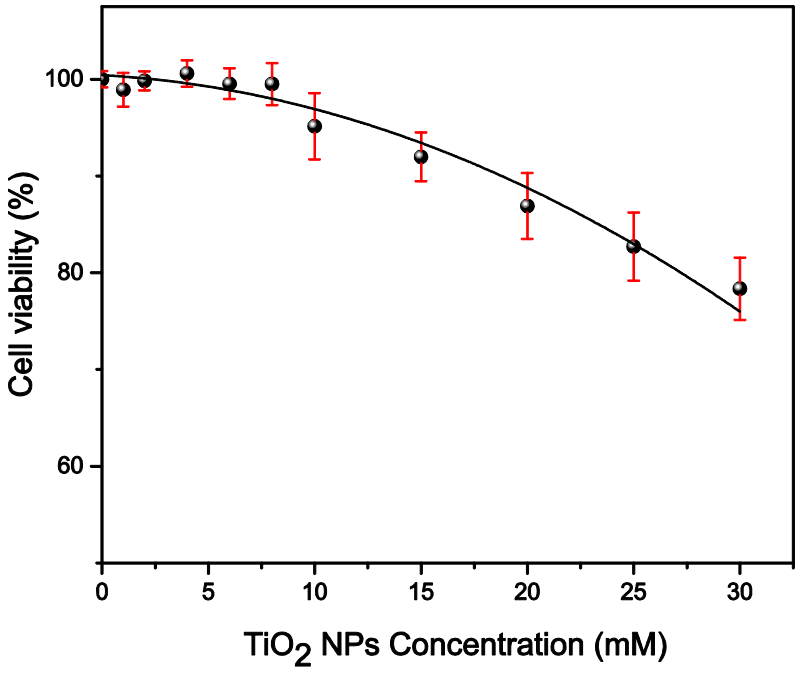

Figure 6-8: Cell viability for HaCaT cells exposed to TiO_2 NPs of concentrations up to 30 mM at 48 h. The errors are standard deviation from three independent experiments (mean ± SD, n=3). The data mean that cell viability drops beyond 8 mM TiO_2 NPs concentrations and is significantly different ($P < 0.05$, ANOVA test).

To conclude, the cytotoxic responses in the HaCaT and DU145 used in this study were found to be independent on the TiO_2 NPs concentrations up to 4 mM post 72 hours incubation in 37 ^oC and 5 % CO_2 which were selected to be used for *in vitro* studies of this thesis.

6.1.3 Radiosensitivity induced by amine functionalised TiO_2 NPs using X-ray radiotherapy

In this study, X-ray radiotherapy energy beams ranging from kilovoltage (kV) to external megavoltage (MV) were employed to determine the radiosensitisation caused by amine functionalised TiO_2 NPs in two types of cells.

6.1.3.1 kV superficial X-ray radiotherapy

Ranges of kV X-ray radiotherapy beams in combination with different concentrations of anatase amine functionalised TiO_2 NPs were employed to investigate the DEF dependence on beam energies at this ranges and its dependence on the particle's concentrations. The effective kV energy that create highest dose enhancement was then selected to be applied for *in vitro* studies of this thesis. **Figures (6-9), (6-10) and (6-11)** shows HaCaT cells survival curves for the three kV X-ray energies (80, 100 and 150 kV) at radiation doses of 0-8 Gy and with 0.5, 1 and 4 mM concentrations of TiO_2 NPs employing MTS assay. Data were plotted as log % percent survival fraction vs nominal dose (nominal dose is a term used for standard dose that has been measured by calibrated ionisation chamber) and fitted with a linear quadratic model. The DEFs are extrapolated at 80 % survival. The DEFs are estimated as a ratio of the control survival fraction to the survival fraction of the treated cells with TiO_2 NPs. At 80 kV X-ray energy, DEFs are 1.21, 1.57 and 1.70 (i.e. radiosensitivity enhancement of 21, 57 and 70% respectively). At 100 kV energy, DEFs for the same concentration are 1.10, 1.21 And 1.37 respectively. At 150 kV energy, DEFs for the same concentration are 1.018, 1.044 And 1.12 respectively.

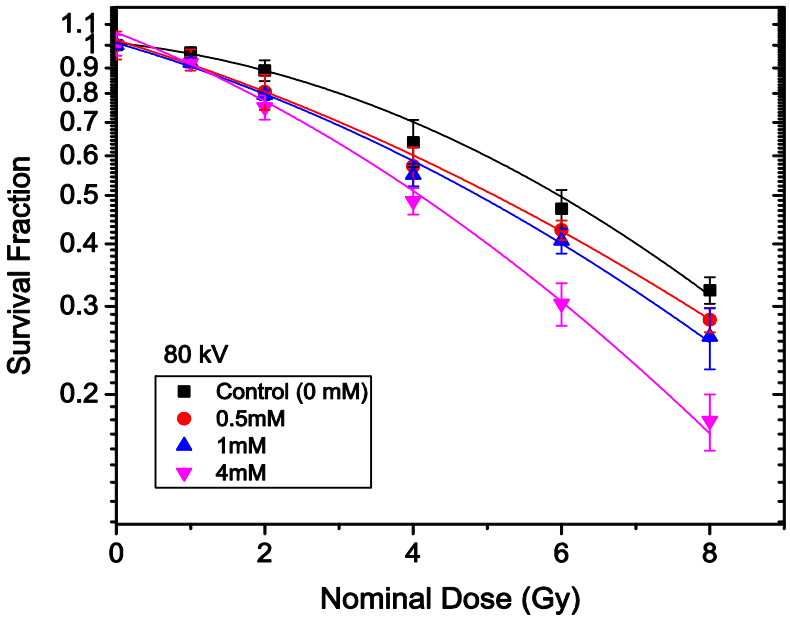

Figure 6-9: Cells survival fractions curves for HaCaT cell line employing MTS assay with various concentrations of TiO_2 NPs irradiated with 80 kV X-rays from SXRT machine. The errors are standard error mean from three independent experiments (mean ± SEM, n=3). The curves are fitted with linear quadratic model and DEF was obtained at 80% survival.

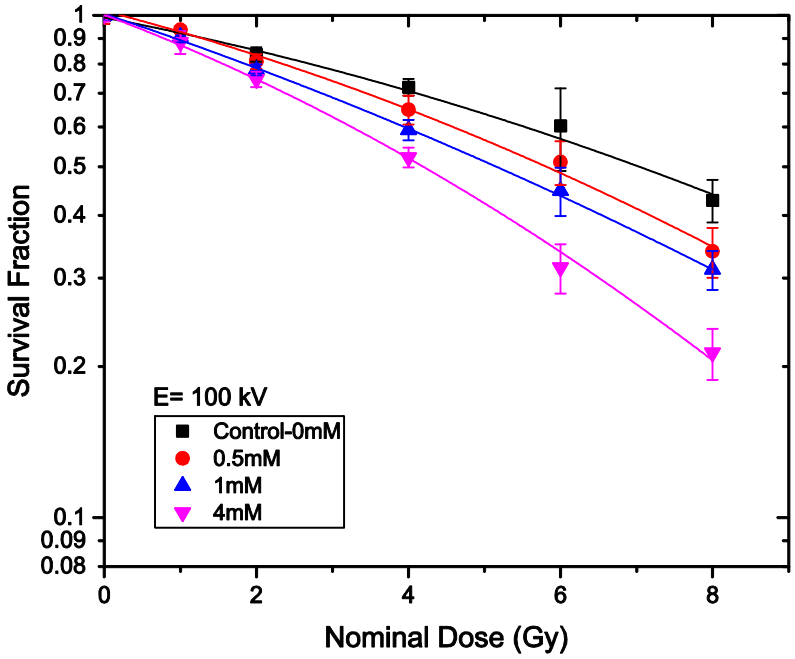

Figure 6-10: Cells survival fractions curves for HaCaT cell line employing MTS assay with various concentrations of TiO_2 NPs irradiated with 100 kV X-rays from SXRT machine. The errors are standard error mean from three independent experiments (mean ± SEM, n=3). The curves are fitted with linear quadratic model and DEF was obtained at 80% survival.

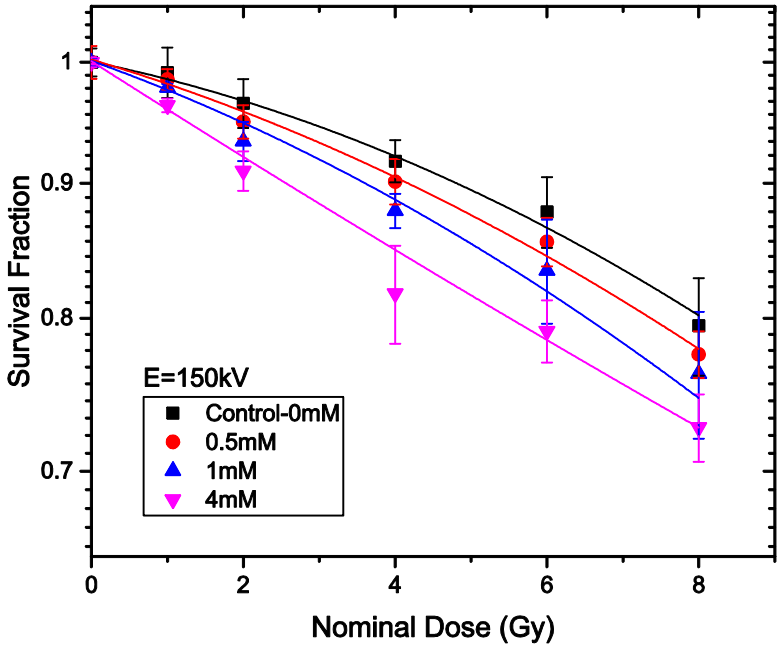

Figure 6-11: Cells survival fractions curves for HaCaT cell line employing MTS assay with various concentrations of TiO_2 NPs irradiated with 150 kV X-rays from SXRT machine. The errors are standard error mean from three independent experiments (mean ± SEM, n=3). The curves are fitted with linear quadratic model and DEF was obtained at 80% survival.

The results indicate that the DEF increases with reducing X-ray energy at kV ranges. The other observation is, with increasing the concentrations of TiO_2 NPs, the DEF is increased and the maximum is at 4 mM. The measured DEFs for 80, 100 and 150 are 1.68, 1.37 and 1.12 respectively at 4 mM (i.e. 68, 37 and 12% dose enhancement). These measurements demonstrate that radiosensitisation was observed to be highest at 80 kV with all the concentrations of TiO_2 NPs. **Figure (6-12)** shows the DEF versus the applied X-ray beam energies at different concentrations of anatase amine functionalised TiO_2 NPs.

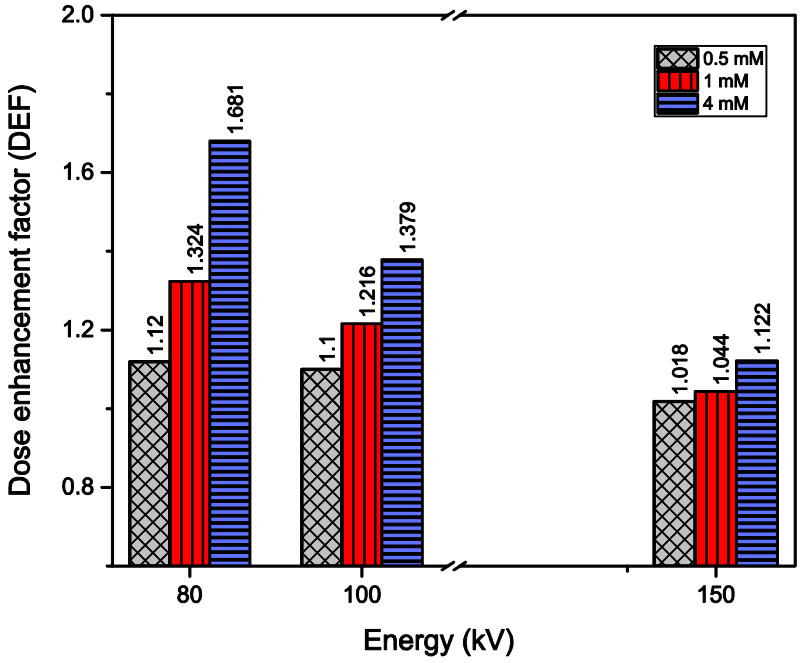

Figure 6-12: DEF comparison of various concentrations of TiO_2 NPs at different kV X-ray beams.

Therefore, for low energy X-ray radiotherapy beams, the main focus was on using 80 kV beam at radiation doses of 0-8 Gy to obtain the DEFs for *in vitro* studies. HaCaT and DU145 cells lines were used to investigate the radiosensitivity effects of anatase amine functionalised TiO_2 NPs at concentrations of 0.5, 1 and 4 mM. Clonogenic and MTS assays were employed for determination of the DEF. Results indicates that there are significant radiosensitisation with TiO_2 NPs concentration. The DEFs for HaCaT cell line with MTS assay are 1.21, 1.57 and 1.70, whereas with clonogenic assay are 1.17, 1.34 and 1.56 for 0.5, 1 and 4 mM concentrations of TiO_2 NPs, respectively. For DU145 cell line, the DEFs for the same concentrations with MTS assay are 1.27, 1.45 and 1.77 while for clonogenic assay are 1.21, 1.40 and 1.68, respectively. The survival curves with and without TiO_2 NPs are displayed in **Figures (6-13) to (6-16),** which shows the effects of TiO_2 NPs concentrations.

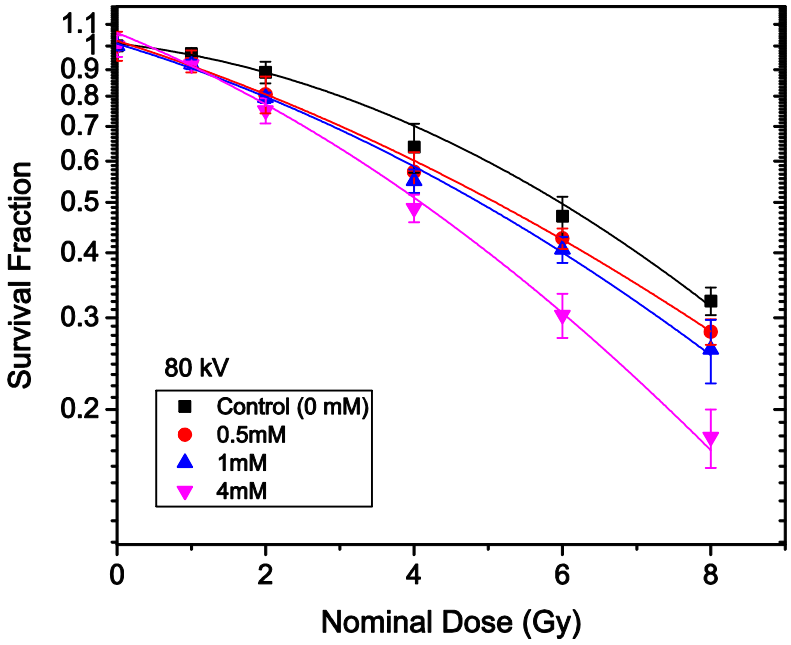

Figure 6-13: Cells survival fractions curves for HaCaT cell line employing MTS assay with various concentrations of TiO_2 NPs irradiated with 80 kV X-rays from SXRT machine. The errors are standard error mean from three independent experiments (mean ± SEM, n=3). The curves are fitted with linear quadratic model and DEF was obtained at 80% survival.

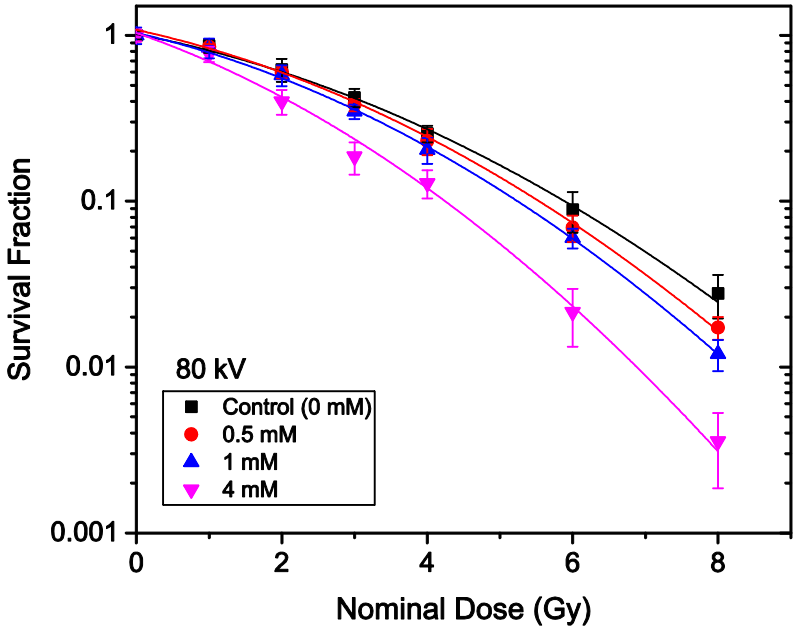

Figure 6-14: Cells survival fractions curves for HaCaT cell line employing clonogenic assay with various concentrations of TiO_2 NPs irradiated with 80 kV X-rays from SXRT machine. The errors are standard error mean from three independent experiments (mean ± SEM, n=3). The curves are fitted with linear quadratic model and DEF was obtained at 80% survival.

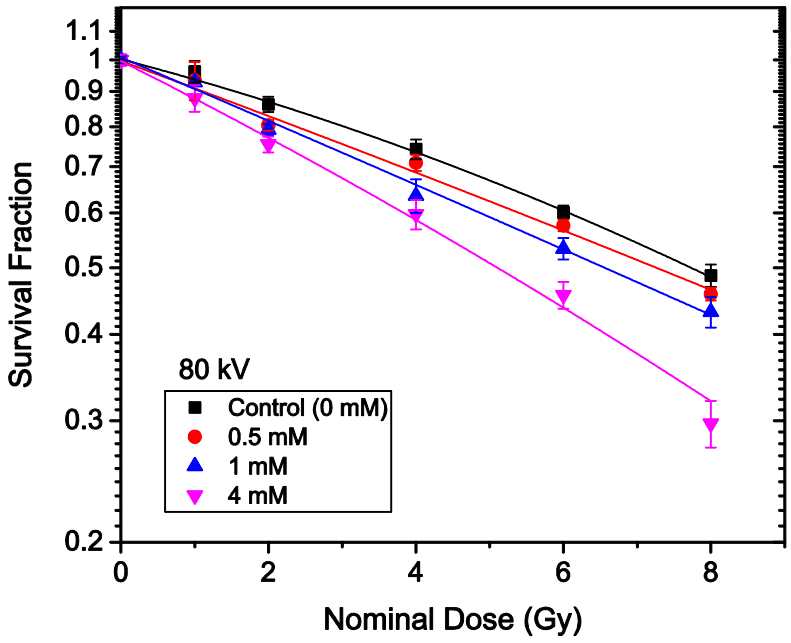

Figure 6-15: Cells survival fractions curves for DU145 cell line employing MTS assay with various concentrations of TiO_2 NPs irradiated with 80 kV X-rays from SXRT machine. The errors are standard error mean from three independent experiments (mean ± SEM, n=3). The curves are fitted with linear quadratic model and DEF was obtained at 80% survival.

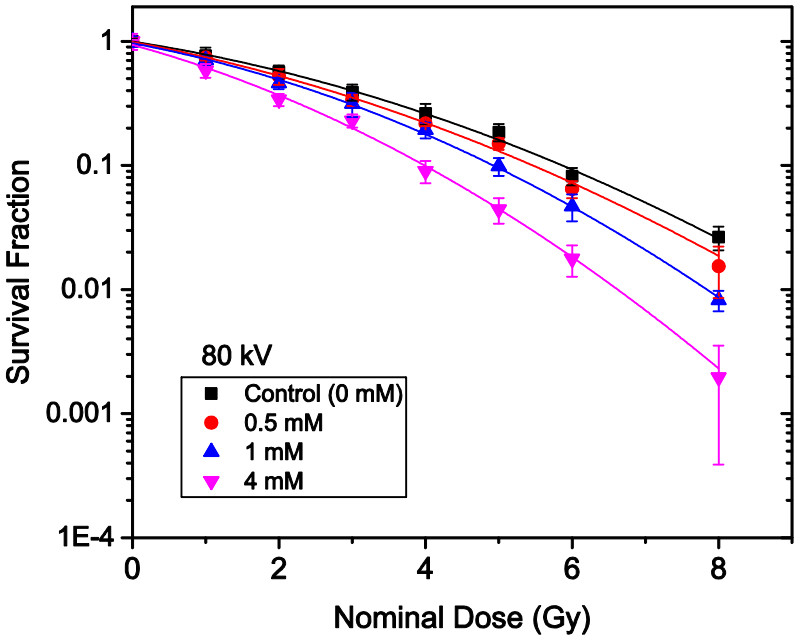

Figure 6-16: Cells survival fractions curves for DU145 cell line employing clonogenic assay with various concentrations of TiO_2 NPs irradiated with 80 kV X-rays from SXRT machine. The errors are standard error mean from three independent experiments (mean ± SEM, n=3). The curves are fitted with linear quadratic model and DEF was obtained at 80% survival.

6.1.3.2 External MV X-ray radiotherapy

Similar method described with kilovoltage as in previous section was repeated to measure the radiosensitivity of amine functionalised TiO_2 NPs for *in vitro* with 6 MV X-ray beams. DEFs for HaCaT cell line with MTS assay are 1.09, 1.19 and 1.50, whereas with clonogenic assay are 1.13, 1.18 and 1.37 for 0.5, 1 and 4 mM concentrations of TiO_2 NPs, respectively. For DU145 cell line, the DEFs for the same concentrations with MTS assay are 1.14, 1.26 and 1.67 while for clonogenic assay are 1.10, 1.19 and 1.43, respectively. Results revealed significant radiosensitisation of ~ 50-67 % following the MTS assays and 37-43 % from the clonogenic assays at TiO_2 NPs concentration of 4 mM. The biological effects on both types of cells by TiO_2 NPs utilising external megavoltage X-ray beams are displayed in **Figures (6-17) to (6-20)**.

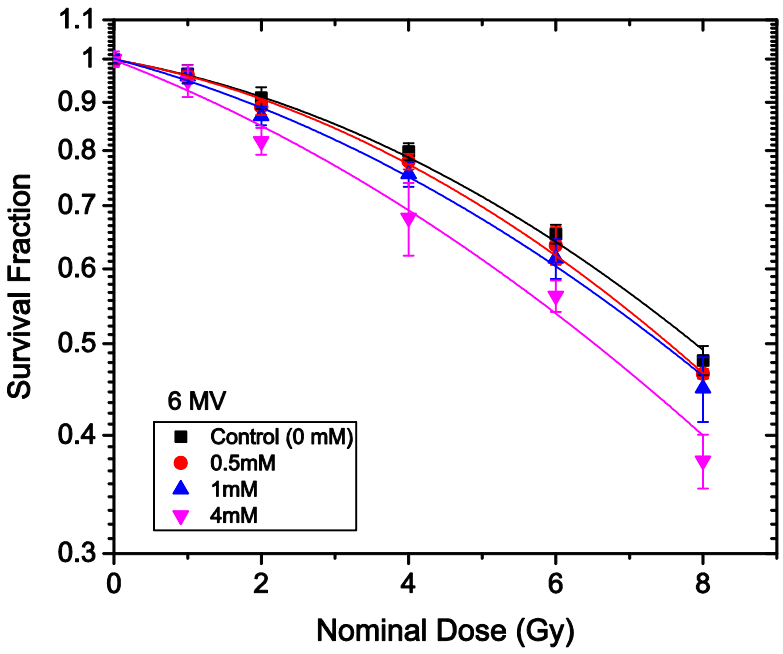

Figure 6-17: Cells survival fractions curves for HaCaT cell line employing MTS assay with various concentrations of TiO_2 NPs irradiated with 6 MV X-rays from LINAC machine. The errors are standard error mean from three independent experiments (mean ± SEM, n=3). The curves are fitted with linear quadratic model and DEF was obtained at 80% survival.

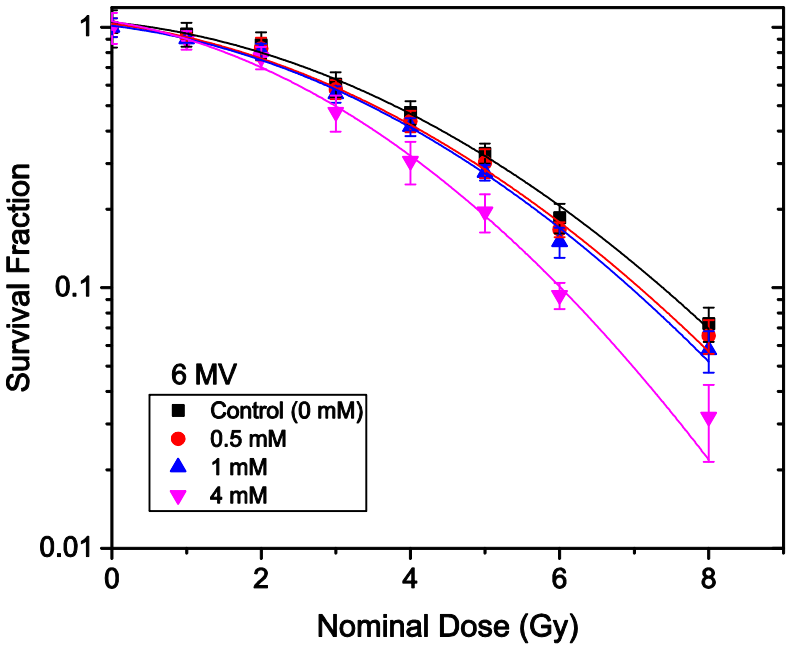

Figure 6-18: Cells survival fractions curves for HaCaT cell line employing clonogenic assay with various concentrations of TiO_2 NPs irradiated with 6 MV X-rays from LINAC machine. The errors are standard error mean from three independent experiments (mean ± SEM, n=3). The curves are fitted with linear quadratic model and DEF was obtained at 80% survival.

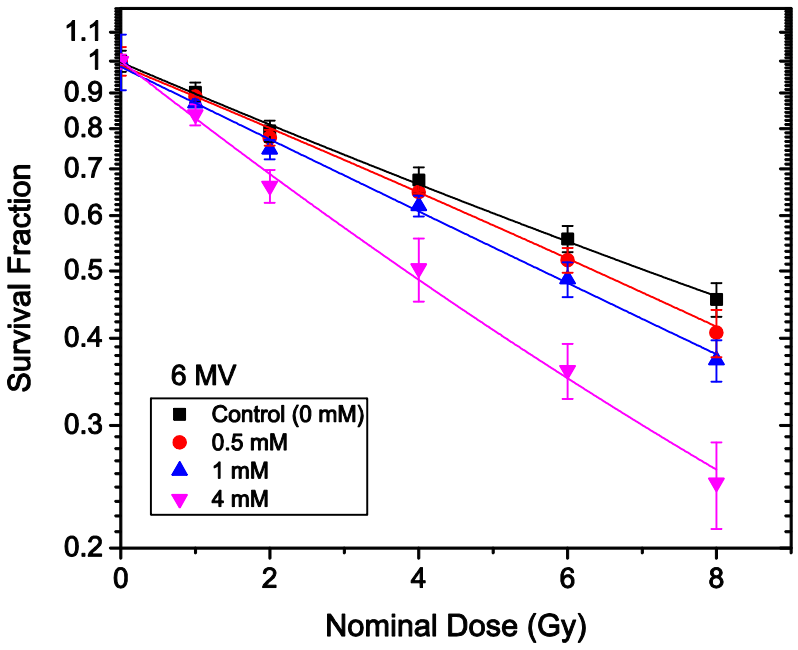

Figure 6-19: Cells survival fractions curves for DU145 cell line employing MTS assay with various concentrations of TiO_2 NPs irradiated with 6 MV X-rays from LINAC machine. The errors are standard error mean from three independent experiments (mean ± SEM, n=3). The curves are fitted with linear quadratic model and DEF was obtained at 80% survival.

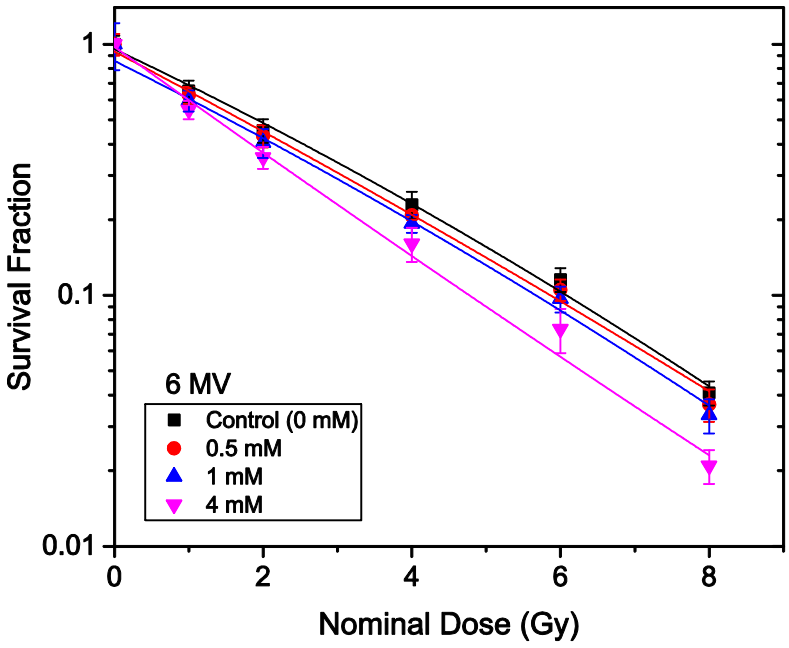

Figure 6-20: Cells survival fractions curves for DU145 cell line employing clonogenic assay with various concentrations of TiO_2 NPs irradiated with 6 MV X-rays from LINAC machine. The errors are standard error mean from three independent experiments (mean ± SEM, n=3). The curves are fitted with linear quadratic model and DEF was obtained at 80% survival.

The results of DEFs value obtained from the cell survival curves at 80% survival using equation (3-4) at both kV and MV X-ray beams with HaCaT and DU145 cell lines indicates that the calculated dose enhancement by MTS assay are higher than that measured by clonogenic assay as tabulated in **Table (6-2)**.

Table 6-2: DEFs for TiO_2 NPs for *in vitro* studies at 80 % cell survival.

Energy	Phantom-*in vitro* study & assay type		TiO_2 NPs concentration (mM)		
			0.5 mM	1 mM	4 mM
80 kV	PRESAGE®		1.12	1.40	-------
	HaCaT	MTS	1.21	1.57	1.70
		Clonogenic	1.17	1.34	1.56
	DU145	MTS	1.27	1.45	1.77
		Clonogenic	1.21	1.40	1.68
6 MV	PRESAGE®		1.04	1.03	-------
	HaCaT	MTS	1.09	1.19	1.50
		Clonogenic	1.13	1.18	1.37
	DU145	MTS	1.14	1.26	1.67
		Clonogenic	1.10	1.19	1.43

6.1.4 Radiobiological parameters of radiosensitivity

Comparison the shape of the cell survival curves in **Figures (6-13) to (6-20)** qualitatively demonstrate that there are more cell killing by irradiation with the presence of anatase amine functionalised TiO_2 NPs compared to the control (without TiO_2 NPs) and the number of killed cells will increase as the concentration of NPs increase. In addition, the type of cells, X-ray energy beams and the type of assay used affects cell surviving by irradiation which is clearly visualized from the different shapes of the cell survival curves. Radiobiological models are typically utilized for quantitatively describing the shape of the cell survival curves and the most widely recognized model is the linear quadratic model. In this study, the experimental data plotted as cell survival curves are fitted by a linear quadratic

model. In this model, two components; the linear part and the quadratic part are employed to describe the DNA damage by the ionising radiations. The linear part is represented by a parameter called alpha (α) while the quadratic part, beta (β). These two terms have been explained in details in chapter one **(Section 1.3.2)**. Tabulated α and β values as parameters fitting the cell survival curves for all beam energies, TiO_2 NPs concentration and assays are displayed in **Table (6-3)**. It is noted that α value tends to increase with the inclusion of TiO_2 NPs much more significantly than β. For example, the cell survival curve for DU145 cell line at 6 MV analysed with clonogenic assay shows that α value for 0, 0.5, 1 and 4 mM are 0.0899, 0.0943, 0.1012 and 0.1578 respectively. The β values and at the same conditions are 0.0134, 0.0162, 0.0194 and 0.022 respectively, which does not show significant changes with the increase of TiO_2 NPs concentrations.

Table 6-3: The radiobiological linear (α) and quadratic (β) values extrapolated from cell survival curves of HaCaT and DU145 cell lines at various concentrations of TiO_2 NPs employing both MTS and clonogenic assays.

Energy	Assay Type	Cell Type	TiO_2 NPs Concentration (mM)							
			Control - 0 mM		0.5 mM		1 mM		4 mM	
			α	β	α	β	α	β	α	β
80 kV	MTS	HaCaT	0.0159	0.00592	0.04526	0.00308	0.04317	0.00396	0.05804	0.00529
		DU145	0.02848	0.00141	0.03562	0.0007784	0.05205	0.0007392	0.04305	0.00256
	Colony	HaCaT	0.10176	0.01228	0.10175	0.1539	0.1037	0.01739	0.18105	0.0162
		DU145	0.08997	0.01346	0.09434	0.01621	0.10122	0.01948	0.15786	0.02202
6 MV	MTS	HaCaT	0.01329	0.00314	0.01393	0.00344	0.02056	0.00268	0.02982	0.00248
		DU145	0.04402	0.0002346	0.04669	0.0001418	0.0517	5.925E-05	0.07538	0.0001592
	Colony	HaCaT	0.02926	0.01465	0.03887	0.01421	0.04537	0.0143	0.07586	0.01496
		DU145	0.13643	0.00381	0.1507	0.00265	0.16133	0.00184	0.17157	0.00347

6.1.5 Generation of ROS by TiO_2 NPs

The 2',7'-Dichlorofluorescin diacetate (DCFDA) (Sigma-Aldrich Pty. Ltd., St Louis, Mo, USA) reagent, a fluorogenic dye that measures primarily hydroperoxide ROS activity [201], was used to detect the reactive oxygen species (ROS) generated from anatase amino functionalised TiO_2 NPs following the method described in chapter three **(Section 3.3.8)**. **Figure (6-21)** shows the ROS detected after 6 MV beam exposure of aqueous solutions without (control) and with TiO_2 NPs as measured using DCFDA. The PBS+DMSO solution was used as a negative control to show that there was no contribution from this solution to the ROS generated. The results clearly indicate that ROS generation was dependent on TiO_2 NPs concentrations. This illustrates that biochemical effects were a key factor for enhancing the cellular radiosensitivity, which would be an important consideration in radiosensitivity measurements. This is just a proof for the dose enhancement measured with high-energy beams where MC simulations have shown that there is no DE [202].

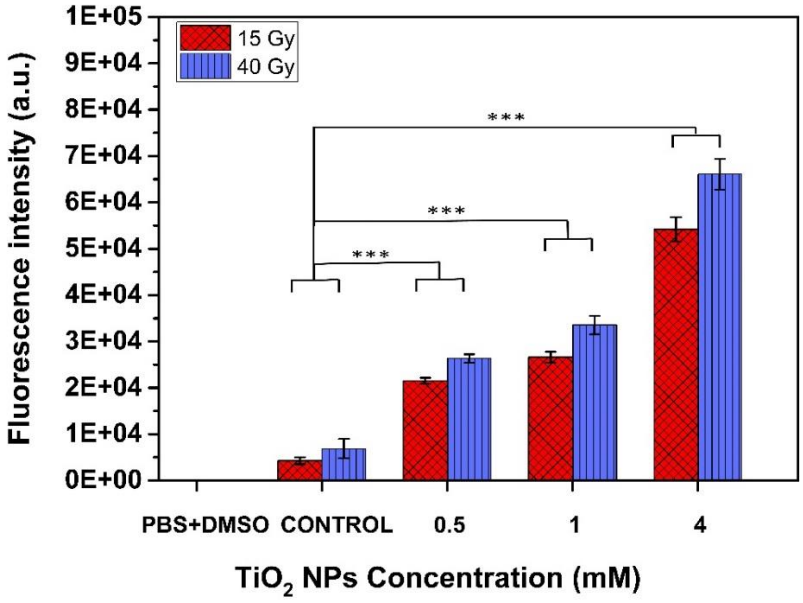

Figure 6-21: ROS generated from TiO_2 NPs, detected by DCFDA after exposed to 6 MV X-ray beam at radiation doses of (15 and 40) Gy. Results are considered to be statistically significant at p values of less than 0.05 (* p < 0.05, ** p < 0.01, *** p < 0.001).

6.2 Discussion

In this section, the reasons behind the main findings will be discussed starting with the association of amine functionalised TiO_2 NPs with cells where TiO_2 NPs were found to be localised inside the cytoplasm of the cells. Furthermore, the amine functionalised TiO_2 NPs were found to be non-toxic to cell up to 8 mM concentration. Finally, the amine functionalised TiO_2 NPs have shown to work as a radiosensitiser agent for *in vitro* studies. In other words, the results just displayed and presented in the previous sections will be discussed in this part;

6.2.1 TiO_2 NPs association with cells

The increased side scatter observed in the flow cytometry for amine functionalised TiO_2 NPs exposed cells as shown in **Figures (6-1) to (6-4)** implies close association (which means particles are either in the cells or attached to them) between the NPs and cells after incubation for about 24 hours. These data does not necessarly indicate uptake. Nevertheless, the NPs will still be in close proximity to the nucleus and intracellular uptake may not be an absolute necessity for radiation dose enhancement [203]. Other *in vitro* studies do indicate that TiO_2 NPs can be internalised by various cell lines [192, 204-205], and it has been demonstrated that in the absence of cytotoxicity, cells can effectively absorb TiO_2 NPs to quite high concentrations [192, 206].

The light microscopy utilised to study the amine functionalised TiO_2 NPs distribution inside the cells post 24 hours incubation revealed that these NPs are clustered in subcellular components in the cell's cytoplasm and appears as a black dots as shown in **Figure (6-5)**.

Other investigations about cellular uptake of TiO_2 NPs have found that, TiO_2 NPs were internalized by both U373 and C6 cells post 24 h of treatment, and were located in large and small vesicles in the cytoplasm. However, they did not observe intracellular location of solid core NPs in cell organelles [207].

In Summary, this study and other researches findings stated above have demonstrated that TiO_2 NPs are mostly aggregated in the perinuclear regions surrounding the nucleus; however, these investigations clearly have shown that there were no NPs inside the nucleus.

6.2.2 Cytotoxicity of TiO_2 NPs

The cytotoxicity results presented in this chapter illustrate that the amine functionalised TiO_2 NPs were cytocompatible up to concentrations of 4 and 8 mM post 72 and 24 h respectively as shown in **Figure (6-6) and (6-7)**. When the concentration was increased up to 30 mM, the cells viability slightly reduced to a maximum of 22% as shown in **Figure (6-8)**. Therefore, the concentration ranges of NPs used *in vitro* in this study (preferable maximum of 4 mM) were suitable for studying radiosensitisation effects without confounders. Conversely, it is not possible to exceed a 1 mM concentration with heavy atoms based NPs such as Au, Ag, Pt, Bi etc…[109, 206]. This finding is in agreement with other studies documented in the literature which have shown that titanium dioxide and titanium nanotubes can penetrate human glioblastoma cells in vitro and stay in the cytosol for over 10 days without inducing cytotoxicity or decreasing DNA repair efficiency after irradiation with a linear accelerator [140, 192, 206].

However, it should be noted that the cytotoxicity of TiO_2 NPs depends on many factors such as crystal structure, the NPs size, surface charge, and on cell type. Regarding the

crystal structure, a study demonstrates that both anatase and rutile TiO_2 NPs has no indication to alter the biological system of pulmonary cells [208] . While others have compared the DNA damaging effects caused by anatase and rutile TiO_2 NPs of 200nm size (we used 30 nm) on human bronchial epithelial cells and they demonstrate a significant enhance in the generation of hydrogen peroxide in cells treated with rutile TiO_2 NPs but not by anatase TiO_2 NPs if incubated in the dark [209]. A sample containing anatase and rutile with equal surface area shows higher toxicity to the cells than the pure anatase samples [209]. In general, studies have shown that cells take up spherical NPs in the range of 20 to 50 nm in highest rates compared to the other NPs sizes; however, this is not the case for all cell types [210]. Furthermore, most NPs with positive surface charge have advantage of higher cellular uptake and disadvantage of greater cytotoxicity in cells which causes plasma-membrane disruption and apoptosis [210, 211]. TiO_2 NPs synthesised as described in this research showed very low toxicity for the cells investigated.

6.2.3 Radiobiological analysis of radiosensitisation

Figures (6-13) to (6-20) show clearly that cells incubated with TiO_2 NPs are more sensitive to radiations by having the slope of the curves shortened. There are many ways of indicating the levels of dose enhancements using these curves. The one used in this thesis is by fitting the survival curves with linear quadratic model and extrapolate the DEFs at 80% survival using equation (6-1). Radiobiological analysis of linear (α) and quadratic (β) parameters derived from the cell survival curves using radiobiological linear quadratic model shows that α significantly increase with the increase of the TiO_2 NPs concentration; however, β values change insignificantly with the concentration of TiO_2 NPs **(Table 6-3)**. Since α is the probability of an interaction between single electron ejected as a result of absorbing X-ray

and two chromosomes breaks [16], hence this is an indication of an enhancement in double strand DNA breaks as a consequence of inclusion TiO_2 NPs. Accordingly, the DEF results **(Table 6-2)** obtained for phantom study and from extrapolation of the cell survival curve for *in vitro* study are in an excellent agreement with the above hypothesis (α increase with the TiO_2 NPs concentration increase).

6.2.4 Radiosensitazation induced by TiO_2 NPs

The results of this study confirm that radiosensitisation induced by amine functionalised TiO_2 NPs on HaCaT and DU145 cell lines at 80 kV is greater than at 6 MV for X-ray energy beams as clearly can be seen in **Table (6-3),** and this supports the work of a large number of investigators for other types of NPs [104, 106 and 109]. The primary difference in the effect of these two energies is the type of radio-biological interaction. At low energies (80 kV), the dominant process of interaction is the photoelectric effect (PE), i.e., absorption of an incident X-ray photon. While at high energies (6 MV), the interaction of X-ray photons is mainly through Compton scattering. Moreover, it is well known that the probability for the photoelectric effect depends strongly on the atomic number (Z). Thus it is anticipated that at 80 kV (where PE is dominant), the interaction of X-ray photons with Ti atoms in the TiO_2 NPs will be much higher than the interaction with the tissues. The effective atomic number of TiO_2 is 18.49 and that of tissue is about 7.4 that were calculated using Mayneord equation (equation 5-1). Therefore, taking the probability of interaction via PE to be dependent on Z^3, the ratio of the probability of PE interaction with TiO_2 NPs compared to that with tissue will be about 15.6. Even though the concentration of Ti is relatively low, this extremely high affinity for the PE interaction could cause a greatly increased interaction probability and lead to the generation of copious secondary electrons [14]. This generation

electrons are reflected in the results of this study, which indicates clearly in both the phantom **(Chapter Five)** and *in vitro* studies that the dose enhancements caused by the inclusion of the TiO_2 NPs were much higher at low energies (80 kV) compared to those measured at high energies (6 MV) [192].

The other point of interest in the results is the observed differences in dose enhancement between the PRESAGE® dosimeter **(Chapter Five)** and cell culture studies, especially at high energies (6 MV). The addition of TiO_2 NPs slightly increased the physical density of the systems, while reducing the density of the free electrons – this is due to the TiO_2 NPs free electron density being about 2.86×10^{23}, whereas in tissue it is 3.34×10^{23}. This will result in a slight reduction in the density of free electrons when TiO_2 NPs are present in the target. Thus in general, there should be no significant physical dose enhancement with the 6 MV beam and this is what the PRESAGE® dosimeter study confirmed.

There is clearly some disagreement between the phantom "PRESAGE® dosimeters" and *in vitro* studies with regards to the level of radiosensitisation. The cell studies showed higher enhancements in radiosensitivity than the phantom dosimeters (Compare figures related to **section (5.1.4.2)** with **section** (**6.1.3.2)**). This can be attributed to the PRESAGE® dosimeters being only able to detect electron free radicals directly generated (the physical effect) and being not suited to the generation of ROS due to a lack of free water molecules. Conversely, cells can be affected by a host of the biochemical events, such as ROS generation, which are additional stresses above those, generated by secondary electrons, and thus results in greater radiosensitivity. This specific point was illustrated in this study through three sets of experiments measuring ROS levels generated by irradiations in the presence and absence of TiO_2 NPs as shown in **Figure (6-21)**. The common ROS generated by TiO_2 NPs when exposed to ionizing radiation are superoxide (O_2^-), hydroxyl radical (·OH), hydrogen peroxide (H_2O_2), and singlet oxygen ($^1O_2$) [138]. As the fluorescence probe (DCFDA) does

not discriminate against different ROS, it is not possible to identify a specific ROS that is responsible for the produced oxidative stress observed in these studies. These results are in agreement with previously documented studies which have shown that upon irradiation, anatase TiO_2 NPs generate free radicals that facilitate the spontaneous generation of reactive oxygen species (ROS), which can damage nucleic acids (e.g., DNA) [138, 139, 188, 192 and 212]. It has also been reported that increasing the mole fraction of oxygen atoms by inclusion of Ti-peroxide can also improve radiosensitisation efficiency [213]. The explanation of X-ray interaction with TiO_2 NPs inside a cell and then resulting in the production of free radicals and ROS via physical and biochemical effects was schematically shown in chapter one **(Figure (1-12) in section 1.3.2)**.

The variations with maximum of 17% in DEFs observed between clonogenic and MTS assays at 80 kV and 6 MV energies for the similar conditions (i.e. same type of cells, concentration of NPs and energy) can be attributed to few reasons. Firstly, it could be due to number of cells plated for example, with MTS assay, the control plate of each HaCaT and/or DU145 cells were seeded at density of 3000 cells/well, whereas for clonogenic assay, the control plates were seeded at densities of 150, 250 cells/well for HaCaT and DU145 respectively **(Table 3-1)**. Secondly, these variations could be due to the proliferation duration after irradiation, which for MTS assay was only 3 days while for clonogenic assay was 14 days. However, the slight variations in DEFs results observed between the two types of cells with similar assay could be due to the difference in their response to the radiations and to their uptake of the TiO_2 NPs.

The findings of radiosensitisation show that TiO_2 NPs improve the efficiency of dose delivery, and demonstrate the potential of TiO_2 NPs for the enhancement of clinically relevant kilovoltage (kV) and megavoltage (MV) radiotherapy beams which has implications for future radiotherapy treatments [192]. Recently, techniques such as kilovoltage X-ray

intraoperative radiotherapy are increasingly used in breast cancer treatment by radiations; therefore, improvement to therapeutic effects generated by TiO_2 NPs also could be highly useful for such treatments [214] also electronic brachytherapy [215]. In the cases of employing extremely high dose rates such as Myofascial Release Techniques (MRT) can also benefit from the addition of TiO_2 NPs in order to reduce the employed high dose [216].

In conclusion, these results clearly demonstrate that with the inclusion of TiO_2 NPs in the target, same fraction of cells were destroyed with lower radiation doses compared to the case of absence of TiO_2 NPs. This means if TiO_2 NPs are added to the target, when kilovoltage and megavoltage X-rays are used for treatment, an external dose reduction can be achieved to deliver the same local control as without the inclusion of TiO_2 NPs. This reduction of radiation dose delivered to the target results in obviously reducing the dose to the surrounding healthy tissue during treatment which is of primary concern in all radiotherapy treatment procedures.

CHAPTER SEVEN

Two-Dimensional Scanning of PRESAGE® Dosimetry Using UV/VIS spectrophotometry and its Potential Application in Radiotherapy

7.1 Summery

The purpose of this investigation was to provide a high-resolution 2-D scanning feasibility study for PRESAGE® dosimeters using UV/VIS spectrophotometry. Previously the light absorbance of PRESAGE® has only been made at a single point using UV/VIS spectrophotometry. The CLARIOstar microplate reader can operate as a 2-D scanning UV/VIS spectrophotometer measuring the light absorbance at multiple points of a PRESAGE® dosimeter. Water equivalent PRESAGE® dosimeters were fabricated in a rectangular shape and were irradiated with 6 and 18 MV X-ray beams using a medical linear accelerator. The optical density values of the PRESAGE® dosimeters were measured pre and post-irradiation using a CLARIOstar microplate reader. Depth dose curves and beam profiles were validated against ionisation chamber measurements. The agreement between the two dose measuring devices is well within experimental uncertainties. This investigation demonstrated that depth dose curves and beam profiles can be measured with high resolution in 2-D for megavoltage X-ray beams with PRESAGE® dosimeters using UV/VIS spectrophotometry. Additionally, one PRESAGE® dosimeter was also fabricated with the inclusion of an inhomogeneity to investigate the effect on the dose distribution beyond the inhomogeneity. There is also the potential to extend this method to obtain 3-D dosimetry scanning.

7.2 Introduction

Due to the current complexity in radiotherapy instrumentation, verification of radiation dose delivery as planned by the treatment planning system is challenging for

techniques such as stereotactic radiosurgery (SRS), intensity modulated radiotherapy (IMRT) and volumaetric modulated radiotherapy (VMAT) [217]. Consequently new three-dimensional (3-D) dosimetry systems such as gel and PRESAGE® dosimeter systems have been developed to potentially measure the dose distribution and/or the absolute dose delivered [218].

PRESAGE® is a 3-D solid radiochromic dosimeter fabricated from clear polyurethane resin combined with a leuco-dye and halogenated carbons [190]. These dosimeters undergo a peak radiochromatic response around 633 nm and can be read using optical CT for 3D dose distribution measurements [64] or UV/VIS spectrophotometry for single point dose measurement [164], and confocal fluorescence microscopy for high resolution [219].

The advantages of PRESAGE® dosimeters over other dosimeters are that they are solid, not sensitive to oxygen, easy to handle, sub-mergeable in water, can be fabricated to any size or shape and optically clear which allows light to pass through with minimum artifacts. In addition PRESAGE® can be formulated to be radiologically tissue or water equivalent [62].

The conventional technique of reading PRESAGE® is with a UV/VIS Spectrophotometer [65]. The main limitation of this technique is the fact that the optical density (OD) is a measure per single point through the whole of the cuvette. Other methods to read PRESAGE® are Optical Computed Tomography (OCT) and laser fluorescence confocal microscopy (LFCM). OCT allows for 3-D dose measurements however the optical CT scanner, reconstruction software and chemicals needed for optical compatibility can be quite expensive and time consuming. Spectral artifacts produced from a mismatch in the refractive index matching fluid and edge artifacts from the edges of the dosimeters are also drawbacks of OCT [75]. LFCM can take high resolution 2-D images at different planes through a sample to produce a 3-D dose distribution however an expensive microscope and expert user are

needed to perform the scanning. The field-of-view is also limited (< 3 mm) and is better suited for small fields.

Radiochromic films, such as gafchromic films, are normally used as dosimeters for two dimensional (2-D) radiation dosimetry measurements in clinical radiation oncology. However, these films have some limitations and drawbacks that affect the accuracy of OD measurements. Variation may arise in the OD from non-uniformity of the scanner light source and light scattering with respect to the scan line direction as well as orientation with the flatbed scanner. In addition, consecutive scans may increase the scanner temperature and change the OD response of the film [220]. Radiochromic films are energy independent in the photon energy range 100 keV to 18 MeV but below 100 keV the absorbed-dose energy dependence is no longer constant which can be attributed to changes in the mass energy absorption coefficient ratios of water to film materials, as well as an increase in the number of electrons being created and scattered in the central surface layer of the film [221]. In contrast to PRESAGE® dosimeters the radiochromic film can be immersed in water for only a very short period, therefore most experiments using radiochromic films have to be conducted using solid water phantoms with air pockets and gaps between the film sheets and the blocks of solid water contributing to the dose uncertainty. High-density heterogeneity experimental dose assessments have been studied using thermoluminescent detectors (TLDs) and were found to be an appropriate choice for measuring the absorbed dose in bone [222]. However the TLD configuration is unrealistic from clinical perspective since solid water was used which leads to the existence of air gaps between its layers and can contribute to dose distribution uncertainty. Similarly dose distributions through inhomogeneities can be investigated with radiochromic film but solid water needs to be used. The PRESAGE® dosimeter however can be manufactured as a dosimeter with inhomogeneities, **Figure (7-1)**.

This configuration allows the investigation of depth and profile dose distribution for low-density in-homogeneities in a sample that can be submerged in water.

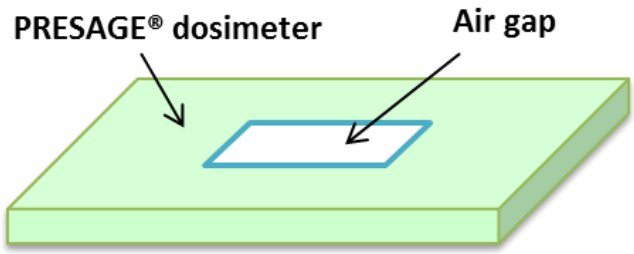

Figure 7-1: Inhomogeneous PRESAGE® dosimeter.

PRESAGE® dosimeters also have better radiological properties than TLDs, and are similar to water, solid water and soft tissue [222-225]. **Table (7-1)** compares radiological properties and the effective atomic number (Z_{eff}) using the Mayneord equation (5-1) [14]. However calculations based on all photon energy absorption processes using the Auto Z_{eff} software [226] is plotted in **Figure (7-2)**. The Z_{eff} of the PRESAGE® dosimeters fabricated matches that of water and soft tissue compared with solid water (RW3) or LiF TLD-100 for effective energies ranging from 10 keV to 10 MeV.

Table 7-1: Mean physical density (ρ), electron density (ρ_e) and relevant effective atomic number (Z_{eff}) of PRESAGE® dosimeters fabricated in this study and gafchromic films compared to water.

Materials	ρ (Kg.m^{-3})	ρe (x10^{29}em^{-3})	Zeff
Water	1000	3.3428	7.42
PRESAGE® (Chloroform)	1045-1047	3.4348	6.62
Radiochromic films	1080-1200	-----	6.84

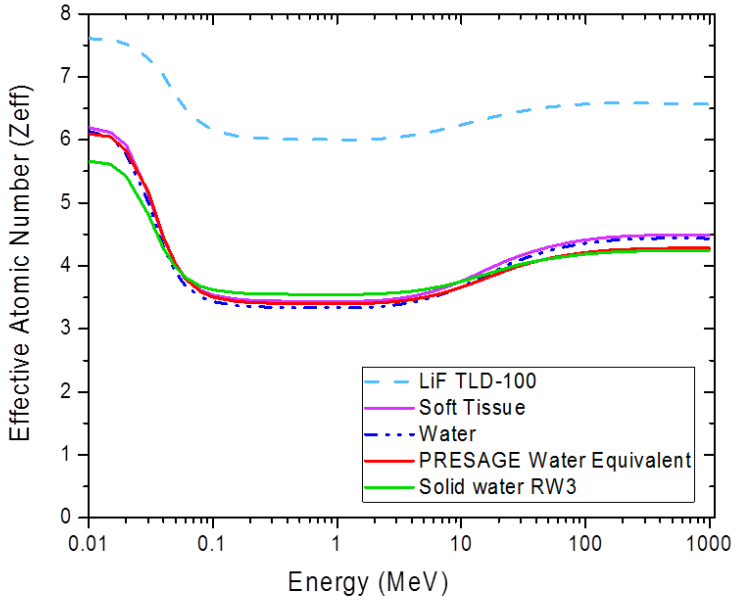

Figure 7-2: Radiological effective atomic number Zeff based on the photon energy absorption processes for water equivalent PRESAGE®, solid water (RW3) and TLDs (LiF).

In this study we have shown that a commercially UV/Vis spectrophotometer (CLARIOstar microplate reader) available in most of chemistry and biology labs can read PRESAGE® samples in 2-D within minutes with an OD accuracy of less than 1%.

7.3 Materials and Methods

7.3.1 PRESAGE® dosimeter fabrication

The PRESAGE® dosimeters used for this work were prepared with Polyurethane resin (Crystal Clear 200, Smooth-On, Easton, PA USA). The detailed fabrication procedure is stated in chapter three **(section 3.2.5)**. The fabricated dosimeters were 6 x 85.5 x 172.7 mm depth, width and length which are shown in **Figure (7-3 A)**. A PRESAGE® dosimeter with

the inclusion of an air cavity inhomogeneity was fabricated by cutting out a rectangle 25 x 35 mm in the PRESAGE® dosimeter block; **Figure (7-3 B)**. The PRESAGE® dosimeters, pre- and post-irradiation, were stored in a dark and cold (-18^{O} C) environment to avoid colour fading and or accidental exposure to external UV light [164].

7.3.2 PRESAGE® irradiation

The PRESAGE® dosimeters were irradiated with 6 MV and 18 MV energy beams using a Varian 21EX medical linear accelerator (Clinic 21EX, Varian Associates Inc., Palo Alto, CA, U.S.A.) at Alfred Health Radiation Oncology, Melbourne, Australia. The PRESAGE® dosimeters were placed in a mini water tank to provide a full scatter condition and positioned centrally on the cross-plane axis of the X-ray beam. The field size was set to 3 x 3 cm for the beam profile experiments and 10 x 10 cm for the percentage depth dose (PDD) experiments. The collimator and gantry angles were set to 0^{0} and a SSD of 100cm to the water surface was used as displayed in **Figure (7-3 C)**. A dose of 15 Gy was delivered to the dosimeters at a dose rate of 600 MU/min.

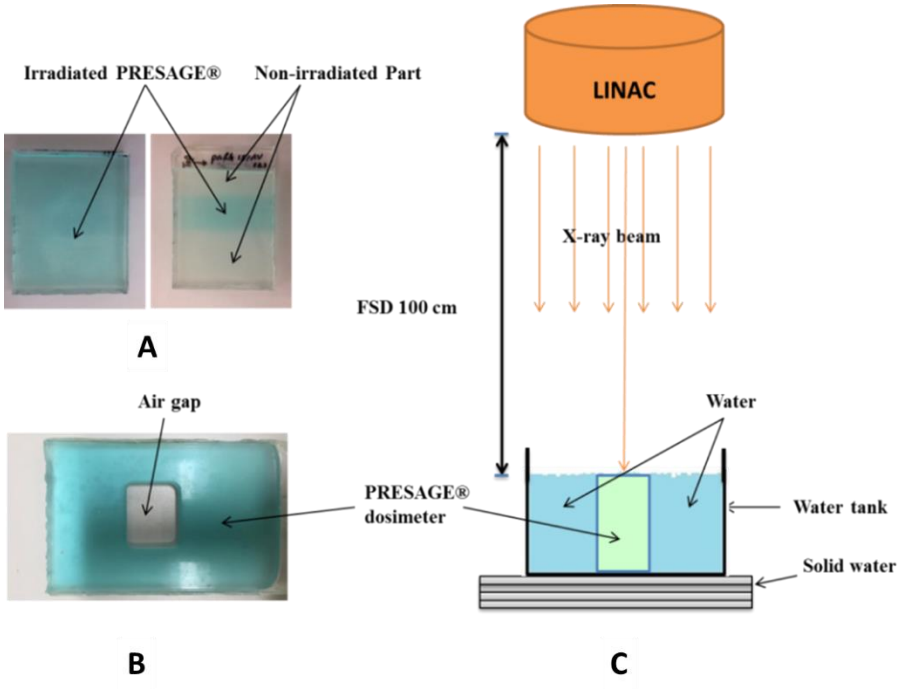

Figure 7-3: A) Samples of PRESAGE® dosimeter, B) inhomogeneous PRESAGE® dosimeter, C) Irradiation process setup. Image is not in scale.

7.3.3 Optical Density Measurements

7.3.3.1 UV/VIS spectrophotometer

The dose distributions in the PRESAGE® dosimeters were read out using a CLARIOstar microplate reader (BMG LABTECH - The Microplate Reader Company, Ortenberg, Germany) operating in the UV/VIS spectrophotometer mode. The microplate reader is an ultra-fast scanning machine capturing all wavelengths from 220 to 1000 nm with a selectable spectral resolution of 1–10 nm, in less than 1 second per point. A high-power xenon flash lamp is used as the light source and the absorbance detected with a low-noise photomultiplier tube. The optical density range is 0-4 with an accuracy of less than 1% at 2 OD [227]. An optical filter was used to specify a wavelength of 633 nm for optimum

absorbance of the PRESAGE® dosimeter and the scanning was performed at 1 mm intervals. The scan direction was in the same direction as the X-ray beam for PDD measurements and across the beam direction for beam profiles, **Figure (7-4)**.

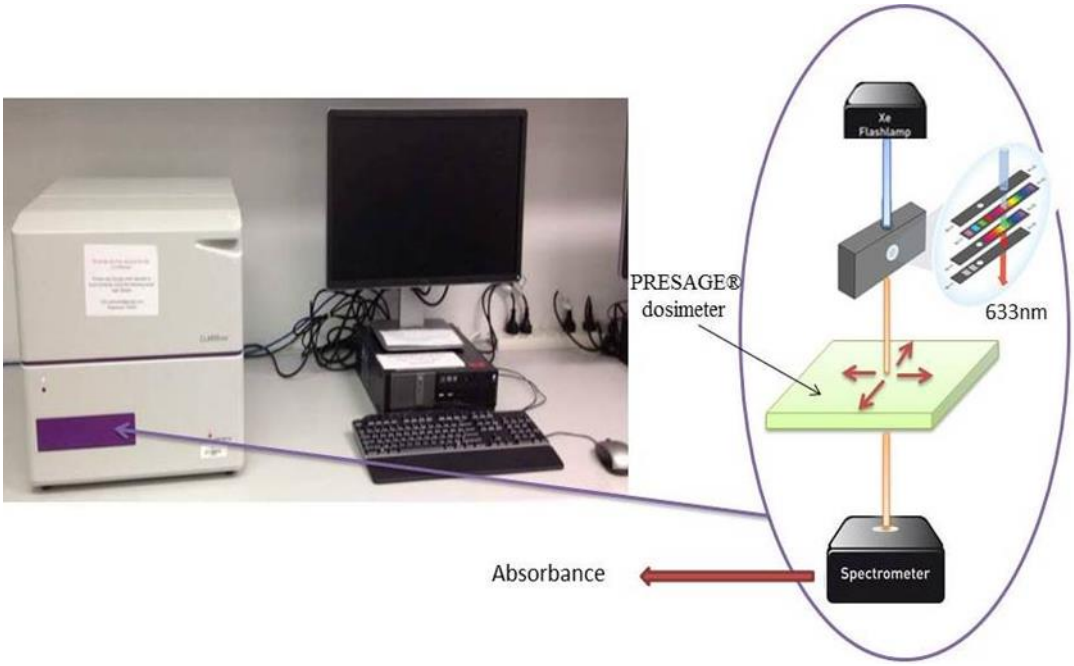

Figure 7-4: CLARIOstar microplate reader for absorbance measurement.

The absorbance, also known as the material's Optical Density (OD), was measured using equation (7-1), which is the logarithmic ratio between the intensity of monochromatic light hitting the dosimeter (I) and the intensity of that very light transmitted through the dosimeter (I_0).

$$OD = -\log \frac{I}{I_0} \quad \ldots\ldots\ldots\ldots \quad (7\text{-}1)$$

Using this method, the PRESAGE® dosimeter was scanned pre- and post- irradiation. Equation (7-2) was applied where (I_B) is the pre-irradiation intensity, (I_{irr}) is the post-irradiation intensity and (I_{blank}) is the intensity of background. The measurement of background and pre-irradiation intensity was conducted in order to eliminate artifacts caused by the plate and dosimeter non uniformity

$$OD = -\log \frac{I_{irr} - I_{blank}}{I_B - I_{blank}} \qquad \text{…….. (7-2)}$$

7.3.3.2 Ion Chamber Measurements

Ion chamber measurements were taken with an IC 13 ionisation chamber in a water phantom (Blue Phantom, IBA Dosimetry, Schwarzenbruck, Germany) with a 100 cm SSD. The chamber was aligned with the long axis of the chamber in the in-plane direction of the X-ray beam to reduce the effect of penumbra widening due to the chamber volume. A percentage depth dose (PDD) profile was taken for a 10 x 10 cm field for both 6 and 18 MV. Cross-plane profiles were taken for a 3 x 3cm field at 2.25 cm depth for 6 MV and 5 cm depth for 18 MV.

7.4 Results

The experimental results obtained from ion chamber measurements and CLARIOstar microplate reader measurements for the percentage depth dose (PDD) and profile irradiations are presented in the following sections.

7.4.1 Percentage Depth Dose (PDD) measurements

Figure (7-5 A and B) represent the experimental depth dose curves acquired using ionisation chamber and PRESAGE® dosimeters for both 6 MV and 18 MV X-ray beam energies respectively. Dose variation with depth was measured up to approximately 10 cm in the PRESAGE® dosimeter.

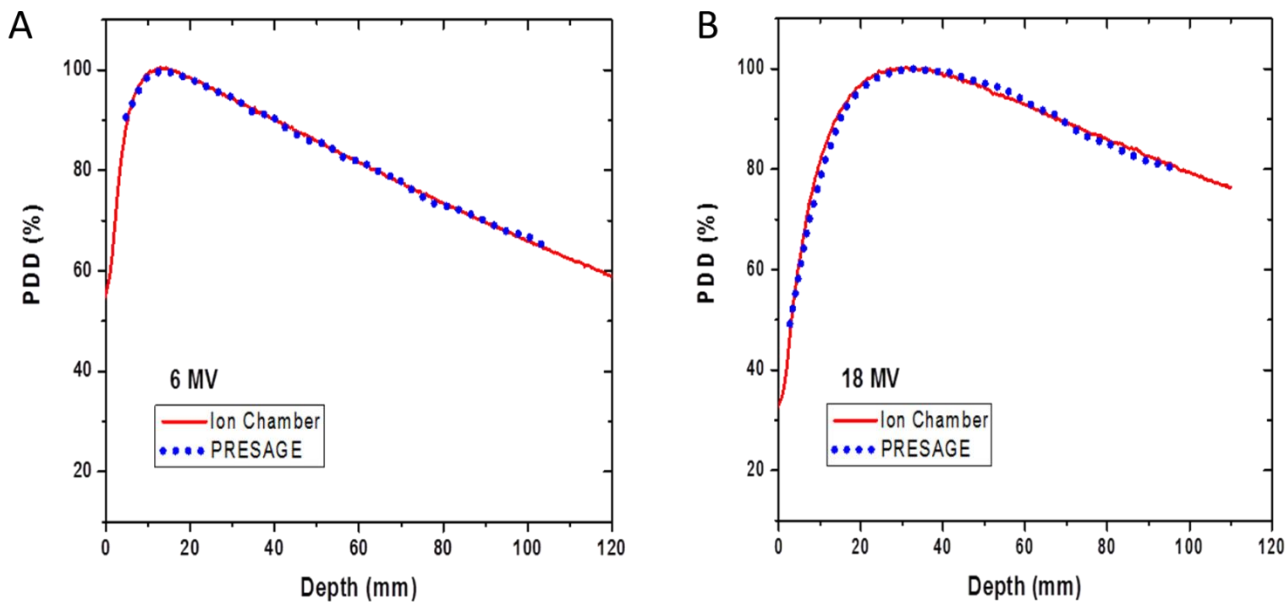

Figure 7-5: PDD curves obtained using an ionisation chamber and PRESAGE®, A) at 6 MV and, B) at 18 MV.

The shape of the PDD curve for both 6 and 18 MV beams in the PRESAGE® dosimeters is similar to the ion chamber measurements. The agreement is within 1% for 6 MV and 2% for 18 MV.

7.4.2 Beam profile measurements

Figure (7-6 A and B) shows the profile across a 3 x 3 cm beam (cross-plane direction) using an ionisation chamber and the PRESAGE® dosimeters. The profile in **Figure (7-6 A)** was taken at 2.25 cm depth for the 6 MV beam and the profile in **Figure (7-6 B)** was taken at 5 cm depth for the 18 MV beam. The 6 MV PRESAGE® profile is within 3% compared with the ion chamber measurements above the 20% of the normalised Relative Optical Density, **Figure (7-6 A)**. There is a discrepancy of 2% at a distance of 20 mm from the isocentre, **Figure (7-6 B)**. The 18 MV PRESAGE® profile is within 2% compared with the ion chamber measurements with the largest discrepancy at the 60 % of the normalised Relative Optical Density; **Figure (7-6 B)**. The 18 MV PRESAGE® profile also displays a similar feature to the 6 MV profile just beyond a distance of 20 mm from the isocentre.

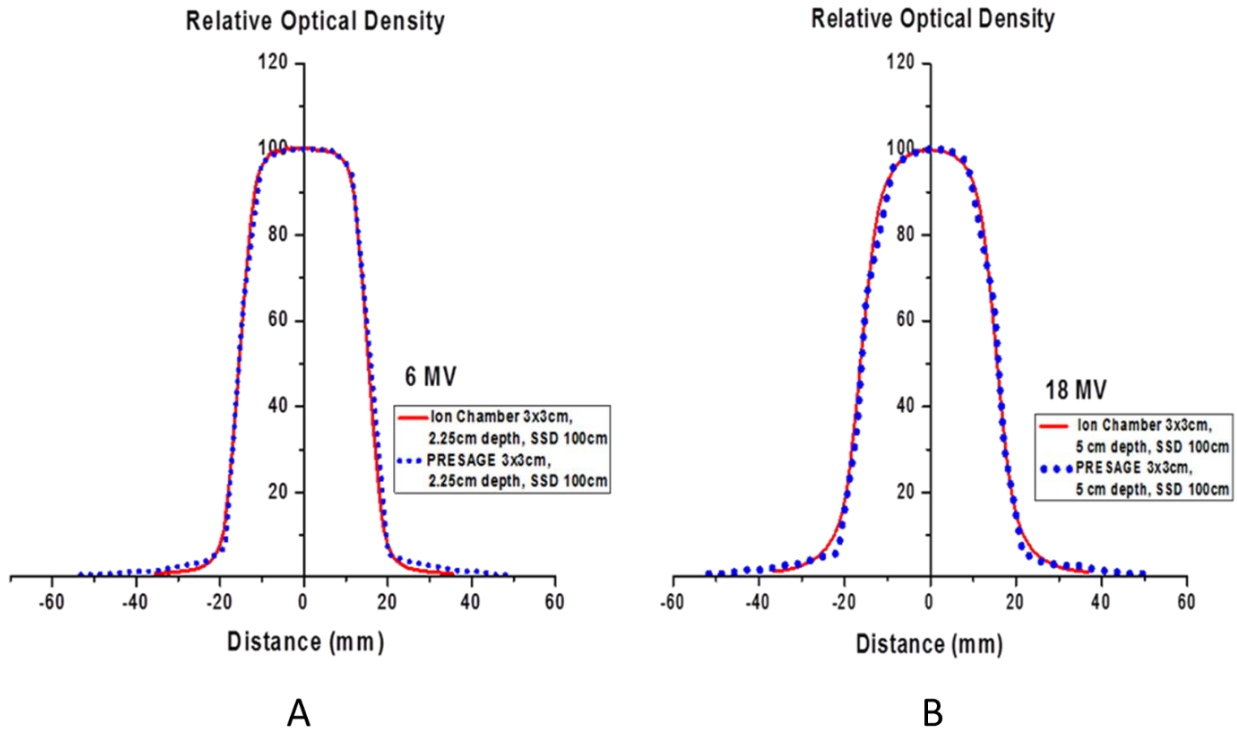

Figure 7-6: Beam profiles acquired from an ionisation chamber and PRESAGE®, A) at 6 MV 2.5cm depth and, B) 18 MV at 5cm depth.

7.4.3 PRESAGE dosimeter with air cavity

The PDD curve of the heterogeneous PRESAGE® dosimeter was measured and compared to the PDD curve of the ion chamber measurements for a 6 MV X-ray beam in water along with the PDD calculated on a TPS (Eclipse, Varian Medical Systems, Palo Atlo, CA) using the AAA algorithm (v11.0.31) shown in **Figure (7-7)**.

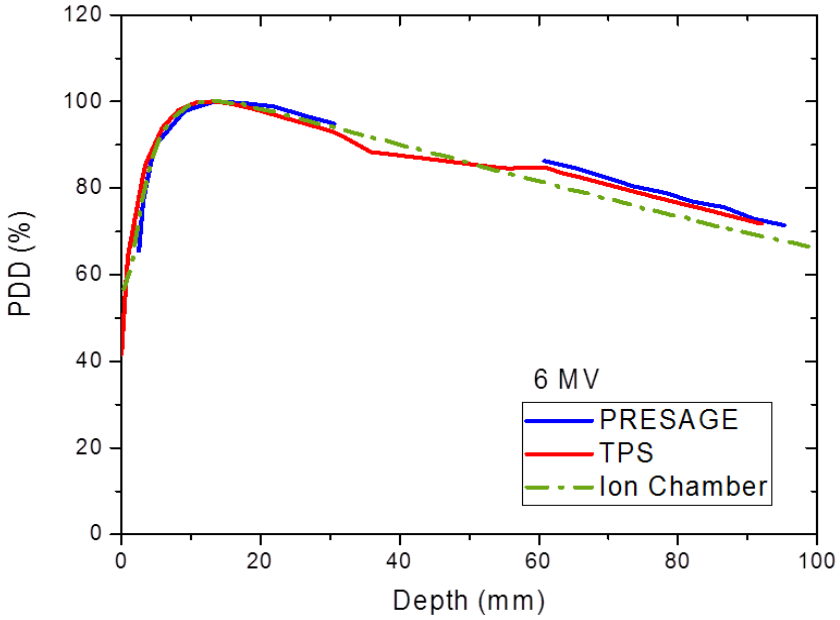

Figure 7-7: PDD's curve obtained from ionisation chamber in water and the in-homogenous PRESAGE® dosimeter and TPS at 6 MV.

The agreement of PDD curves of PRESAGE® dosimeter and ion chamber measurements prior to the an inhomogeneity is within 1.4%, however, the curve of PRESAGE® dosimeter post the inhomogeneity is greater by 4% than the ionization chamber in water curve. This result is anticipated by the fact there is less attenuating material in the beam and is verified by calculation with the TPS.

7.5 Discussion

The PDDs and beam profiles show excellent agreement with the ion chamber measurements. The PDDs for 6 MV and 18 MV display minor ripples in the curve past the

maximum depth dose. The magnitude of these ripples is less than 1.5% and could be due to variations in the thickness of the PRESAGE® dosimeters or the homogeneity of the sample [228]. The rippling effect can be eliminated by smoothing the PRESAGE® curve and by ensuring complete mixing of the precursor chemicals during the fabrication process. The data presented in **Figure (7-5)** are from the central axis of the field however, the CLARIOstar microplate reader can also read off-axis profiles. Therefore the technique could be extended to measure 2-D dose distributions in PRESAGE® phantoms.

The beam profiles in **Figure (7-6)** both have a similar discrepancy at the field edge at approximately 20 mm from the isocentre. The OD of the PRESAGE® dosimeter was measured in 1 mm steps by the CLARIOstar microplate reader and may be of higher spatial dose resolution than the reading by the IC13 chamber at the edge of the field which is a convolution involving the chamber volume and the edge of the field. The bulging of the 18 MV PRESAGE® profile in **Figure (7-6 B)** may be due to the sample shape. Although the PRESAGE® dosimeter was set in a plate designed specifically for the CLARIOstar microplate reader the thickness of the dosimeter may not have a uniform thickness. Any increase or decrease in sample thickness will change the relative optical density at that point and care needs to be taken during fabrication. The symmetrical nature of the discrepancy suggests that this may be the case. Repeating the measurement with PRESAGE® dosimeters of uniform thickness is necessary to confirm the reliability of the PRESAGE® profile.

The beam profile data was compared at 2.25 and 5 cm depth for 6 MV and 18 MV photons however; profiles at any depth in the dosimeter can be scanned to also produce 2-D depth profile distributions. Similarly, for the PDDs off-axis scans are also possible to produce off-axis PDD profiles.

Results presented in **Figure (7-7)**, revealed similar behaviour as with ion chamber measurements before the inhomogeneity, however after the inhomogeneity there is an increase in the dose compared to the ion chamber with no inhomogeneity. The TPS (using AAA algorithm) demonstrates that the dose expected after the air cavity in the phantom will be greater if there was no air cavity however there is a discrepancy of 1-2% between the PRESAGE® and TPS curves. This result demonstrates the ability of the PRESAGE® dosimeter to measure dose distributions in a water equivalent phantom with air cavities.

7-6 Conclusion

We have shown that a UV/Vis spectrophotometry technique using a CLARIOstar microplate reader can be used to generate 2-D dose distributions of megavoltage X-ray beams with PRESAGE® dosimeters. The agreement of the PDD curves and beam profiles demonstrate that performance of CLARIOstar microplate reader as a valid 2-D dosimetry instrument.

The PDDs, profile distributions and in-homogeneity behaviour were easily measured in a water equivalent dosimeter relatively quickly compared to optical CT or film dosimetry. This technique can potentially be extended to 3D through repeat measurements at various PRESAGE® angulations, in much the same way OCT works, and then reconstruct the data in a volume.

CHAPTER EIGHT

Titanium Dioxide Nanoparticles (TiO_2 NPs) Activation by Proton Beam for Radiologic-Imaging

8.1 Summary

This chapter is aims to investigate the activation of TiO_2 NPs by proton beams for imaging as gamma emitters. It covers the materials and experimental methodology used for TiO_2 NPs activation by proton beam including the capsule preparation for holding the NPs, samples irradiation process with proton beam, energy spectrum measurement and the storage condition of the activated TiO_2 NPs. Finally, it presents and discusses the experimental results obtained. There is potential for the activated TiO_2 NPs to be used as theranostic agents (imaging and dose enhancer in the target) since most of this work proved the compatibility of these NPs for dose enhancement of the types used in radiotherapy and this chapter shows also their potential application as imaging source via nuclear medicine techniques.

8.2 Background

Nuclear medicine was established in the middle of last century that initially iodine was used to diagnose and treat thyroid disease [229, 230]. In the recent years, this branch of medicine have employed radiations involving the use of radioactive substances (radioisotopes) produced in a cyclotron to provide information about functioning of human organs and how to treat specific diseases. The stable radioisotopes are linked with different carrier organic chemical depending on the organ and/or purpose of the scan such as glucose (fluorodexoyglucose), protein (cyclo-RGDfC) or hormone (norepinephrine) and are used as a radioactive tracers in the nuclear medicine applications which generally are short lived (short half-life) isotopes [231]. These radioactive tracers after been delivered to the organs by either intravenous injection, direct injection into organ, oral ingesting or inhalation depending on the disease studied, as it decays, it emits positron which instantly combines with a nearby

electron (electron-positron annihilation process) resulting in the simultaneous energy release as two identifiable gamma rays (γ-rays) in opposite directions. The γ-rays are then detected outside the body by detectors from many different angels and are used to image an internal organs or structures tomographically. The formulated images are then utilised for diagnostic techniques in radiotherapy. *In vivo* imaging techniques, the emitted γ-rays are detected by special solid-state detectors. The imaging system based on this principle is known as positron-emission tomography i.e. (PET) another less commonly used system is single photon emission computerised tomography (SPECT). Now, the dual CT/PET scans are the more recent development techniques used for imaging enabling 30% better diagnosis than with traditional gamma camera [232]. The featured advantage of nuclear medicine imaging over X-ray imaging techniques is that the positioning of radiation source within the organs imaged and both soft tissue and bone can be imaged very clear [233].

Currently, the commonly available positron emitter radioisotopes used as radioactive tracers in the nuclear medicine are carbon (^{11}C), nitrogen (^{13}N), oxygen (^{15}O), fluorine (^{18}F), gallium (^{68}Ga) and rubidium (^{82}Rb). Lately, nanoparticles have also been tested as a potential radioactive tracers including metal oxide NPs and particularly TiO_2 NPs for *in vitro* and *in vivo* studies [234-237]. In literature, a very limited number of studies are conducted to investigate the radioisotopes generated from TiO_2 NPs via proton beam activation. Researchers showed that TiO_2 NPs have been successfully radiolabelled with stable vanadium (^{48}V) post activation by cyclotron generated proton beam. In addition, characterisation of the activated TiO_2 NPs using XRD demonstrates that there was no significant modification in the morphological properties of the irradiated NPs. Furthermore, *in vitro* investigation of the uptake of cold non-activated and activated TiO_2 NPs with human cell line Calu-3 was quantified by high resolution γ-ray spectroscopy and inductively coupled plasma mass spectrometry (ICPMS). These indicates that there was no significant alteration

in the uptake quantification between both batches of NPs [238], this refers that radioisotopes did not hamper the uptake of NPs by cells. Others have activated ^{18}O-enriched TiO_2 NPs directly by proton beam to study *in vivo* bio-distribution of NPs via generated positron emitter ^{18}F using PET. Further generated radioisotopes were investigated such as ^{44}Sc, ^{47}V and ^{48}V. Their results demonstrate that short term studies for *in vivo* bio-distribution of NPs in the organs using labelled TiO_2 NPs with radioactive ^{18}F atoms could be performed which aggregation of NPs were observed by PET after 8 h of intravenous and oral administration. Moreover, neither the morphology nor the size of the activated TiO_2 NPs was obviously affected by the proton beam irradiation as demonstrated by TEM and DLS [239].

In this study, the generation of radioisotopes via TiO_2 NPs activation with a cyclotron-generated proton beams are investigated and then the activated TiO_2 NPs are examined to show that it can be used as imaging agent using PET scan in order to be applied in future as a potential radioactive tracer for diagnostic techniques in nuclear medicine. Hence after proving the value of TiO_2 NPs in enhancing the radiation effects at the targets through this research as previously stated **(chapter six)** renders it to be a theranostic agent with dual effects (i.e. imaging and dose enhancer agent) simultaneously if it is in the radiation targets.

8.3 Materials and Methods

The materials and experimental methods followed for activation of 30 nm diameter TiO_2 NPs with proton beams are described in the following sections.

8.3.1 Capsule preparation

The stainless-steel capsule was manufactured locally with outer diameter of 25 mm and the cavity diameter of 15 mm as shown in **Figure (8-1)**. The synthesised anatase TiO_2 NPs according to the previously stated procedure in chapter 3 **(Section 3.1.1)** were loaded in the capsule prior irradiation by the proton beam. The total weight of TiO_2 NPs loaded in the capsule was about 21 mg. The capsule window was sealed with titanium foil of 0.1 mm thickness.

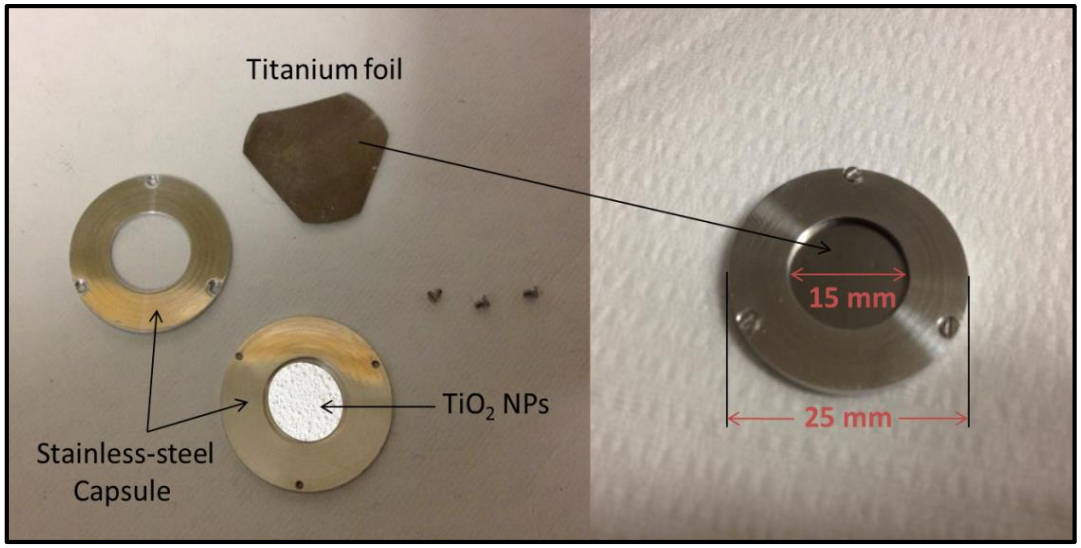

Figure 8-1: Digital image of the special designed capsule for holding TiO_2 NPs in the cyclotron.

8.3.2 TiO_2 NPs irradiation with proton beam

The irradiations were performed using high current (HC) cyclotron (IBA Inc., Louvain-La-Neuve, Belgium) located at the basement of the nuclear medicine department,

Austin Health, Melbourne, Australia, which it can be used to accelerate positive ions including both proton and deuterium ion source. Briefly, a cyclotron consists of two hollow cylindrical metal electrodes shaped like the letter "D" hence; these electrodes are called "dees". The dees are placed face to face and separated slightly along the diameter with a narrow gap and then creating a cylindrical space within them for the charged particles to move and these dees are enclosed in an evacuated chamber. A very high frequency and a high voltage oscillator is connected to these dees. A source of positive ions is placed in the centre of the cylindrical space. The dees and the positive ion source are placed between two poles of a large electromagnet as shown in **Figure (8-2)**. The positive ions are accelerated in to the negatively charged D_1 due to the electrostatic attraction and when the alternating current shifts the positive terminal to the negative terminal, the positive ions moves in to D_2 and continuous this process with the presence of magnetic field perpendicular to the electrode plane, the positive ions follow circular path as a result of Lorentz force. As the positively charged particle gain energy from electric field during each time crossing the gap between dees; therefore, their rotational radius increases and the ions spiral out from the dees through a small gap and bombard the target located at the exit point of the chamber arm and result in a nuclei reaction [240-242].

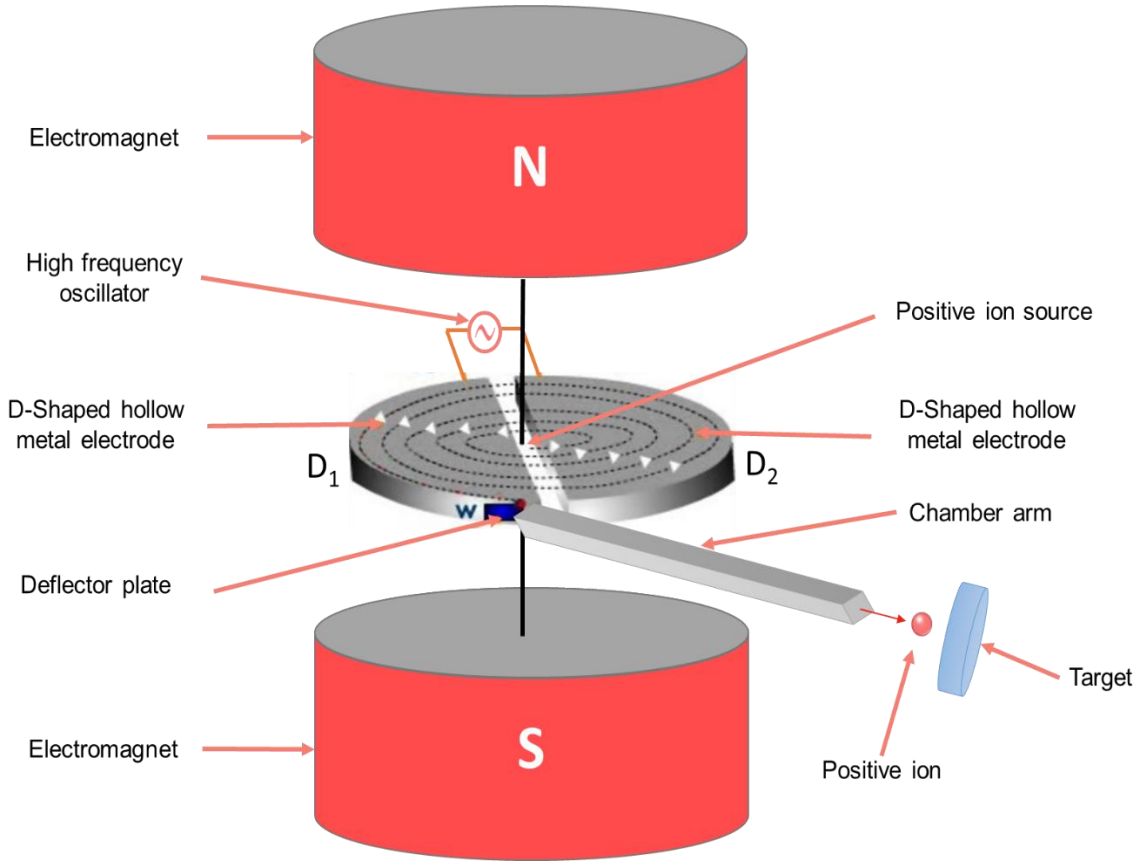

Figure 8-2: Schematic diagram showing the components of cyclotron. The image is not in scale.

In this work, the capsule loaded with TiO_2 NPs was inserted in a cyclotron holder **(Figure 8-3)** that allowed direct cooling system from both front and rear side, which this is essential for limiting the generated heat on the TiO_2 NPs in order to preserve the properties of the NPs during the proton bombardment. The cyclotron proton energy was set to 13 MeV where this energy covers the maximum reaction cross section of the proposed radioisotopes produced from TiO_2 NPs post proton activated such as reaction cross-section of $^{48}Ti(p,n)^{48}V$. The target, collimator and stripper current were set to 5, 0.2 and 5 µA respectively. The beam

time of 10 mins was applied. Finally, the D-voltage was set on 34.5 kV as this voltage makes the beam less diffusive and with less noise.

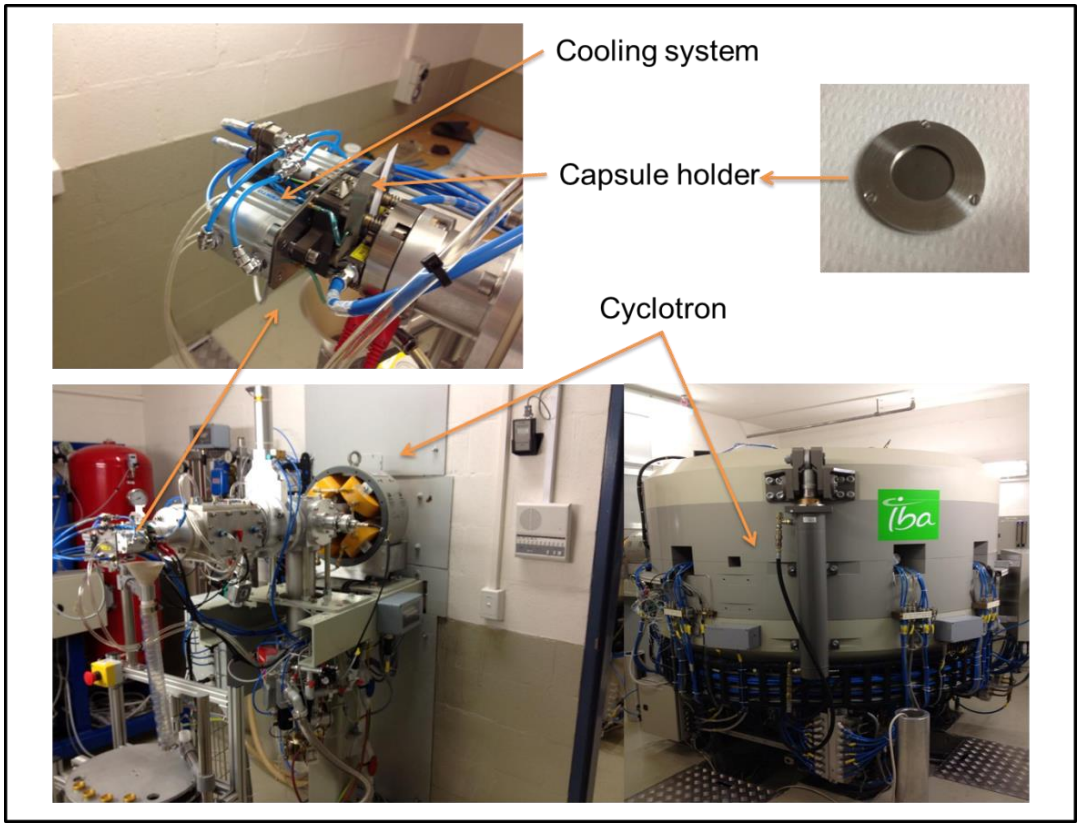

Figure 8-3: Cyclone 18/9 –HC cyclotron system showing the capsule holder and the cooling system. Inset: digital image of capsule in the top right.

8.3.3 Energy Spectrum by Germanium (Ge) γ-ray detector

The energy spectrum of the activated TiO_2 NPs was acquired using gamma spectrometer. The high resolution GC4020 GE Co-Axial hyper pure-germanium (Ge) γ-ray detector (CANBERRA, USA) as shown in **Figure (8-4)** was utilized to quantify and identify the γ-ray emitting radionuclides in an activated TiO_2 NPs. The Ge-detector was calibrated at efficiency and energy by using certified radioactive standard sources. A model 747 series lead shield was used to prevent any effects of the background counts. The measurements

were conducted directly after irradiation at times (0, 20, 40) min and then post 72 h. The acquired γ-ray spectra's were analyzed using the Genie 200 software package (CANBERRA, USA).

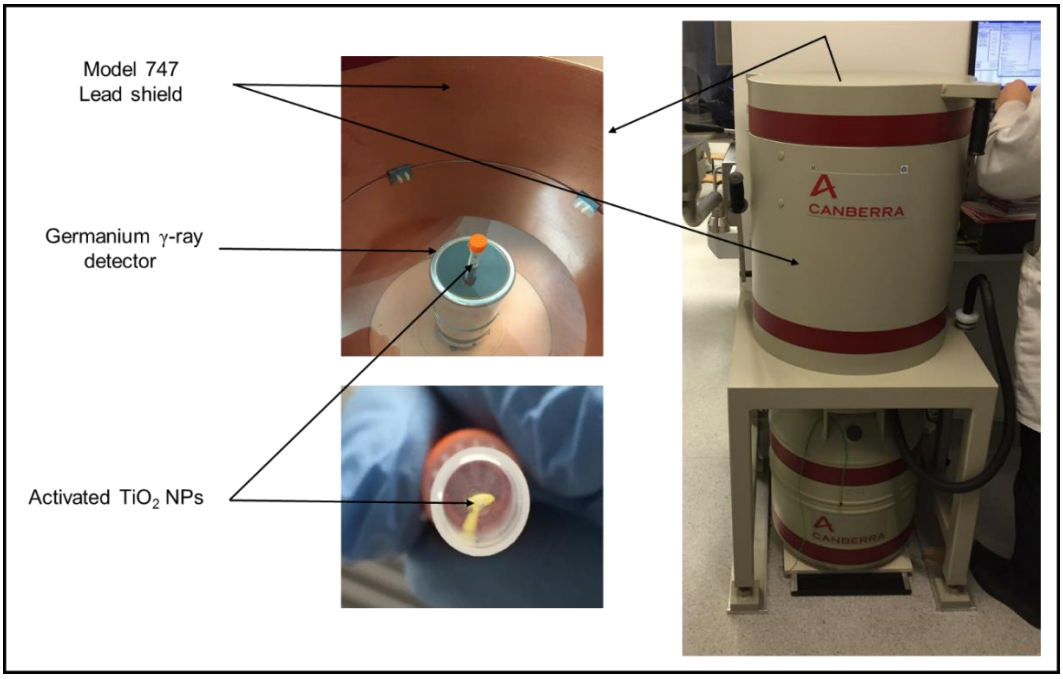

Figure 8-4: Image showing germanium γ-ray detector, activated TiO_2 NPs and the lead shield.

8.3.4 Imaging using positron emission tomography (PET) scanner

The positron emission tomography imaging was performed on Mediso nanoScan PET/MRI small animal testing system (Mediso Medical Equipment Developing and Service Ltd., Budapest, Hungary) at Molecular Imaging and Therapy/Nuclear Medicine department, Austin Health, Melbourne, Australia, and was used for imaging the radiolabeled anatase TiO_2 NPs with proton beam. The working principle of PET scan is when the radiotracers are injected into the patient bloodstream, after one hour they accumulates in body tissues with a high energy demand, especially tumours. These radiotracers decays within the tumour cells,

emitting positrons, and these positrons interact with nearby electrons in an annihilation reaction, producing a pair of gamma rays in opposite directions. These pairs of gamma rays are detected by the gamma camera in the PET scanner (**Figure 8-5 A**), hence are used to create a 3D image of the body showing the area of tumour tissue [243]. In this study the anatase TiO_2 NPs activated with proton beam were allowed to decay for few days before performing PET imaging. The NPs were placed in uniform prospects and then scanned with PET scanner as shown in **Figure (8-5 B**). The duration of the scanning was 10 min resulting in capturing a total of 235 images by PET scanner. The 3D image was then reconstructed and the total activity produced was measured.

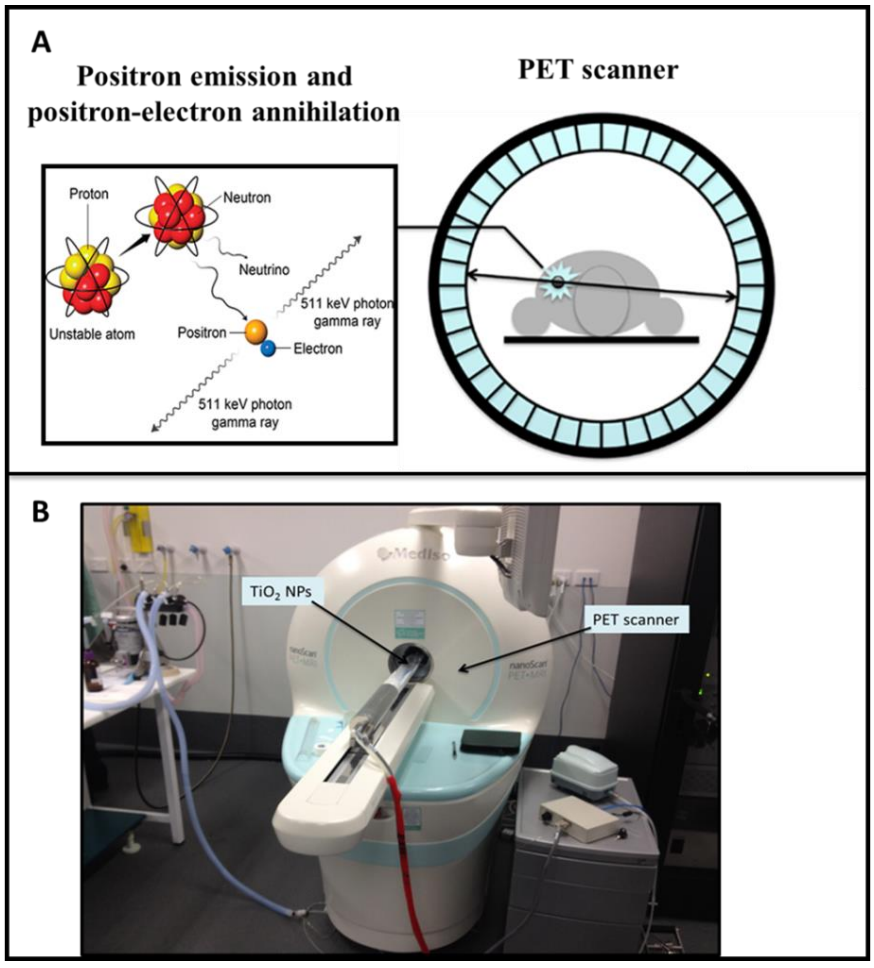

Figure 8-5: PET scanner, A) Basic principle of electron-positron annihilation and releasing two-gamma photons useg for PET imaging. B) Image of Mediso nanoScan PET/MRI small animal testing system performing imaging of activated TiO_2 NPs.

8.3.5 Risk & Safety control

The hazard associated with radiations and/MRI radioisotopes during the experiments were controlled by following the general safety guidelines described by engineers at cyclotron facility, Austin Health, Melbourne, Australia and these include the safe use of radioactive materials, handling and storage. Prior to the conduction of the experiments, a training session was conducted aimed at understanding how to work with the radiations around cyclotron and control the risk associated with handling of radioactive materials. The typical instructions followed were wearing a laboratory coat, disposable gloves and personal radiation monitoring device at all times during the experiment. In addition, monitor clothing, hands and shoes before leaving the facility area at a spot of low contamination background. Furthermore, controlling the radiation hazard during irradiation, handling and spectrum measurement were by utilising shielding materials such as concrete and lead in order to reduce the radiation effect to an acceptable low level. The activated TiO_2 NPs were clearly labelled and stored at a special lead shielding room for radioactive material storage at the cyclotron facility, Austin Health.

8.4 Results

The high resolution γ-ray spectra of the TiO_2 NPs activated by13 MeV proton beam were acquired after the removal of NPs from the capsule i.e. after activation. The measurement presented are conducted at times (15, 45, 85) min and 72 h after the end of the irradiation process. The energy spectrum of 15 min post irradiation is shown in **Figure (8-6).** The results demonstrate that high intensity peak was observed at 511 keV which correspond to the γ-ray resulted from electron-positron annihilation, while less intense signals were

detected at energies of 944.2, 984.55 and 1312.08 keV which all corresponds to Vanadium-^{48}V ($T_{1/2}$ = 15.97 days). The γ-ray peaks of the radioisotope at energies of 1390, 1551 and 1796 keV corresponds to the Vanadium-^{47}V ($T_{1/2}$ = 32.6 min). The peak at 1157 keV corresponds to Scandium (Sc)- ^{44g}Sc ($T_{1/2}$ = 3.93 h). **Figures (8-7) and (8-8)** shows the γ-ray energy spectra acquired for the time frames of 45 and 85 min. It is observed that ^{44g}Sc (1157) peak diminished with time whereas two peaks of 159.27 and 271.2 keV appeared which corresponds to ^{47}Sc ($T_{1/2}$ = 3.35 d) and ^{44m}Sc ($T_{1/2}$ = 2.44 d), respectively. Post 72 h from irradiation, only the major signals corresponding to ^{47}Sc (159.27 keV), ^{44m}Sc (271.2 keV), the electron-positron annihilation (511 keV) and to ^{48}V γ-ray emission (928.3, 944.2, 984.55 and 1312.08) keV were detected in addition to the peaks (1494.55 and 1823.08) keV resulting from the sum of (983.55+511) and (1312.08+511) γ-rays, while both ^{47}V and ^{44g}Sc signals were vanished from the γ-ray spectrum as shown in **Figure (8-9)**.

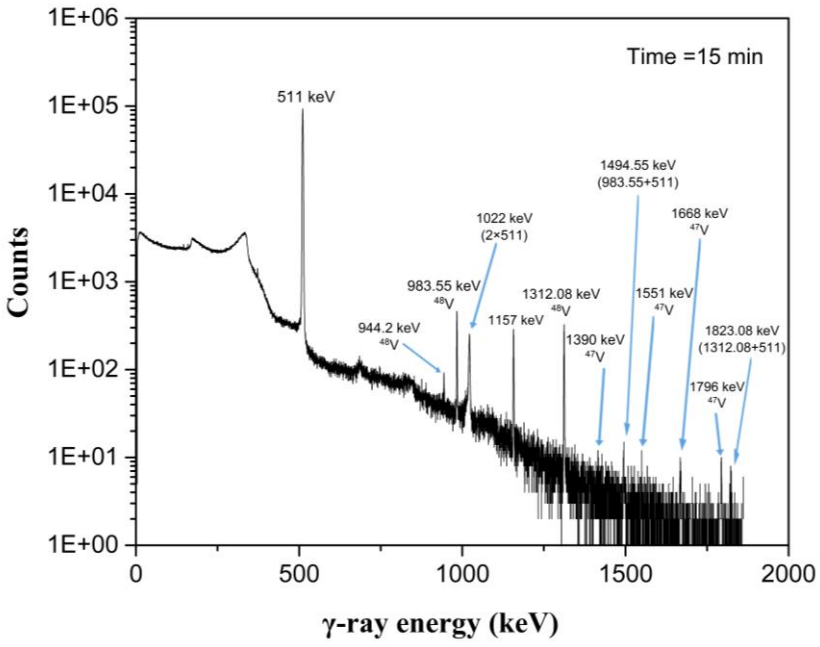

Figure 8-6: Gamma ray spectrum of the proton irradiated TiO_2 NPs showing the electron-positron annihilation peak (511 keV) in addition to γ-rays emission peaks for ^{48}V and ^{47}V after 15 min the end of irradiation process.

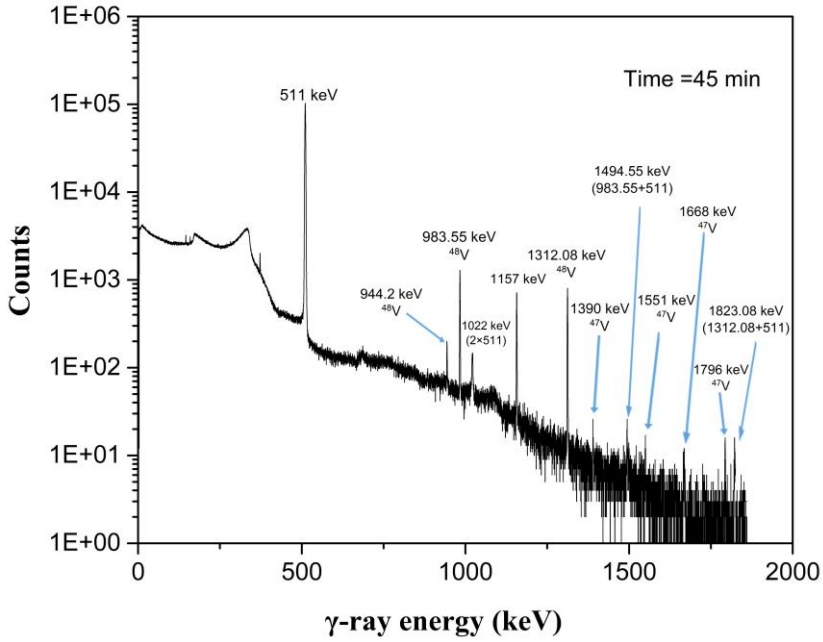

Figure 8-7: Gamma ray spectrum of the proton irradiated TiO_2 NPs showing the electron-positron annihilation peak (511 keV) in addition to γ-rays emission peaks for ^{48}V and ^{47}V after 45 min the end of irradiation process.

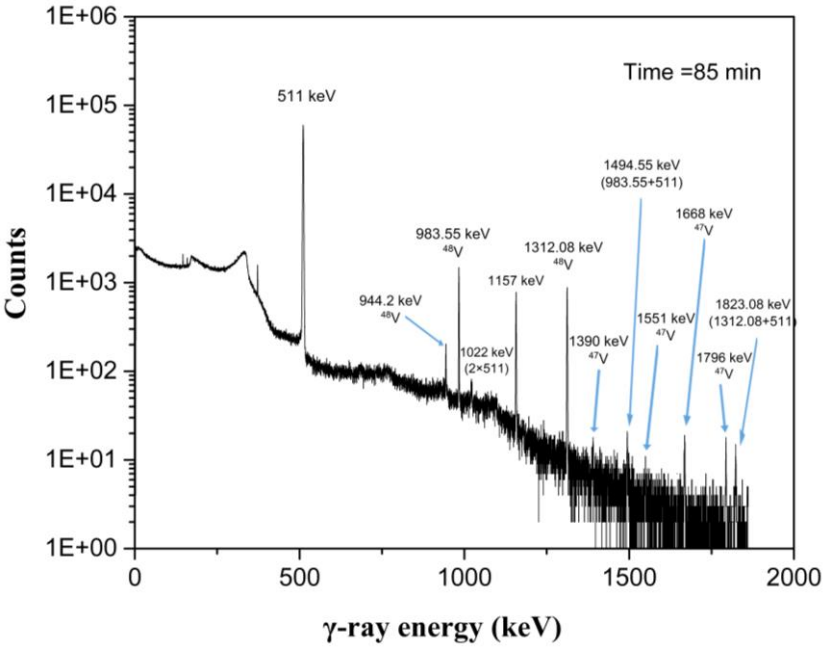

Figure 8-8: Gamma ray spectrum of the proton irradiated TiO_2 NPs showing the electron-positron annihilation peak (511 keV) in addition to γ-rays emission peaks for ^{48}V and ^{47}V after 15 min the end of irradiation process.

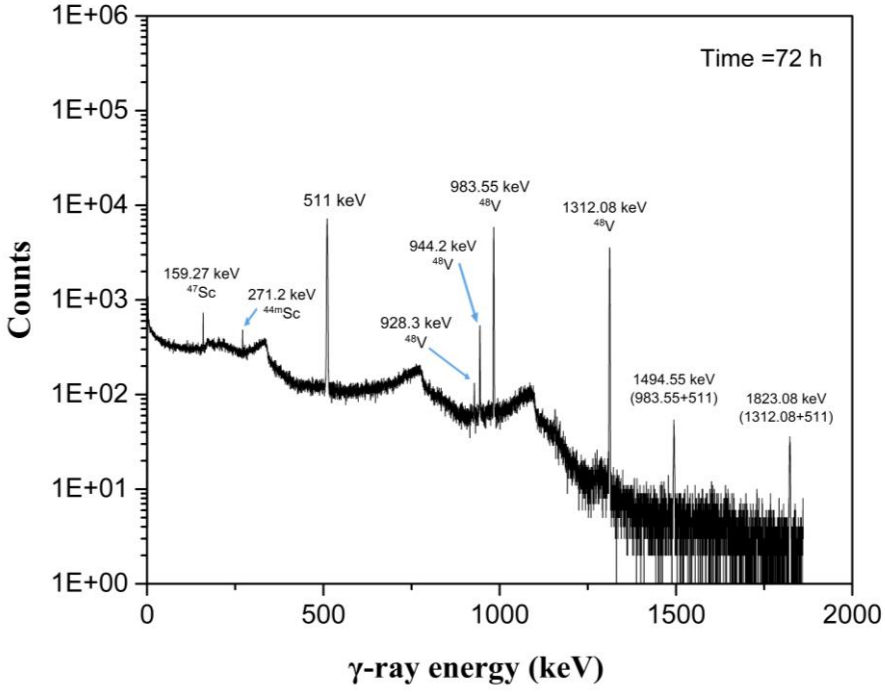

Figure 8-9: Gamma ray spectrum of the proton irradiated TiO_2 NPs showing the electron-positron annihilation peak (511 keV) in addition to γ-rays emission peaks for ^{47}Sc (159.27 keV), ^{44m}Sc (271.2 keV) and ^{48}V (928.3, 944.2, 983.55 and 1312.08 keV) after 72 h the end of irradiation process.

Figure (8-10) is an example of images acquired as a rotating 3D maximum intensity projection (MIP) of the image volume obtained from PET scanning the proton activated anatase TiO_2 NPs. The black spot represent the signal of radiolabeled anatase TiO_2 NPs. The activity of ^{48}V was measured from images obtained with acquisition of PET scans performed on small sample of irradiated TiO_2 NPs. The image reports activity of 404 kBq based on ^{18}F. Once correcting for the ^{18}F branching ratio (0.9686) and the system Decay Correction Correction Factor (DCCF) (0.9692) as calculated by specific software for the start of the 10-minutes acquisition, the activity was lowered by about 6% for ^{48}V to be 380 kBq as measured at the imaging time. In nuclear physics, the branching fraction or ratio for decay is the

fraction of particles that decay by an individual decay mode with respect to the total number of particles, which decay.

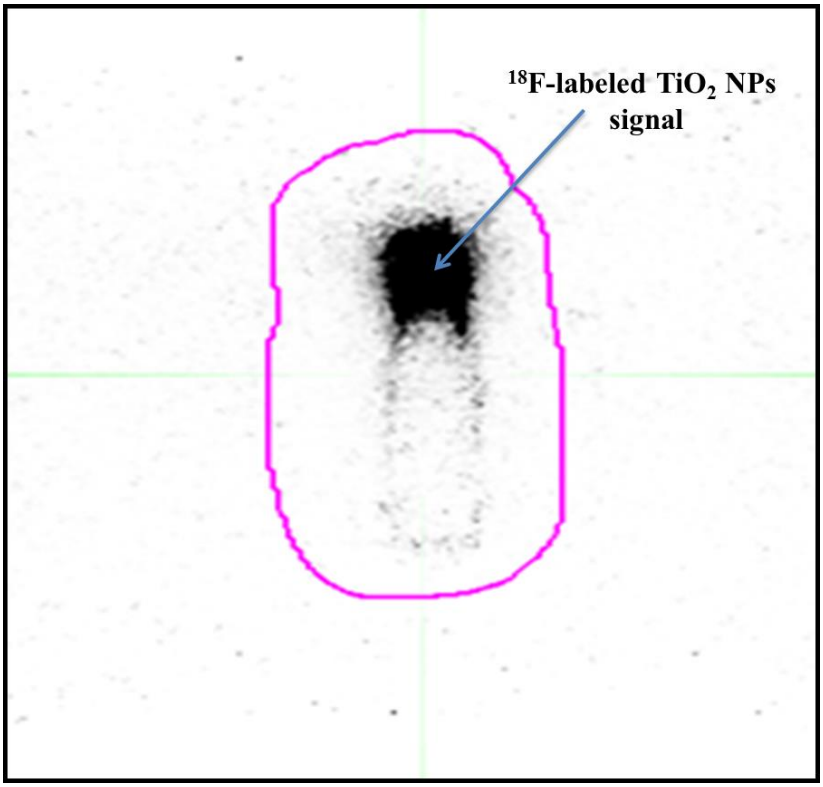

Figure 8-10: Maximum intensity projection (MIP) PET image of ^{18}F-labeled TiO_2 NPs.

8.5 Discussion

In discussion, TiO_2 NPs can be proposed as a potential candidate for producing nuclear medical radioisotopes via proton activation since only limited radioisotopes for the nuclear medicine applications are currently available. It is obvious from the results that the main radionuclides generated from TiO_2 NPs activation are ^{47}Sc, ^{44m}Sc, ^{44}Sc, ^{48}V as shown in **Figures (8-6) and (8-9)**. The radionuclide ^{47}Sc is produced via direct nuclear reaction of either ^{48}Ti(p,γ)^{47}Sc or ^{47}Ti(p,n)^{47}Sc [244]. Recently, β^- and α emitters are potentially suggested by several innovators for new radiopharmaceutical applications. Therefore, ^{47}Sc

radionuclide is a promising therapeutic agent for preparing radiolabeled antibodies due to its favorable β^- emission energy (162 keV) which decays to stable ^{47}Ti (100% β^- emission), and to its moderate half-life ($T_{1/2}$ = 3.35 d) [245]. On the other hand, ^{47}Sc (β^-) is accompanied to γ-ray (159.2 keV) that can be used for *in vivo* imaging; therefore, the simultaneously presence of β^- and γ could make ^{47}Sc an alternative to the currently employed radionuclides (^{67}Cu or ^{177}Lu) for targeted radionuclide therapy [245, 246]. The other generated radioisotopes is ^{44}Sc which has a long-lived isomeric state radionuclide ^{44m}Sc ($T_{1/2}$ = 2.44 d) formed from the nuclear reaction of ^{47}Ti(p,α)^{44m}Sc and ^{48}Ti(p,nα)^{44m}Sc and a short-lived ground state of ^{44g}Sc ($T_{1/2}$ = 3.93 h) resulted from the reaction of ^{47}Ti(p,α)^{44g}Sc and ^{48}Ti(p,nα)^{44g}Sc via TiO_2 NPs-proton activation [239, 247 and 248]. The presence of ^{47}V in the energy spectrum could be due to the ^{47}Ti(p,n)^{47}V and (less probably) ^{46}Ti(p, γ)^{47}V nuclear reactions resulting from the low energy incident protons [247, 249]. The ^{47}V and ^{44g}Sc are short-lived isotopes (32.6 min, 3.93 h) respectively; therefore, both were decayed (compare **Figures (8-7, 8-8) to (8-6))** and almost quantitatively eliminated from the spectrum after 72 h of irradiation shown in **Figure (8-9)**. Also, the energy spectra taken at 15 min post irradiation has a very low signal to noise level ratio, which resulted in hiding the peaks of ^{47}Sc (195.2 keV) and ^{44m}Sc (271.2 keV). After 72 h the target activity dies down and the noise count rate dropped significantly making these two peaks became more obvious **(Figure 8-9)**. The γ-ray peak produced at 511 keV in the energy spectrum corresponds to the positron annihilation and are the most important radioisotopes for potential nuclear medicine imaging applications particularly for PET. Whereas the long-lived radioisotope ^{48}V ($T_{1/2}$ = 15.9 d) can effectively be formed by the direct nuclear reaction ^{48}Ti(p,n)^{48}V and completely decays to stable ^{48}Ti nuclide by 100% electron capture process. The half-live of ^{48}V made it suitable for biological tracer tests [238]. The radioladeled anatase TiO_2 NPs show its feasibility to be employed as radioactive tracer

for PET imaging as clearly can be seen in **Figure (8-10)**. This has potential to be used for nuclear medicine applications.

8.6 Conclusion

In this study, the direct proton irradiation of anatase TiO_2 NPs can be successfully activated through generation of the positron emitters (0.511 MeV) that potentially can be employed for *in vivo* imaging application using PET. Simultaneously to the formation of positrons, other radionuclides, such as ^{47}V, ^{44g}Sc, and ^{48}V, are generated by the irradiation as demonstrated using high-resolution Germanium detector. The generated radionuclides with a certain activity level especially ^{48}V can be used for radiotracing applications. Therefore, anatase TiO_2 NPs can be considered as a potential radiologic imaging agent for nuclear medicine applications.

In the previous chapters (5 and 6) it was shown that TiO_2 NPs can be used for enhancing radiation doses especially for radiotherapy. Combining the outcome of this chapter with those of chapters five and six clearly demonstrates that TiO_2 NPs can act as therapeutic and imaging agents, i.e. theranostic agents.

CHAPTER NINE

General Conclusions
And
Future Directions

9. Conclusions and future directions

This chapter presents the general conclusions of the experimental results around thesis whole and then it is followed by suggestions for further studies to answer the research questions raised during the process of answering the main ones.

9.1 Conclusions

This thesis is based on novel and original work and innovative methods and techniques of employing nanotechnology in medical radiations in general and radiotherapy in particular. The inspiration behind this research is that anatase TiO_2 NPs nanoparticles can effectively radiosensitise the target via biochemical effects beside the physical effects. In addition, the nanoparticles can be successfully activated by the proton beam, hence used as a potential radioactive tracer for diagnostic imaging techniques in the nuclear medicine applications rendering it to be a theranostic agent (i.e. imaging and enhance radiotherapeutic ratio).

The main findings of this thesis were, firstly, explore and discuss the characterisations of synthesised TiO_2 NPs. Secondly, the influence of TiO_2 NPs on radiation dose enhancement at low and high energy X-ray beams have been comprehensively analysed through *in vitro* and phantom based studies. Finally, the feasibility of employing the activated TiO_2 NPs by proton beam as a radioactive isotope for imaging purposes in nuclear medicine was investigated. Over the preceding eight chapters of this thesis, we have addressed the main achievements of this work that includes the following:

1. This thesis comprised investigation and discussions of the results for several characteristics of TiO_2 NPs which make them potentially suited for applications in radiotherapy. The TiO_2 NPs were typically synthesised to achieve highly pure anatase nanocrystalline structures. This selected form creates more free radicals and effectively generates more ROSs since it has larger surface to volume ratio. These features have a high impact in damaging DNA molecule of biological systems during irradiations. The XPS analysis reveals that the binding energy of the synthesised NPs are referred to titanium and oxygen signals in the TiO_2 lattice, whereas the XRD analysis indicates that anatase crystal structure was with negligible levels of impurities. Furthermore, the synthesised anatase TiO_2 NPs were surface modified with either 3-aminopropyl trimethoxysilane (APTS) or poly (ethylene glycol) propyl trimethoxysilane (PEGTS) to afford amino- and PEG-functionalised NPs that could be easily dispersed in aqueous and organic solutions, respectively. The surface coatings were analysed using FTIR and TGA. The results show that amino and PEG surface coatings were successfully grafted on the TiO_2 NPs as analysed by FTIR while coating mass was only ~ 6-7 % of the total NPs mass as analysed by TGA which is an indicator that the observed dose enhancement is mainly due to the TiO_2 NPs itself.

2. In phantom studies, the influence of radical initiators including chloroform and iodoform employed in this study on the physical and radiological characteristics of the PRESAGE® dosimeter was investigated. The results obtained refers that physical density of PRESAGE® dosimeter with iodoform radical initiator was higher than PRESAGE® dosimeter with chloroform radical initiator, this is because of high density and atomic number (Z) of iodine (Z=53) compared to the chlorine (Z=17). With regards to the radiological properties, it is noted that the incorporation of these radical initiators in the PRESAGE® dosimeter composition resulted in variations of the dosimeter sensitivity to the radiation doses. The

change in sensitivity mainly depends on the type and concentration of the radical initiator used. The results indicate that the slope of the dose response curve for iodoform-based PRESAGE® formulation showed significantly higher sensitivity than chloroform-based PRESAGE® formulation which proves that iodoform radical initiator enhances the sensitivity of the PRESAGE® dosimeter to radiation doses more than chloroform at the same halocarbons molar concentration and applied radiation dose. This enhancement in sensitivity is believed to be linked directly to the carbon-halogen bond dissociation energy. Furthermore, the post-response photostability of the PRESAGE® dosimeter with both radical initiators were stable over the period of 10 days. Finally, the phantom's water-equivalency characteristic was evaluated experimentally. The PDD results showed that the PRESAGE® dosimeters are water-equivalent; hence, there is no need to apply dosimetric correction factors in order to determine doses to tissue.

The radiation-modifying effects of anatase PEGS functionalised TiO_2 NPs in the formulation of the PRESAGE® dosimeter were explored. The 3D PRESAGE® dosimeters were utilized to quantify the DEF produced by the inclusion of the PEG functionalised TiO_2 NPs and then validated these results with the biological studies. The results clearly demonstrates that the sensitivity of the dosimeter increases to the radiation doses with the concentration of the TiO_2 NPs incorporated into the composition of the PRESAGE® dosimeter. Furthermore, the measured dose enhancements were significant at 80 kV compared to the negligible dose enhancement detected at 6 MV X-ray energy beams which is mainly due to contribution of PE as the energy spectrum of the MV beam shows some residual low energy and PEs.

3. The PRESAGE® dosimeter was used for the first time to simulate the tissue inhomogeneity behavior using CLARIOstar microplate reader (UV/Vis spectrophotometry).

This UV/Vis spectrophotometry technique was used to measure the 2D dose distribution prior and after the inhomogeneous section. The PDD results measured by this technique reveals similar trend as with ion chamber measurements before the inhomogeneity. However, an increase in dose was measured post inhomogeneity compared to the ion chamber measurement with no inhomogeneity. A discrepancy of 1-2% was noted between the Treatment Planning System and actual PRESAGE® dosimeter curves post inhomogeneity. This technique can potentially be extended to 3D by obtaining measurements at 360 angels as similar way OCT works, and then reconstruct the data in a volume. This will lead to many clinical applications such as determining the 3D dose distributions around and inside an inhomogeneity and then validate treatments for sophisticated techniques such as tomotherapy and IMRT.

4. *In vitro* studies; the localisation of amino functionalised anatase TiO_2 NPs inside the cells was observed in this research to determine whether the NPs are taken-up inside the cells. HaCaT and DU145 cells were incubated with TiO_2 NPs for 24 h to include the NPs into both types of cell lines. Various techniques were employed to investigate cellular association and/or uptake of NPs such as FCM and immunohistochemistry cell staining technique using light microscopy. The results of FCM conforms an increase of the scattered visible light in the case of NPs presence which the forward scatter were slightly changed suggesting no change in object size while the side scatter was increased with the increase of TiO_2 NPs concentrations and suggesting a high association between cells and the NPs. The distribution of TiO_2 NPs inside the cells was studied by light microscopy and the results reveals that TiO_2 NPs were clustered as a black dot in the cell's cytoplasm and did not enter its nucleus.

5. Assessments of cytotoxicity of amine functionalised TiO_2 NPs on HaCaT and DU145 were explored with different concentrations of NPs and incubation times. The toxicity induced by anatase TiO_2 NPs was tested by measuring the cell viability which is a percentage of treated cultures (with TiO_2 NPs treatment) to untreated controls (without TiO_2 NPs treatment) [250]. The results of cytotoxicity investigations for both types of cells shows that the anatase amine functionalised TiO_2 NPs does not alter the biological system for the concentrations of up to 4 mM post 72 h of treatment as the cell viability for these concentrations of TiO_2 NPs did not show any statistically significant changes ($p > 0.05$) in the cells' viability. These results are in agreement with findings of other researchers [32, 149]. Therefore, in this study, the TiO_2 NPs concentrations (maximum of 4 mM) used *in vitro* were suitable for studying radiosensitisation effects without any health concern. Contrary to other NPs such as gold and bismuth NPs which it is not possible to exceed a 1 mM concentration.

6. In this thesis, the radiosensitisation produced by inclusion of anatase amino functionalised TiO_2 NPs using HaCaT and DU145 cell lines irradiated with 1-8 Gy ranges of radiation doses at 0.5, 1 and 4 mM TiO_2 NPs concentrations was quantified for low (kilovoltage) and high (megavoltage) energies external X-ray radiation sources by two methods: MTS and clonogenic assays. The DEFs were deduced from the data analysed in the form of cell survival curve. The results indicate that radiosensitisation induced by TiO_2 NPs was significant at kilovoltage range of energy where the maximal dose enhancement was observed at 80 kV. Furthermore, significant radiosensitisation was observed for *in vitro* study at megavoltage energy beam. In addition, the slight variations in regards of DEF observed between HaCaT and DU145 cell lines could be due to the difference in their response to the

radiations and to the inclusion of the TiO_2 NPs as it is known that cells have different response to the same radiations [16]. With the inclusion of TiO_2 NPs in the target, same fraction of cells were destroyed with lower radiation doses compared to the case of absence of TiO_2 NPs which these nanoparticles result in the observable effect on the measured DEF values and the DEF was increased with the TiO_2 NPs concentration increase. This means if the TiO_2 NPs are added to the biological target, a reduction of external dose of an order of magnitude can be achieved to deliver the same local control as without the inclusion of TiO_2 NPs for treatments with kilovoltage and megavoltage X-rays beams. This is because of ROSs and further secondary electron generation with the presence of NPs in the target which makes cells more sensitive to the radiations. This reduction of delivered radiation dose to the target will lead to reducing the dose to the surrounding normal tissues during treatment which is the primary concern in all radiotherapy treatment procedures. Hence, TiO_2 NPs are considered to be an efficient dose enhancer agent and have a great potential value for future clinical radiotherapy applications.

The interesting point of the dose enhancement results is the observed differences and disagreement in the level of produced DEF between *in vitro* and phantom based studies, especially at high energies (6 MV). The PRESAGE® dosimeters showed lower enhancements in radiosensitivity than cells in culture studies. The main reason behind this is that PRESAGE® dosimeters being only sensitive to the directly generated free electron due to the methods of interactions of radiations with matter such as photoelectric effect, Compton scatter and/or Auger effect not being suited to detect the generated ROS (Biochemical effects) due to a lack of free water molecules in its structure. Contrariwise, cells can be affected by many other biochemical factors, such as the generated ROS which is added to the physical effect including the stress caused by generated electron free radicals, and this result in higher radiosensitivity.

7. Ranges of kV radiotherapy X-ray beams (80, 100 and 150 kV) in combination with different concentrations (0.5, 1 and 4 mM) of anatase TiO_2 NPs were employed to investigate the DEF dependence on beam energies at this ranges. The results for both *in vitro* and phantom based studies predict that the optimal kV energy that create highest DEF was obtained at 80 kV which later was selected to be applied for both studies (*in vitro* and phantom) of this thesis.

8. The radiobiological effects of amino functionalised anatase TiO_2 NPs on HaCaT and DU145 cell lines were analysed and the experimental data plotted as cell survival curves were fitted with linear quadratic model. The linear (α) and the quadratic (β) parameters were extracted from these data in order to describe the DNA damage by radiations. The results clearly demonstrate that α value significantly increases with the inclusion of TiO_2 NPs while β value insignificantly changes. This increase in α value indicates that the probability of double strand DNA breakage by different secondary electrons increases with the presence of NPs in the target. This is expected as the presence of TiO_2 NPs will enhance production of low energy free radicals and also ROSs which would lead to increase the likelihoods of DNA strands breakages.

9. In this work, the ROS generated from amino functionalised anatase TiO_2 NPs upon exposed to radiotherapy X-ray energy beam was investigated. Aqueous solutions without (control) and with the presence of TiO_2 NPs was exposed to 6 MV beam. The result clearly shows that ROS were detected and the level of generated ROS was proportionally dependent on the TiO_2 NPs concentration. This explains that biochemical effects need to be considered as a key factor for enhancing the cellular radiosensitivity with the presence of nanoparticles

which would be an important consideration for *in vitro* and *in vivo* radiosensitivity measurements.

10. In this thesis, the direct proton irradiation of anatase TiO_2 NPs allowed sufficient activation through generation of the positron emitter which can be used to perform *in vivo* imaging using PET. However, the further radionuclides generated have an advantage to be employed as radiotracer agents for nuclear medicine applications.

9.2 Future Direction

Certainly, this work has addressed many issues which could have impact on radiotherapy and investigated and answered many questions for better understanding of resolving these issues in future. However, further theoretical and experimental investigations are required to be tackled in future. Currently, few investigations are in progress to complement the primary findings of this thesis as follows;

1. This thesis focused on both low energy (kilovoltage) and high energy (megavoltage) radiotherapy X-ray beams for investigation of radiosensitisation. However, it will be of great value for radiotherapy field to extend such investigation into other radiotherapy beams such as electron beam, synchrotron based microbeams and more importantly proton beams which are increasingly becoming important and expanding. This is currently in the planning stages for our group.

2. The dose enhancement induced by anatase TiO_2 NPs were investigated for *in vitro* and phantom based studies in this work. It will be of great value to extend these ideas into *in vivo* studies.

3. Only one type of the ROS generated from anatase TiO_2 NPs at megavoltage X-ray energy beam was detected in this study which was hydroxyl radical (•OH). However, further investigations are in progress to detect the other types of ROS generated from TiO_2 NPs and from other types of NPs. In addition, employing proton beam is under investigation to explore for any possible ROS generation from NPs. Also measuring the ROS levels generated with low energy X-rays.

4. Employing PRESAGE® dosimeter for clinical applications is one of the challenges. However, for the first time a work is under investigation to validate the surface dose distribution for a patient been treated with radiotherapy electron beams at Barwon Health Andrew Love Cancer Centre (Barwon Health: Geelong Hospital, Geelong, VIC, Australia).

5. Further measurements are being conducted to evaluate the importance of the radioisotopes generated from activated anatase TiO_2 NPs via cyclotron proton beam for the potential nuclear medicine application.

6. It will be valuable to repeat the measurements of this research using different sizes of anatase TiO_2 NPs. This will allow for better understand the underpinning of the physical and radiobiological effects on radiation dose enhancement.

7. As a consequence of rapid development in the area of nano-biotechnology, testing different types of nano-compound structures such as mixture of anatase/rutile TiO_2 NPs and/or silver/titanium dioxide composite nanoparticles could be of great value.

References

1. Smith MA, Seibel NL, Altekruse SF, Ries LA, Melbert DL, O'Leary M, Smith FO, Reaman GH. *Outcomes for children and adolescents with cancer: challenges for the twenty-first century*. Journal of Clinical Oncology. 2010. **28**(15): p.2625-34.
2. Baskar R, Lee KA, Yeo R, Yeoh KW. *Cancer and radiation therapy: Current advances and future directions*. Int J Med Sci. 2012; **9**(3):193-9.
3. Hershman DL, Shao T. *Anthracycline cardiotoxicity after breast cancer treatment. Oncology*. 2009; **23**(3):227-34.
4. Bhide SA, Nutting CM. *Recent advances in radiotherapy*. BMC Medicine. 2010; **8**(25):1-5.
5. Connell PP, Hellman S. *Advances in radiotherapy and implications for the next century: A historical perspective*. Cancer Res. 2009; **69**(2):383-92.
6. Bernier J HE, Giaccia A. *Radiation oncology: a century of achievement.* Nat Rev Cancer 2004; **4**(9):737-47.
7. Jaffray DA, Siewerdsen JH, Wong JW, Martinez AA. *Flat-panel cone-beam computed tomography for image-guided radiation therapy*. Int J Radiat Oncol Biol Phys. 2002; **53**(5):1337-49.
8. Pisani L, Lockman D, Jaffray D, Yan D, Martinez A, Wong J. *Setup error in radiotherapy: on-line correction using electronic kilovoltage and megavoltage radiographs*. Int J Radiat Oncol Biol Phys. 2000; **47**(3):825-39.
9. Dewerd LA, Venselaar JLM, Ibbott GS, Meigooni AS, Stump KE, Thomadsen BR, et al. *Overview on the dosimetric uncertainty analysis for photon-261emitting brachytherapy sources, in the light of the AAPM Task Group No 138 and GEC-ESTRO report.* Metro. 2012; **49**(5):S253-S8.
10. Hoppe BS, Mamalui-Hunter M, Mendenhall NP, Li Z, Indelicato DJ. *Improving the therapeutic ratio by using proton therapy in patients with stage I or II seminoma*. Am J Clin Oncol: Cancer Clinical Trials. 2013; **36**(1):31-7.
11. Nilsson G, Holmberg L, Garmo H, Terent A, Blomqvist C. *Radiation to supraclavicular and internal mammary lymph nodes in breast cancer increases the risk of stroke*. Br J Cancer. 2009; **100**(5):811-6.
12. Yu JB, Soulos PR, Herrin J, Cramer LD, Potosky AL, Roberts KB, et al. *Proton versus intensity-modulated radiotherapy for prostate cancer: Patterns of care and early toxicity*. J Natl Cancer Inst. 2013; **105**(1):25-32.
13. Rinaldi I, Brons S, Gordon J, Panse R, Voss B, Jäkel O, et al. *Experimental characterization of a prototype detector system for carbon ion radiography and tomography*. Phys Med Biol. 2013; **58**(3):413-27.
14. Khan F.M. and J.P. Gibbons. *Khan's the Physics of Radiation Therapy*. 4th Edition. Baltimore, MD: Lippincott Williams & Wilkins; 2014.
15. Podgorsak E. *Radiation Physics for Medical Physicists*. 2nd Edition. Springer; 2010.

16. Hall, E.J., *Radiobiology for the Radiologist.* Lippincott Williams & Wilkins; 2006.

17. Campbell N.A., Reece J.B., *Biology*. 7th Edition. Pearson-Benjamin Cummings; 2005.

18. Dale R. *Use of the linear-quadratic radiobiological model for quantifying kidney response in targeted radiotherapy*. Cancer Biotherapy and Radiopharmaceuticals. 2004; **19**(3):363-70.

19. Subiel A, *Ashmore R, Schettino G. Standards and methodologies for characterizing radiobiological impact of high-Z nanoparticles.* Theranostics. 2016; **6**(10):1651.

20. Lim AY, Ma J, Boey YC. *Development of Nanomaterials for SALDI-MS Analysis in Forensics*. Advanced Materials. 2012; **24**(30):4211-6.

21. Eustis, S., El-Sayed M.A, *Why gold nanoparticles are more precious than pretty gold: Noble metal surface plasmon resonance and its enhancement of the radiative and nonradiative properties of nanocrystals of different shapes* Chemical Society Reviews 2006. **35**: p. 209-217.

22. Maryanski MJ, Gore JC, Kennan RP, Schulz RJ. *NMR relaxation enhancement in gels polymerized and cross-linked by ionizing radiation: a new approach to 3D dosimetry by MRI.* Magn Reson Imaging. 1993; **1**:253-8.

23. Ferrari, M., *Cancer nanotechnology*: Oppurtunity and Challenges Nature 2005. **5**: p.161-171.

24. Yezhelyev M.V., Gao X, Xing Y , Al-Hajj A, Nie S., O'Regan R.M. *Emerging use of nanoparticles in diagnosis and treatment of breast cancer*. Lancet Oncol, 2006. **7**: p. 657-67.

25. ASTM International. *E 2456-06 Terminology for nanotechnology*. West Conshohocken, PA: ASTM International; 2006.

26. Daniel MC, Astruc D., *Gold nanoparticles: Assembly, supramolecular Chemistry, Quantum Size Related Properties and Applications toward Biology*, Catalysis and Nanotechnology Chem Rev. 2004; **104**: 293-346.

27. Rivera P, Oberdörster G, Elder A, Puntes V, Parak WJ. *Correlating Physico-Chemical with Toxicological Properties of Nanoparticles: The Present and the Future*. ACS Nano. 2010; **4**(10):5527-31.

28. Albanese A, Tang PS, Chan WC. *The Effect of Nanoparticle Size, Shape, and Surface Chemistry on Biological Systems*. Annu Rev Biomed Eng. 2012; **14**(1):1-16.

29. Eustis S, El-Sayed MA. *Why gold nanoparticles are more precious than pretty gold: Noble metal surface plasmon resonance and its enhancement of the radiative and nonradiative properties of nanocrystals of different shapes*. Chem Soc Rev. 2006; **35**(3):209-17.

30. Katti KV, Kannan R, Katti K, Kattumori V, Pandrapraganda R, Rahing V, et al. *Hybrid gold nanoparticles in molecular imaging and radiotherapy*. CzJPh. 2006; **56**(4):D23-D34.

31. Burda C, Chen X, Narayanan R, El-Sayed MA. *Chemistry and Properties of Nanocrystals of Different Shapes*. Chem Rev. 2005; **105**(4):1025-102.

32. Sayes CM, Wahi R, Kurian PA, Liu Y, West JL, Ausman KD, Warheit DB, Colvin VL. *Correlating nanoscale titania structure with toxicity: a cytotoxicity and inflammatory response study with human dermal fibroblasts and human lung epithelial cells*. Toxicol Sci 2006, **92**:174–185.

33. Chen, X. and S.S. Mao. *Titanium Dioxide Nanomaterials: Synthesis, Properties, Modifications, and Applications*. Chemical Reviews, 2007. **107**(7): p. 2891-2959.

34. Chen, X. and A. Selloni. *Introduction: Titanium Dioxide (TiO_2) Nanomaterials*. Chemical Reviews, 2014. **114**(19): p. 9281-9282.

35. Warheit DB, Webb TR, Reed KL, Frerichs S, Sayes CM. *Pulmonary toxicity study in rats with three forms of ultrafine-TiO_2 particles: differential responses related to surface properties.* Toxicology 2007, **230**:90–104.

36. Xue C, Wu J, Lan F, Liu W, Yang X, Zeng F, Xu H. *Nano titanium dioxide induces the generation of ROS and potential damage in HaCaT cells under UVA irradiation*. J Nanosci Nanotechnol 2010, **10**:8500–8507.

37. Petkovic J, Zegura B, Stevanovic M, Drnovsek N, Uskokovic D, Novak S, Filipic M. *DNA damage and alterations in expression of DNA damage responsive genes induced by TiO_2 nanoparticles in human hepatoma HepG2 cells*. Nanotoxicology 2011, **5**:341–353.

38. Wang C, Li Y. *Interaction and nanotoxic effect of TiO(2) nanoparticle on fibrinogen by multi-spectroscopic method*. Sci Total Environ 2012, **429**:156–160.

39. Tedja R, Lim M, Amal R, Marquis C: *Effects of serum adsorption on cellular uptake profile and consequent impact of titanium dioxide nanoparticles on human lung cell lines*. ACS Nano 2012, **6**:4083–4093.

40. Saber AT, Jensen KA, Jacobsen NR, Birkedal R, Mikkelsen L, Moller P, Loft S, Wallin H, Vogel U. *Inflammatory and genotoxic effects of nanoparticles designed for inclusion in paints and lacquers*. Nanotoxicology 2012, **6**:453–471.

41. Doran SJ. *The history and principles of chemical dosimetry for 3-D radiation fields: Gels, polymers and plastics*. Appl Radiat Isot. 2009; **67**(3):393-8.

42. Baldock C, De Deene Y, Doran S, Ibbott G, Jirasek A, Lepage M, *et al. Polymer gel dosimetry*. Phys Med Biol. 2010; **55**(5):R1-R63.

43. Maryanski MJ, Ibbott GS, Eastman P, Schulz RJ, Gore JC. *Radiation therapy dosimetry using magnetic resonance imaging of polymer gels*. Med Phys. 1996; **23**(5):699-705.

44. Schreiner LJ. *Review of Fricke gel dosimeters*. J Phys: Conf Ser. 2004; **3**(1):9.

45. Alqathami M, Blencowe A, Yeo UJ, Doran SJ, Qiao G, Geso M. *Novel multicompartment 3-dimensional radiochromic radiation dosimeters for nanoparticle-enhanced radiation therapy dosimetry*. Int J Radiat Oncol Biol Phys. 2012 3; **84**(4):549-555.

46. Guo P, Adamovics J, Oldham M. *Characterization of a new radiochromic three-dimensional dosimeter*. Med Phys. 2006; **33**(5):1338-456.

47. Harold Q. Fuller, Richard M. Fuller, Robert G. Fuller. *Physics, Including Human Applications*. 3rd Edition. Michigan. Harper & Row, 1978.

48. Hooshang N, Shuzo U, Dimitris E. *Interaction of Radiation with Matter*. 1st Edition, Taylor and Francis Group, Florida, 2012.

49. Niu CJ, Foltz WD, Velec M, Moseley JL, Al-Mayah A, Brock KK. *A novel technique to enable experimental validation of deformable dose accumulation*. Med Phys. 2012; **39**(2):765-76.

50. Adamovics J, Guo P, Burgess D, Manzoor A, Oldham M. *PRESAGE™ - Development and optimization studies of a 3D radiochromic plastic dosimeter–Part 2*. J Phys: Conf Ser. 2006; **56**(1):176.

51. Adamovics J, Jordan K, Dietrich J. PRESAGE™ - *Development and optimization studies of a 3D radiochromic plastic dosimeter-Part 1*. J Phys: Conf Ser. 2006; **56**(1):172-5.

52. Selike S., Culter J., Hernandez R. *Plastics packaging: Properties, processing, applications, and regulations*. 2nd Edition: Hanser; 2004.

53. Werner B, He ZA, Hessell ET. *Catalysis of the isocyanate-hydroxyl reaction by non-tin catalysts*. Prog Org Coat. 1999; **35**(1-4):19-29.

54. Zuo M, Takeichi T. *Preparation and characterization of poly(urethane–imide) films prepared from reactive polyimide and polyurethane prepolymer*. Polymer. 1999; **40**(18):5153-60.

55. Gogolewski S. *Selected topics in biomedical polyurethanes. A review*. Colloid Polym Sci. 1989; **267**(9):757-85.

56. Blank WJ, He ZA, Picci ME. *Catalysis of blocked isocyanates with non-tin catalysts*. Abstracts of Papers of the American Chemical Society. 1998; **216**:U849.

57. Issam A, Sankar G. *Catalysis of secondary alcohol blocked isocyanate-hydroxyl terminated polybutadiene cure reaction*. Polymer Science Series B. 2011; **53**(1):52-6.

58. Carroy A, Hintermann T, Baudin G, Bauer D, Contich P, Dietliker K, et al. *Novel latent catalysts for 2K-PUR systems*. Prog Org Coat. 2010; **68**(1-2):37-41.

59. Senthilkumar N, Luqman M. *Metal-containing polyurethanes*: An overview. Mater Sci For. 2010; **657**:1-25.

60. Denisov E.T, Denisova T.G, Pokidova T.S. *Handbook of free radical initiators*. New Jersey: John Wiley & Sons, Inc., 2003.

61. Alqathami M, Blencowe A, Qiao G, Butler D, Geso M. *Optimization of the sensitivity and stability of the PRESAGE™ dosimeter using trihalomethane radical initiators*. Radiat Phys Chem. 2012; **81**(7):867-873.

62. Muthyala. M. *Chemistry and applications of leuco dyes*. 1 Edition. New York: Springer; 1997.

63. Adamovics J, Maryanski MJ. *Characterisation of PRESAGE™: A new 3-D radiochromic solid polymer dosemeter for ionising radiation.* Radiat Prot Dosim. 2006; **120**(1-4):107-112.

64. Adamovics J, Maryanski MJ. *New 3D radiochromic solid polymer dosimeter from leuco dyes and a transparent polymeric matrix*. Med Phys. 2003; **30**(6):1349.

65. Doran SJ, Thomas R, Hollingdale R, Adamovics J, Nisbet A. *Electron dosimetry in the presence of small cavities*. J Phys: Conf Ser. 2010; **250**(1):012090.

66. Annabell N, Yagi N, Umetani K, Wong C, Geso M. *Evaluating the peak-to-valley dose ratio of synchrotron microbeams using PRESAGE fluorescence*. J Synchr Radiat. 2012; **19**(3):332-9.

67. Grant RL, Crowder ML, Ibbott GS, Simon J, Frank RK, Rogers J, et al. *Three-dimensional dosimetry of a beta-emitting radionuclide using PRESAGE dosimeters*. J Phys: Conf Ser. 2010; **250**(1).

68. Zhao L, Newton J, Oldham M, Das IJ, Cheng CW, Adamovics J. *Feasibility of using PRESAGE® for relative 3D dosimetry of small proton fields*. Phys Med Biol. 2012; **57**(22):N431-43.

69. Zhao L, Das IJ, Zhao Q, Thomas A, Adamovics J, Oldman M. *Determination of the depth dose distribution of proton beam using PRESAGETM dosimete*r. J Phys: Conf Ser. 2010; **250**(1):012035.

70. Guo P, Adamovics J, Oldham M. *Characterization of a new radiochromic three-dimensional dosimeter*. Med Phys. 2006; **33**(5):1338-456.

71. Berger M J, Hubbell J H, Seltzer S M, Chang J, Coursey J S, Sukumar R, *et al. ESTAR, PSTAR, and ASTAR: Computer Programs for Calculating Stopping-Power and Range Tables for Electrons, Protons, and Helium Ions*. 1.2.3 Edition: National Institute of Standards and Technology. Gaithersburg, MD; 2005.

72. Hubbell JH, Seltzer SM. *Tables of x-ray mass attenuation coefficients and mass energy absorption coefficients 0.01 to 100 MeV for elements Z = 1 to 92*. National Institute of Standards and Technology. Gaithersburg, MD; 2004.

73. Gorjiara T, Hill R, Kuncic Z, Bosi S, Davies J, Baldock C. *Radiological characterization and water equivalency of genipin gel for x-ray and electron beam dosimetry*. Phys Med Biol. 2011; **56**(15):4685-99.

74. Podgorsak E. Radiation Oncology Physics: *A Handbook for Teachers and Students*. International Atomic Energy Agency; 2005.

75. Thomas A, Newton J, Adamovics J, Oldham M. *Commissioning and benchmarking a 3D dosimetry system for clinical use.* Med Phys. 2011; **38**(8):4846-4857.

76. Guo P, Adamovics J, Oldham M. *Simple 3D validation experiments for PRESAGE TM /optical-CT dosimetry*. J Phys: Conf Ser. 2006; **56**(1):187.

77. Al-Nowais S, Doran SJ, Kacperek A, Krstajic N, Adamovics J, Bradley DA. Preliminary *analysis of LET effects in the dosimetry of proton beams using PRESAGE(TM) and optical CT*. Appl Radiat Isot. 2009; **67**(3):415-8.

78. Al-Nowais S, Nisbet A, Adamovics J, Doran SJ. *An attempt to determine the saturation dose for PRESAGEtm*. J Phys: Conf Ser. 2009; **164**.

79. Connell, P.P. and S. Hellman. *Advances in radiotherapy and implications for the next century: a historical perspective*. Cancer research. 2009; **69**: 383-392.

80. Bhide, S. and C. *Nutting. Recent advances in radiotherapy*. BMC medicine. 2010; **8**: 1.

81. Begg AC, Stewart FA, Vens C. *Strategies to improve radiotherapy with targeted drugs*. Nat Rev Cancer. 2011; **11**(4):239-53.

82. Jain S, Hirst DG, O'Sullivan JM. *Gold nanoparticles as novel agents for cancer therapy*. Br J Radiol. 2012; **85**(1010):101-13.

83. Oronsky BT, Knox SJ, Scicinski J. *Six degrees of separation: The oxygen effect in the development of radiosensitizers*. Translational Oncology. 2011; **4**(4):256-65.

84. Wu W, Yang Q, Li T, Zhang P, Zhou R, Yang C. *Hemoglobin-based oxygen carriers combined with anticancer drugs may enhance sensitivity of radiotherapy and chemotherapy to solid tumors*. Arti Cells Blood Subst Biotech. 2009; **37**(4):163-5.

85. Dische S. *A review of hypoxic cell radiosensitization*. Int J Radiat Oncol Biol Phys. 1991; **20**(1):147-52.

86. Corde S, Biston MC, Elleaume H, Esteve F, Charvet AM , Joubert A, et al. *Lack of cell death enhancement after irradiation with monochromatic synchrotron x-rays at the k-shell edge of platinum incorporate in living SQ20B human cells as cis-Diamminedichloroplatinum (II)*. Radiat Res. 2002; **158**:763-70.

87. Spiers F.W., *the Influence of Energy Absorption and Electron Range on Dosage in Irradiated Bone*. Br. J. Radiol. 1949. **22**: p. 521-533.

88. Spiers F.W., *A Review of the Theoretical and Experimental Methods of Determining Radiation Dose in Bone*. Br. J. Radiol, 1966; **39**: p. 216-221.

89. Alm Carlsson, G., *Dosimetry of interfaces. Theoretical Analysis and Measurements by Means of Thermolumines-cent LiF*. . Acta Radiologica, 1973; Suppl 332.

90. Das, I.J., Chopra K.L., *Backscatter Dose Perturbation in Kilovoltage Photon Beams at High Atomic Number Interfaces*. Medical Physics, 1995; **22**: p. 767–773.

91. Das, I.J., *Forward dose perturbation at high atomic number interfaces in kilovoltage X-ray beams*. Medical Physics, 1997; **24**: p. 1781–1787.

92. Morkovin D., Feldman. A., *Dosimetry in living cells irradiated on glass: a correction*. . Br. J. Radiol., 1959; **32**: p. 282.

93. Zellmer D.L., Chapman J.D., Stobbe C.C., Xu F. , Das, I. J., *Radiation fields backscattered from material interfaces: I. Biological effectiveness*. Radiation Research, 1998; **50**: p. 406–415.

94. Jain, S., D. Hirst, and J. O'sullivan. *Gold nanoparticles as novel agents for cancer therapy*. The British journal of radiology. 2014.

95. Regulla, D., L. Hieber, and M. Seidenbusch. *Physical and biological interface dose effects in tissue due to X-ray-induced release of secondary radiation from metallic gold surfaces.* Radiation research. 1998; **150**: 92-100.

96. Matsudaira H, Ueno AM, Furuno I. *Iodine contrast medium sensitizes Cultured Mammalian cells to x rays but not to γ rays*. Radiat Res. 1980; **84**: 144-8.

97. Garnica-Garza HM. *A Monte Carlo comparison of three different media for contrast enhanced radiotherapy of the prostate*. Tech Cancer Res Treat. 2010; **9**(3):271-8.

98. Adam JF, Biston MC, Joubert A, Charvet AM, Le Bas JF, Estève F, et al. *Enhanced delivery of iodine for synchrotron stereotactic radiotherapy by means of intracarotid injection and blood–brain barrier disruption: 272 Quantitative iodine biodistribution studies and associated dosimetry*. Int J Radiat Oncol Biol Phys. 2005; **61**(4):1173-82.

99. Bahreyni M, Ghorbani M, Mehrpouyan M, Akbari F, Sabet LS, Meigooni AS. *A Monte Carlo study on tissue dose enhancement in brachytherapy: A comparison between gadolinium and gold nanoparticles*. Australas Phys Eng Sci Med. 2012; **35**(2):177-85.

100. Garnica-Garza HM. *Treatment planning considerations in contrast-enhanced radiotherapy: Energy and beam aperture optimization*. Phys Med Biol. 2011; **56**(2):341-55.

101. Regulla D.F., Hieber L. B. , Seidenbusch M., *Physical and biological interface dose effects in tissue due to x-ray induced release of secondary radiation from metallic gold surfaces.* Radiation Research, 1998; **150**: p. 92–100.

102. Herold D.M., Das I.J., Stobbe C.C., Iyer R.V., Chapman J.D., *Gold Microspheres: a selective technique for producing biologically effective dose enhancement*. Int. J. Radiat. Biol., 2000; **76**: p. 1357-1364.

103. Hainfeld JF, Slatkin DN, Focella TM, Smilowitz HM. *Gold nanoparticles: a new X-ray contrast agent*. Br J Radiol. 2006; **79**(939):248-53.

104. Hainfeld J.F., Slatkin D.N., Smilowitz H.M. *The use of gold nanoparticles to enhance radiotherapy in mice*. Phys. Med. Biol., 2004; **49**: p. 309-315.

105. Xi D, Dong S, Meng X, Lu Q, Meng L, Ye J. *Gold nanoparticles as computerized tomography (CT) contrast agents*. RSC Advances. 2012; **2**(33):12515-24.

106. Zhang X, Xing JZ, Chen J, Ko L, Amanie J, Gulavita S, et al. *Enhanced radiation sensitivity in prostate cancer by gold-nanoparticles*. Clin Investi Med. 2008; **31**(3):E160-E7.

107. Kong T, Zeng J, Wang X, Yang X, Jing Y, McQuarrie S, McEwan A, Roa W, Chen J and Xing JZ. *Enhancement of radiation toxicity in breast cancer cells by localized attachment of gold nanoparticles*. Small. 2008; **4**(9):1537-43.

108. Liu CJ, Wang CH, Chen ST, Chen HH, Leng WH, Chien CC, et al. *Enhancement of cell radiation sensitivity by pegylated gold nanoparticles*. Phys Med Biol. 2010; **55**(4):931-45.

109. Rahman WN, Bishara N, Ackerly T, He CF, Jackson P, Wong C, et al. *Enhancement of radiation effects by gold nanoparticles for superficial radiation therapy*. Nanomed: Nanotech Biol Med. 2009; **5**(2):136-42.

110. Hainfeld JF, Dilmanian FA, Slatkin DN, Smilowitz HM. *Radiotherapy enhancement with gold nanoparticles*. J Pharm Pharmacol. 2008; **60**(8):977-85.

111. Jain S, Coulter JA, Hounsell AR, Butterworth KT, McMahon SJ, Hyland WB, et al. *Cell-Specific Radiosensitization by Gold Nanoparticles at Megavoltage Radiation Energies*. Int J Radiat Oncol Biol Phys. 2011; **79**(2):531-9.

112. Sperling RA, Rivera Gil P, Zhang F, Zanella M, Parak WJ. *Biological applications of gold nanoparticles*. Chem Soc Rev. 2008; **37**(9):1896-908.

113. Chithrani DB, Jelveh S, Jalali F, Van Prooijen M, Allen C, Bristow RG, et al. *Gold nanoparticles as radiation sensitizers in cancer therapy*. Radiat Res. 2010; **173**(6):719-28.

114. Sang Hyun C, Bernard LJ, Sunil K. *The dosimetric feasibility of gold nanoparticle-aided radiation therapy (GNRT) via brachytherapy using low-energy gamma-/x-ray sources*. Phys Med Biol. 2009; **54**(16):4889-905.

115. Sang Hyun C. *Estimation of tumour dose enhancement due to gold nanoparticles during typical radiation treatments: a preliminary montecarlo study*. Phys Med Biol. 2005; **50**(15):163-73.

116. McMahon SJ, Mendenhall MH, Jain S, Currell F. *Radiotherapy in the presence of contrast agents: a general figure of merit and its application to gold nanoparticles*. Phys Med Biol. 2008; **53**(20):5635-51.

117. Zhang SX, Gao J, Buchholz TA, Wang Z, Salehpour MR, Drezek RA, et al. *Quantifying tumor selective radiation dose enhancements using gold nanoparticles: a Monte Carlo simulation study*. Biomed Microdevices 2009; **11**:925-33.

118. Garnica-Garza H. *Contrast-enhanced radiotherapy: feasibility and characteristics of the physical absorbed dose distribution for deep-seated tumors*. Phys Med Biol. 2009; **54**(18):5411-25.

119. Leung MK, Chow JC, Chithrani BD, Lee MJ, Oms B, Jaffray DA. *Irradiation of gold nanoparticles by x-rays: Monte Carlo simulation of dose enhancements 276 and the spatial properties of the secondary electrons production*. Med Phys. 2011; **38**(2):624-31.

120. McMahon SJ, Hyland WB, Muir MF, Coulter JA, Jain S, Butterworth KT, et al. *Nanodosimetric effects of gold nanoparticles in megavoltage radiation therapy*. Radiother Oncol. 2011; **100**(3):412-6.

121. Cho S.H., *Estimation of tumour dose enhancement due to gold nanoparticles during typical radiation treatments: a preliminary Monte Carlo study*. Phys. Med. Biol., 2005; **50**: p. 163-173.

122. Cho S.H., Jones B.L., Krisnan S., *The dosimetric feasibility of gold nanoparticle aided radiation therapy (GNRT) via brachytherapy using low-energy gamma-/x-ray sources*. Phys. Med. Biol., 2009; **54**: p. 4889-4905.

123. Alqathami M, Blencowe A, Yeo UJ, Doran SJ, Qiao G, Geso M. *Novel multicompartment 3-dimensional radiochromic radiation dosimeters for nanoparticle-enhanced radiation therapy dosimetry*. Int J Radiat Oncol Biol Phys. 2012 3; **84**(4):e549-e55.

124. Panagiotis T, Bo L, Fulya C, Wilfred FN, Ross IB, Constantin K, et al. *Impact of beam quality on megavoltage radiotherapy treatment techniques utilizing gold nanoparticles for dose enhancement*. Phys Med Biol. 2013; **58**(3):451-64.

125. Lechtman E, Chattopadhyay N, Cai Z, Mashouf S, Reilly R, Pignol JP. *Implications on clinical scenario of gold nanoparticle radiosensitization in regards to photon energy, nanoparticle size, concentration and location*. Phys Med Biol. 2011; **56**(15):4631-47.

126. Tiekink ERT. *Antimony and bismuth compounds in oncology*. Crit Rev Oncol/Hematol. 2002; **42**(3):217-24.

127. Mohan R. *Green bismuth*. Nat Chem. 2010; **2**(4):336.

128. Rabin O, Perez JM, Grimm J, Wojtkiewicz G, Weissleder R. *An X-ray computed tomography imaging agent based on long-circulating bismuth sulphide nanoparticles*. Nat Mater. 2006; **5**(2):118-22.

129. Kinsella JM, Jimenez RE, Karmali PP, Rush AM, Kotamraju VR, Gianneschi NC, et al. *X-Ray Computed Tomography Imaging of Breast Cancer by using Targeted Peptide-Labeled Bismuth Sulfide Nanoparticles*. Angew Chem Int Ed. 2011; **50**(51):12308-11.

130. Ai K, Liu Y, Liu J, Yuan Q, He Y, Lu L. *Large-Scale Synthesis of Bi2S3 Nanodots as a Contrast Agent for In Vivo X-ray Computed Tomography Imaging*. Adv Mater. 2011; **23**(42):4886-91.

131. Carter JD, Cheng NN, Qu Y, Suarez GD, Guo T. *Nanoscale Energy Deposition by X-ray Absorbing Nanostructures*. J Phys Chem B. 2007; **111**(40):11622-5.

132. Algethami M, Geso M, Piva T, Blencowe A, Lu L, Ai K, Harty P, Gan E. *Radiation dose enhancement using Bi2S3 nanoparticles in cultured mouse PC3 prostate and B16 melanoma cells*. NanoWorld Journal. 2015; **1**(2): 97-102.

133. McMahon, S.J. and F.J. Currell, *Chapter 3 - Gold Nanoparticles for Imaging and Radiotherapy*, in *Frontiers of Nanoscience*, S. Huw Editor. Elsevier, 2013; p. 65-93.

134. Jiang, J., et al., *Does nanoparticle activity depend upon size and crystal phase?* Nanotoxicology, 2008. **2**(1): p. 33-42.

135. Park, E.-J., et al., *Oxidative stress and apoptosis induced by titanium dioxide nanoparticles in cultured BEAS-2B cells.* Toxicology Letters, 2008. **180**(3): p. 222-229.

136. Yin, J.-J., et al. *Phototoxicity of nano titanium dioxides in HaCaT keratinocytes—generation of reactive oxygen species and cell damage*. Toxicology and applied pharmacology. 2012; **263**: 81-88.

137. Babaei, M. and M. Ganjalikhani. *The potential effectiveness of nanoparticles as radio sensitizers for radiotherapy*. Bioimpacts. 2014; **4**: 15.

138. Jin, C., et al., *Cellular toxicity of TiO_2 nanoparticles in anatase and rutile crystal phase.* Biological trace element research, 2011. **141**(1-3): p. 3-15.

139. Townley, H.E., J. Kim, and P.J. Dobson, *In vivo demonstration of enhanced radiotherapy using rare earth doped titania nanoparticles.* Nanoscale, 2012. **4**(16): p. 5043-5050.

140. Mirjolet, C., et al., *The radiosensitization effect of titanate nanotubes as a new tool in radiation therapy for glioblastoma: A proof-of-concept.* Radiotherapy and Oncology, 2013. **108**(1): p. 136-142.

141. Jiang, J., et al. *Does nanoparticle activity depend upon size and crystal phase?* Nanotoxicology. 2000; **2**: 33-42.

142. Roeske JC, Nuñez L, Hoggarth M, Labay E, Weichselbaum RR. *Characterization of the theorectical radiation dose enhancement from nanoparticles*. Techn Cancer Rese Treat. 2007; **6**(5):395-401.

143. Estève F, Corde S, Elleaume H, Adam JF, Joubert A, Charvet AM, et al. *Enhanced radio sensitivity with iodinated contrast agents using 277 monochromatic synchrotron x-rays on human cancerous cells*. Acad Radiol. 2002; **9**(2):S540-S3.

144. Corde S, Joubert A, Adam JF, Charvet AM, Le Bas JF, Esteve F, et al. *Synchrotron radiation-based experimental determination of the optimal energy for cell radiotoxicity enhancement following photoelectric effect on stable iodinated compounds*. Br J Cancer. 2004; **91**(3):544-51.

145. Li W, Zeng T. *Preparation of TiO_2 Anatase Nanocrystals by TiCl4 Hydrolysis with Additive H2SO4*. PLoS ONE. 2011; **6** (6): e21082.

146. B. GRADZIK, M. EL FRAY, E. WIŚNIEWSKA, *Surface modification of TiO_2 and SiO_2 nanoparticles for application in polymeric nanocomposites,* CHEMIK 2011; **65**(7): 621-626.

147. Zhao, J., et al., *Surface modification of TiO_2 nanoparticles with silane coupling agents.* Colloids and Surfaces A: Physicochemical and Engineering Aspects, 2012; **413**(0): p. 273-279.

148. Sabzi, M., et al., *Surface modification of TiO_2 nano-particles with silane coupling agent and investigation of its effect on the properties of polyurethane composite coating.* Progress in Organic Coatings, 2009; **65**(2): p. 222-228.

149. Mano, S.S., et al., *Effect of Polyethylene Glycol Modification of TiO_2 Nanoparticles on Cytotoxicity and Gene Expressions in Human Cell Lines.* International Journal of Molecular Sciences, 2012. **13**(3): p. 3703-3717.

150. Pan, H. Wang, X. Xiao, Sh. Yu, L. Zhang, ZhiJun, *Preparation and characterization of TiO_2 nanoparticles surface-modified by octadecyltrimethoxysilane*, NISCAIR-CSIR. 2013; **20**: 561-567.

151. Kumar PM, Badrinarayanan S, Sastry M. *Nanocrystalline TiO_2 studied by optical, FTIR and X-ray photoelectron spectroscopy: correlation to presence of surface states*. Thin Solid Films. 2000; **358**(1):122-30.

152. Williams DB, Carter CB. *The transmission electron microscope*. In Transmission electron microscopy Springer Us. 1996: pp. 3-17.

153. Miao J, Ishikawa T, Johnson B, Anderson EH, Lai B, Hodgson KO. *High resolution 3D x-ray diffraction microscopy*. Physical review letters. 2002; **89(**8):088303.

154. Hirech K, Payan S, Carnelle G, Brujes L, Legrand J. *Microencapsulation of an insecticide by interfacial polymerisation*. Powder Technology. 2003; **130**(1):324-30.

155. Smith BC. *Fourier transform infrared spectroscopy*. CRC, Boca Raton, FL. 1996.

156. Yen JH, Lin KH, Wang YS. *Acute Lethal Toxicity of Environmental Pollutants to Aquatic Organisms*. Ecotoxicol Environ Saf. 2002; **52(**2):113-6.

157. Hawkins DM, Basak SC, Kraker J, Geiss KT, Witzmann FA. *Combining Chemodescriptors and Biodescriptors in Quantitative Structure−Activity Relationship Modeling*. J Chem Inf Model. 2005; **46**(1):9-16.

158. Savolainen K, Pylkkänen L, Norppa H, Falck G, Lindberg H, Tuomi T, et al. *Nanotechnologies, engineered nanomaterials and occupational health and safety – A review*. Saf Sci. 2010; **48**(8):957-63.

159. Aschberger K, Micheletti C, Sokull-Klüttgen B, Christensen FM. *Analysis of currently available data for characterising the risk of engineered nanomaterials to the environment*

and human health — Lessons learned from four case studies. Environ Int. 2011; **37**(6):1143-56.

160. Alqathami M, Blencowe A, Qiao G, Adamovics J, Geso M. *Optimizing the sensitivity and radiological properties of the PRESAGE® dosimeter using metal compounds*. Radiat Phys Chem. 2012; **81**(11):1688-95.

161. Jancar J, Douglas JF, Starr FW, Kumar SK, Cassagnau P, Lesser AJ, Sternstein SS, Buehler MJ. *Current issues in research on structure–property relationships in polymer nanocomposites*. Polymer. 2010; **51**(15):3321-43.

162. Mandzy N, Grulke E, Druffel T. B*reakage of TiO2 agglomerates in electrostatically stabilized aqueous dispersions*. Powder Technol. 2005; **160**(2):121-6.

163. Liu Y, Cheng C, Prud'homme RK, Fox RO. *Mixing in a multi-inlet vortex mixer (MIVM) for flash nano-precipitation*. Chem Eng Sci. 2008; **63**(11):2829-42.

164. Alqathami M, Adamovics J, Benning R, Qiao G, Geso M, Blencowe A. *Evaluation of ultra-sensitive leucomalachite dye derivatives for use in the PRESAGE® dosimeter*. Radiation Physics and Chemistry. 2013; **85**: 204-209.

165. Krstajić, Nikola, Doran SJ. *Characterization of a parallel-beam CCD optical-CT apparatus for 3D radiation dosimetry*. Phys Med Biol. 2007; **52**(13):3693-13.

166. Rahman ATA, Brauer-Krisch E, Brochard T, Adamovics J, Clowes SK, Bradley D, et al. *Sophisticated test objects for the quality assurance of optical computed tomography scanners*. Phys Med Biol. 2011; **56**(14):4177-99.

167. Olding T, Holmes O, Schreiner LJ. *Cone beam optical computed tomography for gel dosimetry I: scanner characterization*. Phys Med Biol. 2010; **55**(10):2819-40.

168. Olding T, Schreiner LJ. *Cone-beam optical computed tomography for gel dosimetry II: imaging protocols*. Phys Med Biol. 2011; **56**(5):1259-79.

169. Papadakis AE, Zacharakis G, Maris TG, Ripoll J, Damilakis J. *A New Optical-CT Apparatus for 3-D Radiotherapy Dosimetry: Is Free Space Scanning Feasible?* Med Imag, IEEE Transa on. 2010; **29**(5):1204-12.

170. Thomas A, Newton J, Oldham M. *A method to correct for stray light in telecentric optical-CT imaging of radiochromic dosimeters*. Phys Med Biol. 2011; **56**(14):4433-51.

171. Youkahana, Esho Qasho, Frank Gagliardi, and Moshi Geso. *"Two-dimensional scanning of PRESAGE® dosimetry using UV/VIS spectrophotometry and its potential application in radiotherapy."* Biomedical Physics & Engineering Express. 2016; **2**(4): 045009.

172. Rahman WN, Wong CJ, Ackerly T, Yagi N, Geso M. *Polymer gels impregnated with gold nanoparticles implemented for measurements of radiation dose enhancement in synchrotron and conventional radiotherapy type beams*. Australasian physical & engineering sciences in medicine. 2012; **35**(3):301-9.

173. Shi H, Magaye R, Castranova V, Zhao J. *Titanium dioxide nanoparticles: a review of current toxicological data*. Particle and fibre toxicology. 2013; **10**: 1.

174. *Technical bulletin: CellTiter 96® AQueous One Solution Cell Proliferation Assay*.www.promega.com, 2009.

175. Slavotinek A., McMillan T.J., Steel C.M., *Measurement of radiation survival using the MTT assay.* European Journal of Cancer, 1994. **30A**: p. 1376-1382.

176. Elkind, M. E. and Whitmore, G. F. *In vitro survival curves, in The Radiobiology of Cultured Mammalian Cells*. Gordon and Breach, New York, NY. 1976; pp. 53–115.

177. Puck, T. T. and Marcus, P. I. Action of X-rays on mammalian cells. J. Exp. Med. 1956; **103**: 653–666.

178. Hall, E. J. *Cell survival curves, in Radiobiology for the Radiologist*. 5th Edition. (Hall, E. J., ed.), Philadelphia, J.B. Lippincott. 2000; pp. 32–50.

179. Munshi A, Hobbs M, Meyn RE. *Clonogenic cell survival assay*. Chemosensitivity: Volume 1 *In Vitro* Assays. 2005; **21**: p.8.

180. Franken NA, Rodermond HM, Stap J, Haveman J, Van Bree C. *Clonogenic assay of cells in vitro.* Nature protocols. 2006; **1**(5):2315-9.

181. Kollbek K, Sikora M, Kapusta C, Szlachetko J, Zakrzewska K, Kowalski K, et al. *X-ray spectroscopic methods in the studies of nonstoichiometric TiO_2−x thin films*. Applied Surface Science. 2013; **281**: 100-104.

182. Antic Z, Krsmanovic RM, Nikolic MG, Cincovic MM, Mitric M, Polizzi S, et al. *Multisite luminescence of rare earth doped TiO_2 anatase nanoparticles*. Mat.Chem.Phys. 2012; **135**: 1064-1069.

183. Rahim S, Ghamsari MS, Radiman S. *Surface modification of titanium oxide nanocrystals with PEG*. Scientia Iranica. 2012; **19**: 948-953.

184. Yin, J.-J., et al. *Phototoxicity of nano titanium dioxides in HaCaT keratinocytes—generation of reactive oxygen species and cell damage*. Toxicology and applied pharmacology. 2012; **263**: 81-88.

185. Jin, C., et al. *Cellular toxicity of TiO_2 nanoparticles in anatase and rutile crystal phase*. Biological trace element research. 2011; **141**: 3-15.

186. Townley, H.E., J. Kim, and P.J. Dobson. *In vivo demonstration of enhanced radiotherapy using rare earth doped titania nanoparticles*. Nanoscale. 2012; **4**: 5043-5050.

187. György E, Del Pino AP, Serra P, Morenza JL. *Depth profiling characterisation of the surface layer obtained by pulsed Nd: YAG laser irradiation of titanium in nitrogen.* Surface and Coatings Technology. 2003; **173**(2):265-70.

188. Babaei, M. and M. Ganjalikhani. *The potential effectiveness of nanoparticles as radio sensitizers for radiotherapy*. Bioimpacts. 2014; **4**: 15.

189. Juang T, Newton J, Niebanck M, Benning R, Adamovics J, Oldham M. *Customising PRESAGE® for diverse applications*. IOP Publishing: Conference Series 2013; **444** (1): p. 012029.

190. Alqathami M. *Novel 3D radiochromic dosimeters for advanced radiotherapy techniques*. Doctoral dissertation, RMIT University, 2013.

191. Meesat R, Jay-Gerin JP, Khalil A, Lepage M. *Evaluation of the dose enhancement of iodinated compounds by polyacrylamide gel dosimetry*. Phys Med Biol.2009; **54**(19):5909.

192. Youkhana E. Q., Feltis B., Blencowe A., Geso M. *Titanium Dioxide Nanoparticles as Radiosensitisers: An In vitro and Phantom-Based Study*. International Journal of Medical Sciences. 2017; **14**(6): 602-614.

193. Alqathami M, Blencowe A, Geso M, Ibbott G. *Quantitative 3D determination of radiosensitization by Bismuth-based nanoparticles*. Journal of Biomedical Nanotechnology. 2016; **12**: 464-471.

194. Mostaar A, Hashemi B, Zahmatkesh MH, Aghamiri SMR, Mahdavi SR. *A basic dosimetric study of PRESAGE: The effect of different amounts of fabricating components on the sensitivity and stability of the dosimeter*. Phys Med Biol. 2010; **55**(3):903-12.

195. Blanksby SJ, Ellison GB. *Bond Dissociation Energies of Organic Molecules*. Acc Chem Res. 2003; **36**(4):255-63.

196. Glassman I, Yetter RA. *Appendix D - Bond Dissociation Energies of Halocarbons*. Combustion (4th Edition). Burlington: Academic Press; 2008.

197. Caine MA, McCabe RW, Wang L, Brown RG, Hepworth JD. *The inhibition of triphenylmethane primary dye fading in carbonless copying paper systems by singlet oxygen quenching bis(dithiocarbamato)nickel(II) complexes*. Dyes and Pigments. 2002; **52**(1):55-65.

198. Oda H. *New developments in the stabilization of leuco dyes: effect of UV absorbers containing an amphoteric counter-ion moiety on the light fastness of color formers.* Dyes and Pigments. 2005; **66**(2):103-8.

199. Gorjiara T, Hill R, Kuncic Z, Adamovics J, Bosi S, Kim JH, et al. *Investigation of radiological properties and water equivalency of PRESAGE® dosimeters.* Med Phys. 2011; **38**(4):2265-74.

200. Malich G, Markovic B, Winder C. *The sensitivity and specificity of the MTS tetrazolium assay for detecting the in vitro cytotoxicity of 20 chemicals using human cell lines*. Toxicology. 1997; **124**(3):179-92.

201. Pogue AI, Jones BM, Bhattacharjee S, Percy ME, Zhao Y, Lukiw WJ. *Metal-sulfate induced generation of ROS in human brain cells: detection using an isomeric mixture of 5-and 6-*

carboxy-2', 7'-dichlorofluorescein diacetate (carboxy-DCFDA) as a cell permeant tracer. International journal of molecular sciences. 2012; **13**(8):9615-9626.

202. Anijdan SM, Shirazi A, Mahdavi SR, Ezzati A, Mofid B, Khoei S, Zarrinfard MA. *Megavoltage dose enhancement of gold nanoparticles for different geometric set-ups: Measurements and Monte Carlo simulation*. Iran. J. Radiat. Res. 2012; **10**(3-4):183-6.

203. Turnbull T, Douglass M, Paterson D, Bezak E, Thierry B, Kempson I. *Relating Intercellular Variability in Nanoparticle Uptake with Biological Consequence: A Quantitative X-ray Fluorescence Study for Radiosensitization of Cells.* Analytical chemistry. 2015; **87**(21): p.10693-7.

204. Zhao, Y., et al., *Exposure to titanium dioxide nanoparticles induces autophagy in primary human keratinocytes.* Small, 2013; **9**(3): p. 387-392.

205. Kenzaoui, B.H., et al., *Induction of oxidative stress, lysosome activation and autophagy by nanoparticles in human brain-derived endothelial cells.* Biochemical Journal, 2012; **441**(3): p. 813-821.

206. Lopes VR, Loitto V, Audinot JN, Bayat N, Gutleb AC, Cristobal S. *Dose-dependent autophagic effect of titanium dioxide nanoparticles in human HaCaT cells at non-cytotoxic levels*. Journal of nanobiotechnology. 2016; **14**(1):1.

207. Márquez-Ramírez SG, Delgado-Buenrostro NL, Chirino YI, Iglesias GG, López-Marure R. *Titanium dioxide nanoparticles inhibit proliferation and induce morphological changes and apoptosis in glial cells*. Toxicology. 2012; **302**(2): p. 146-56.

208. Ferin J, Oberdörster G. *Biological effects and toxicity assessment of titanium dioxides: anatase and rutile*. The American Industrial Hygiene Association Journal. 1985; **46**(2): p. 69-72.

209. Gerloff K, Fenoglio I, Carella E, Kolling J, Albrecht C, Boots AW, Förster I, Schins RP. *Distinctive toxicity of TiO2 rutile/anatase mixed phase nanoparticles on Caco-2 cells*. Chemical research in toxicology. 2012; **25**(3): p. 646-55.

210. Fröhlich E. *The role of surface charge in cellular uptake and cytotoxicity of medical nanoparticles.* Int J Nanomedicine. 2012; **7**(1): p. 5577-5591.

211. Hsiao IL, Huang YJ. *Effects of various physicochemical characteristics on the toxicities of ZnO and TiO 2 nanoparticles toward human lung epithelial cells*. Science of the Total Environment. 2011; **409**(7): p. 1219-1228.

212. Yin JJ, Liu J, Ehrenshaft M, Roberts JE, Fu PP, Mason RP, Zhao B. *Phototoxicity of nano titanium dioxides in HaCaT keratinocytes—generation of reactive oxygen species and cell damage*. Toxicology and applied pharmacology. 2012; **263**(1):81-88.

213. Nakayama M, Sasaki R, Ogino C, Tanaka T, Morita K, Umetsu M, Ohara S, Tan Z, Nishimura Y, Akasaka H, Sato K. *Titanium peroxide nanoparticles enhanced cytotoxic effects of X-ray irradiation against pancreatic cancer model through reactive oxygen species generation in vitro and in vivo*. Radiation Oncology. 2016; **11**(1):91.

214. Ortega R., Biston M.C., Devès G., Bohic S., Carmona A., *Nuclear microprobe determination of platinum quantitative distribution in rat brain tumors after cisplatin or carboplatin injection for PAT treatment of glioma.* Nucl. Instr. and Meth., 2005; **B231**: p. 321-325.

215. Cifter G, Chin J, Cifter F, Altundal Y, Sinha N, Sajo E, Ngwa W. *Targeted radiotherapy enhancement during electronic brachytherapy of accelerated partial breast irradiation (APBI) using controlled release of gold nanoparticles*. Physica Medica. 2015; **31**(8):1070-1074.

216. Laissue J.A., Geiser G., Spanne P.O., Dilmanian F.A., Gebbers J.O., Geiser M., Wu X.Y., Makar M.S., Micca P.L., Nawrocky M.M., Joel D.D., Slatkin D.N., *Neuropathology of ablation of rat gliosarcomas and contiguous brain tissues using a microplanar beam of synchrotron-Wiggler-generated x-rays.* Int. J. Cancer., 1998; **78**: p. 654-660.

217. Moran, J.M., et al., *Safety considerations for IMRT: executive summary.* Medical physics, 2011; **38**(9): p. 5067-5072.

218. Vandecasteele, J. and Y. De Deene, *Evaluation of radiochromic gel dosimetry and polymer gel dosimetry in a clinical dose verification.* Physics in medicine and biology, 2013; **58**(18): p. 6241.

219. Gagliardi FM, Cornelius I, Blencowe A, Franich RD, Geso M. *High resolution 3D imaging of synchrotron generated microbeams*. Medical physics. 2015; **42**(12):6973-86.

220. Lynch BD, Kozelka J, Ranade MK, Li JG, Simon WE, Dempsey JF. *Important considerations for radiochromic film dosimetry with flatbed CCD scanners and EBT GAFCHROMIC® film*. Medical physics. 2006; **33**(12):4551-6.

221. Sutherland, J. and D. Rogers, *Monte Carlo calculated absorbed-dose energy dependence of EBT and EBT2 film.* Medical physics, 2010; **37**(3): p. 1110-1116.

222. Bueno M, Carrasco P, Jornet N, Muñoz-Montplet C, Duch MA. *On the suitability of ultrathin detectors for absorbed dose assessment in the presence of high-density heterogeneities*. Medical physics. 2014; **41**(8).

223. Richley L, John AC, Coomber H, Fletcher S. *Evaluation and optimization of the new EBT2 radiochromic film dosimetry system for patient dose verification in radiotherapy*. Physics in medicine and biology. 2010; **55**(9):2601.

224. Devic S, Seuntjens J, Abdel-Rahman W, Evans M, Olivares M, Podgorsak EB, Vuong T, Soares CG. *Accurate skin dose measurements using radiochromic film in clinical applications*. Medical physics. 2006; **33**(4):1116-24.

225. Iqbal K, Gifford KA, Ibbott G, Grant RL, Buzdar S. *Comparison of an anthropomorphic PRESAGE® dosimeter and radiochromic film with a commercial radiation treatment planning system for breast IMRT: a feasibility study*. Journal of applied clinical medical physics. 2014; **15**(1).

226. Taylor ML, Smith RL, Dossing F, Franich RD. *Robust calculation of effective atomic numbers: The Auto-Zeff software*. Medical physics. 2012; **39**(4):1769-78.

227. http://www.bmglabtech.com/en/products/clariostar/

228. Dumas, M. and J.T. Rakowski, *Sensitivity and variability of Presage dosimeter formulations in sheet form with application to SBRT and SRS QA.* Medical physics, 2015. **42**(12): p. 7138-7143.

229. Singh KC. *Basic Physics*. New Delhi: PHI Learning Pvt. Ltd. 2009; pp. 211-212.

230. de Lima JJ. *Radioisotopes in medicine*. European journal of physics. 1998; **19**(6):485.

231. Cherry SR, Sorenson JA, Phelps ME. *Physics in nuclear medicine*. Elsevier Health Sciences; 2012.

232. Mariani G, Bruselli L, Kuwert T, Kim EE, Flotats A, Israel O, Dondi M, Watanabe N. *A review on the clinical uses of SPECT/CT*. European journal of nuclear medicine and molecular imaging. 2010; **37**(10):1959-85.

233. Prince JL, Links JM. *Medical imaging signals and systems*. Upper Saddle River, New Jersey: Pearson Prentice Hall; 2006.

234. Cho J, Wang M, Gonzalez-Lepera C, Mawlawi O, Cho SH. *Development of bimetallic (Zn@ Au) nanoparticles as potential PET-imageable radiosensitizers*. Medical Physics. 2016; **43**(8):4775-88.

235. Zhou J, Yu M, Sun Y, Zhang X, Zhu X, Wu Z, Wu D, Li F. *Fluorine-18-labeled $Gd^{3+/}Yb^{3+/}Er^{3+}$ co-doped NaYF 4 nanophosphors for multimodality PET/MR/UCL imaging*. Biomaterials. 2011; **32**(4):1148-56.

236. Jin M, Hao G, Sun X, Chen W. *Nanoparticle-based positron emission tomography and single photon emission computed tomography imaging of cancer*. Reviews in Nanoscience and Nanotechnology. 2012; **1**(1):3-21.

237. Pérez-Campaña C, Gómez-Vallejo V, Martin A, San Sebastián E, Moya SE, Reese T, Ziolo RF, Llop J. *Tracing nanoparticles in vivo: a new general synthesis of positron emitting metal oxide nanoparticles by proton beam activation*. Analyst. 2012; **137**(21):4902-6.

238. Abbas K, Cydzik I, Del Torchio R, Farina M, Forti E, Gibson N, Holzwarth U, Simonelli F, Kreyling W. *Radiolabelling of TiO2 nanoparticles for radiotracer studies*. Journal of Nanoparticle Research. 2010; **12**(7):2435-43.

239. Pérez-Campaña C, Sansaloni F, Gómez-Vallejo V, Baz Z, Martin A, Moya SE, Lagares JI, Ziolo RF, Llop J. *Production of 18F-Labeled Titanium Dioxide Nanoparticles by Proton Irradiation for Biodistribution and Biological Fate Studies in Rats*. Particle & Particle Systems Characterization. 2014; **31**(1):134-42.

240. Wilson RR. *Theory of the Cyclotron*. Journal of Applied Physics. 1940; **11**(12):781-96.

241. Livingston MS. *The Cyclotron*. II. Journal of Applied Physics. 1944; **15**(2):128-47.

242. Schlyer DJ, Ruth TJ. *Accelerator Production of Radionuclides*. Industrial Accelerators and Their Applications. 2012:**139**.

243. Townsend DW. *Physical principles and technology of clinical PET imaging*. Annals-Academy of Medicine Singapore. 2004; **33**(2):133-45.

244. Mamtimin M, Harmon F, Starovoitova VN. *Sc-47 production from titanium targets using electron linacs*. Applied Radiation and Isotopes. 2015; **102**:1-4.

245. Khandaker MU, Kim K, Lee MW, Kim KS, Kim GN, Cho YS, Lee YO. *Investigations of the nat Ti (p, x) 43, 44m, 44g, 46, 47, 48 Sc, 48 V nuclear processes up to 40MeV*. Applied Radiation and Isotopes. 2009; **67**(7):1348-54.

246. Rane S, Harris JT, Starovoitova VN. *47 Ca productions for $^{47}Ca/^{47}Sc$ generator system using electron linacs*. Applied Radiation and Isotopes. 2015; **97**:188-92.

247. Iwata R, Ido T, Brady F, Takahashi T, Ujiie A. *[^{18}F] Fluoride production with a circulating [^{18}O] water target*. International Journal of Radiation Applications and Instrumentation. Part A. Applied Radiation and Isotopes. 1987; **38**(11):979-84.

248. Khandaker MU, Kim K, Lee MW, Kim KS, Kim GN, Cho YS, Lee YO. *Investigations of the nat Ti (p, x) 43, 44m, 44g, 46, 47, 48 Sc, 48 V nuclear processes up to 40MeV*. Applied Radiation and Isotopes. 2009; **67**(7):1348-54.

249. S. R. Kennet, L. W. Mitchell, M. R. Anderson, D. G. Sargood, Nucl. Phys. 1981, **A368**, p-337.

250. Babich H, Borenfreund E. *Cytotoxicity of T-2 toxin and its metabolites determined with the neutral red cell viability assay*. Applied and environmental microbiology. 1991; **57**(7):2101-2103.

Appendices

Appendix I: Permission to reproduce published materials in chapter 7.

RMIT UNIVERSITY

Esho Youkhana <esho.youkhana@rmit.edu.au>

Request Permissions for Published Materials

Permissions <permissions@iop.org> 2 March 2017 at 01:49
To: Esho Youkhana <esho.youkhana@rmit.edu.au>

Dear Esho Youkhana,

Thank you for your email and for taking the time to seek this permission.

Regarding:

Esho Qasho Youkahana et al 2016 Biomed. Phys. Eng. Express 2 045009

When you transferred the copyright in your article to IOP, we granted back to you certain rights, including the right to include all or part of the Final Published Version of the article within any thesis or dissertation. Please note you may need to obtain separate permission for any third party content you included within your article.

Please include citation details, "© IOP Publishing. Reproduced with permission. All rights reserved" and for online use, a link to the Version of Record.

The only restriction is that if, at a later date, your thesis were to be published commercially, further permission would be required.

Please let me know if you have any further questions.

In the meantime, I wish you the best of luck with the completion of your dissertation.

Kind regards,

Kathryn Shaw

Copyright & Permissions Team
Gemma Alaway – Senior Rights & Permissions Adviser
Kathryn Shaw - Rights & Permissions Assistant

Contact Details
E-mail: permissions@iop.org

For further information about Copyright and how to get Permissions: http://iopscience.iop.org/page/copyright

Please see our Author Rights Policy http://ioppublishing.org/author-rights/

Please note: We do not provide signed permission forms as a separate attachment. Please print this email and provide it to your institution as proof of permission.

Please note: Any statements made by IOP Publishing to the effect that authors do not need to get permission to use any content where IOP Publishing is not the publisher is not intended to constitute any sort of legal advice. Authors must make their own decisions as to the suitability of the content they are using and whether they require permission for it to be published within their article.

From: Esho Youkhana <esho.youkhana@rmit.edu.au>
To: permissions@iop.org, Moshi Geso <moshi.geso@rmit.edu.au>, "Gagliardi, Frank" <frank.gagliardi@wbrc.org.au>,
Date: 01/03/2017 04:58
Subject: Request Permissions for Published Materials

[Quoted text hidden]

Appendix II: Two-dimensional scanning of PRESAGE® dosimetry using UV/VIS spectrophotometry and its potential application in radiotherapy.

IOP Publishing *Biomed. Phys. Eng. Express* **2** (2016) 045009 doi:10.1088/2057-1976/2/4/045009

Biomedical Physics & Engineering Express

PAPER

Two-dimensional scanning of PRESAGE® dosimetry using UV/VIS spectrophotometry and its potential application in radiotherapy

RECEIVED
2 May 2016

REVISED
28 June 2016

ACCEPTED FOR PUBLICATION
11 July 2016

PUBLISHED
29 July 2016

Esho Qasho Youkahana[1,3], **Frank Gagliardi**[1,2] **and Moshi Geso**[1,4]

[1] Medical Radiation Discipline, School of Health and Biomedical Science, RMIT University, Bundoora, Victoria, Australia
[2] Alfred Health Radiation Oncology, Melbourne, Australia
[3] Physics Department, Faculty of Science, University of Duhok, Duhok, Iraq
[4] Author to whom any correspondence should be addressed.

E-mail: esho.youkhana@rmit.edu.au, frank.gagliardi@wbrc.org.au and moshi.geso@rmit.edu.au

Keywords: PRESAGE®, CLARIOstar microplate reader, 2D UV/Vis spectroscopy

Abstract

The purpose of this investigation was to provide a high resolution 2D scanning feasibility study for PRESAGE® dosimeters using UV/VIS spectrophotometry. Previously the light absorbance of PRESAGE® has only been made at a single point using UV/VIS spectrophotometry. The CLARIOstar microplate reader can operate as a 2D scanning UV/VIS spectrophotometer measuring the light absorbance at multiple points of a PRESAGE® dosimeter. Water equivalent PRESAGE® dosimeters were fabricated in a rectangular shape and were irradiated with 6 and 18 MV x-ray beams using a medical linear accelerator. The optical density values of the PRESAGE® dosimeters were measured pre and post-irradiation using a CLARIOstar microplate reader. Depth dose curves and beam profiles were validated against ionisation chamber measurements. The agreement between the two dose measuring devices is well within experimental uncertainties. This investigation demonstrated that depth dose curves and beam profiles can be measured with high resolution in 2D for megavoltage x-ray beams with PRESAGE® dosimeters using UV/VIS spectrophotometry. Additionally, one PRESAGE® dosimeter was also fabricated with the inclusion of an inhomogeneity to investigate the effect on the dose distribution beyond the inhomogeneity. There is also the potential to extend this method to obtain 3D dosimetry scanning.

1. Introduction

Due to the current complexity in radiotherapy instrumentation, verification of radiation dose delivery as planned by the treatment planning system is challenging for techniques such as stereotactic radiosurgery, intensity modulated radiotherapy and volumaetric modulated radiotherapy [1]. Consequently new three-dimensional (3D) dosimetry systems such as gel and PRESAGE® dosimeter systems have been developed to potentially measure the dose distribution and/or the absolute dose delivered [2].

PRESAGE® is a 3D solid radiochromic dosimeter fabricated from clear polyurethane resin combined with a leuco-dye and halogenated carbons [3]. These dosimeters undergo a peak radiochromatic response around 633 nm and can be read using optical CT for 3D dose distribution measurements [4] or UV/VIS spectrophotometry for single point dose measurement [5], and confocal fluorescence microscopy for high resolution [6].

The advantages of PRESAGE® dosimeters over other dosimeters are that they are solid, not sensitive to oxygen, easy to handle, sub-mergeable in water, can be fabricated to any size or shape and optically clear which allows light to pass through with minimum artifacts. In addition PRESAGE® can be formulated to be radiologically tissue or water equivalent [7].

The conventional technique of reading PRESAGE® is with a UV/VIS Spectrophotometer [8]. The main limitation of this technique is the fact that the optical density (OD) is a measure per single point through the whole of the cuvette. Other methods to read PRESAGE® are optical computed tomography (OCT) and laser fluorescence confocal microscopy (LFCM). OCT allows for 3D dose measurements however the optical CT scanner, reconstruction software and chemicals needed for optical compatibility can be

Appendix III: Permission to reproduce published materials in chapter 3, 4, 5 and 6.

RMIT UNIVERSITY

Esho Youkhana <esho.youkhana@rmit.edu.au>

RE: [IJMS Inquiry] Request Permissions for Published Materials

IJMS Publishing Team <ijms@medsci.org> 16 July 2017 at 09:43
To: esho.youkhana@rmit.edu.au

Thanks for your email. As an author or co-author of the article, you are free to include or reuse the materials in other articles or thesis or other publications that you write, with citation of the original source. There is no need to obtain permission since permission is automatically granted.

Kind regards,
Publishing Team
International Journal of Medical Sciences
http://www.medsci.org

-----Original Message-----
From: International Journal of Medical Sciences [mailto:ijms@medsci.org]
Sent: Friday, July 7, 2017 12:40 AM
To: ijms@medsci.org
Subject: [IJMS Inquiry] Request Permissions for Published Materials

Dear Si/Madam,

I am PhD student from RMIT University, Melbourne-Australia. I have published a paper in International Journal of Medical Sciences, titled:

"Titanium Dioxide Nanoparticles as Radiosensitisers: An In vitro and Phantom-Based Study"

Author(s): Esho Qasho Youkhana, Bryce Feltis, Anton Blencowe, Moshi Geso
doi: 10.7150/ijms.19058
Published on 15 May 2017 - 14(6): 602-614

I just need a permission to reproduce part of these published materials in my thesis. Kindly can you provide me a permission letter?

Kind regards
--
Esho Youkhana
PhD Student
Bulding 214, Postgraduate Room
School of Health and BioMedical Sciences
RMIT university-Bundoora West Campus
Victoria, Australia
Mob. 0061414418806

Sender record
Name: Esho Qasho Youkhana
Sender Email: esho.youkhana@rmit.edu.au
Sender Host: 115.70.150.150
Sender Institution: RMIT University -Australia

Subject category: Reprints/permissions/subscriptions

Appendix IV: Titanium Dioxide Nanoparticles as Radiosensitiser: An *In vitro* and Phantom-Based Study.

Int. J. Med. Sci. 2017, Vol. 14 602

IVYSPRING INTERNATIONAL PUBLISHER

International Journal of Medical Sciences

2017; 14(6): 602-614. doi: 10.7150/ijms.19058

Research Paper

Titanium Dioxide Nanoparticles as Radiosensitisers: An *In vitro* and Phantom-Based Study

Esho Qasho Youkhana[1], Bryce Feltis[2], Anton Blencowe[3], Moshi Geso[1]✉

1. Discipline of Medical Radiations, School of Health and Biomedical Sciences, RMIT University, Bundoora, Victoria, Australia;
2. Pharmaceutical Sciences Discipline, School of Health and Biomedical Sciences, RMIT University, Bundoora, Victoria, Australia;
3. School of Pharmacy and Medical Science, Division of Health Sciences, The University of South Australia, Adelaide, SA 5000, Australia.

✉ Corresponding author: A/Prof Moshi Geso, Tel: +61401730320, Email: moshi.geso@rmit.edu.au

Received: 2017.01.05; Accepted: 2017.03.29; Published: 2017.05.15

Abstract

Objective: Radiosensitisation caused by titanium dioxide nanoparticles (TiO_2-NPs) is investigated using phantoms (PRESAGE® dosimeters) and *in vitro* using two types of cell lines, cultured human keratinocyte (HaCaT) and prostate cancer (DU145) cells.

Methods: Anatase TiO_2-NPs were synthesised, characterised and functionalised to allow dispersion in culture-medium for *in vitro* studies and halocarbons (PRESAGE® chemical compositions). PRESAGE® dosimeters were scanned with spectrophotometer to determine the radiation dose enhancement. Clonogenic and cell viability assays were employed to determine cells survival curves from which the dose enhancement levels "radiosensitisation" are deduced.

Results: Comparable levels of radiosensitisation were observed in both phantoms and cells at kilovoltage ranges of x-ray energies (slightly higher *in vitro*). Significant radiosensitisation (~67 %) of control was also noted in cells at megavoltage energies (commonly used in radiotherapy), compared to negligible levels detected by phantoms. This difference is attributed to biochemical effects, specifically the generation of reactive oxygen species (ROS) such as hydroxyl radicals (·OH), which are only manifested in aqueous environments of cells and are non-existent in case of phantoms.

Conclusions: This research shows that TiO_2-NPs improve the efficiency of dose delivery, which has implications for future radiotherapy treatments. Literature shows that Ti_2O_3-NPs can be used as imaging agents hence with these findings renders these NPs as theranostic agents.

Key words: Titanium dioxide, Nanoparticles, Reactive oxygen species, Radiosensitisation.

Introduction

There have been various advancements in the field of radiotherapy resulting in safer and more reliable treatments [1]. Most of these developments have been technological improvements used to confine the beams to the targets and reduce radiation damage to the surrounding healthy tissues [2]. However, these technological improvements can also be combined with an advanced understanding of tumour radiobiology to provide the greatest impact on treatment regimens [3, 4]. Thus, improving the efficiency of radiotherapy treatments requires a combination of these complementary approaches, such as the use of radiosensitisation agents [4].

Tumour radiosensitivity can be modified by agents, which enhance the radiation effects in the tumour, with the objective of delivering efficient radiation doses that can eradicate cancer cells without exceeding normal tissue tolerances [5]. In many cases the radiosensitising agents can selectively target tumour cells [4]. Currently, some radiosensitising agents, such as fluorouracil are used clinically particularly in adjuvant radiotherapy treatments [4].

Early investigations used high atomic number (Z) materials [4], such as gold with the aim of increasing the cross-sectional radiation interaction and production of free radicals, which enhances radiation dose through extra photoelectron production [6-11]. As the increase in cross-sectional